12-1-2012

Molecular Forensic Science Analysis of Nuclear Materials

Dallas Reilly
University of Nevada, Las Vegas

MOLECULAR FORENSIC SCIENCE ANALYSIS

OF NUCLEAR MATERIALS

By

Dallas David Reilly

LA-UR: 12-27106

Bachelor of Arts
Carthage College
2008

A dissertation submitted in partial fulfillment
of the requirements for the

Doctor of Philosophy in Radiochemistry

Department of Chemistry
College of Sciences
Graduate College

University of Nevada, Las Vegas
December 2012

UNLV
UNIVERSITY OF NEVADA LAS VEGAS

THE GRADUATE COLLEGE

We recommend the dissertation prepared under our supervision by

Dallas David Reilly

entitled

Molecular Forensic Science Analysis of Nuclear Materials

be accepted in partial fulfillment of the requirements for the degree of

Doctor of Philosophy in Radiochemistry
Department of Chemistry

Kenneth Czerwinski, Ph.D., Committee Co-Chair

Kenton Moody, Ph.D., Committee Co-Chair

Julie Gostic, Ph.D., Committee Member

Marianne Wilker, Ph.D., Committee Member

Steve Conradson, Ph.D., Committee Member

Ralf Sudowe, Ph.D., Graduate College Representative

Tom Piechota, Ph.D., Interim Vice President for Research &
Dean of the Graduate College

December 2012

ABSTRACT

Molecular Forensic Science Analysis of Nuclear Materials

By

Dallas D. Reilly

Dr. Kenneth R. Czerwinski, Examination Committee Chair
Professor of Chemistry
Chair of the Department of Radiochemistry
University of Nevada, Las Vegas

Concerns over the proliferation and instances of nuclear material in the environment have increased interest in the expansion of nuclear forensics analysis and attribution programs. A new related field, molecular forensic science (MFS) has helped meet this expansion by applying common scientific analyses to nuclear forensics scenarios. In this work, MFS was applied to three scenarios related to nuclear forensics analysis. In the first, uranium dioxide was synthesized and aged at four sets of static environmental conditions and studied for changes in chemical speciation. The second highlighted the importance of bulk versus particle characterizations by analyzing a heterogeneous industrially prepared sample with similar techniques. In the third, mixed uranium/plutonium hot particles were collected from the McGuire Air Force Base BOMARC Site and analyzed for chemical speciation and elemental surface composition. This work has identified new signatures and has indicated unexpected chemical behavior under various conditions. These findings have lead to an expansion of basic actinide understanding, proof of MFS as a tool for nuclear forensic science, and new areas for expansion in these fields.

ACKNOWLEDGEMENTS

This work could not have been completed without the help and support of the mentors and colleagues that have helped me along the way. I would like to express my gratitude to my advisor, Ken Czerwinski who has been a phenomenal mentor and has helped me grow into the scientist I am today. Perhaps more importantly, he established the extremely successful radiochemistry program that spurred my graduate career. At the end of my second year of graduate work, I was lucky enough to continue and expand my work to Los Alamos National Laboratory. I am grateful for this opportunity; LANL allowed me to work with scientists at the top of their fields. I would like to acknowledge Olga Batuk, Alison Costello, Will Kinman, Brian Scott, and Greg Wagner, who each played a role in my progression at LANL. Steve Conradson, one of the most experienced and knowledgeable EXAFS scientists in the world, served as my "EXAFS advisor" and committee member. Marianne Wilkerson served as my advisor during my time at LANL and on my thesis committee. I was one of her first students, but she has been one of the best mentors I've ever had. Her insights in science, networking, and project organization have been invaluable. I would also like to thank the remaining members of my thesis committee. Ralf Sudowe has provided a wealth of knowledge during my graduate career, from my course work to my research. Julie Gostic not only provided valuable comments on my work, she was also a mentor during my time at UNLV. I am also fortunate enough to have Kenton Moody on my committee, who literally wrote the book on nuclear forensics. His knowledge of actinide science and nuclear forensics has been a big help.

At each step in my life, I have considered myself lucky. I have worked hard, but the credit should go to my friends and family. Without their help, love, and support, I would not have completed this journey. I came from small beginnings, but with the support my parents, Dave and Lisa Reilly; I have come this far and will continue to honor them, my many friends, colleagues, and mentors by continuing to further myself as a scientist and person.

TABLE OF CONTENTS

LIST OF TABLES

LIST OF FIGURES

CHAPTER 1

INTRODUCTION

1.1 Justification of Work

The work presented in this dissertation centers on a new and increasingly critical field of study developing as part of an expansion of current state of the art nuclear forensics and attribution programs, molecular forensic science (MFS). This field seeks to provide information and develop new signatures for nuclear forensics based on the chemical speciation, structure, morphology, and trace composition of nuclear materials. Although these analyses can be applied to many nuclear forensics scenarios, the work discussed herein is only concerned with pre-detonation materials. Pre-detonation interdiction scenarios typically rely on traditional criminal forensics, intelligence gathering, and standard nuclear forensics. The latter relies heavily on isotopic information through radiometric and mass-based analyses[1, 2]. Isotopic analysis yields information on reactor type, sample irradiation time, age, and level of enrichment. This evidence can imply intent and answer other questions vital in nuclear forensics scenarios[1, 3-9]. Obviously, these aspects of nuclear forensics are extremely important and functional, but methodologies identifying the chemical nature of interdicted materials are only loosely and sparingly applied[1, 4, 5, 10]. Understanding this chemical information is important because the extensive history of most actinide materials provides for information that aids nuclear forensics information gathering. Table 1 outlines the basic steps in mining, fabrications, and reprocessing including the types of compounds produced and some examples within those categories.

Table 1. The general processes involved in the nuclear fuel cycle including the types of compounds in each step and more specific examples of those compounds[11, 12].

Process	Category	Example Compounds
Mining	Uranium Ores	Hundreds of Minerals[13, 14]
Milling	"Yellowcake"	Uranium Oxides, Carbonates, Nitrates
Conversion/ Enrichment	Fluorides or Oxides	Uranium Fluorides, Oxides
Fuel/Weapon Fabrication	Fuels and Metals	Oxides, Alloys, Metals, Mixed Oxides
Dissolution/ Separation	Aqueous Species/ Organics	Aqueous Species, Organic Complexes
Precipitation/ Concentration	Precipitates	Oxalates, Peroxides, Nitrates, Carbonates
Waste Preparation	Waste Forms	Glasses, Aqueous Species, Other Solids

Uranium is extracted with a multitude of mining techniques and leaching methods[12]. The resulting ore is further converted to “yellowcake”-like compounds that can have a specific set of contaminants and chemical forms based on the converting entity’s preferred processes and the geographic location from which it was mined. Yellowcake is then converted to uranium hexafluoride; again, this can depend on an entity’s preferred methods of processing, resulting in specific signatures to the origin of the material[14-18]. Finally, uranium hexafluoride is enriched to various levels for assorted purposes. It is enriched for civilian energy (low levels of enrichment on the order of 5% ^{235}U), research reactors (on the order of 20% ^{235}U)[9, 12], and more highly enriched for naval reactors[19] or nuclear weapons[20]. Plutonium is treated with various chemical procedures to produce mixed fuels, metal-based fuels, or weapons material after being separated from irradiated fuel. Furthermore, due to the complex chemical nature of many actinide

compounds, materials produced at given points along a processing scheme are not inert and may react to form other species based on exposure conditions. The picture is clear: studying chemical information of nuclear materials provides vital details[21-23] or can confirm conclusions gathered from intelligence and isotopics that traditional nuclear forensics analyses might otherwise neglect.

In recent decades the U.S. government and international entities have identified the need for a current and competent nuclear forensics and attribution programs, which include the expansion and development of new techniques. The major legislation to outline and direct this expansion within the U.S. was the Nuclear Forensics and Attribution Act, House Resolution 730[24]. This act outlined responsibilities for the Department of Homeland Security and the National Technical Nuclear Forensics Center including the development and implementation of capabilities in order to support source term attribution and the improvement and integration of new capabilities. The Nuclear Security Summits of 2010 and 2012 highlighted nuclear forensics as an important aspect of countering illicit trafficking, as well as the importance of collaboration and the need to develop capabilities[25, 26]. It is apparent that the need for research that expands these capabilities, such as the work presented herein, is essential to meet these goals.

1.2 Molecular Forensic Science

Molecular Forensic Science is the combination and application of techniques common in other scientific fields that probe material for chemical speciation, morphology, and trace elemental content that contributes to the chemical form in

order to expand the state of the art role of nuclear forensics. In many ways MFS overlaps with environmental science of nuclear materials. Environmental analyses seek to project into the future and understand the fate and transport of nuclear materials in environmental systems. Using the same techniques, MFS seeks to look into the past of nuclear materials in order to answer questions pertinent to nuclear forensics. This can include material origin, intended use, utilized chemical processes, and information related to storage. The overlap in identifying where a material has been and where it is going in these fields extends to the techniques used (Table 2).

Table 2. Some analytical techniques applicable to MFS along with the chemical information they yield.

Technique	**Information**
X-Ray Diffraction	Long Range Order/Chemical Structure, Relative Mixture Ratios, Crystallite Size
X-Ray Fluorescence Analyses	Surface Composition, Fractionation, Presence of Elements
Energy Dispersive X-Ray Spectroscopy	Surface Composition, Fractionation, Presence of Elements
X-Ray Absorption Near Edge Structure Spectroscopy	Oxidation State, Some Structure Information
Extended X-Ray Absorption Fine Structure Spectroscopy	Local Structure, Bonding, Elemental or Structural Contributions
Infrared Spectroscopies	Molecular and Lattice Vibrations
Scanning Electron Microscopy	Particle Size, Particle/Grain Shape, Morphology
Light-Scattering Particle Size Distribution	Particle Size Distribution, Ease of De-Agglomeration
Thermogravimetric/Differential Thermal Analyses	Hydration/Energy Information
Mass Spectrometry	Trace Element Content, Isotopics
Secondary Ion Mass Spectrometry	Elements/Isotopic Maps

Environmental sciences have employed most of these techniques successfully, but the application of the same techniques to nuclear forensics is still in the research and development stage. Not only does the work herein serve as a proving ground for this research and development, but it also provides for new areas and signatures related to this work that can be expanded upon in the future. Obstacles in using many of the techniques mentioned in Table 2 stem from lack of standards and understanding of their selectivity, sensitivity, and reproducibility. The research presented in Chapter 3 seeks to use well-controlled conditions and highly pure starting materials to establish some base for standard compounds. The research discussed in other chapters seeks to avoid this issue by analyzing materials with well-known history. Throughout this work (and in the expansion of MFS), the selectivity, sensitivity, and reproducibility are a main concern.

There is a wealth of chemical information that is rarely sought after in nuclear forensics scenarios. Predominant are X-ray analyses such as X-ray fluorescence (XRF), X-ray diffraction (XRD), and X-ray absorption spectroscopy techniques, namely extended X-ray absorption fine structure (EXAFS) spectroscopy. This work will include discussions and applications of both synchrotron-based and in-house analysis techniques.

In synchrotron-based XRF, a monochromatic X-ray is rastered over a sample surface, ionizing an atomic electron shell. This ionization causes characteristic X-ray emissions, which are detected to construct elemental surface maps. Surface composition helps identify unexpected elements in a sample and when used as part of an imaging system, can identify mixtures of elements on the surface of materials

and any fractionation or separation that may have occurred during the material's history. As a standalone analysis, the utility of XRF is apparent. Section 1.3.4 discusses a number of scenarios in which XRF was vital to determining source term information on actinide particles. Synchrotron-based XRF is especially advantageous because of the high intensity of synchrotron X-rays, ability to tune photon energy allowing for elimination of interfering element fluorescence, and the ability to use fluorescence maps to select specific areas for chemical speciation analyses. Section 2.8.2 gives a more technical description of this technique.

The two techniques for chemical speciation that will be of particular importance within this work are XRD and EXAFS. X-ray diffraction is a well-characterized and accessible technique[27] that probes for long-range order to determine structure and mixtures of compounds and in some cases can give relative concentrations of those mixtures. EXAFS probes for local chemical structure and can be applied to a much larger range of materials, i.e. amorphous and liquid samples. A faster analysis that only looks at the near edge of absorption spectra, X-ray absorption near edge structure (XANES) spectroscopy also has its place in MFS[28-31]. When characterized standards are used along with samples, one can discern relative oxidation states. EXAFS will be discussed more thoroughly in the following chapter, and XANES will be mentioned as part of a background investigation into some previous studies related to this work. Both EXAFS and XANES are primarily synchrotron-based techniques. The majority of the XRF analysis and some of the XRD analysis were performed at a synchrotron as well. Synchrotron work was performed at the Stanford Synchrotron Radiation Lightsource (SSRL).

In addition to the X-ray techniques discussed above, MFS encompasses many other methods. In this study scanning electron microscopy (SEM) was used to qualitatively examine morphology and particle size. Energy dispersive X-ray (EDX) spectroscopy is a fluorescence measurement capability common on SEM systems, and was used in this work to further probe areas with interesting morphology or unusual elemental signatures. Laser scattering analysis was also used to study particle size, distribution, and ease of breakup of agglomerated particles. Inductively coupled plasma mass spectrometry (ICP-MS) was used to examine trace element content. The benefits and limitations of these tools will be discussed within this work. Although not used within these studies, some of the techniques listed in Table 2 would help expand this type of research. Some examples include XANES, infrared spectroscopies, thermogravimetric analysis, differential thermal analysis, and secondary ion mass spectrometry (SIMS)[32-34]. The analyses that are discussed in this manuscript were applied to both bulk and particle investigations.

1.3 Background

1.3.1 Introduction

The information discussed in this section will include solution (including material describing colloid formation for actinides of concern) and solid phase chemistry for uranium and plutonium, as well as a review of previous particle work. A discussion of uranium and plutonium in both solution and solid phases is important for this work for two reasons. First, in the environment the forms being studied (particles or precipitates) often either initially originate from aqueous

solutions or they are frequently exposed to aqueous conditions such as rain and other precipitation that could affect their chemical state and behavior over time. Second, the chemical speciation discussed herein is primarily focused on uranium and plutonium oxides, so inclusion of some background the chemistry of these compounds is vital for this work.

Environmental plutonium has been described by Choppin[35] as being in two categories: 1) source independent - in equilibrium with its environment after some interactions, typically from waste scenarios, and 2) source dependent - in a state of equilibrium based on where it originated; it has changed little in the environment (i.e. high fired oxides)[36]. This qualification can be applied to the other actinides such as uranium. Beyond this simple classification, many geochemical reactions affect actinide speciation in the environment including redox reactions, solubility of species and their hydrolysis products, complexation, sorption of species and hydrolysis products, colloid formation, and microbial interaction[36]. These interactions seem daunting, so a simple way to imagine these systems is to group into one of three categories: 1) ionic/molecular/polynuclear species in solution, 2) mobile and immobile colloidal species that can be considered soluble solid phases, and 3) immobile solid phases[37].

1.3.2 Solution Phase Chemistry

Uranium and plutonium cations are considered hard acids, so they form preferential bonds with hard bases like oxygen and fluorine (water, hydroxide, fluorides, oxides, etc.), with the bond strength depending on effective nuclear charge.

Pentavalent and hexavalent ions form AnO_2^+ and AnO_2^{2+} in solution (where An is an actinide). The effective nuclear charges of commonly available species are usually ordered as follows: An^{4+} > AnO_2^{2+} > An^{3+} > AnO_2^+[18, 38, 39]. This trend in complexation strength is the major factor in the hydrolysis, colloid formation, and sorption of actinides. At naturally occurring pH values (6-9) hydrolysis is significant except for the pentavalent state.

Plutonium has the (III), (IV), (V), (VI), and (VII) oxidation states available in solution[18, 40]. In natural waters it is usually in two or three states at once[35]. Most environmental plutonium exists in marine waters[41] and is associated with humic substances[42]. In these waters, dissolved plutonium is most common in the pentavalent state[43-46], but depending on conditions both reduced and oxidized species have been seen. These are typically limited by the insolubility of hydrolysis products such as $Pu(OH)_4$[35], which over time becomes less soluble due to the formation of PuO_2(aq), which is even more insoluble and the most kinetically stable form of plutonium[35]. In sediments, plutonium is likely to exist in the tetravalent state[40, 43, 47].

Uranium in solution also exists in the (III), (IV), (V), and (VI) oxidation states, but only the tetravalent and hexavalent are of interest. The trivalent is easily oxidized and the pentavalent state has a small window of occurrence (disproportionation)[18]. The most stable form of uranium in natural waters is the hexavalent oxidation state, which as noted above exists as UO_2^{2+}. Both the tetravalent and hexavalent oxidation states of uranium easily hydrolyze, but unlike

plutonium hydrolysis products, these cations form mostly dissolved aqueous species under environmental conditions[48-50].

Colloid formation can be an important step on the route to particle formation and has a large impact on actinide migration. Extensive work has been performed on actinide colloids in the environment[51-62]. For this work, actinide colloid formation is important due to the affects on particle formation and mobility in the environment. Actinides form colloids by sorbing onto groundwater colloids or if their concentration is high enough, they undergo polymerization, hydrolysis, or precipitation in solution to form true colloids[52, 59]. Tetravalent actinide colloid formation over time can cause the increase in solubility of the oxide or hydroxides from the colloid species resulting in equilibrium of ions/colloids/precipitates making the prediction of these species difficult. Tetravalent plutonium colloids have been characterized extensively by Cleveland[63]. They are produced in neutral solutions and are stable over time. In one study tetravalent plutonium was seen as small discrete particles of both amorphous and crystalline structure[58]. The hexavalent species also hydrolyze easily[51] and can form colloids. Pentavalent oxidation states are most stable against hydrolysis due to their low effective nuclear charge[57]. Colloid formation of uranium species is less common due to the higher solubility, but it should still be included in particle formation discussions, especially when in the presence of other actinide species. A comprehensive discussion of colloids is not necessary for this work as the primary concerns are the affects of colloids on the particle formation, speciation, and migration of actinides in the environment.

Understanding chemical speciation and how species are affected by the conditions in a given environment are vital to understanding potential particle formation and subsequent migration. Analysis of actinides in the environment has spanned from simple Geiger counters to more advanced radiometric counting techniques and finally to advanced separation and counting methods with the aid of high purity tracers and dilution standards[64, 65]. These techniques have worked in gathering very basic chemical speciation information, but are not of the highest confidence due to the processes involved (pH changes, separation efficiencies, etc.). Some spectroscopic techniques are less destructive, but the most common historically, UV-Visible absorption analysis is sometimes inadequate for environmental scenarios due to the low concentrations of actinides in the environment. Laser-based techniques can have a lower detection limit and analyze a range of oxidation states and species[66-69].

Many studies of environmental actinides rely on radiometric counting methods and very low concentrations can be probed with the use of preconcentration and microprecipitations, but dissolution changes chemical speciation. Methods to characterize colloids for size distribution include SEM with ultrafiltration[70], light scattering techniques[70, 71], photon correlation spectroscopy, photoacoustic detection of light scattering[72], and laser-induced breakdown spectroscopy[73, 74]. The chemical speciation analyses discussed herein work well because they can probe environmental samples directly (soils, solutions, polymers), but must be applied to fairly concentrated samples because of the higher detection limits.

1.3.3 Solid Phase Chemistry

The solid phase chemical behavior of uranium and plutonium is complicated and dynamic. Their oxides make up a large majority of environmental and commercial uranium and plutonium compounds. Table 3 and Table 4 summarize the most common oxides along with their number of polymorphs and note whether hydrolysis is common.

Table 3. Common oxides of uranium. The number of polymorphs and the possibility of hydrolysis are noted for each oxide. This data was interpreted from Section 5.7.2 of the Chemistry of the Actinides and Transactinides[18].

Oxides	UO_2	UO_{2+x}	U_4O_9	U_3O_7	U_3O_8	UO_3
Polymorphs	1	NA	3	3	2	7
Hydrolysis	No	No	No	No	No	Yes

Table 4. Common oxides of plutonium. The number of polymorphs and the possibility of hydrolysis are noted for each oxide. This data was interpreted from Section 7.8.5 of the Chemistry of the Actinides and Transactinides[18].

Oxides	Pu_2O_3	PuO_{2-x}	PuO_2	PuO_{2+x}
Polymorphs	2+	1	1	1
Hydrolysis	No	No	No	Yes

The oxides exist in some capacity in many chemical and structural forms in nature, although plutonium only exists in very small quantities due to nuclear reactions of uranium[13, 14]. The metals of both uranium and plutonium are pyrophoric and rapidly oxidize to a stable oxide form when introduced to oxygen and/or water. As noted in Table 3, there are a number of common uranium oxides. Some of these have multiple phases, hydrolysis products, intermediates, and mixed phases[14, 75]. This variety results in dozens of possible compounds. The stable plutonium oxides are shown in Table 4. Although there are fewer identified compounds, they are much more ambiguous. There is some debate over the

sesquioxide polymorphs, their occurrence, and their synthesis. There is a range of intermediate compounds between the sesquioxide and the dioxide compounds. Finally, there is still some discussion on what the most highly oxidized solid state form is, and that structure has still not been definitively determined[18].

The oxidation of these actinides has been a focus of many research efforts over the years, but there are still gaps in their understanding. A number of studies have sought to model the kinetics and oxidation of uranium oxides[76-79], with the most recent by Andersson et al employing density functional calculations and the introduction of interstitial oxygen defect clusters to model the oxidation of UO_2 to U_4O_9[80-82]. Similar theoretical work with plutonium is ongoing. Extensive experimental studies, both controlled laboratory conditions[83-86], and more complicated environmental or oxidizing conditions[17, 87-91] have also been performed. The large body of work into this area underscores the complexity of these binary systems.

The endpoint for uranium oxidation is generally accepted to be uranyl oxy-hydroxide[18, 92-94], $UO_3 \cdot xH_2O$. Historically the accepted plutonium oxidation endpoint has been PuO_2, but recent studies have determined that hyperstoichiometric plutonium dioxide, PuO_{2+x} (where $x \leq 0.27$) is the more stable form under many conditions, especially when found in the environment or after high-firing scenarios[18, 92-96]. The final form and time to reach the endpoint for these actinides are highly dependent on the source material and surrounding conditions. Often, the primary factors are starting material, temperature, and relative humidity. In more complex environmental scenarios, soil pH, redox

conditions, and microbial activity also play a role[23]. Furthermore, particle size, shape, and oxidation gradients through a particle, powder, or pellet can lead to breaking up and therefore increased weathering, oxidation, or greater ease in physical movement[10, 23]. Their chemistry is further complicated by the interaction of plutonium and uranium with one another[10, 97-101] and other materials within their vicinity.

1.3.4 Particles: Particle Versus Bulk and Previous Particle Work

Since the dawn of the nuclear era, uranium and plutonium have been distributed in the environment due to nuclear weapons testing, accidents with nuclear weapons, and activities associated with the nuclear fuel cycle[102]. Most of the investigations of actinides in the environment have been concerned with bulk analysis. Sometimes there is confusion over what this term, "bulk analysis" actually refers to. It could mean a large amount of material used for analysis, but more often in the nuclear forensics realm the term is used to describe a representative sample. What quantity of material is considered representative is relative to each scenario. In many environmental and forensics scenarios, bulk may refer to a few grams of soil as opposed to a few single particles. Bulk measurements have included a range of analytical techniques with some based on mass or radioactivity for isotopic analysis, while others probe for chemical speciation with those same techniques, or other methods as outlined in Table 2. The drawback with bulk analysis in these scenarios is the assumption that actinides in the environment have a homogeneous distribution and that the average chemical speciation of a bulk sample represents

the true nature of the samples in question. It has been shown in many studies that the bulk of environmental contamination exists as particles[10, 22, 43, 103-105]. For the studies discussed herein, particles are considered on the order of a micron to millimeters in diameter. These particles are commonly heterogeneous with respect to their size, composition, chemical speciation, and distribution within a location of interest[23]. Heterogeneities can not only result in misleading or anomalous data for bulk measurements, but failing to study individual particles can mean missing out on more information about a material[102]. In order for molecular forensic science to contribute to the field of nuclear forensics, the techniques must be applied to both bulk and particle analyses. This section will discuss particle formation, previous works relating to actinide particles in the environment, and how the chapters concerned with particles within this manuscript can not only improve and expand upon the previous studies, but also contribute to nuclear forensic science.

As mentioned in Section 1.3.2, one route of particle formation results from aggregation of colloids or the sorption of these species or their colloids onto insoluble materials. A few important routes of heterogeneous particle formation include anomalies in typical processing methods (Chapter 4) and the high firing of uranium and plutonium metals (Chapter 5). For the former, any number of processes can form particles of varying chemical speciation, morphology, trace element content, and particle size distribution. For the latter, there are a number of nuclear material accidents that have caused the spread of heterogeneous particles over large areas[106, 107]. Other routes of formation include weapons testing and

nuclear fuel cycle activities. The author has been involved in the analysis of particles from many sites resulting from various formation scenarios, but most of that work will not be discussed in this manuscript.

The particle analyses discussed herein are directed primarily at chemical speciation and composition. There are basic analyses that the author had access to including morphological imaging, trace element, and size distribution analyses that will also be discussed, but because these are relatively well characterized throughout the literature, only a selective comparison with previous work in these areas will be incorporated. Other aspects common in actinide particle analyses that will not be considered are radiometric counting, in-depth mass analysis, isolation, and separation techniques.

Particles from weapons testing sites including Maralinga, Australia[108-111], the Marshall Islands[112-114], the Nevada Test Site, now called the Nevada National Security Site[106, 107], atolls in French Polynesia[22, 105, 115], Semipalatinsk, Kazakhstan[98, 100, 116, 117], and Novaya Zemlya, Russia[118] have been studied previously. These studies included elemental/surface composition analyses with SEM (and EDX), SIMS, synchrotron-based XRF, and a range of nuclear counting studies. Although surface composition was established as an excellent tool for the analysis of radioactive particles, no chemical speciation information was gained.

Accidents from nuclear reactor accidents have produced particles[119, 120]. The Chernobyl accident is of particular importance because of the speciation analyses included in the evaluation of resulting particles. Particles were characterized similarly to those from weapons tests. The results were used to estimate locations

within the accident, timeline of formation, and temperatures involved in the accident[10, 102, 121]. The work discussed herein will not broach that subject, but it should be noted that chemical speciation and surface composition can lead to important details on the formation and source term of actinide particles from accidents involving high temperatures.

Chemical speciation of uranium deposited in the environment was undertaken in some studies[98-101]. Those works by Salbu et al used XANES, μ-XANES, and μ-XRF to identify two types of particles from the accident: ones with a UO_2 core and an oxidized surface (up to U_3O_8), and ones with a UO_2 core with a reduced surface. The reduced surface may have originated from interaction with carbon or zirconium. These elements were correlated in the studies in question, possibly indicating that reduced states of other elements may prevent oxidation of actinides, or that their oxidation reduces uranium. This phenomenon of correlated elements preventing oxidation is important and will be discussed in more detail in Chapter 5. Discovery of these two particle types are consistent with the information available on the release of materials from the site[98-101, 122]. It is evident that bulk analysis alone may not have been able to differentiate between these two types of particles. Instead, analyzing for particles led to additional information for environmental impact assessments and detailed data on their sources.

Incidents involving accidental release of material from non-nuclear weapon destruction and use of depleted uranium munitions have resulted in hot particles in some areas. A weapons accident in Thule, Greenland produced particles that were studied with imaging techniques as well as μ-XANES[22, 123]. The use of XANES

showed that uranium was in the tetravalent state, while plutonium particles were either made up of mostly the tetravalent species or in a 1:2 mixture of tetravalent:hexavalent. Depleted uranium particles from munitions left over in Kuwait and Kosovo were also studied with μ-XANES and μ-XRD[124-126]. The outcome from these analyses was that the resulting particles were highly dependent on the source term. It is clear that identifying source term information is vital for both forensics and environmental impact assessments.

Chemical speciation analysis has only been performed on a few environmental actinide particle scenarios. When chemical speciation was probed, it was only performed with XANES and XRD. These two methods worked well in gaining information for remediation efforts, health concerns, and characterization of source terms, but there is more information to be obtained. Results from XANES analysis are highly dependent on the ligands of the absorbing atoms, which are not always definitive from XRD and XANES alone. For example, a U(IV) species may look more like U(V) or even U(VI) depending on the chemical speciation of uranium in the sample. If EXAFS were used, both the oxidation state and chemical speciation would be probed, allowing for this differentiation. Furthermore, the more in depth characterization that EXAFS provides would have not only gained more information for the studies' intended purposes, but also expanded knowledge of the basic chemistry and formation of actinide particles in the given scenarios. In this work, the use of XRF, XRD, and especially EXAFS will have a major contribution to studies of similar scenarios and the future of this area of study.

1.4 Research Overview

1.4.1 Research Goals

Occasionally, the investigations involving nuclear material interdictions include some aspects of MFS, but when used they suffer from inconsistent application and a lack of optimal integration[1, 4-6, 8, 10, 127]. Due to this lack in understanding and the relatively new approach of looking for molecular signatures for forensics analyses, the work presented herein serves as a proving ground and establishment of basic systems to add to the current melee of nuclear forensic science. By probing for chemical speciation, MFS can imply information regarding a material's history that criminal forensics and isotopic analysis might not even seek to discern. Molecular analysis may pinpoint a specific process that a material underwent based on chemical speciation, structure, or trace analysis. Some techniques might work better in a given scenario than others, so seeking a consistent method of integration is vital to the field. If all useful techniques are streamlined as part of a nuclear forensics analysis scenario, it will be hard to miss important chemical information. The body of research discussed here seeks to establish a protocol for just a few of the possible analytical methods available for molecular forensics analysis.

Although forensics analysis is the primary focus, it should be noted that this work also serves to fill gaps in the understanding of uranium and plutonium oxides and their subsequent oxidation under various conditions. This work seeks to gain a better understanding of this basic chemical behavior not only to expand the basic knowledge of these systems, but also aides in answering questions related to

nuclear forensics of these materials. The specific projects and their relevance are outlined in sections 1.4.2-1.4.4.

1.4.2 Thesis Organization

This dissertation includes seven chapters in total with Chapter One being this introduction, Chapter Two outlining the materials, methods, and instrumentation used, Chapters Three to Chapter Six discussing the projects for this dissertation, and Chapter Seven being the conclusion and discussion of future work. The following sections briefly outline the projects in Chapters Three through Chapter Six.

1.4.3 Aging of Uranium Dioxide Under Various Conditions

Information important to nuclear forensic science make the understanding of uranium and plutonium oxides aging of paramount importance. Not only is this information important to nuclear forensics, but also stockpile stewardship, environmental impact assessments, nuclear nonproliferation, and fuel/waste storage. If a highly oxidized form or a compound with unusual oxidation is discovered, MFS is only worth using if there is an understanding of how the original source reached the form it was discovered in. Because of this, an analysis of the environmental aging of uranium oxides has been performed. As shown in Table 3, uranium oxides fall under a number of common forms. In addition, those forms are expanded by the existence of various polymorphs and hydrolysis products. In order to study the transformation of these compounds to more highly oxidized species UO_2 and U_3O_8 were prepared. Amorphous UO_3 was also prepared to study its

hydrolysis. To mimic a range of atmospheric conditions, aging vessels were set up to produce a specific and static set of temperatures and relative humidities to contain and age these compounds. The compounds were analyzed at regular time intervals to study their chemical transformations over the course of two years. Analyses included EXAFS, XRD, and SEM. This project also included the aging of five samples from industrially prepared processes, but they will not be discussed within this manuscript.

1.4.4 Particle Analysis of a Heterogeneous Industrial Sample

One of the challenges in nuclear forensics analysis or studies related to environmental concerns is sample heterogeneity. Bulk samples may or may not appear to be chemically homogeneous but are sometimes composed of materials of varying chemical makeup. In uranium processing conditions, heterogeneity can result from a number of means including use of different starting materials, mixing post-process material, or variance in a process. Characterization of these materials can provide even greater source term information, but their analysis can be much more difficult. As was discussed in Section 1.3.4, there has been marked interest for distinguishing between bulk and particle data and increasing the overall efficacy of particle analysis. The work in Chapter 4 is an excellent proof of practice for MFS particle characterizations.

As a portion of the author's work, a large number of samples prepared under typical industrial processes were available and analyzed with a number of analytical tools. One of these samples was clearly heterogeneous to the naked eye. It consisted

of orange and black uranium oxide particles. These two types of particle were manually separated, and each material was analyzed with powder X-ray diffraction (pXRD), μ-XRF, μ-EXAFS, SEM, and ICP-MS.

1.4.5 Analysis of Actinide Hot Particles from an Accident Site

Section 1.3.3 outlined possible formations of actinide particles in the environment. One means of formation seen throughout the world has stemmed from accidents with nuclear weapons material. Occasionally materials from accident sites are available for analysis and sampling. Not only do these instances allow for the practice of traditional nuclear forensics and environmental analyses, but they also allow for the expansion of those traditional means. For MFS, practice with real world samples is vital for determining capabilities, limitations, and areas where expansion is possible.

In 2007, the Radiochemistry department at UNLV was able to collect samples from the McGuire Air Force Base BOMARC Missile Site where a fire caused the spread of nuclear material[10]. The group collected soil cores containing hot particles composed of this nuclear material. A number of analyses were performed on the soil cores and hot particles, but an overriding theme to their work was analysis on the basis of practicing traditional nuclear forensics. Analyses included hot particle isolation and separation aided with computed tomography, alpha spectroscopy, gamma spectroscopy, dissolution, sample preparation with coprecipitation, environmental impact analysis, SEM imaging, and μ-XRF[10, 128].

Two particles were selected for MFS analysis. The SEM results from a previous study[10] were extensive and proved of use to nuclear forensics. Those measurements and results revealed that the fire caused particles to form in multiple ways. Analysis with SEM was not performed in this study, but other measurements (namely μ-XRF) were consistent with the previous results. Furthermore, μ-XRF work only included a few elements of interest, had a larger resolution (5 x 5 μm versus 2 x 2 μm in this study), and the particles' surfaces were polished. This process not only moves elements/compounds on the surface, but also heats the material leading to changes in chemical speciation; polished particles are no longer representative of the source term. The particles selected for analysis in the work discussed here were probed with μ-XRF, μ-XRD, and μ-EXAFS.

1.4.6 The Effects of Ball-Milling on Uranium Dioxide

As part of the preparation for EXAFS analysis, samples are often ground with a mortar and pestle or some other device. For many of the samples discussed within this manuscript, a Wig-L-Bug milling device was used to reduce particle size and mix with boron trinitride. Historically, this procedure has worked well to achieve quality EXAFS spectroscopy results. In an attempt to improve results, this preparation was expanded and integrated with a number of other analytical techniques to apply to scenarios related to the work discussed throughout this manuscript. Samples were ground in a Wig-L-Bug device for extended periods before preparations for SEM, laser scattering particle size distribution analysis, XRD, and EXAFS spectroscopy analyses.

Other collaborators had performed simple experiments with Wig-L-Bug devices to study the effects of milling on the particle size of titanium dioxide as a function of ball size, number of balls, and time in the Wig-L-Bug in order to determine an optimal preparation method for samples. These experiments included unrealistic milling times (on the order of a day) and did not address oxidation in the Wig-L-Bug (not only does the device heat up after ~5 minutes but allows for mixing of air). However, the results did show an almost linear relationship of particle size versus milling time. Those experiments were useful, but no analysis on uranium oxides was performed, which provided uncertainty on the oxidation effects of using the device for extended periods or with a setup that rapidly damages particles. Furthermore, no investigations on the effects of morphology, particle size, or damage to particles were performed. In this experiment, fresh uranium dioxide samples were either left untreated, ground in a mortar and pestle for 5 minutes, or milled in the Wig-L-Bug device for 5, 30, or 60 minutes. All samples were then analyzed with EXAFS, XRD, SEM, and laser scattering particle size distribution analysis. These analyses seek to find an optimal set of parameters for quick sample preparation for the best EXAFS data, while at the same time limiting particle damage and oxidation.

1.5 Conclusion

An advanced nuclear forensics analysis program is vital as a nuclear threat deterrent and for aiding nuclear attribution[1]. The field has advanced and branched into new areas, but there is a need for continued development of new

capabilities. Molecular forensic science seeks to aide this expansion by applying techniques from many other areas to nuclear forensics scenarios to probe for chemical information. Nuclear forensics has focused primarily on criminal forensics, intelligence, isotopic analyses, and basic chemical analyses. Molecular forensic science integrates techniques to give a broader picture of the chemical makeup of nuclear materials. Information can include chemical speciation, structure, morphology, and trace content. This evidence helps answer both traditional questions in nuclear forensics and new questions that were previously more difficult to ascertain. Analyzing materials for chemical speciation, morphology, and trace content could reveal a more complete history on a nuclear material by providing information on that material's past, including the geologic location from which it was mined, the chemical processes that were used in milling and converting it, and the storage conditions under which it may have been exposed. This dissertation discusses a number of experiments that have helped establish molecular forensic science as a legitimate source for nuclear forensics information by showing how integrated analytical approaches can yield important information on the history of nuclear materials.

CHAPTER 2

MATERIALS, METHODS, AND INSTRUMENTATION

2.1 Introduction

A description of the procedures, instrumentation, and methods used throughout this work will be presented in this chapter. In Chapter Three to Chapter Six, experimental sections will reference the information within this chapter. Some experimental sections will include more detail when appropriate.

2.2 Synthesis of Uranium Oxides

The author used well-established procedures for synthesis of uranium oxides outlined by technical staff members at LANL who were experienced with synthesis routes for the desired compounds. Peer-reviewed citations for the synthesis procedures were not available, but the procedures closely matched what is commonly used from the literature[18] and are outlined below. Uranium oxides synthesized for the experiments were UO_2, U_3O_8, and amorphous-UO_3 (A-UO_3).

2.2.1 Standard Reference Materials

The materials synthesized with uranium of natural isotopics were prepared from National Bureau of Standards Standard Reference Material U960; the same material was later purchased from New Brunswick National Laboratory, called Standard Reference Material A-112, which will be referred to hereafter as SRM A-112. The uranium assay of this material certified the ^{234}U, ^{235}U, and ^{238}U values shown in Table 5.

Table 5. Assay results (current at start of project) for SRM U960/A112.

Isotope	^{234}U	^{235}U	^{238}U
Atom %	0.0052458	0.72017	99.27458
% Uncertainty	0.0000081	0.00039	0.00039

Standard reference material A-112 was received as metallic uranium bars in 4-6 g quantities. It had been stored under atmosphere, and so it had an oxidized surface.

2.2.2 Dissolution

Trace metal grade hydrochloric acid (HCl), A.C.S. certified 30% hydrogen peroxide (H_2O_2), and trace metal grade ammonium hydroxide (NH_4OH) were obtained from *Fischer Scientific* for the following procedures. Milli-Q purified water at approximately 18.2 MΩ·cm resistivity was used when necessary.

Hydrochloric acid was added dropwise over the uranium. Contact with HCl generated gas and a black precipitate commonly seen in this dissolution, likely hydrated uranium (III-IV) oxide[17]. The volume of HCl added depended on the quantity of uranium being dissolved, but was on the order of 10 mL for ~3 g of metal. A few drops of H_2O_2 were added to fully dissolve the remaining. The solution was left to stir overnight to ensure complete dissolution. Uranium oxides required less concentrated acid, less volume, and generated less gas to dissolve.

2.2.3 Purification

Glass columns were setup for the separation of uranium daughter products remaining in the material. Reillex-100HPQ anion exchange resin was chosen for this purification step, a poly(4-vinylpyridine) cross-linked methyl chloride quaternary

salt (Sigma-Aldrich, SKU 436399). The structure of the resin base molecule of is shown Figure 1.

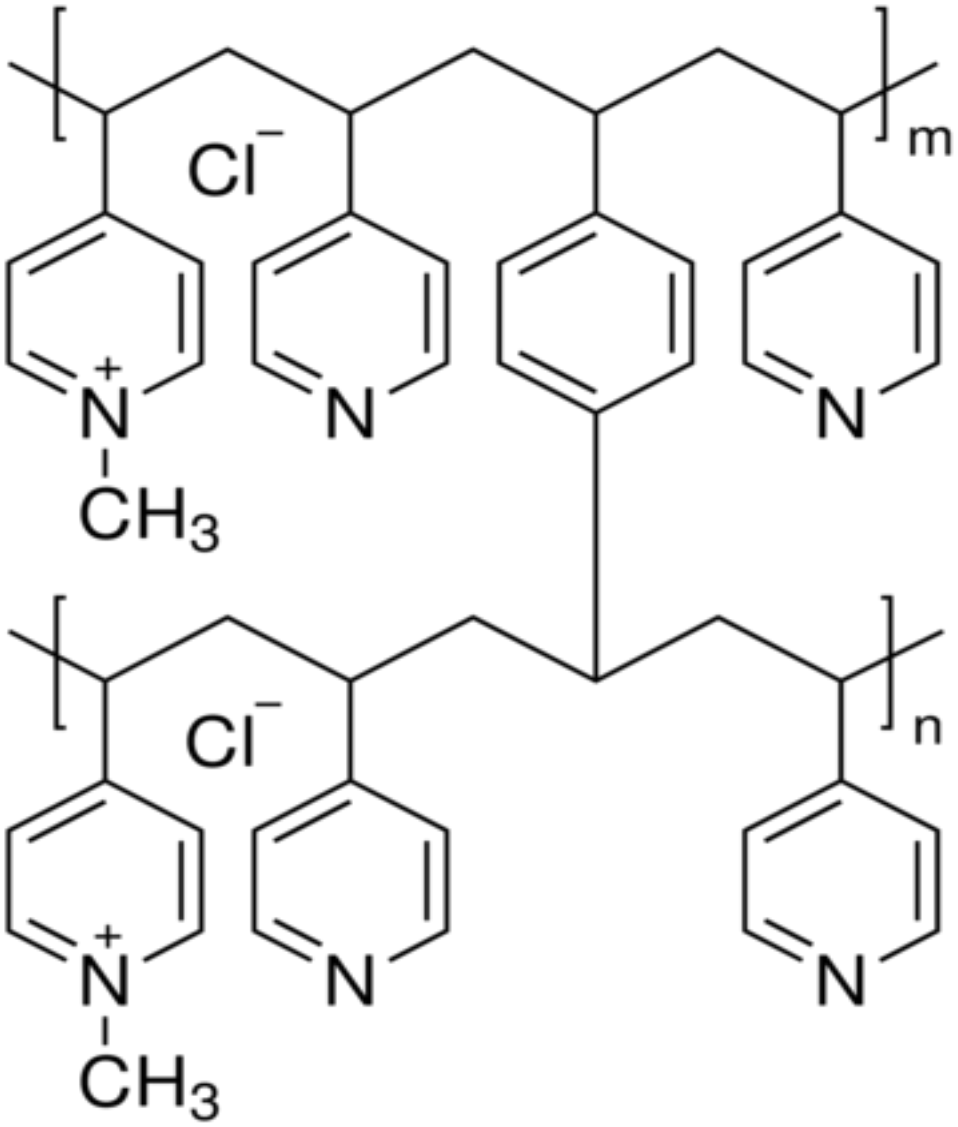

Figure 1. Reillex-100HPQ ion-exchange resin (structure from Sigma-Aldrich).

This resin is commonly used in the nitrate form for plutonium separations, but it is suitable for separating uranium when in the chloride form. The resin was stored in dilute HCl or water, suspended with light stirring, and poured into each column.

This was repeated until most of the column was filled with resin. Enough space was left at the top for the addition of a few mLs of solution. The column was rinsed thoroughly with water followed by concentrated HCl. Washing with concentrated HCl (two times the column volume in this case) ensured the chloride form of the resin. Uranyl in HCl has the form UO_2Cl_2. When exposed to the resin under high acid HCl concentration, the form is $UO_2Cl_4^{-2}$, which adsorbs to the column[129].

To determine approximate load quantity for each column, uranyl chloride solution from the dissolution in Section 2.2.2 was loaded 0.5 mL at a time until the solution was seen exiting the column, obvious due to its yellow color. Based on the total solution volume and quantity initially dissolved, about 50% of the maximum capacity was chosen for purification at a time. This quantity was loaded onto the column with a glass pipette and rinsed with concentrated HCl until the eluent appeared clear and colorless. Washing removes trace metal contaminants and uranium daughter products that have grown over time.

To remove uranyl from the column, 0.01 M HCl was added. Reducing the chloride concentration converts $UO_2Cl_4^{-2}$ back to the neutral species, allowing it to flow freely from the column. Once the eluent appeared yellow, a new container was placed to collect the purified uranyl chloride. Once the eluent appeared clear and colorless, the loading and washing procedure was repeated until the desired quantity of purified solution was obtained. A photo of the column and precipitate formed in section 2.2.4 is shown in Figure 2.

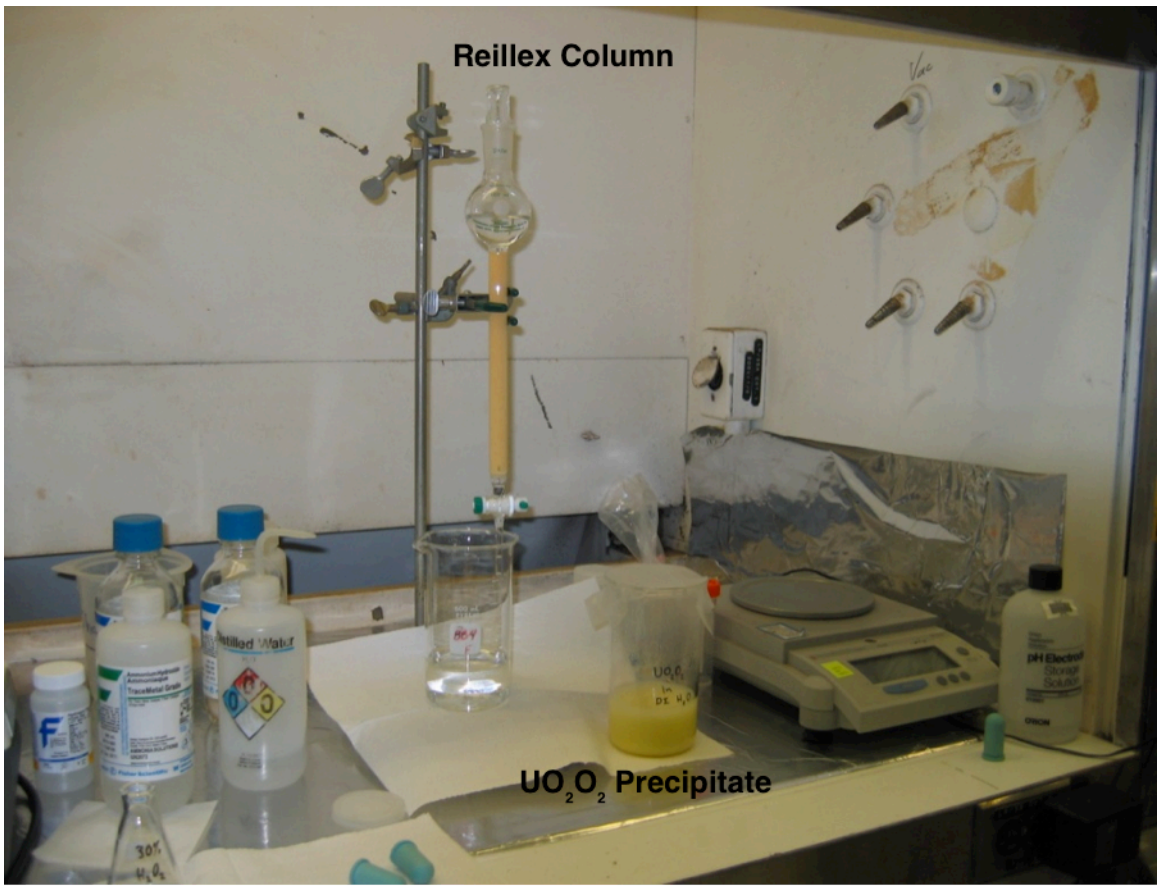

Figure 2. Ion exchange column packed with Reillex-100HPQ ion exchange resin and wet uranyl peroxide ($UO_2O_2 \cdot xH_2O$) precipitate.

2.2.4 Uranyl Peroxide Precipitation

Purified uranyl chloride solution in approximately 0.01 M HCl was poured into a 500 mL round bottom flask with magnetic a stir bar. Water was added to fill the flask about one third full. The flask was put on a Corning PC-420 hot/stir-plate and set to stir at a moderate, steady pace. An Orion 710A pH/ISE Meter pH probe was placed into solution so that the tip was fully submerged, but would not disturb the stir bar at the bottom of the flask. Ammonium hydroxide was added dropwise until the pH reached a value of 3.0, within the optimal range to maximize yield for a uranyl peroxide precipitation. The precipitation works at a range of pH values, but if

it goes too high (>~4) an orange precipitate (an undesired ammonium complex). The formation of the ammonium complex is difficult to reverse and produces undesirable physical characteristics in the resulting precipitate mixture. If the pH remains at a maximum of 3.0, the uranyl peroxide precipitate will exhibit a consistent and soft texture that is easy to work with and helps ensure quick reaction completion when heating. Adding NH_4OH caused a temporary precipitate in the solution; the time for this precipitate to dissolve back into solution was noted for the time to be used before adding more H_2O_2. Once a pH value of 3.0 was maintained, a few drops of H_2O_2 were added to precipitate UO_2O_2 and reduce the pH to a value of about 1.0. More NH_4OH was added to return the pH to 3.0 and the solution was allowed to stabilize based on the time noted above. More H_2O_2 was added and this procedure repeated until the addition of H_2O_2 causes no drop in pH, signaling the endpoint of the precipitation.

Uranyl peroxide precipitation not only serves to provide a desirable starting material for further uranium oxide syntheses, but it also serves as a purification step. The remaining impurities are soluble in water, whereas the UO_2O_2 is not, so the solution was filtered with a solid frit under vacuum and washed with 50 mL water 5-6 times. Filtration did not dry the material completely, so the material was dried further under vacuum over night.

2.2.5 Synthesis of Standard Compounds

The oven used for the following heat treatments was a Thermo Scientific Lindberg Blue M Mini-Mite Tube Furnace (model TF55030A-1, UT150). Ceramic

boats approximately 10 mL in size lined with a platinum foil (Alfa Aesar 0.025 mm thick, 99.9% purity), and custom-made quartz tubes with ground-glass end fittings from Technical Glass Products were used for all heating steps.

The UO_2O_2 precipitate remained a wet, "pasty" consistency, so it was dried further by slowly heating the material in the tube furnace to 100 °C under atmosphere. To make A-UO_3, UO_2O_2 was heated to 400 °C for at least 6 hours. The literature notes that the endpoint can be reached in as little as 2 hours, but a high confidence level was desired in the final product so samples were heated longer than required. The resulting A-UO_3 was heated to 800 °C for 24 hours to make U_3O_8 (all U_3O_8 in this work was α-phase). Either UO_3 or U_3O_8 was reduced at 500 °C under ultrapure H_2 gas for at least 12 hours to make UO_2. The material was taken out of the oven halfway through the synthesis to mix the material, ensuring complete and consistent contact with the reducing gas. The resulting UO_2 was allowed to cool under H_2 to inhibit formation of hyperstoichiometric UO_{2+x}[18]. Some literature procedures claim a temperature range of 800-1100 °C, but other studies have shown the synthesis of ordered UO_2 under 500 °C[76, 89]. Products were verified for structure and purity with powder X-ray diffraction. Refer to Equations 1-5 for a summary of the synthesis routes. Figure 3 and Figure 4 show the oven setup and the products through the synthesis scheme outlined in the equations below.

Equation 1. $UO_2O_2 \cdot xH_2O \xrightarrow{100\,°C,\ \sim 4\,h} UO_2O_2 \cdot xH_2O\ (dried)$

Equation 2. $UO_2O_2 \cdot x - yH_2O \xrightarrow{400\,°C,\ \sim 6\,h} A - UO_3$

Equation 3. $A - UO_3 \xrightarrow{485\,°C,\ \sim 4\,d} \alpha - UO_3$

Equation 4. $U_3O_8 \xrightarrow{500\,°C,\ H_2,\ \sim 24\,h} UO_2$

Equation 5. $A - UO_3 \xrightarrow{500\,°C,\ H_2,\ \sim 24\,h} UO_2$

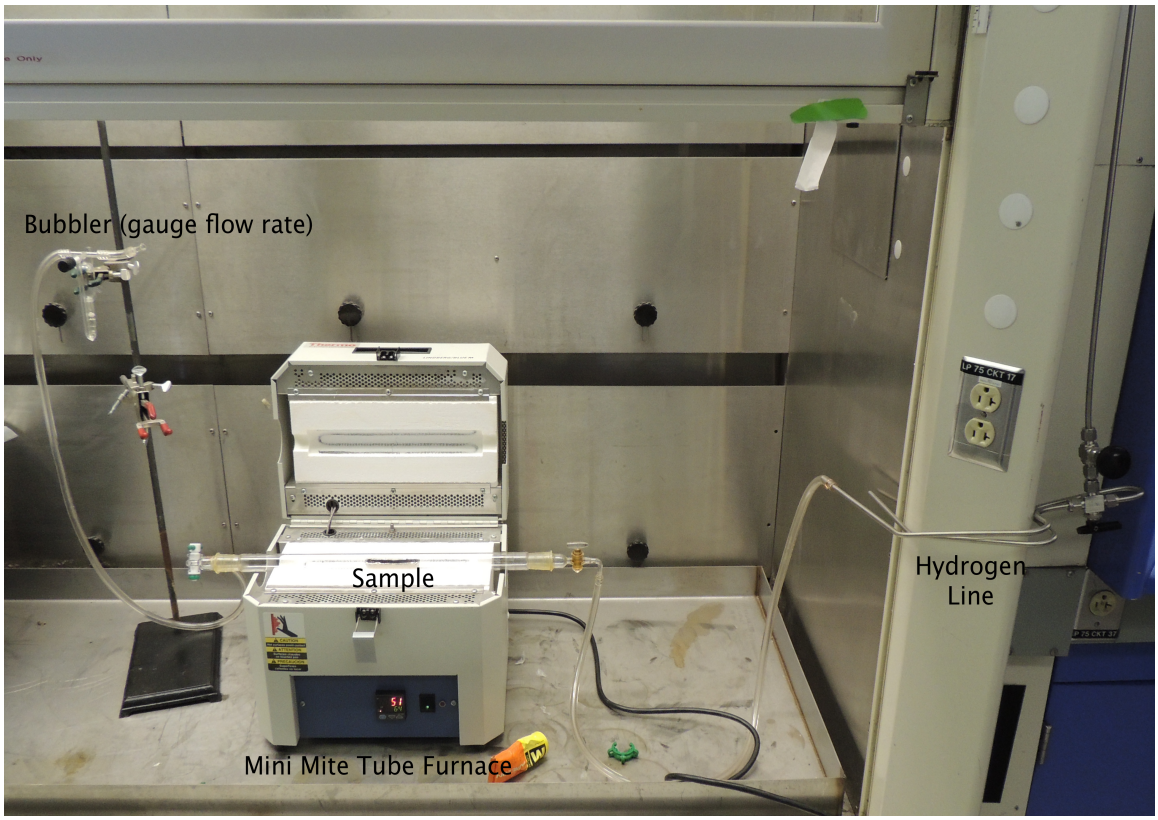

Figure 3. Oven setup for synthesis of uranium oxides. Hydrogen flow system is show in this picture.

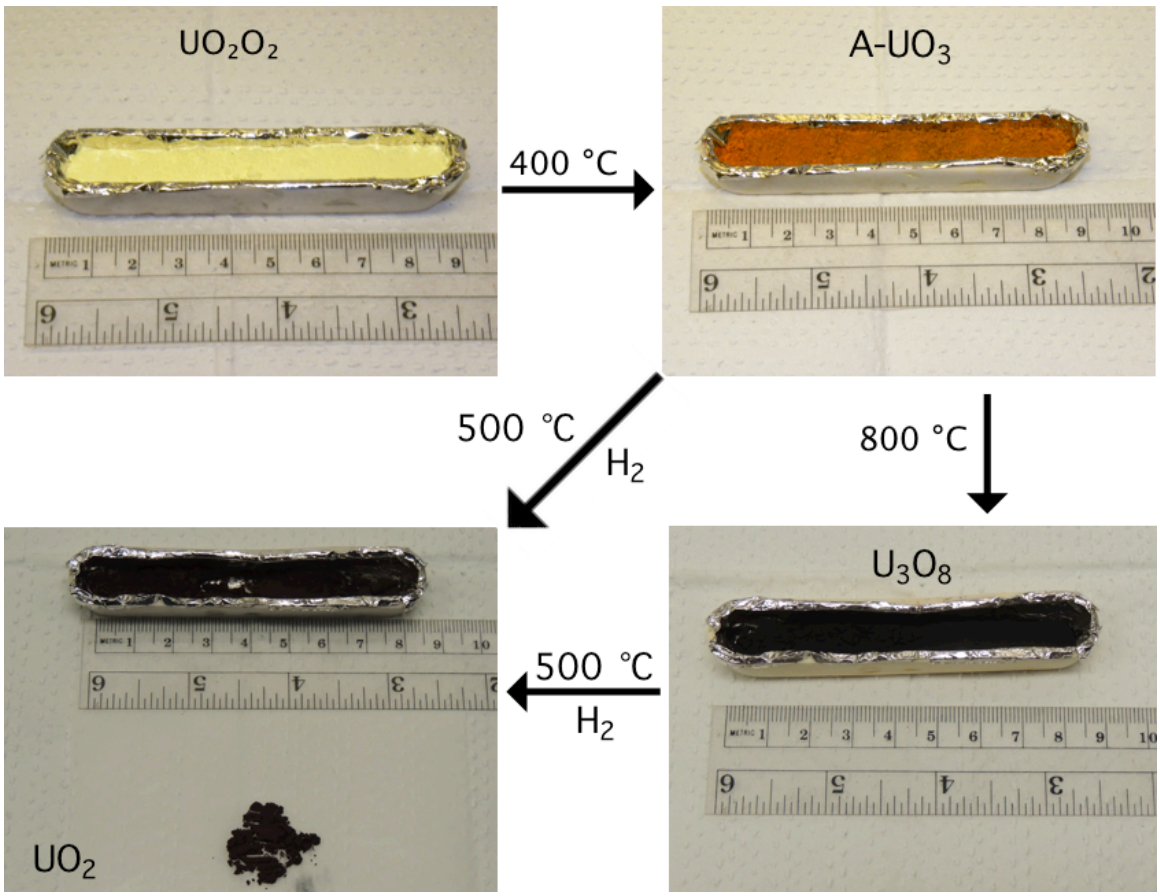

Figure 4. Synthesis schematic starting with UO_2O_2 to UO_2 (the brick red color noted earlier for of UO_2 is difficult to discern from this photo).

2.3 Sample Aging

The standards synthesized at LANL (UO_2, U_3O_8, and A-UO_3) and 5 of the received samples were aged under various temperature and humidity conditions. A constant relative humidity (RH) in a closed environment within a few error percent can be produced with exposure to a given saturated salt solution and temperature. This phenomenon is outlined by Equation 6, where *A* and *B* are constants for a specific salt, and *T* is temperature[130].

Equation 6. $$RH = A \cdot e^{(B/T)}$$

The salts chosen were lithium iodide (LiI, 99%, Acros Organics, product code 203590500) and potassium nitrate (KNO_3, 99%, Sigma-Aldrich, SKU 221295) because they allowed for a range of conditions using both a low and high temperature (relative to common environmental conditions). The salt solutions and temperatures used, the resulting relative humidities, and the sample descriptions/identifications used throughout this project are shown in Table 6.

Table 6. Salts used for the aging baths along with the temperature of the baths, the resulting relative humidities, and the condition description and abbreviations used throughout.

Salt	**Temp °C**	**RH**	**Sample Description/ID**
LiI	5	25%	Low Humidity Low Temperature/LHLT
LiI	40	15%	Low Humidity High Temperature/LHHT
KNO_3	5	97%	High Humidity Low Temperature/HHLT
KNO_3	40	89%	High Humidity High Temperature/HHHT

Vessels were fabricated from Swagelok VCR fittings made of stainless steel (316) to house samples. The vessel design was based on work by Anovitz[131], Figure 5. Part A is the base of the vessel that contains the saturated salt solution in a Teflon cup. The holes and mesh bottom in Part B allow for the sample to continuously contact the atmosphere within the vessel. The copper gasket provides a tight seal between parts A and C, such that once the vessel was closed and sealed, it could be suspended into a circulating water bath without leaking. Approximately 0.5 g of material was placed in each vessel for aging.

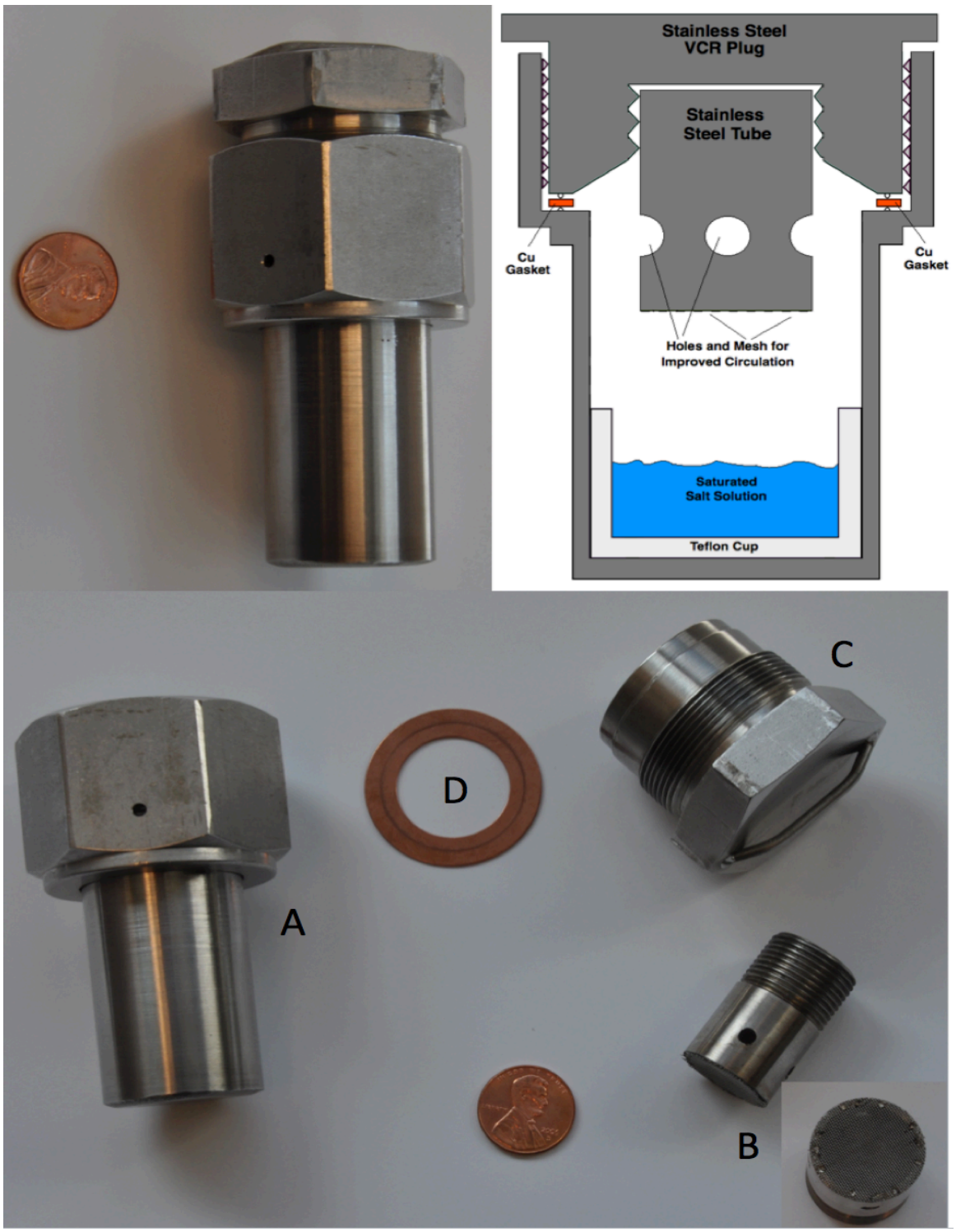

Figure 5. Photographs of an assembled aging vessel (top left) with cross section schematic (top right) and disassembled showing individual parts (bottom). Part A is the base of the vessel that holds a Teflon cup with the salt solution. Part B is a stainless steel tube with holes drilled in the side and a mesh bottom that contains a sample inside a polyfluoro vial. Part B is screwed beneath Part C, which is made of the stainless steel VCR plug and nut[131].

Aging vessels were placed in water baths (Thermo Scientific Haake V26/B, controlled by a Thermo Scientific DC10 Controller) maintained at 5 °C and 40 °C (Figure 6). Sampling was performed at time = 3, 6, 12, 18, and 24 months.

Figure 6. Water baths (top) and the aging vessels placed inside one (bottom).

2.4 Extended X-ray Absorption Fine Structure Spectroscopy

Collaborators at LANL executed a portion of the data collection for many of the analytical techniques discussed within this manuscript; the author performed the preparations and some analysis. For extended X-ray absorption fine structure (EXAFS) spectroscopy, the author performed the preparations, data collection, and data analyses, so a more detailed discussion will be included. X-ray absorption spectroscopies rely on the absorption of a photon by an atom of choice. Every element has a unique electronic structure, which allows for selection of X-ray energy ranges to analyze a specific element within a sample[31]. Figure 7 shows the X-ray absorption as a function of energy for a typical sample, with a zoomed in region showing a specific absorption edge.

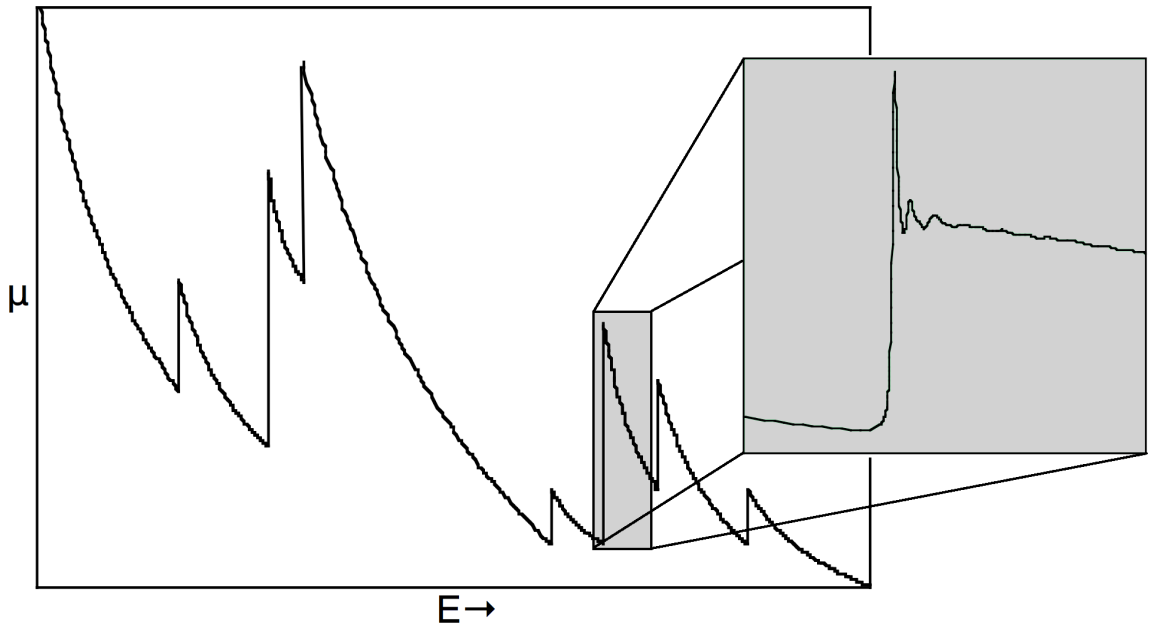

Figure 7. Absorption as a function of energy (10's of keV) for a typical sample, with a zoomed in region showing a specific absorption edge and the resulting EXAFS.

Over this range, sample absorbance decreases except when photon energy resonates with a core electron shell of an element within the sample. These dramatic increases at core electron resonance are commonly referred to as absorption edges[31].

When an atom absorbs incoming photons, a photoelectron wave is emitted and backscattered off neighboring atoms resulting in constructive and destructive interferences with the original (Figure 8). The interference is constructive with respect to the first shell of atoms and therefore increases the final state's wave function amplitude (Figure 8, a). Destructive interference causes a decrease in this wave function (Figure 8, b)[31, 132]. Waves interfere constructively and destructively many times as energy increases past the absorption edge, causing extended modulation of the absorption spectrum. EXAFS spectroscopy is a measure of the modulation caused by these interferences. The kinetic energy of the electron wave increases near both the absorber and scatterer. Increased kinetic energy decreases the time to travel the absorber-scatterer distance and back, shifting the sin wave applied to the data. This shift propagates through to r-space, causing a shifts in the distances of fitted shells. This will be discussed in more detail in Section 2.4.2.

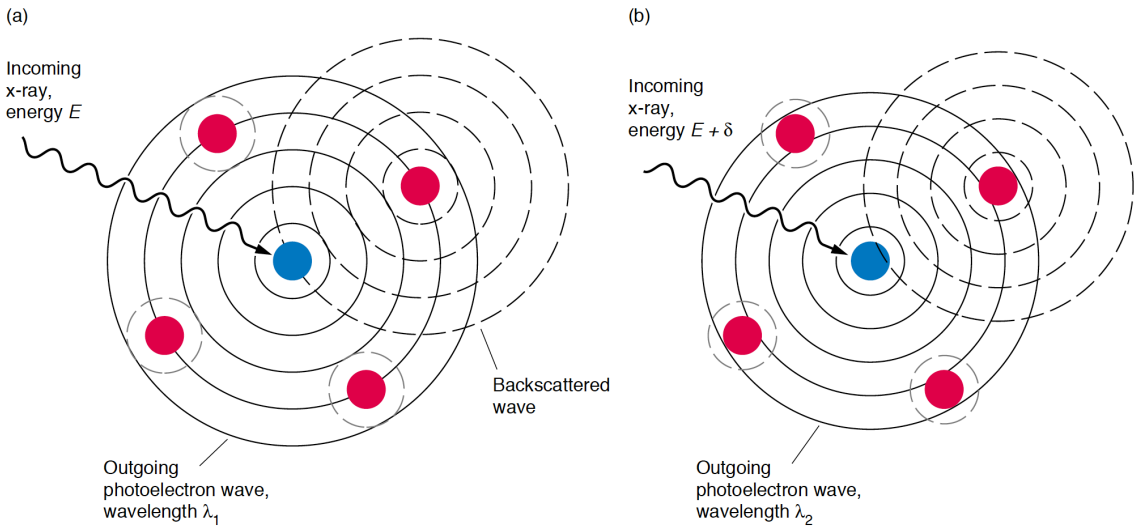

Figure 8. A representation of an atom absorbing a photon and producing a photoelectron wave that backscatters off neighbor atoms[132].

2.4.1 Synchrotron and Beamline Setup

All data was collected at the Stanford Synchrotron Radiation Lightsource (SSRL). Some parameters of the facility changed during the time the experiments in question were performed, but this discussion will reflect the most recent parameters available as of the final data collection included in this work. For example, the current of the synchrotron varied from 80-100 mA during the author's first experimental run, but had been upgraded to 300-500 mA for the most recent data collection.

Briefly, a synchrotron (sometimes called a storage ring, as it stores electrons in a ring) accelerates electrons around a ring with a large circumference (~100-1000 m). When these electrons change direction at relativistic speeds, they emit a high-flux of X-rays dipole radiation. Individual beamlines use various "insertion devices" to further increase this flux and branch off tangentially from the synchrotron. X-ray direction and energy are controlled with various optics, slits, and

monochromators[133]. Figure 9 shows a map of beamlines at SSRL, and Figure 10 shows a simplified schematic of the beamline setup used for the bulk EXAFS measurements in this work.

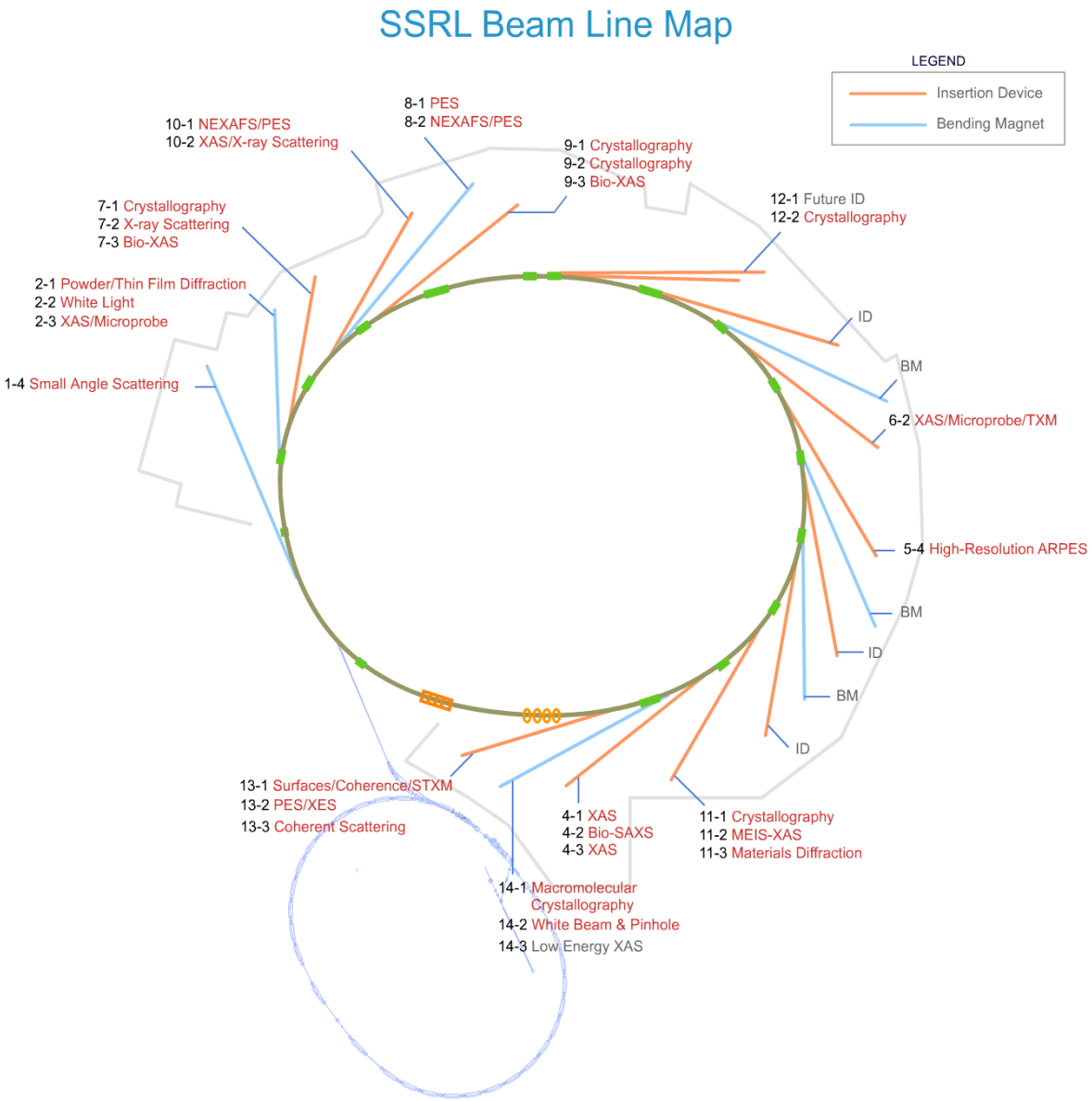

Figure 9. Map of the Stanford Synchrotron Radiation Lightsource, SSRL website.

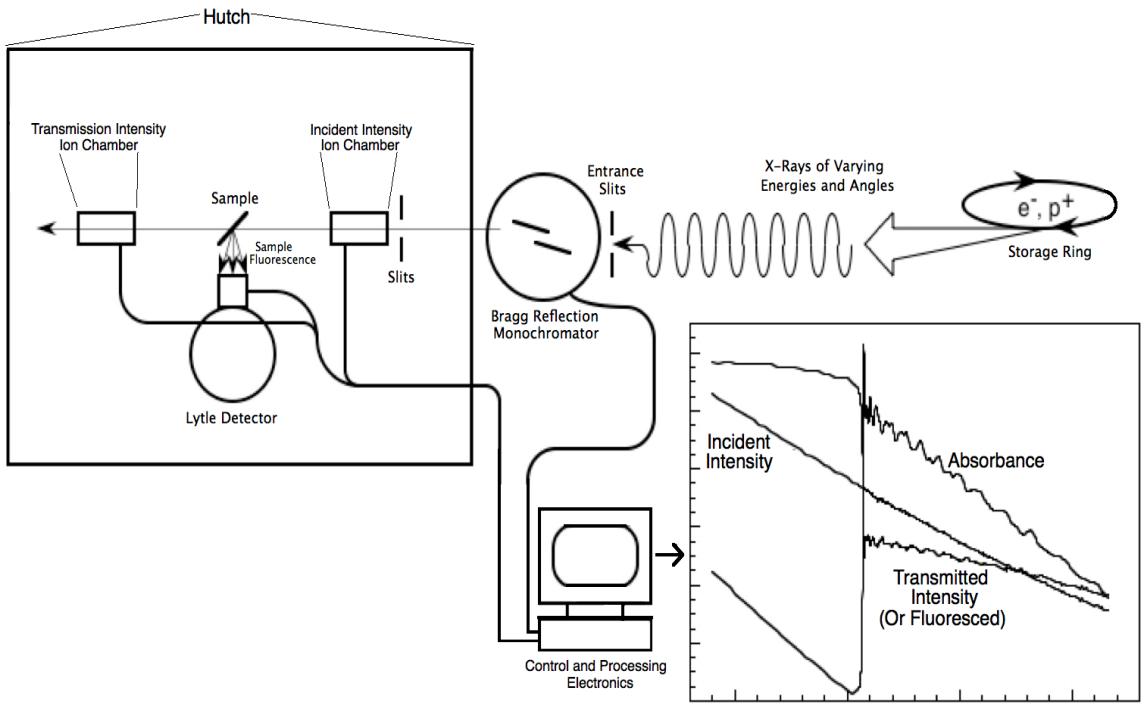

Figure 10. Simplified schematic of a typical beamline setup.

Bulk EXAFS data was taken at Beamline 11-2 under dedicated operating conditions (3.0 GeV, 300-500 mA) using a silicon (220) double crystal monochromator. Sample holders were attached to the cold finger of a liquid nitrogen reservoir cryostat providing temperatures of 80-90 K. The uranium L_{III} absorption edge (17166 eV) was measured in fluorescence mode using a Lytle fluorescence detector, or in transmission mode using a gas ionization detector depending on data quality. The uranium L_{III} absorption edge was calibrated to the yttrium K edge, at 17038.25 eV and E_0 at 17166 eV. The data were analyzed using standard procedures[92, 93], which are discussed in more detail in section 2.4.2.

2.4.2 EXAFS Data Analysis

The EXAFS data were extracted from the absorption spectra, Figure 11 (a), by subtracting the sum of an arctangent function and a Gaussian peak (not shown) at the absorption edge and a polynomial spline function above the edge[132]. A spline function applies multiple polynomial functions to selected regions. The functions meet up at the intersection of regions. The points at which they meet are called "knots". How smooth the function is over the EXAFS has a significant impact on the data. The function should have enough freedom (more regions or higher order polynomials) for a good fit of the EXAFS, but not so much that it fits individual waves. Over a compared set of samples, how closely the fitting parameters are to one another can have a major impact on final outcome of an analysis. Many of the samples analyzed within this manuscript involve comparison with standards, between materials exposed to different storage conditions, or between samples prepared in different ways.

Further problems result from abnormalities in the beam intensity or energy. Some of these include crystal defects or "glitches" (the synchrotron beam direction and energy are controlled with various crystals), variations in beam size/shape, or electron fills. When these abnormalities do not ratio out of the data, repairs can be attempted by often times repairs can have a greater impact on the data than the original abnormality. This highlights the need to do a complete analysis of the data and make educated decisions on errors in the data.

In Figure 11 (b), the x-axis has been converted from energy to a wave vector, k. This plot shows the resulting background-subtracted k^3-weighted EXAFS $\chi(k)$

spectra, weighted arbitrarily to emphasize scattering contributions at longer distances[29]. Each shell of neighboring atoms within a compound produces a modified sine wave defined by a distinct frequency, phase, and amplitude with the sum of the shells' functions equaling the total EXAFS. To extract the individual parameters, a non-linear least squares curve fit was applied, and Fourier transformed to a radial structure function as in Figure 11 (c). The k-range of the transformations varied from sample to sample, with bulk data typically ranging from 2-15 at the maximum. Transform moduli alone start to imply certain atomic shells. The individual frequencies of the EXAFS were extracted and fitted, followed by shell curve-fitting analysis. At that point, the shells and their parameters become more clearly defined. Curve-fits utilized amplitudes and phases calculated by FEFF7 (or when possible FEFF8)[134] code based on uranium oxide crystal structures available from the Inorganic Crystal Structure Database[135]. The Debye-Waller factor (σ, a measure of thermal motion), and the number of atoms (N) were varied where applicable while the distance (R) of absorber-scatterer pairs was varied for all fits. Figure 11 (c) shows the radial structure function of the data (top portion), its fit (top), the resulting individual shells (bottom), and some of the shell parameters for the face centered cubic structure of platinum as a simplified example. The Debye-Waller factor (a cross section) can be varied for improved fits, but was fixed throughout this work to limit the degrees of freedom[136]. Because of this, errors for σ are not reported. Many of the fits discussed herein show unusual numbers of atoms, so one should take note of σ values for ideal comparison. If σ is fixed to be larger (for improved fit), a shell will have more atoms and vice versa.

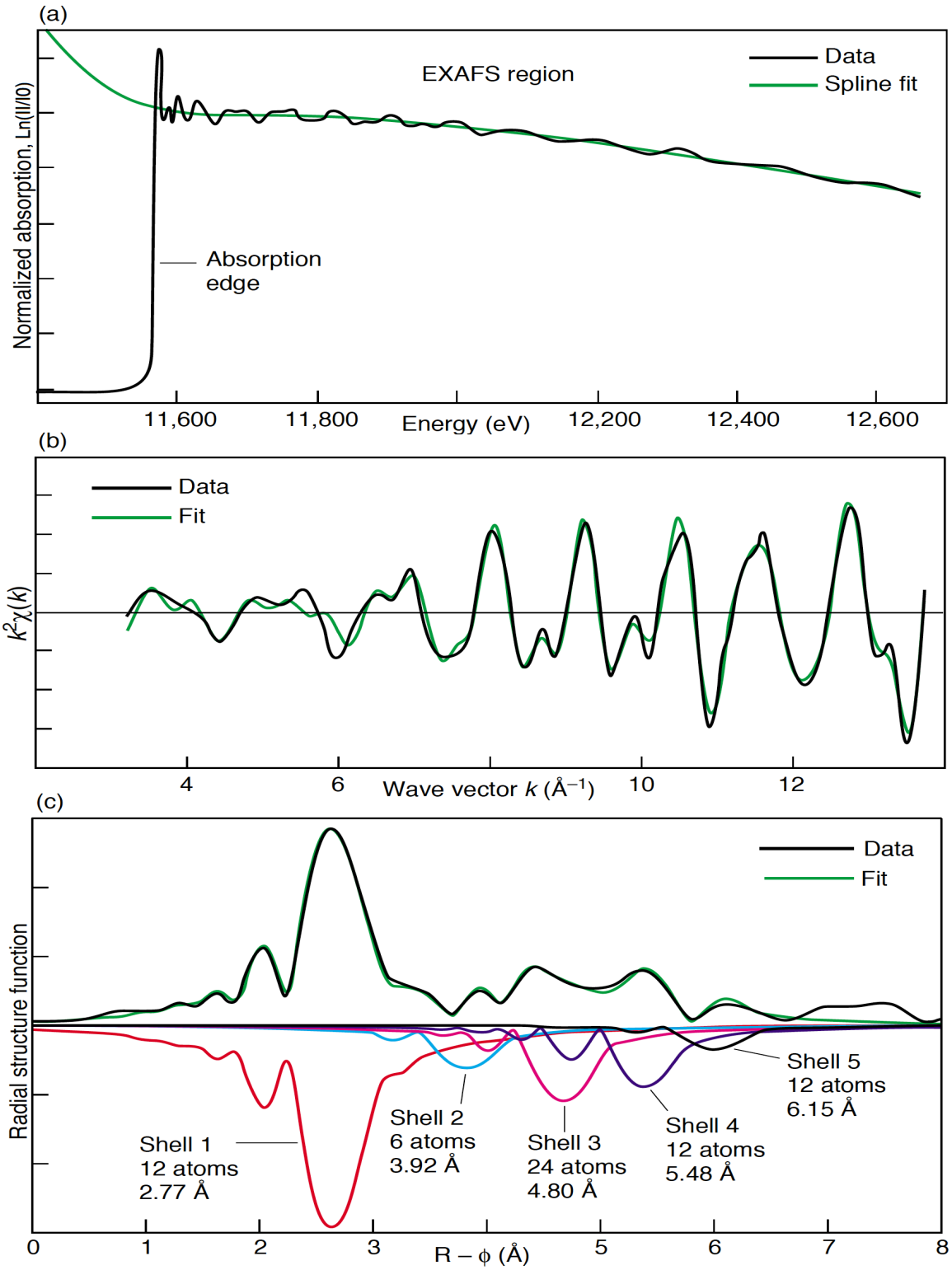

Figure 11. Plots showing basic steps of EXAFS data analysis. (a) Spline function is fitted to EXAFS for subtraction, (b) Resulting EXAFS fitted with wave function, and (c) Individual EXAFS waves are used to calculate Fourier transform modulus and fitted with individual atomic shells[132]. This data is for the face centered cubic structure of platinum.

2.4.3 Bulk EXAFS Sample Preparation

Samples for bulk EXAFS spectroscopy must be prepared so that they are highly concentrated enough to produce adequate counts for both transmission and fluorescence, but dilute enough so that self-absorption effects are minimized[30]. Self-absorption results when a sample is mixed unevenly within a cell and/or too much material. These effects result in abnormalities in the raw data. Based on previous experiments, known calculations, the sample holder window size, and the typical size of the incoming X-ray beam, about 10 mg of uranium oxide material is required per sample. The density of uranium oxides varies depending on the specific compound, but they are small enough that the mass ranges used for the preparations discussed herein resulted in consistent data. To further limit random occurrences of self-absorption, boron trinitride was added (60-80 mg) to help spread the uranium uniformly for each sample. These quantities were weighed out and either ground in a mortar and pestle or placed in a Wig-L-Bug grinder/mixer with a 1/8" polystyrene bead. This process reduced the occurrence of uranium oxide aggregates (reducing self-absorption) and mixed the two compounds consistently. The mixture was put into each sample window and pressed with a plastic backing. Containment layers, as required for SSRL samples, included the primary container (glued kapton) and the secondary container (glued kapton and pressed indium wire creating a vacuum seal). These samples were attached to a cold finger, placed in the beamline hutch, and analyzed as outlined in Section 2.4.1.

2.5 Powder X-ray Diffraction Analysis

Powder X-ray diffraction (pXRD) was used for synthesis verification, analysis of received and aged samples, and analysis of other technical concepts studied in this work. Samples were prepared by grinding the oxides in a mortar and pestle for approximately five minutes, and spread over a grease-coated sample holder to affix the powdered oxide in place. A thin layer of spray-adhesive was applied as a layer of containment. X-ray diffraction data for t = 0 and 1 year samples were collected on a Bruker D8 Discover using copper radiation conditioned by a Göbel mirror ($K\alpha_1/K\alpha_2$ = 10), and either a scintillation detector or multi-wire gas proportional detector (Hi-Star). Data for 2 year samples was collected on a Bruker D8 Advance using unconditioned copper radiation, and a 1-D silicon strip detector (Lynxeye). Qualitative analysis was performed using Jade software[137], and the International Center for Diffraction Data powder data files[138].

2.6 Scanning Electron Microscopy

Samples were prepared for scanning electron microscopy by pouring a small quantity (~0.05 mg) of material onto conductive carbon tape. Loose material was removed from the tape. For cases in which the material was made of macroscopic agglomerated particles, material was crushed and spread on the stub. Backscatter and secondary electron imaging were performed using a FEI Quanta 200F field emission scanning electron microscope. Qualitative energy dispersive x-ray spectra (EDS) were collected using an EDAX Genesis XM4 analyzer system and Apollo 40 EDS detector. Images were taken at magnifications ranging from 50x to 25000x.

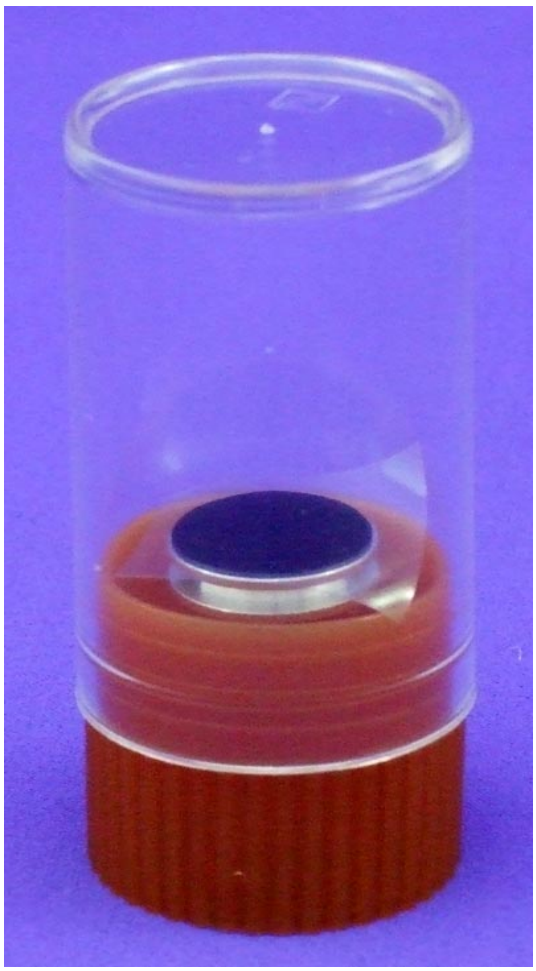

Figure 12. The SEM stub coated with sticky carbon tape.

2.7 Trace Element and Isotopic Analysis

Approximately 100 mg of each uranium oxide was dissolved in 20 g ultrapure ~8 M nitric acid (HNO_3) obtained from Fischer Scientific. The dissolution process generally required heating a capped sample for 24 hours on a hotplate at 90 ˚C. The dissolved uranium material was diluted to make a 100 µg uranium/g HNO_3 (referred to hereafter as an A-dilution; uranium mass percent of 85% was assumed - mass percent U ranges from about 88% to 83% from UO_2 to UO_3). This uranium concentration of the A-dilution was low enough that it did not significantly suppress the ionization of the trace elements but was also high enough to prevent the dilution

of most trace elements below method detection limits[139]. An exact mass of each A-dilution was combined by mass with an internal standard solution containing ^{6}Lithium and Indium. Internal standards were used to correct for drift within an analysis sequence. Trace element analyses were run on a Thermo Element XR double focusing magnetic sector inductively coupled plasma mass spectrometry (ICP-MS) operated in low (M/DM =300), medium (M/DM =4,000), and high (M/DM =10,000) mass resolution modes. Trace element concentrations were determined from drift, background, and interference (for select isotopes) and a five-point external calibration curve.

An additional dilution (hereafter B-dilution) was prepared to have a uranium concentration of approximately 85 ng/g. This trace element method is detailed in Zimmer et al[140]. Uranium isotopic analyses were run on untraced fractions of each B-dilution using a two-magnet jump and sample standard bracketing (for mass bias correction) method on a Thermo Neptune multicollector ICP-MS. New Brunswick Laboratory certified reference materials CRM-112 and U-010 were used for mass bias correction. An exact mass aliquot of B-dilution was mixed with an isotope dilution tracer (^{233}U) to determine an accurate concentration of uranium in each A-dilution. The uranium certified reference material IRMM-74/1 was used for mass bias correction of measured ^{238}U/^{233}U ratios.

2.8 Particle Analysis with Synchrotron Radiation

As discussed in the introduction, the ability to analyze individual particles is an integral concern within the nuclear forensics community. In cases where bulk

information is limited or a bulk sample contains differentiable particles (based on mass, color, density, size, activity, etc.), analysis of those individual particles can provide a more complete picture. In other cases, there may only be a very small amount of material to work with and individual particles must be examined as a representative of the larger sample.

Particle samples were analyzed at SSRL Beamline 2-3 (BL 2-3), which has a microfocus capability for XRF, XRD, and EXAFS. This beamline is very similar in setup to the one discussed in 2.4.1, but with a movable stage, optics for aid in locating particles, and a detector that allows fluorescence analysis for many different elements in a given sample.

2.8.1 Hot Particle Isolation and Sample Preparation

For particles contained in soil cores as in the case of the BOMARC accident site discussed in Chapter 5, a handheld sodium-iodide detector with lead collimators was used to localize them within soil cores. The same setup was used to locate particles within specific fractions of soil after initial removal. The particles were large enough to be manipulated with tweezers, making the total time of separation about an hour in about a cubit foot of soil. Uranium oxide particles from bulk samples were chosen based on difference in color, and were large enough to be isolated with tweezers. Once isolated, they were placed on a small paper containing a bromine-doped ink grid, facilitating the elemental mapping process. A toluene/polystyrene mixture was used to fix the particles in place and serve as a layer of containment. The paper grid was placed in a sample holder designed for

further containment and microfocus experiments at Beamline 2-3. This process is outlined briefly in Figure 13.

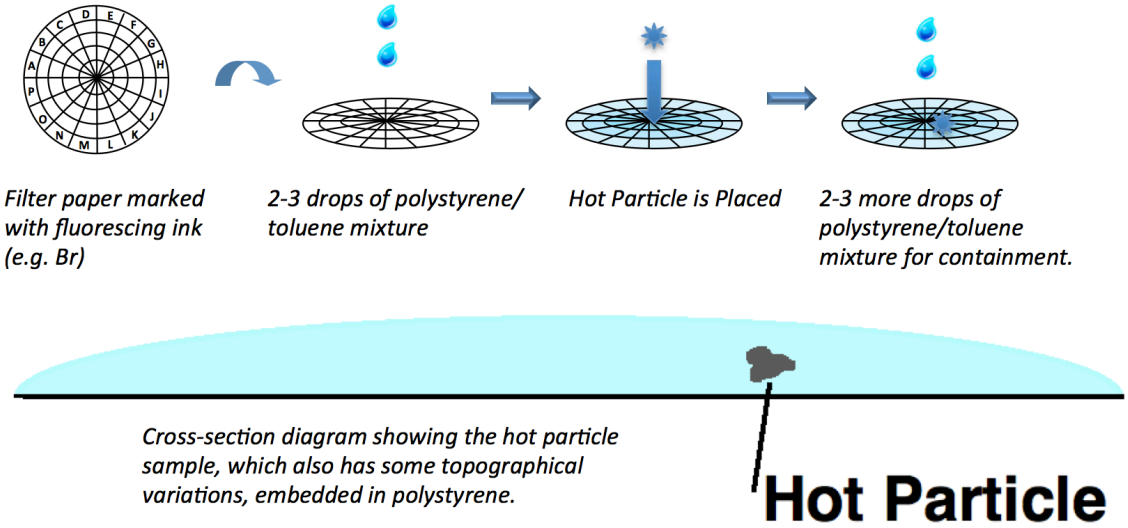

Figure 13. Steps in preparing a particle sample for BL 2-3.

2.8.2 Elemental Mapping: μ-X-Ray Fluorescence

Elemental mapping μ-XRF images were collected at the SSRL on BL 2-3 under dedicated operating conditions (3.0 GeV, 300-500 mA) using a silicon (220) double crystal monochromator. The beam (2 x 2 μm) was focused with a platinum-coated Kirkpatrick-Baez mirror pair (Xradia Inc.). For fluorescence imaging, the incident X-ray energy was set at three different values: 18100 eV (above the plutonium L_{III} edge: ~18060 eV), 18000 eV (below the plutonium L_{III} edge and above the uranium L_{III} edge) and 17000 eV (below both the plutonium L_{III} and uranium L_{III} edges). These settings allow for elimination of interference from overlapping emission energies and enhance the separate identification of uranium and plutonium. The uranium Lα, plutonium Lα, and gallium Kα fluorescence emission lines, the total

count rates, and the total fluorescence spectrum were measured at room temperature using a Vortex silicon drift detector (SII NanoTechnology USA Inc.). The images were acquired by mounting the samples 45° to the incident X-ray beam and spatially rastering the samples in the micro-focused beam using a Newport VP-25XA-XYZ stage. The ink grid discussed previously in conjunction with BL 2-3's variable resolution settings, allows particles on the micron scale to be located relatively quickly. The beamline hutch and experimental setup are shown in Figure 14.

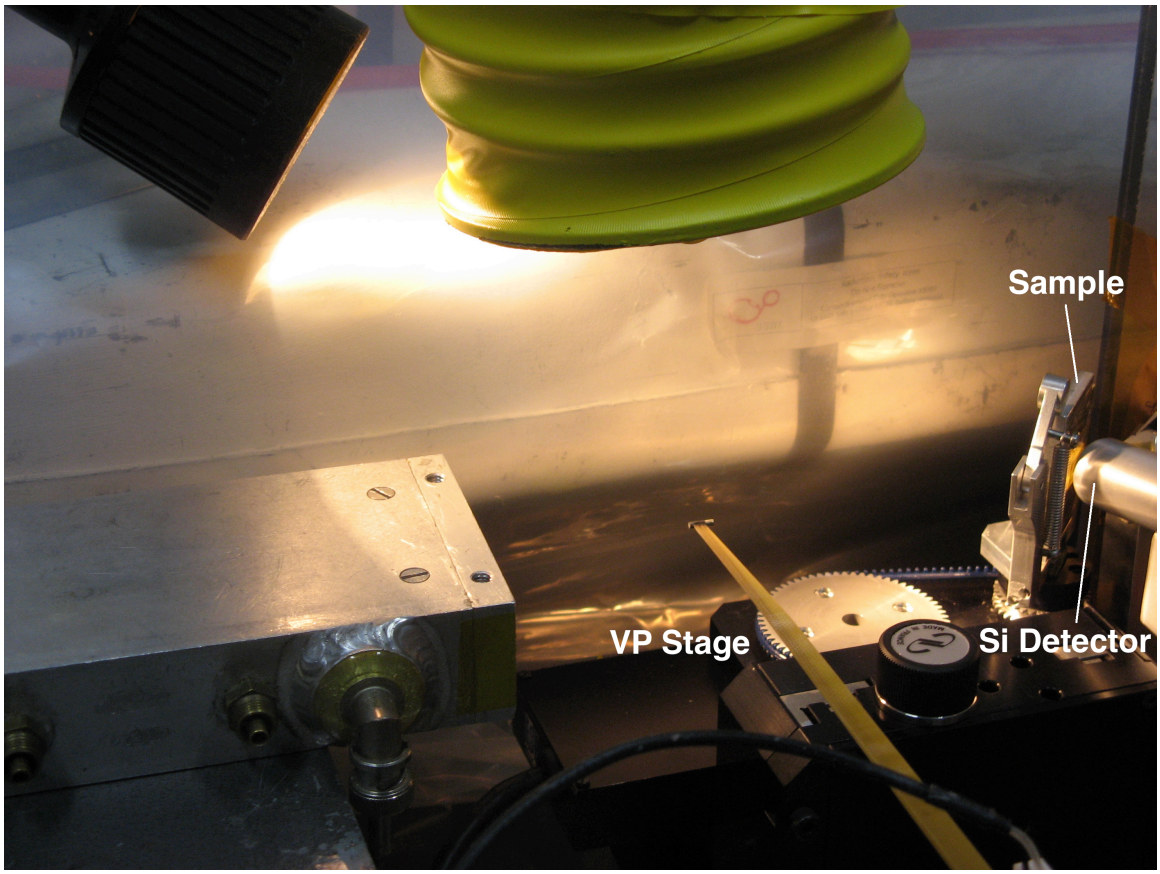

Figure 14. The setup at BL 2-3 at SSRL. Incoming beam would come from right side, through the sample set at 45° to the silicon detector. The VP stage moves the sample for mapping.

2.8.3 μ-EXAFS and μ-XRD

As noted above, BL 2-3 at SSRL has microfocus capabilities for synchrotron-based analyses including μ-EXAFS and μ-XRD. Data for these measurements were taken at specifically chosen points on samples based on initial data quality and the elemental maps that BL 2-3 collects. Extended X-ray absorption fine structure data were measured in the fluorescence mode, using a nitrogen-filled ion chamber for the incident intensity and the fluorescence detection apparatus described above. Multiple scans (typically two-three) were collected at each location of interest and subsequently averaged during the data analysis process. The data were analyzed using standard procedures as outlined previously in Section 2.4.2. Samples were calibrated to the zirconium K edge at 17998 eV and E_0 set at 18060 eV. The k^3-weighted EXAFS $\chi(k)$ spectra were fit using plutonium-oxygen and uranium-oxygen curve-fitting parameters calculated by FEFF7 (or when possible FEFF8). The Debye-Waller factor, σ, and the distance, R, from the absorber-scatterer pairs were varied for all fits, and the number of atoms, N, was varied where applicable.

X-ray diffraction patterns for each location of interest were measured with a charge coupled device camera. Patterns were obtained by taking two measurements of 120 seconds exposure time (at 17500 eV) each. A lanthanum hexaboride standard was used to calibrate the distance between the sample and the detector in an attempt to obtain accurate d-spacings. Diffraction patterns were analyzed and indexed with the software package available at BL 2-3.

2.9 Laser-Scattering Particle Size Distribution Analysis

Approximately 250 mg of each uranium oxide sample was set aside for laser scattering analysis in order to probe for particle size distribution and gain some understanding on how aggregated particles were. The system used was a Horiba LA-950 laser scattering particle size distribution analyzer. Each sample (or particle size standard) was placed in a sample bath with ethylene glycol. There is an ultrasound stage so that each time the material is cycled through the system and subsequently analyzed with laser, it is broken up, eventually reaching the base-size of the material which gives information on how agglomerated the particles of a given sample are. The instrument outputs mean diameter of particles as a function of percent of total particles, and how many cycles/how long it took to reach an endpoint size.

CHAPTER 3

AGING OF URANIUM DIOXIDE UNDER VARIOUS CONDITIONS

3.1 Abstract

Uranium oxides are among the most important compounds for the nuclear fuel cycle and weapons production, but gaps in the mechanisms for transition between compounds are still not well understood. Analysis of chemical speciation as a function of aging condition presents possibilities for increasing the base of knowledge for uranium oxides and evaluation of aging conditions for purposes related to nuclear forensics and attribution, as well as stockpile stewardship, fuel/waste storage, and nuclear nonproliferation. In this study, uranium dioxide was selected as a starting compound to build this base of knowledge due to its commonality in the nuclear fuel cycle and its simple structure (initially). Uranium dioxide was aged under specific controlled atmospheric conditions with different relative humidities and temperatures. Sampling of the aging uranium dioxide was performed at regular time intervals at which point powder X-ray diffraction (pXRD) analysis and extended X-ray absorption fine structure (EXAFS) spectroscopy were performed. This experiment demonstrated the utility in using the combination of these two techniques to reduce effects resulting from their respective limitations. The aging of uranium dioxide proved to imply differing mechanisms depending on which condition the compound was exposed to. Identifying mechanisms will become clearer with more frequent analyses. Finally, although pinpointing a specific storage condition of nuclear material for forensics purposes is somewhat optimistic, this study was a quality proof of concept for developing this signature in the future.

3.2 Introduction

Uranium has been a technologically important element and corresponding set of compounds for over a century. It has many uses[141, 142], but the most significant and common are within the realm of the nuclear fuel cycle and nuclear weapons. These fields highlight the importance of uranium oxide study due to the rapid oxidation of uranium metal under atmosphere, the commonality of UO_2 nuclear fuel, the storage of fuels, and environmental exposure following the release of uranium oxides in fires, processing wastes, or reactor failures. Unlike the lanthanides, the 5f orbitals and 6d orbitals are close enough to allow complex hybridization allowing for a range of oxidation states and complex behavior in the actinides. This is especially true for uranium and its oxides. The uranium oxygen system includes many compounds, some with multiple phases, intermediates, mixed phases, and possible hydrolysis products[14, 75]. A number of studies have sought to model the kinetics and oxidation of uranium oxides[76-79], with the most recent by Andersson et al employing density functional calculations and the introduction of interstitial oxygen defect clusters to model the oxidation of UO_2 to U_4O_9[80-82]. Along with the theoretical work, there have been numerous experimental studies for the oxidation of uranium oxides under both static/laboratory conditions[83-86], and more complicated environmental or oxidizing conditions[17, 87-91]. Even so, there are still aspects of the uranium oxygen system that are not well understood. Starting and ending points are known, but the species transition mechanisms are still unclear. As mentioned above, there are a number of stable oxides, but the dioxide form is arguably the most important. It is the form used in nuclear fuels, and is often

a precursor to other compounds. In order to begin to understand uranium oxidation, the dioxide is a good starting point due to its simplicity and ease in synthesis.

Concerns over proliferation and environmental impact have sparked research with more specific directions. Two of those areas seek information regarding fate and transport of nuclear materials in the environment and source term characterization for nuclear forensics analysis[1, 5]. The author's group at LANL has analyzed samples from environmental sites with similar objectives[21, 103, 143]. That research and the previous work have provided insight into uranium oxidation. Even so, these studies often involve more complicated exposure conditions (true environmental exposure with daily and seasonal fluctuations) and unusual sample sources (more complicated starting materials or samples with questionable origin). In this work high purity uranium dioxide has been synthesized and exposed to four sets of atmospheric conditions for extended periods of time. Aging was followed by analysis with pXRD and EXAFS to study changes in the structure and chemical speciation over time in order to gain a better understanding of oxidation mechanisms and how these two techniques can be combined for optimal analysis for these tasks.

Analysis with pXRD results in the long-range order of materials and can identify mixtures of compounds and relative concentrations. Diffraction experiments, including the use of neutron spallation[83] and synchrotron radiation sources[85], are commonly used in a number of applications including environmental[144, 145], in situ oxidation[79, 83-85], synthesis verification, and forensics[1, 4] to name a few. X-ray diffraction is somewhat limited in many cases due to its inability to measure

amorphous or disordered compounds. EXAFS spectroscopy determines local structure, even in amorphous compounds including liquids or soils[21, 23, 28, 103, 143, 146, 147]. The technique has limitations of its own such as interference of absorption edges or uncertainty of elements assigned to an atomic shell. These two techniques are complimentary. Both are valuable for chemical information, but they haven't been combined to study uranium dioxide under a set of static atmospheric storage conditions. In this study high purity uranium dioxide was synthesized and aged under a set of four different static storage conditions. At regular time intervals sampling was performed and the material was analyzed with pXRD and EXAFS to gain information on the oxidation processes of uranium dioxide to help address nuclear forensics and environmental concerns.

3.3 Experimental

3.3.1 Synthesis

Standard natural uranium metal (New Brunswick National Laboratory, Standard Reference Material A-112) was dissolved with concentrated hydrochloric acid and hydrogen peroxide. Uranyl peroxide (UO_2O_2) was precipitated from uranyl chloride in solution at a max pH of 3.0. The precipitate was dried under vacuum at room temperature and then in a tube furnace at 100 °C. The material was heated to 500 °C to make A-UO_3, followed by 800 °C to make U_3O_8, and finally at 500 °C under hydrogen gas to make UO_2. Uranium dioxide was allowed to cool under hydrogen gas and equilibrated with atmosphere over about 24 hours. Each heating step was about 8 hours to ensure completion.

3.3.2 Aging

The aging vessels and salts were setup as discussed in Chapter 2, Section 2.3. About 500 mg of each material was placed in each aging vessel with various salts (LiI and KNO_3) at two temperatures (5 °C and 40 °C) in order to produce specific relative humidities (RH) based on the equation $RH = A \cdot e^{(B/T)}$[130], where A and B are constants for specific salts. Sampling and analysis of aliquots were performed every 3-6 months. Refer to Section 2.3, Table 6 for the selected aging conditions. These conditions were selected to mimic various atmospheric conditions: LHLT is a cold dry day, LHHT is a hot dry day, HHLT is a cold humid day, and HHHT is a hot humid day.

3.3.3 pXRD Analysis

Samples were prepared by grinding the oxides in a mortar and pestle and spreading over a grease-coated sample holder to affix the powdered oxide in place. A thin layer of spray-adhesive was applied as a layer of containment. X-ray diffraction data for unaged and 15 month samples were collected on a Bruker D8 Discover using copper radiation conditioned by a Göbel mirror ($K\alpha_1/K\alpha_2 = 10$), and either a scintillation detector or multi-wire gas proportional detector (Hi-Star). Data for 19 month and 27 month samples were collected on a Bruker D8 Advance using unconditioned copper radiation, and a 1-D silicon strip detector (Lynxeye). Qualitative analysis was performed using Jade software[137], and the International Center for Diffraction Data powder data files[138].

3.3.4 EXAFS Spectroscopy

Extended X-ray absorption fine structure data was taken at the Stanford Synchrotron Radiation Lightsource Beamline 11-2 (3.0 GeV, 500 mA) using a silicon (220) double crystal monochromator. The sample holder was cooled with a liquid nitrogen cryostat at 80-90 K. The uranium L_{III} absorption edge (17166 eV) was measured in fluorescence mode using a Lytle fluorescence detector, or in transmission mode using a gas ionization detector depending on data quality. The uranium L_{III} absorption edge was calibrated to the yttrium K edge, at 17038.25 eV and E_0 17166 eV. The data were analyzed using standard procedures[92, 93]. The EXAFS was extracted from the absorption spectra by subtracting the sum of an arctangent function and a Gaussian at the absorption edge and a polynomial spline function above the edge and then converted from energy to a wave vector, k. A non-linear least squares curve fit was applied to the resulting background-subtracted k^3-weighted EXAFS $\chi(k)$ spectra and Fourier transformed to a radial structure function. The k-range of each comparison was kept constant. The individual frequencies of the EXAFS were extracted, fitted, and curve-fit utilizing amplitudes and phases calculated by the FEFF7 (or when possible FEFF8)[134] code based on uranium oxide compound crystal structures available from the Inorganic Crystal Structure Database[135]. The Debye-Waller factor, σ, and the distance, R, from the absorber-scatterer pairs were varied for all fits, and the number of atoms, N, was varied where applicable. It's important to keep in mind the phase shift in R, ϕ, when comparing the following EXAFS data.

3.4 Results and Discussion

3.4.1 Low Humidity Low Temperature

The samples exposed to 5 °C and 25% RH were selected for pXRD analysis at 15 and 27 months and for EXAFS at 3, 19, and 27 months. The collected pXRD results, including the un-aged material are presented in Figure 15. All the pXRD figures will include the literature lines and relative intensities of both UO_2[83] and metaschoepite[148], $UO_3 \cdot 2H_2O$, the endpoint implied by diffraction results. As discussed in Section 3.3.3, two different diffractometers were used on these samples; un-aged UO_2 and the sample aged for 27 months have considerably greater signal to noise, but the changes over time are readily discernable. Even with the increased noise for the 15-month sample, the most intense peak of $UO_3 \cdot 2H_2O$ is visible at about 12°. At 27 months it is more obvious, but still quite broad.

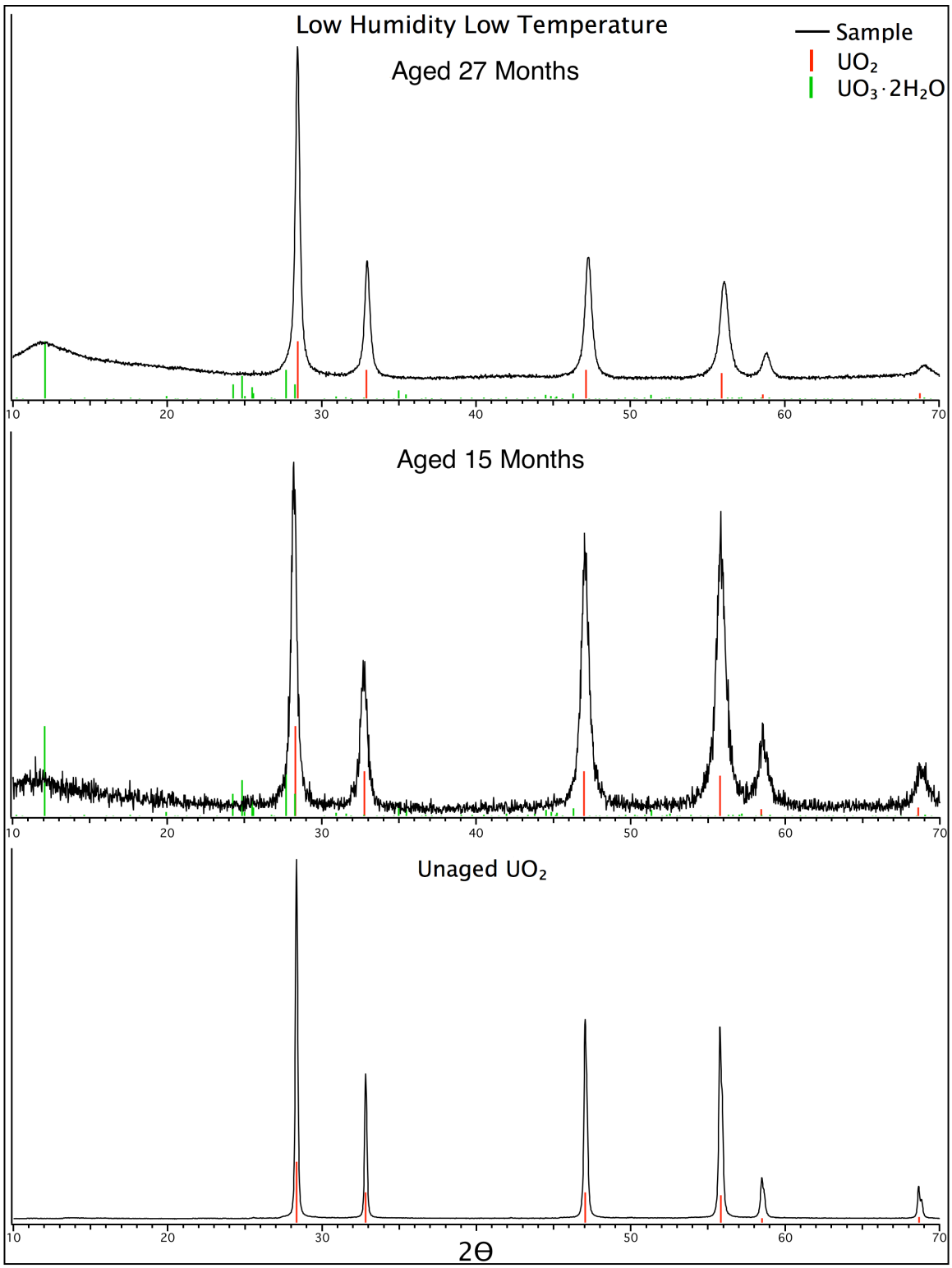

Figure 15. Diffraction spectra for un-aged UO_2 and the LHLT samples taken at 15 and 27 months. Reference lines and relative intensities are shown for UO_2 and $UO_3 \cdot 2H_2O$.

A simple comparison of the EXAFS data for these compounds is a direct overlay of their Fourier transforms and real contributions (Figure 16). Crystallographic $UO_{2.00}$ has three bonds: ~2.37 Å uranium-oxygen, ~3.87 Å uranium-uranium, and ~4.53 Å uranium-oxygen[83]. The overlay shows a clear decrease in amplitude these shells and the ones in the non-crystallographic region beyond 5 Å, indicating a large amount of disorder as the aging process continues. There is also in increase in the region below ~2 Å relative to the ~2.37 Å bond. The real components are quite close and converge nearly everywhere except for in the region about 2 Å after which the aged samples converge with one another better than un-aged UO_2, indicating a real change in chemical speciation and some bonding contribution in that area.

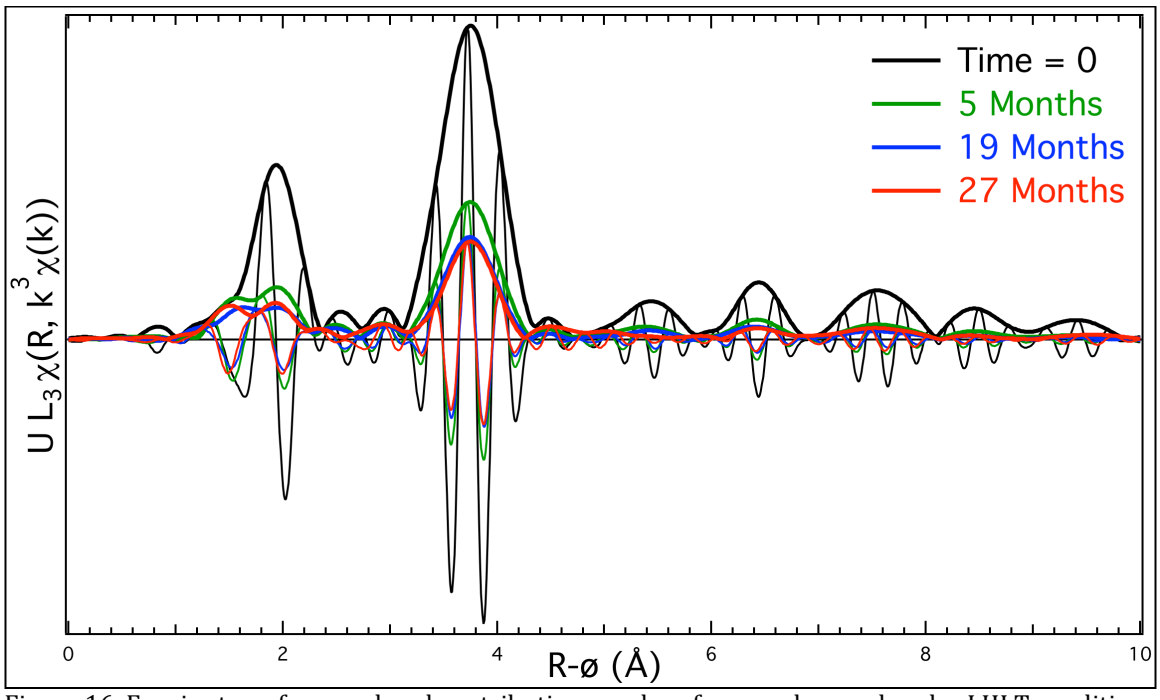

Figure 16. Fourier transform and real contribution overlays for samples aged under LHLT conditions (3.03-14.20 k).

EXAFS fits for transmission data of each sample are shown in Figure 17 through Figure 20. The parameters for these fits (bond distance, R, number of atoms, N, and Debye-Waller Factor, σ) are summarized in Table 7. For the un-aged material, the fit is somewhat unusual. In order to obtain a quality fit, a uranium-oxygen at ~1.76 Å was also included, indicative of a more highly oxidized species. Throughout the author's work at LANL, many seemingly highly ordered stoichiometric $UO_{2.00}$ compounds (including freshly reduced and single crystal compounds) have exhibited this feature. The presence of this oxo contribution leads to two possibilities: either the compounds that are seemingly pure $UO_{2.00}$ are actually oxidized to some degree, or the feature results from an EXAFS spectroscopy phenomenon that has not yet been determined. More analysis of these standard compounds, in conjunction with aqueous species that have a higher confidence in their stoichiometry must be performed. This oxo bond was included in nearly every fit for these aging studies. However, the un-aged materials typically have a very low fraction of that contribution, which grows over time.

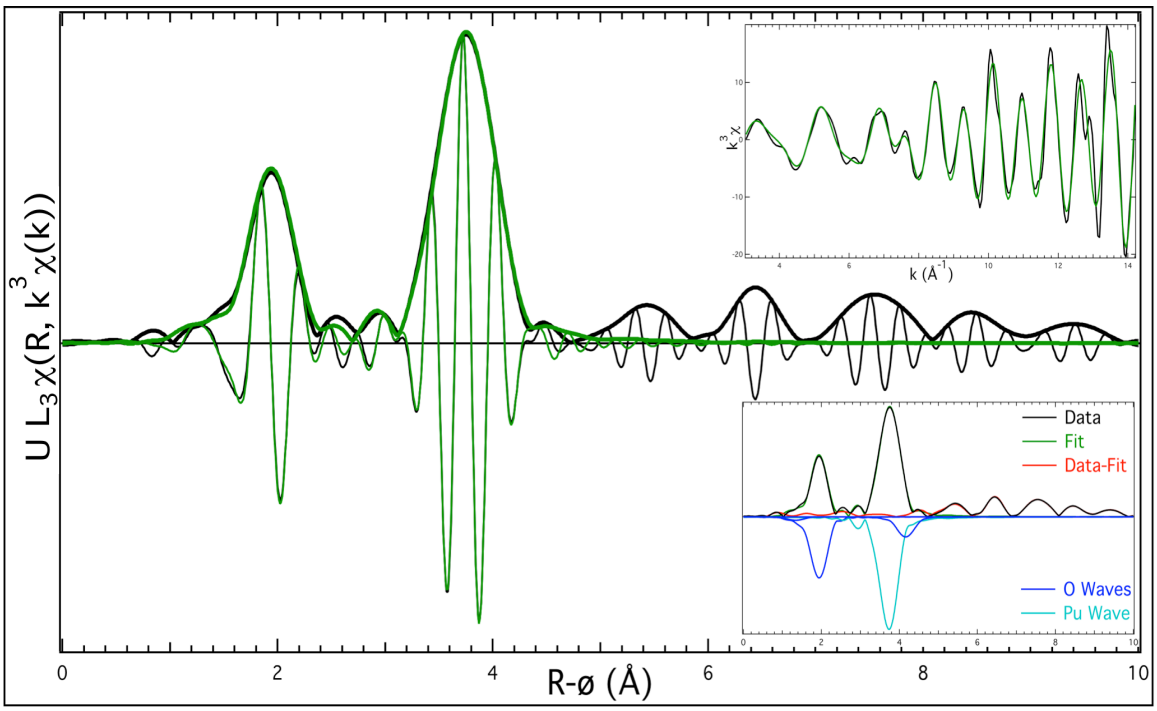

Figure 17. Uranium L_{III} EXAFS spectrum for un-aged UO_2 (3.03-14.20 k). Data is shown in black and the curve-fits in green. $k^3\chi$ plots are shown in the upper inset and individual shell contributions on the lower inset.

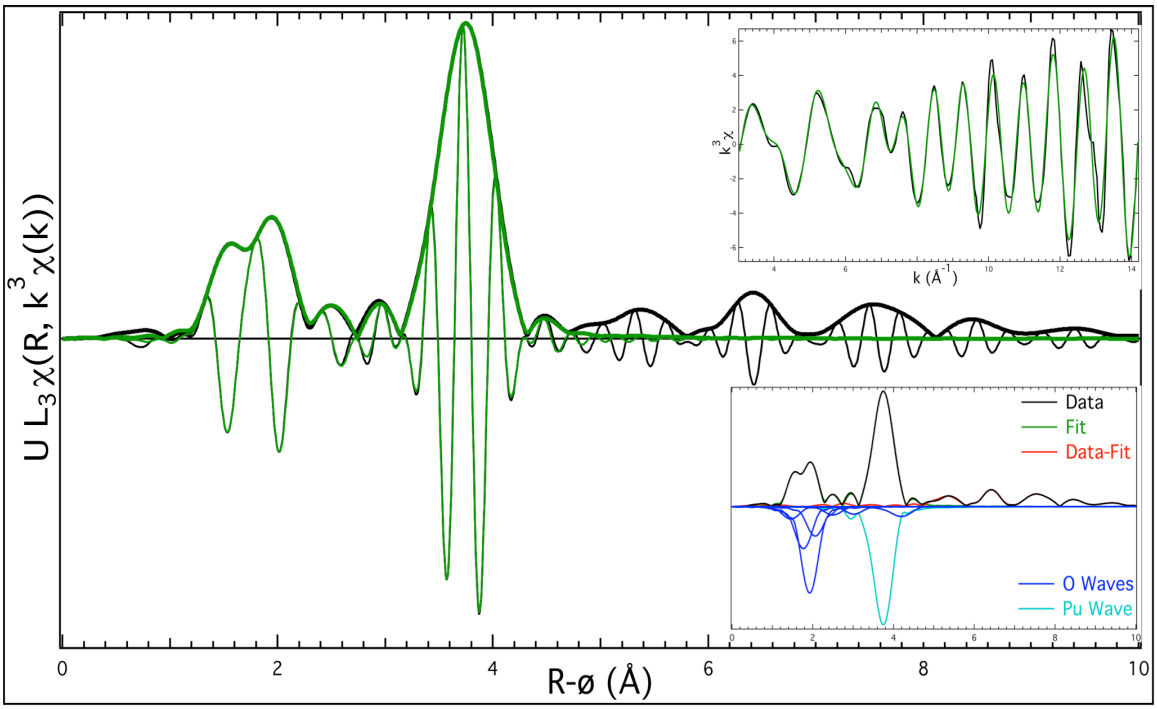

Figure 18. Uranium L_{III} EXAFS spectrum for UO_2 aged 5 months under LHLT conditions (3.03-14.20 k). Data is shown in black and the curve-fits in green. $k^3\chi$ plots are shown in the upper inset and individual shell contributions on the lower inset.

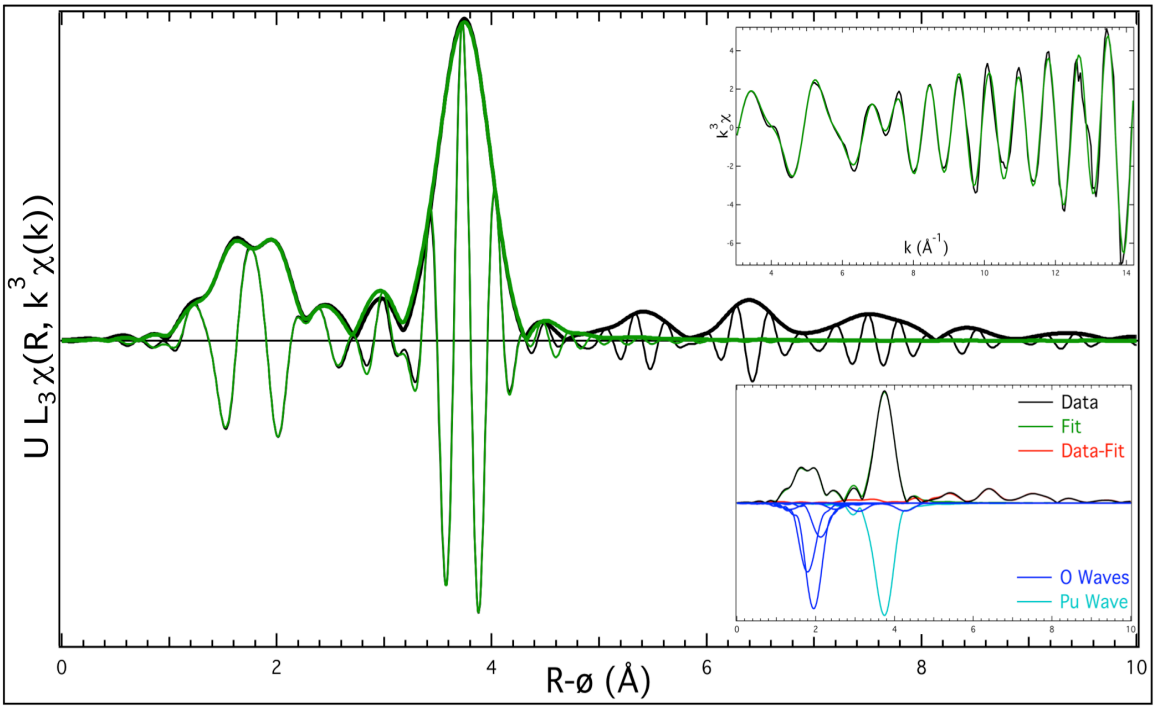

Figure 19. Uranium L_{III} EXAFS spectrum for UO_2 aged 19 months under LHLT conditions (3.03-14.20 k). Data is shown in black and the curve-fits in green. $k^3\chi$ plots are shown in the upper inset and individual shell contributions on the lower inset.

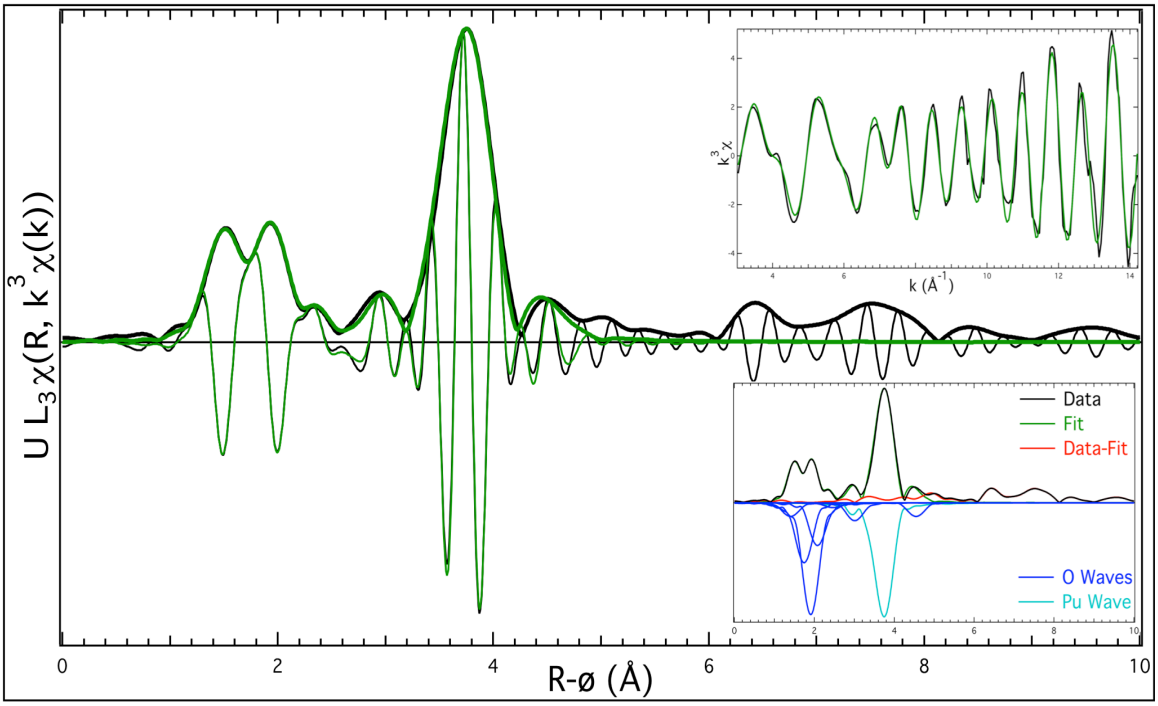

Figure 20. Uranium L_{III} EXAFS spectrum for UO_2 aged 27 months under LHLT conditions (3.03-14.20 k). Data is shown in black and the curve-fits in green. $k^3\chi$ plots are shown in the upper inset and individual shell contributions on the lower inset.

Table 7. Summarized fit results from the LHLT samples.

Sample	Shell	R (Å)	N	σ
Un-aged	O	1.762 (0.058)	0.259 (0.085)	0.079
	O	2.361 (0.019)	7.496 (2.139)	0.069
	U	3.863 (0.001)	9.194 (2.228)	0.021
	O	4.571 (0.018)	17.495 (5.466)	0.071
T = 5 Months	O	1.868 (0.017)	0.260 (0.082)	0.050
	O	2.190 (0.017)	1.591 (0.454)	0.060
	O	2.337 (0.014)	3.144 (0.781)	0.050
	O	2.473 (0.017)	1.200 (0.360)	0.050
	O	2.915 (0.017)	0.555 (0.175)	0.060
	O	3.418 (0.159)	0.504 (0.159)	0.040
	U	3.866 (0.010)	5.272 (1.131)	0.042
	O	4.608 (0.029)	10.737 (3.342)	0.119
T = 19 Months	O	1.754 (0.018)	0.082 (0.026)	0.044
	O	2.198 (0.012)	1.370 (0.344)	0.034
	O	2.356 (0.012)	2.739 (0.620)	0.044
	O	2.523 (0.013)	0.757 (0.0215)	0.014
	O	2.910 (0.020)	0.288 (0.091)	0.054
	O	3.489 (0.016)	0.414 (0.130)	0.034
	U	3.868 (0.009)	3.420 (0.702)	0.033
	O	4.640 (0.024)	3.330 (1.050)	0.091
T = 27 Months	O	1.815 (0.018)	0.191 (0.060)	0.050
	O	2.164 (0.016)	1.563 (0.425)	0.060
	O	2.323 (0.013)	2.835 (0.0672)	0.050
	O	2.480 (0.014)	0.870 (0.248)	0.020
	O	2.881 (0.018)	0.222 (0.071)	0.060
	O	3.412 (0.016)	0.844 (0.261)	0.040
	U	3.865 (0.009)	3.556 (0.808)	0.042
	O	4.830 (0.018)	2.601 (0.811)	0.056

Although the Fourier transform overlay indicated disordered compounds, the scaling on fit figures show that ordered UO_2 is still present. Both the crystallographic and non-crystallographic shells are seen at each time period. The non-crystallographic shells become slightly distorted and decreased in relative amplitude over time, but are still present. The change evident in both the overlay

and the fit figures is the growth of the oxygen bond contributions below ~2 Å. Previous studies[92, 93] have postulated that this is predominantly a hexavalent uranium-oxo bond. Combined with the presence of the uranyl oxy-hydroxide species in the pXRD and stability of hexavalent species over the pentavalent ones, this contribution in the aged samples' Fourier transforms is consistent with the previous studies. The fitted oxo bond distance ranges (1.754-1.868 Å), likely a result of an overall small number of fitted oxygen atoms in this region and abnormalities with the EXAFS data.

The multisite oxygen distribution seen in the aged samples is common in uranium oxides[29, 92, 93]. These contributions may point to the bonding of specific ligands (i.e. a bond at ~2.2 Å may indicate a hydroxide species[149]), or presence of another uranium oxide. However, due to the small difference in resolution ($\pi/2k$ = ~0.14 Å) and shells in these distributions, there is lower confidence in assigning these contributions. Furthermore, the large number of possible bonds based on crystallographic data for some of the simple oxides (Table 8) provides more uncertainty. Another trend from these fits is that the longer crystallographic uranium-oxygen is steadily decreasing in amplitude (~17.5 down to 2.6 atoms) and increasing in distance (~4.57 up to 4.83 Å). This suggests formation of a new bond, or distortion due to higher uncertainty from decreasing amplitude.

Table 8. The approximate number of separate uranium-oxygen (two ranges) and uranium-uranium bonds identified by crystallographic data in the literature for selected uranium oxides.

Compound	**U-O, 1.6-2.7 Å**	**U-O, 2.7-4.75 Å**	**U-U, 3.7-4.2 Å**
UO_2[83]	1	1	1
α-U_4O_9[150]	4	8	4
α-U_3O_7[83]	7	18	12
α -U_3O_8[151]	2	2	5
α -UO_3[152]	3	1	1
$UO_3{\cdot}2H_2O$[148]	7	14	5

The appearance of lines indicative of $UO_3{\cdot}2H_2O$ in all pXRD data makes comparison with that literature structure of more importance. It has a large number of bonds, very few of which are more intense than others. This and the lack of overlap between the literature structure and fitted shells make this comparison difficult so a detailed comparison will not be included in this discussion.

3.4.2 Low Humidity High Temperature

Samples exposed to 40 °C and 15% RH were selected for pXRD analysis at 15 and 27 months and for EXAFS analysis at 3, 19, and 27 months. The collected pXRD results, including the un-aged material are presented in Figure 21. In this 15-month sample, the signal to noise is much better than the one aged under LHLT. Here, the growth of $UO_3{\cdot}2H_2O$ is barely noticed at 15 months, but at 27 months a number of its peaks are apparent. These are more intense and much sharper than the one peak seen in the sample aged under LHLT, indicating a more ordered compound.

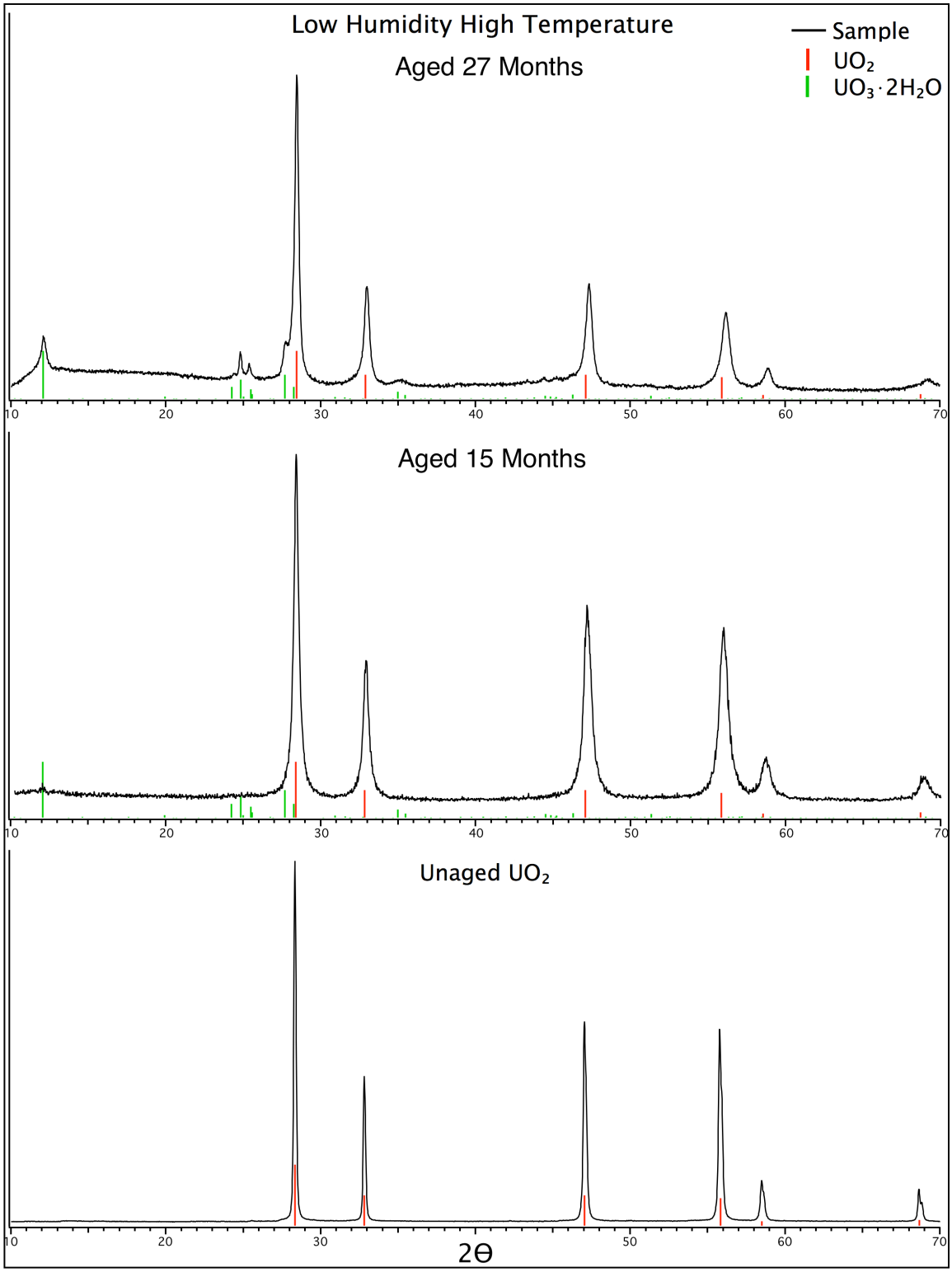

Figure 21. Diffraction spectra for un-aged UO_2 and the LHHT samples taken at 15 and 27 months. Reference lines and relative intensities are shown for UO_2 and $UO_3 \cdot 2H_2O$.

The EXAFS Fourier transform overlay is shown in Figure 22. Again, there is an overall decrease of both nearest-neighbors and the non-crystallographic contributions. The most significant decrease is at 5 months. There is a steady decrease in amplitude for the uranium-uranium region and crystallographic ~2.37 oxygen. This disordering of the UO_2 lattice is accompanied by an increase in amplitude for the region below ~2.3 Å. The real contributions for all samples are similar to the LHLT samples in that they are quite close except for the region below the first crystallographic oxygen. At that point, the aged samples match one another more closely than un-aged UO_2.

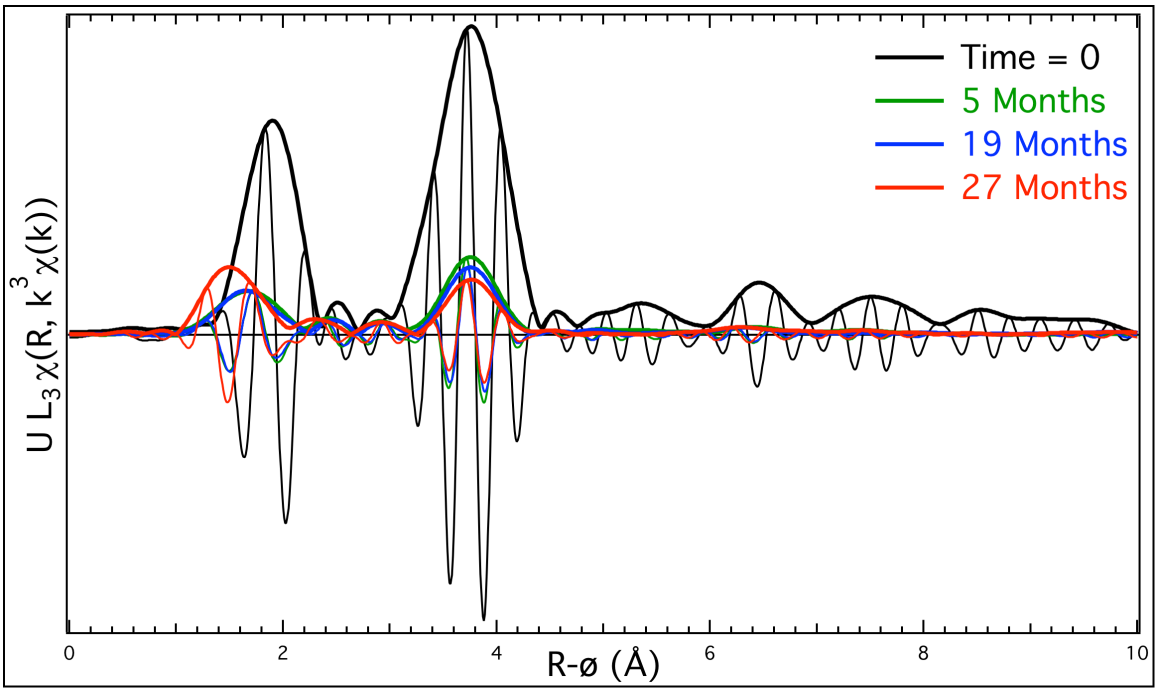

Figure 22. Fourier transform and real contribution overlays for samples aged under LHHT conditions (3.05-13.70 k).

Fits for individual samples are shown in Figure 23 through Figure 26. The parameters for these fits (bond distance, R, number of atoms, N, and Debye-Waller

Factor, σ) are summarized in Table 9. The non-crystallographic shells are still present, but the amplitudes are within the noise for the material aged 27 months. The uranium-uranium bond decreases through 19 months. The amplitudes at 27 months are lower but the larger Debye-Waller Factor at 19 months increased its number of atoms compared to the number at 27 months. Not taking into account the fairly small difference in k-range fitted (3.03-13.70 versus 3.03-14.20 in the LHLT samples), the total number of uranium atoms fitted is less than the LHLT samples (3.56 versus 2.41), indicating a more oxidizing environment. When a quick was fit was performed on the same k-range as LHLT samples, the number of atoms for the uranium-uranium shell was still only 3.34. Even though the k-range didn't contribute to the decrease in uranium-uranium atoms, it did decrease resolution in the nearest neighbor oxygen region, resulting in a less defined, broad multisite oxygen distribution below ~2.3 Å. Similar to the LHLT conditions, as aging continued, the region below ~2.3 Å began to dominate relative to the crystallographic oxygen shell at ~2.37 Å. Although the LHHT environment may be more oxidizing than the LHLT environment, the fits didn't produce any shells indicative to specific oxidized species, namely $UO_3 \cdot 2H_2O$. Exhaustive fitting was attempted for the crystallographic shell at ~4.53 Å, but no shells were applied due to a poor fit.

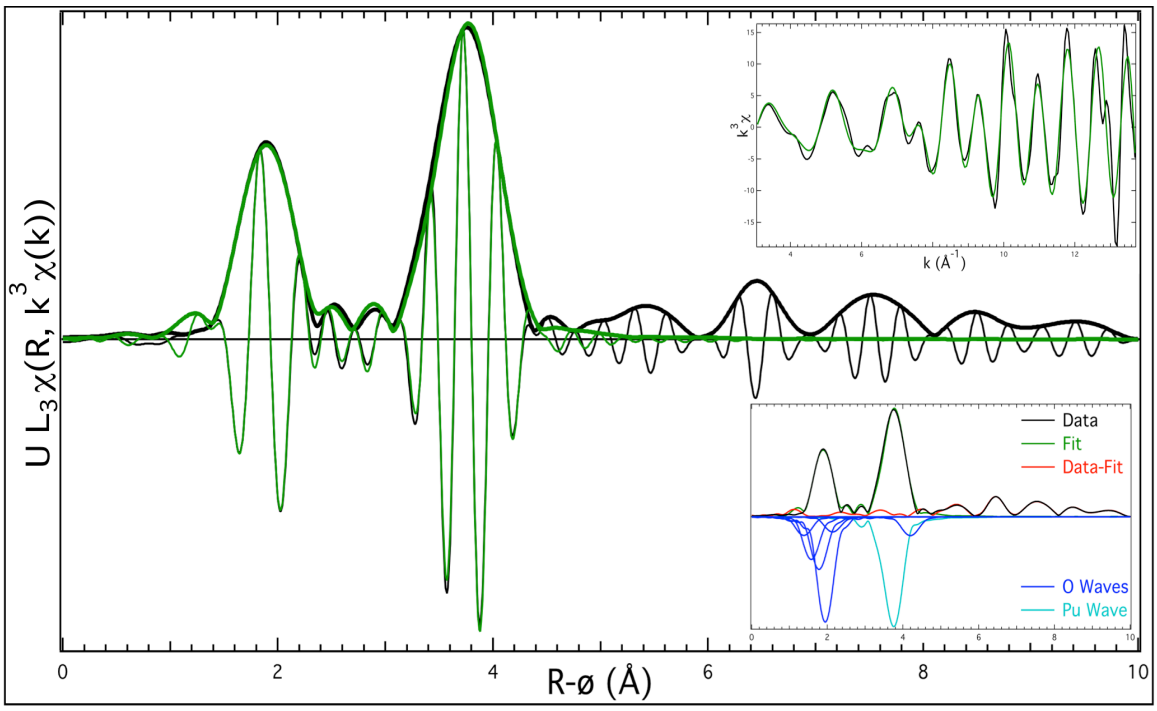

Figure 23. Uranium L_{III} EXAFS spectrum for un-aged UO_2 (3.05-13.70 k). Data is shown in black and the curve-fits in green. $k^3\chi$ plots are shown in the upper inset and individual shell contributions on the lower inset.

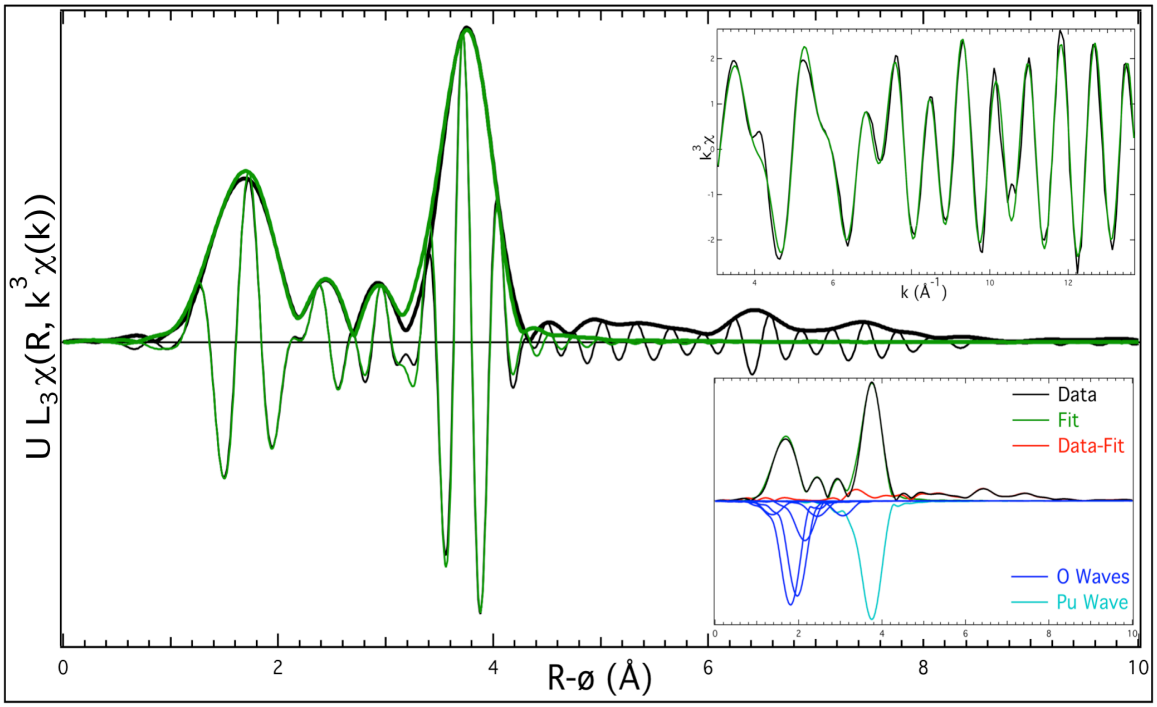

Figure 24. Uranium L_{III} EXAFS spectrum for UO_2 aged for 5 months at the LHHT conditions (3.05-13.70 k). Data is shown in black and the curve-fits in green. $k^3\chi$ plots are shown in the upper inset and individual shell contributions on the lower inset.

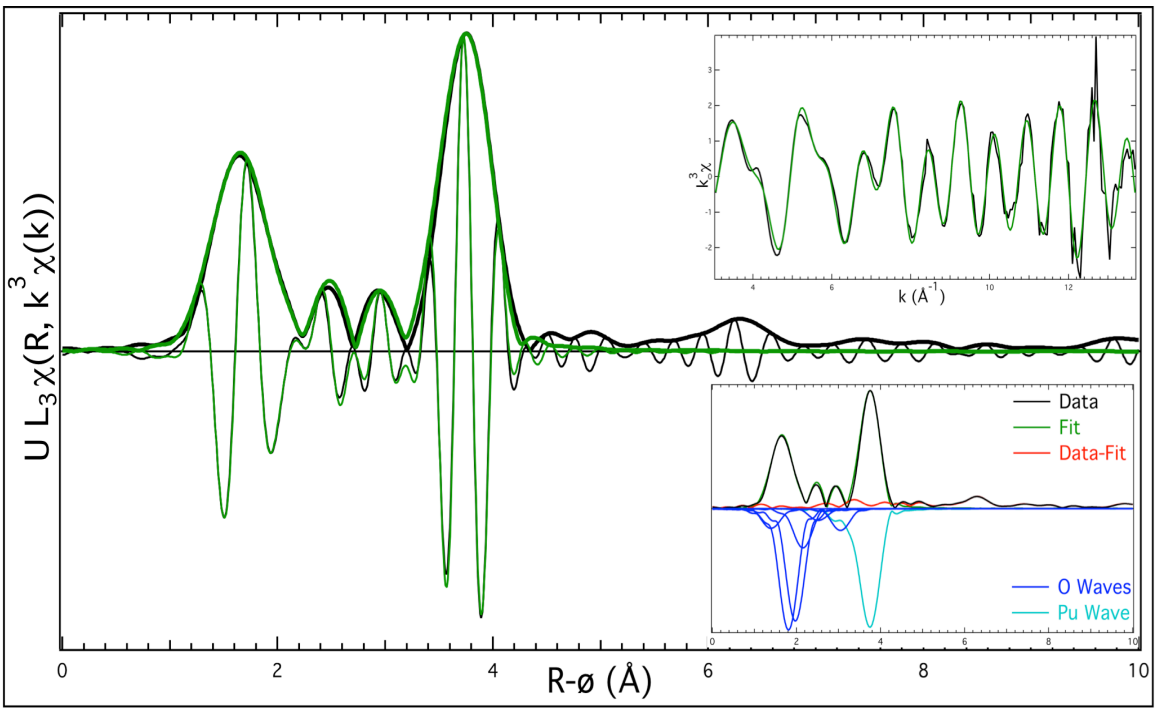

Figure 25. Uranium L_{III} EXAFS spectrum for UO_2 aged for 19 months at the LHHT conditions (3.05-13.70 k). Data is shown in black and the curve-fits in green. $k^3\chi$ plots are shown in the upper inset and individual shell contributions on the lower inset.

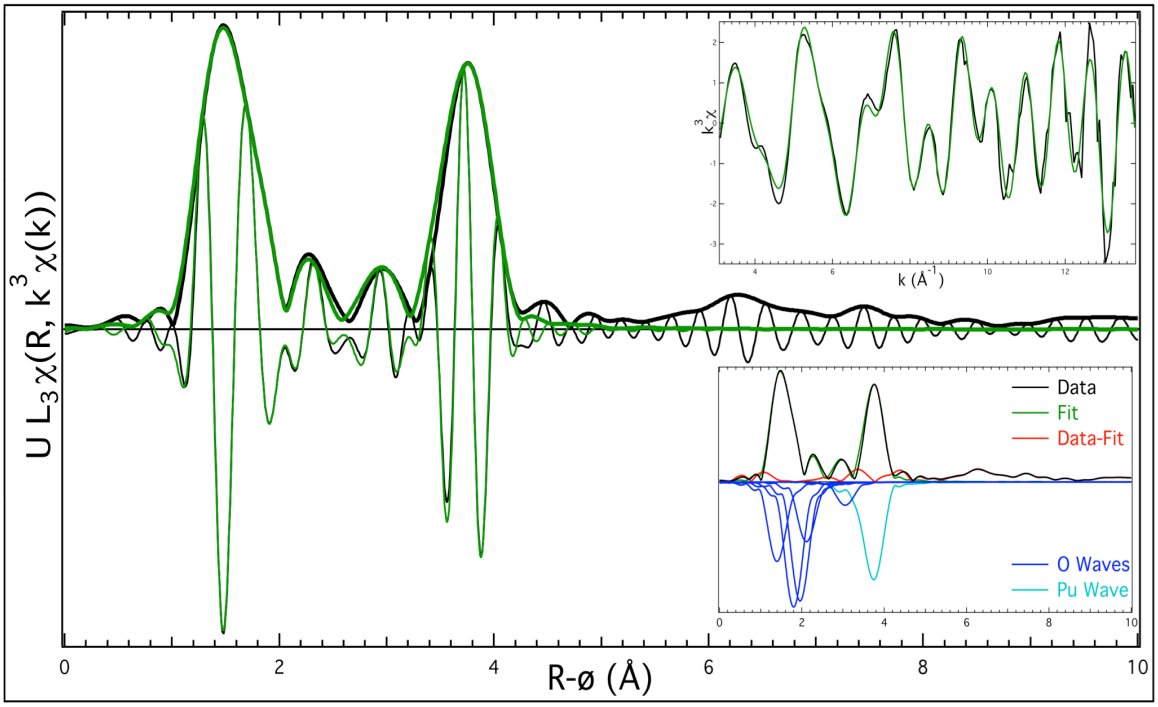

Figure 26. Uranium L_{III} EXAFS spectrum for UO_2 aged for 27 months at the LHHT conditions (3.05-13.70 k). Data is shown in black and the curve-fits in green. $k^3\chi$ plots are shown in the upper inset and individual shell contributions on the lower inset.

Table 9. Summarized fit results from the LHHT samples.

Sample	Shell	R (Å)	N	σ
Un-aged	O	1.793 (0.016)	0.669 (0.210)	0.035
	O	1.991 (0.016)	2.090 (0.627)	0.035
	O	2.203 (0.016)	3.203 (0.961)	0.035
	O	2.369 (0.014)	8.324 (2.204)	0.045
	O	2.559 (0.017)	1.245 (0.391)	0.035
	U	3.871 (0.011)	8.978 (2.228)	0.019
	O	4.592 (0.020)	13.476 (4.268)	0.065
T = 5 Months	O	1.792 (0.015)	0.145 (0.045)	0.050
	O	2.229 (0.014)	2.374 (0.530)	0.070
	O	2.383 (0.013)	2.073 (0.472)	0.060
	O	2.561 (0.018)	1.074 (0.298)	0.070
	O	2.864 (0.020)	0.581 (0.182)	0.070
	O	3.460 (0.017)	0.684 (0.211)	0.060
	U	3.864 (0.010)	3.555 (0.718)	0.056
T = 19 Months	O	1.809 (0.015)	0.154 (0.048)	0.036
	O	2.226 (0.014)	1.892 (0.452)	0.056
	O	2.384 (0.013)	1.725 (0.418)	0.046
	O	2.557 (0.018)	0.727 (0.218)	0.056
	O	0.291 (0.016)	0.240 (0.075)	0.036
	O	3.445 (0.016)	0.698 (0.209)	0.046
	U	3.868 (0.011)	3.557 (0.842)	0.062
T = 27 Months	O	1.803 (0.013)	0.573 (0.153)	0.030
	O	2.213 (0.012)	1.635 (0.386)	0.045
	O	2.363 (0.012)	1.649 (0.398)	0.040
	O	2.512 (0.015)	0.764 (0.219)	0.030
	O	3.445 (0.018)	0.685 (0.447)	0.040
	U	3.863 (0.011)	2.405 (0.625)	0.053

3.4.3 High Humidity Low Temperature

Samples exposed to 5 °C and 97% RH were selected for pXRD (Figure 27) analysis at 15 and 27 months and EXAFS at 3, 15, and 27 months. Diffraction signal to noise is more consistent and $UO_3 \cdot 2H_2O$ peaks aren't significant until 27 months. At 27 months the peak at 12° is more resolved than the LHHT sample analyzed at 27 months, but lower in intensity (other peaks are also lower than the LHHT sample).

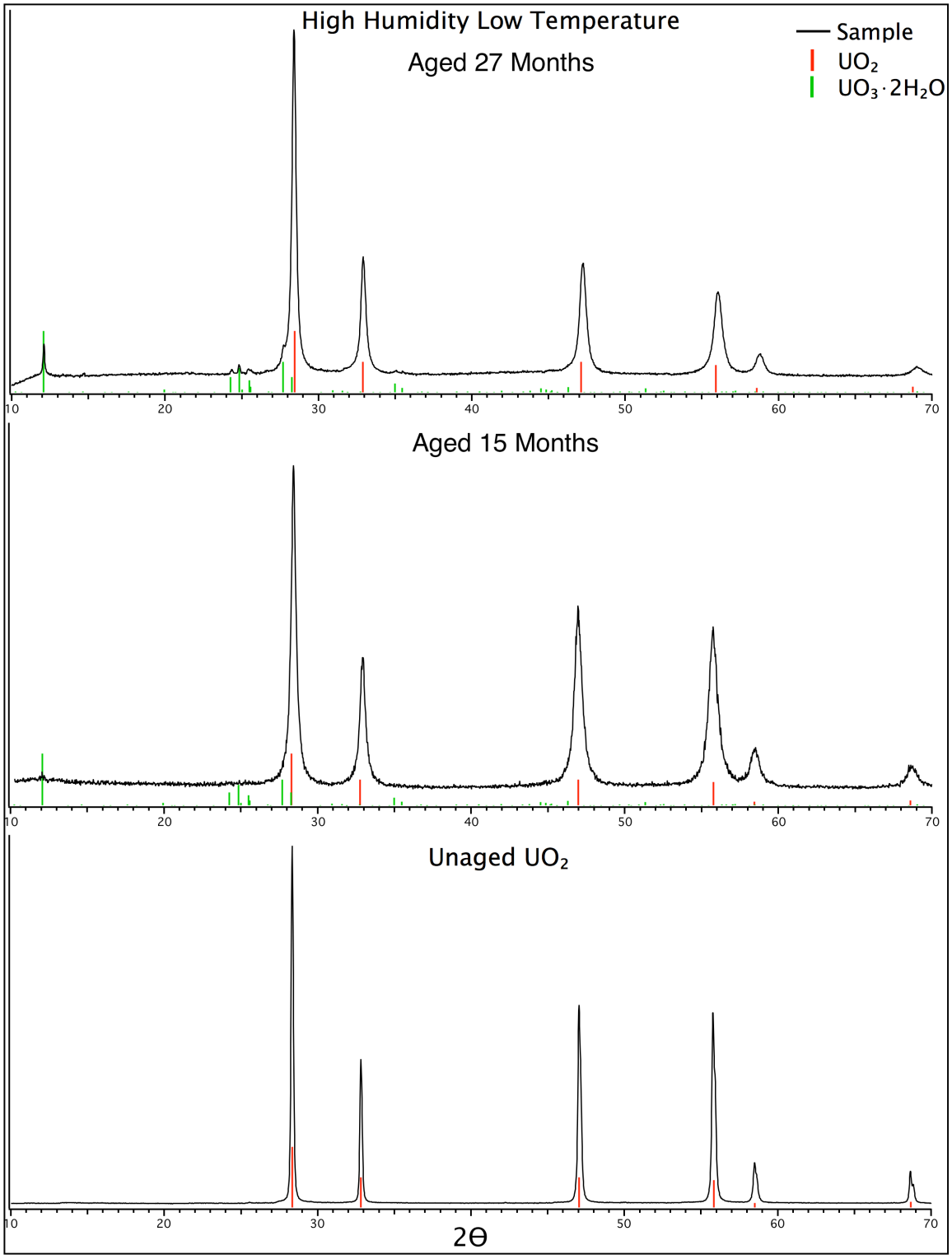

Figure 27. Diffraction spectra for un-aged UO_2 and the HHLT samples taken at 15 and 27 months. Reference lines and relative intensities are shown for UO_2 and $UO_3 \cdot 2H_2O$.

The EXAFS Fourier transform overlay is shown in Figure 28. Again, contributions indicative of UO_2 decrease in significantly through 5 and 19 months, and increase slightly at 27 months. It's not clear why there is an increase, but the difference is small and the oxygen around ~2.37 Å continued to decrease in amplitude.

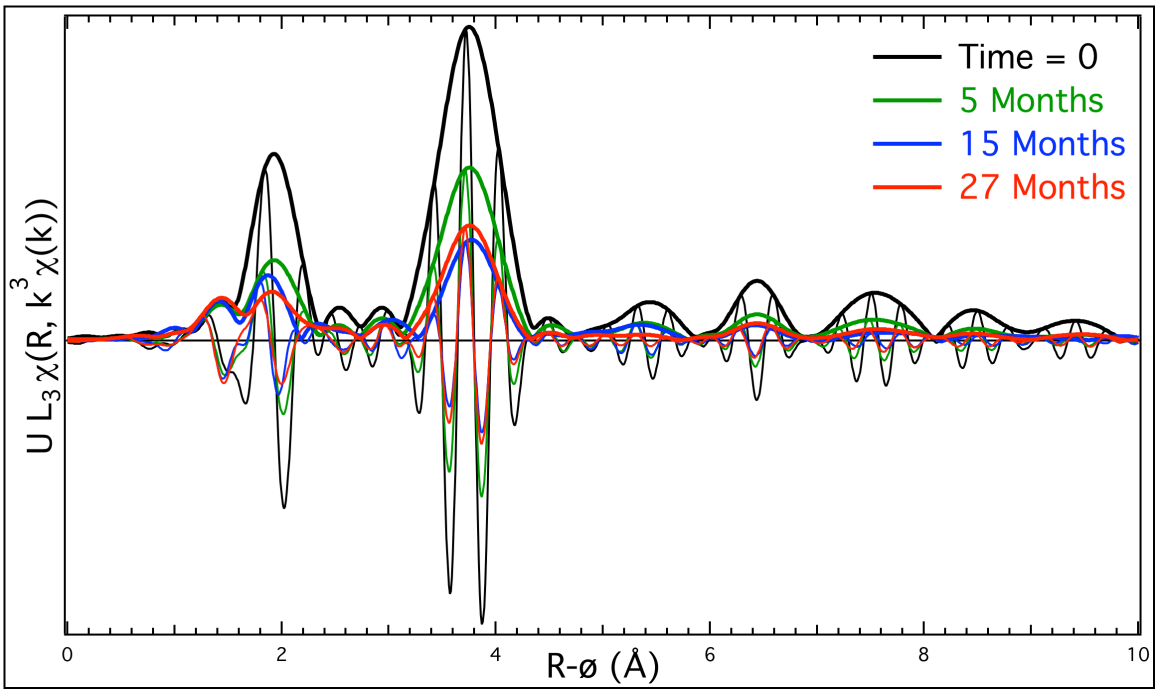

Figure 28. Fourier transform and real contribution overlays for samples aged under HHLT conditions (3.03-14.15 k).

Fits for individual samples are shown in Figure 29 through Figure 32. Fit parameters are summarized in Table 10. The non-crystallographic shells are present at 3 months, but beyond that they aren't discernible. The fit included more atoms in the uranium-uranium shell fit than other conditions at 27 months. The data was analyzed over a k-range of 3.03-14.15, and so the multisite oxygen region has comparable resolution to the LHLT data.

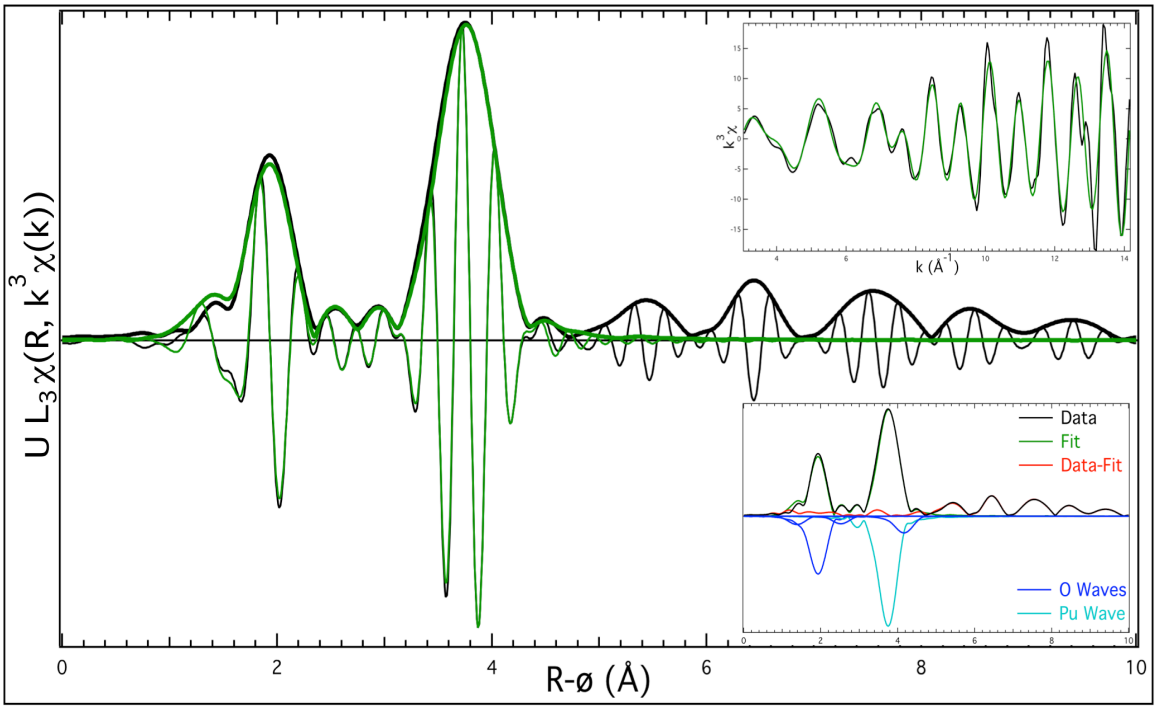

Figure 29. Uranium L_{III} EXAFS spectrum for un-aged UO_2 (3.05-14.15 k). Data is shown in black and the curve-fits in green. $k^3\chi$ plots are shown in the upper inset and individual shell contributions on the lower inset.

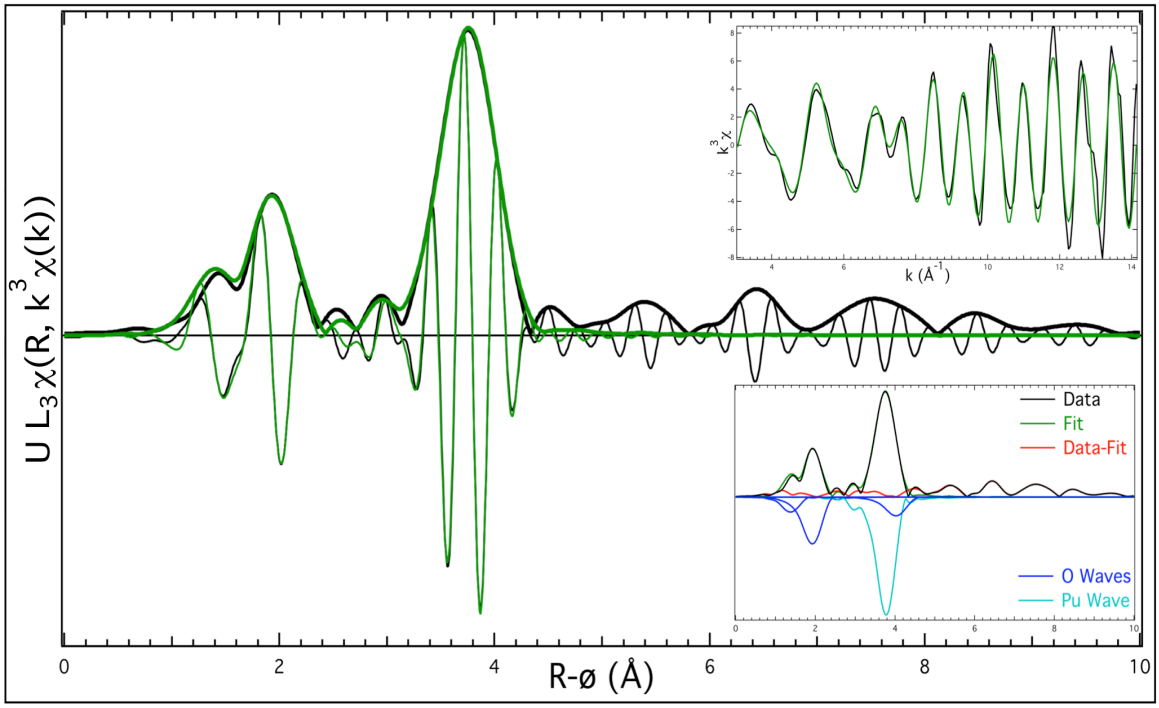

Figure 30. Uranium L_{III} EXAFS spectrum for UO_2 aged 5 months under HHLT conditions (3.05-14.15 k). Data is shown in black and the curve-fits in green. $k^3\chi$ plots are shown in the upper inset and individual shell contributions on the lower inset.

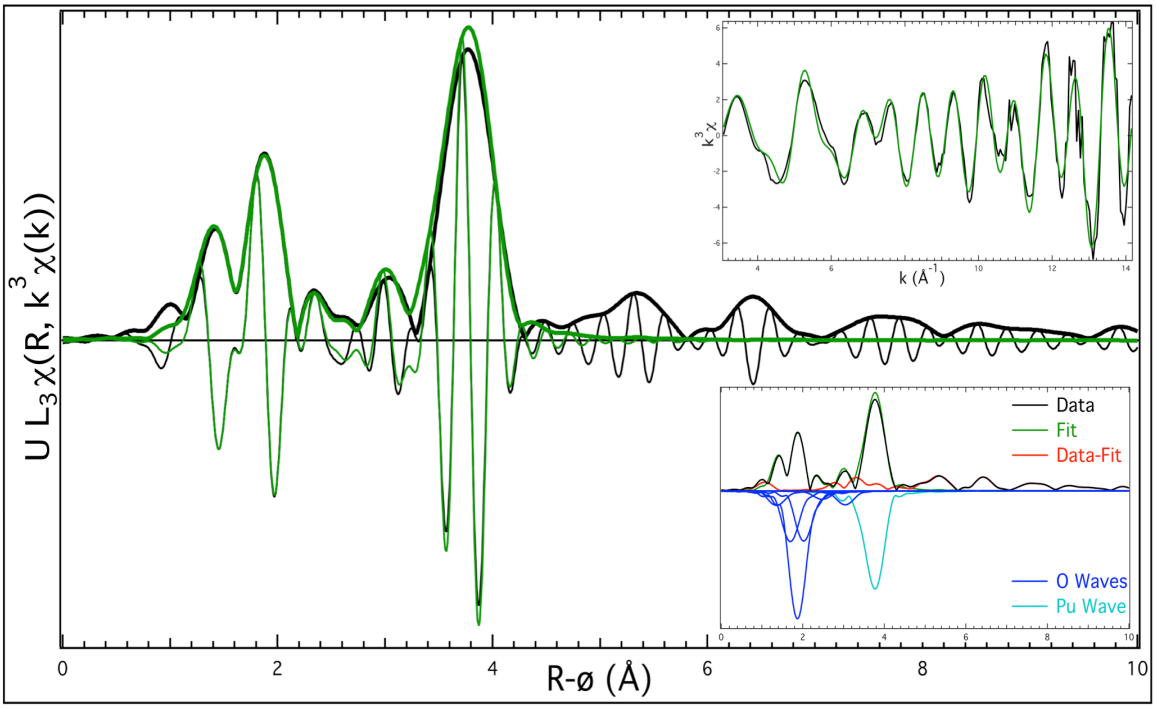

Figure 31. Uranium L_{III} EXAFS spectrum for UO_2 aged 15 months under HHLT conditions (3.05-14.15 k). Data is shown in black and the curve-fits in green. $k^3\chi$ plots are shown in the upper inset and individual shell contributions on the lower inset.

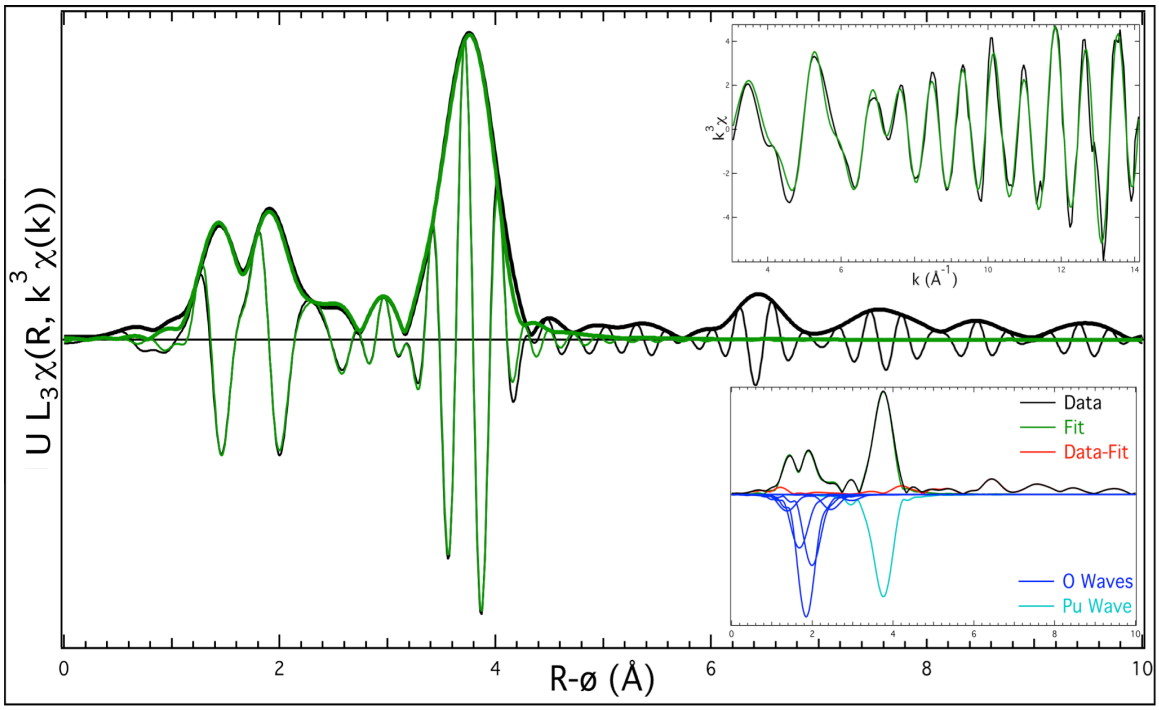

Figure 32. Uranium L_{III} EXAFS spectrum for UO_2 aged 27 months under HHLT conditions (3.05-14.15 k). Data is shown in black and the curve-fits in green. $k^3\chi$ plots are shown in the upper inset and individual shell contributions on the lower inset.

Table 10. Summarized fit results from the HHLT samples.

Sample	Shell	R (Å)	N	σ
Un-aged	O	1.797 (0.015)	0.501 (0.159)	0.065
	O	2.356 (0.021)	8.164 (2.351)	0.075
	O	2.932 (0.015)	1.343 (0.427)	0.065
	U	3.870 (0.010)	10.143 (2.553)	0.031
	O	4.582 (0.024)	25.056 (7.850)	0.095
T = 5 Months	O	1.786 (0.017)	0.537 (0.181)	0.070
	O	2.356 (0.025)	6.135 (1.760)	0.100
	U	3.874 (0.011)	9.500 (2.291)	0.057
	O	4.483 (0.029)	25.401 (8.280)	0.115
T = 15 Months	O	1.761 (0.015)	0.166 (0.053)	0.004
	O	2.117 (0.015)	1.216 (0.351)	0.039
	O	2.285 (0.012)	3.359 (0.814)	0.034
	O	2.438 (0.014)	1.314 (0.378)	0.019
	O	2.896 (0.019)	0.518 (0.165)	0.059
	O	3.459 (0.014)	1.115 (0.356)	0.054
	U	3.874 (0.010)	3.851 (0.959)	0.039
T = 27 Months	O	1.785 (0.017)	0.239 (0.074)	0.036
	O	2.103 (0.014)	1.205 (0.330)	0.036
	O	2.266 (0.011)	3.173 (0.720)	0.036
	O	2.409 (0.012)	1.813 (0.467)	0.021
	O	2.878 (0.016)	0.667 (0.209)	0.041
	O	3.405 (0.018)	0.490 (0.161)	0.056
	U	3.868 (0.010)	4.065 (0.933)	0.041

3.4.4 High Humidity High Temperature

Samples exposed to 40 °C and 89% RH were selected for pXRD analysis (Figure 33). For diffraction, at 15 months, noise is comparable to the LHLT 15-month sample, but $UO_3 \cdot 2H_2O$ peaks are more intense than any other set of aging conditions. The most intense UO_2 peaks are very weak, but still evident. At 27 months, only very defined peaks consistent with $UO_3 \cdot 2H_2O$ are present, indicating a complete change in chemical speciation and the growth of an ordered metaschoepite-like species.

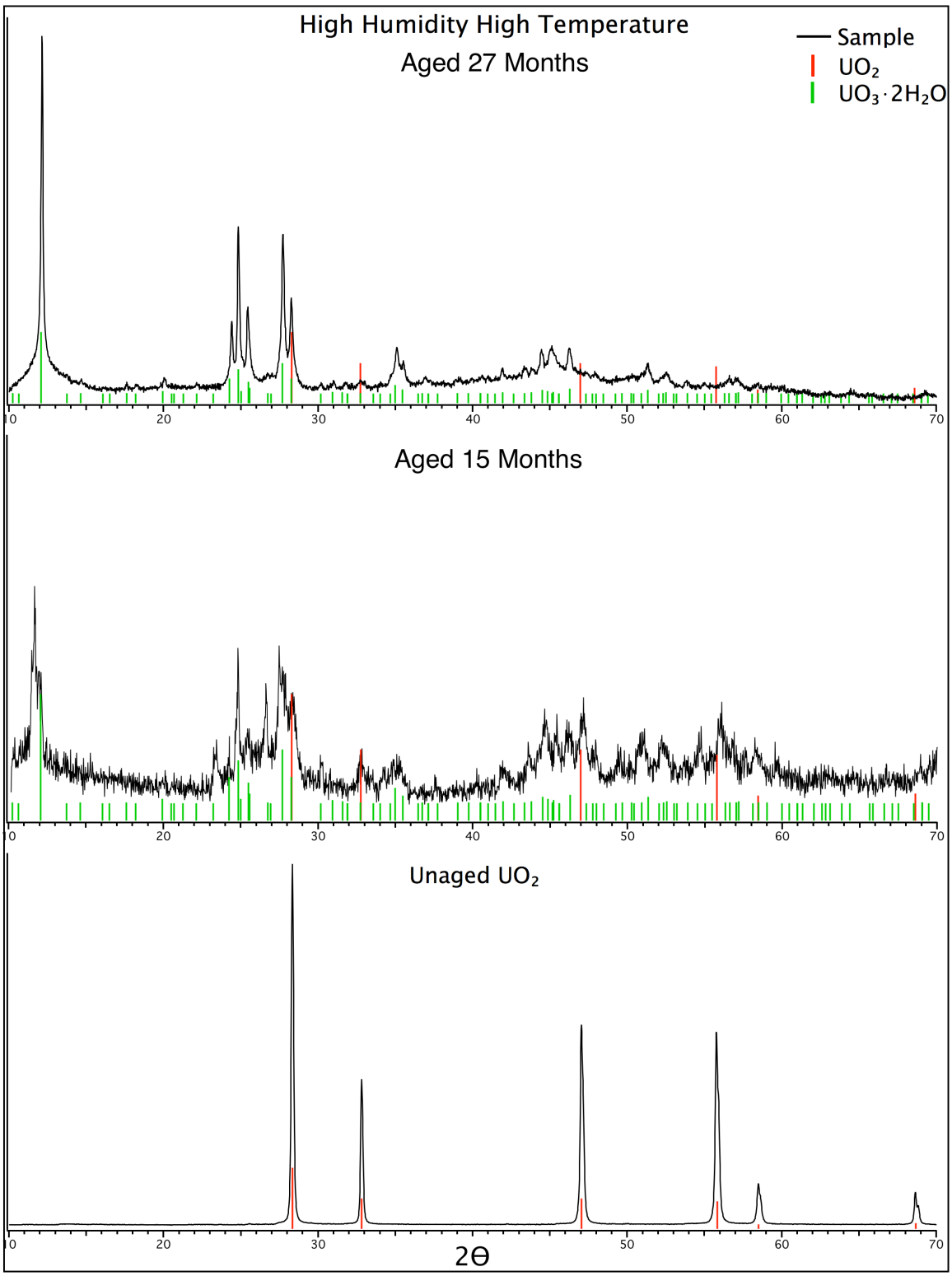

Figure 33. Diffraction spectra for un-aged UO_2 and the HHHT samples taken at 15 and 27 months. Reference lines and relative intensities are shown for UO_2 and $UO_3 \cdot 2H_2O$.

The EXAFS Fourier transform for HHHT is shown in Figure 34. The decreases in amplitude of shells for UO_2 are most dramatic. Disorder is most significant through 5 months. The region below ~2.3 Å is increasing in amplitude significantly over time. At 27 months, uranium-uranium disorders further, but the region below ~2.3 Å increases significantly.

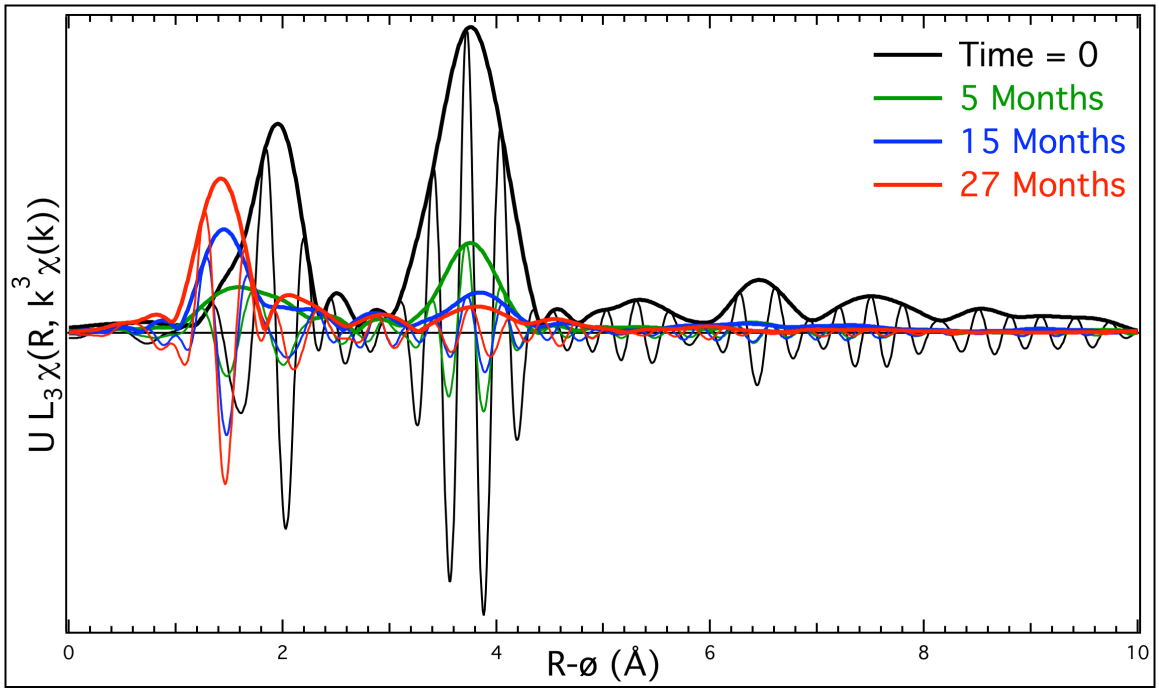

Figure 34. Fourier transform and real contribution overlays for samples aged under HHHT conditions (2.80-13.25 k).

Fits for individual samples are shown in Figure 34 through Figure 38. Fit parameters are summarized in Table 11. One crystallographic contribution remains at 5 months. The k-range (2.80-13.25) was quite short, so the resolution in the oxygen region is fairly poor. Even so, the region below ~2.3 Angstroms begins to dominate. Metaschoepite is the dominant compound from pXRD, but it's not clear if any of the fitted shells are consistent with that structure.

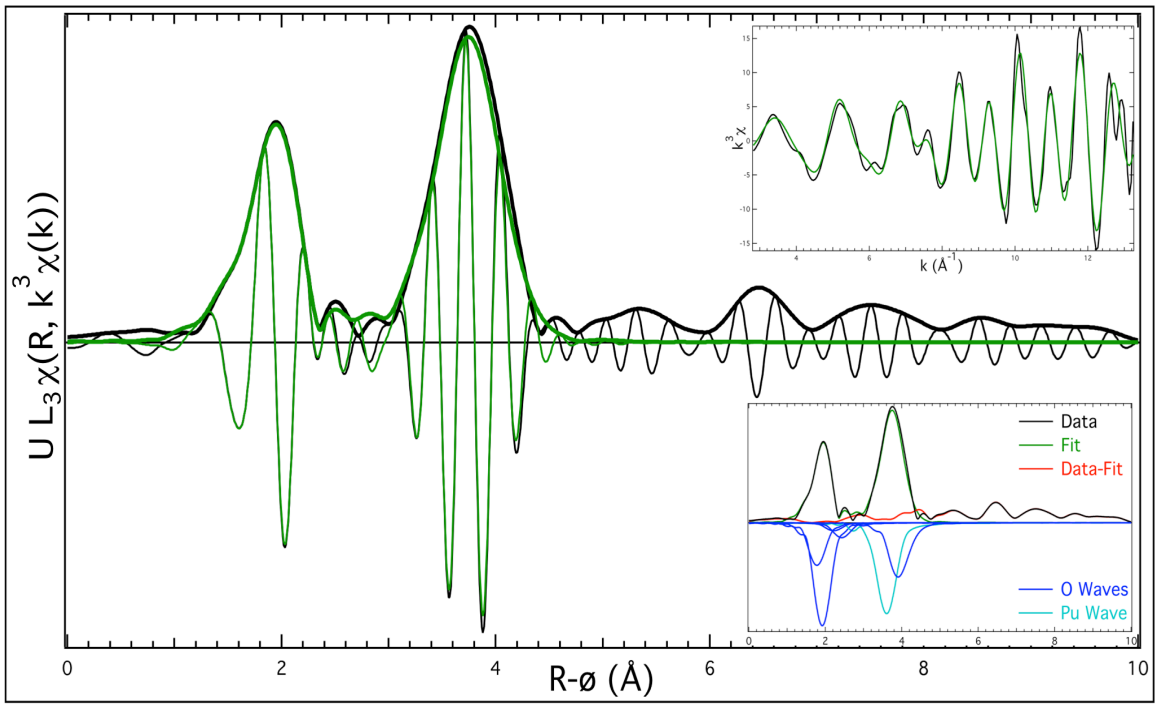

Figure 35. Uranium L_{III} EXAFS spectrum for un-aged UO_2 (2.80-13.25 k). Data is shown in black and the curve-fits in green. $k^3\chi$ plots are shown in the upper inset and individual shell contributions on the lower inset.

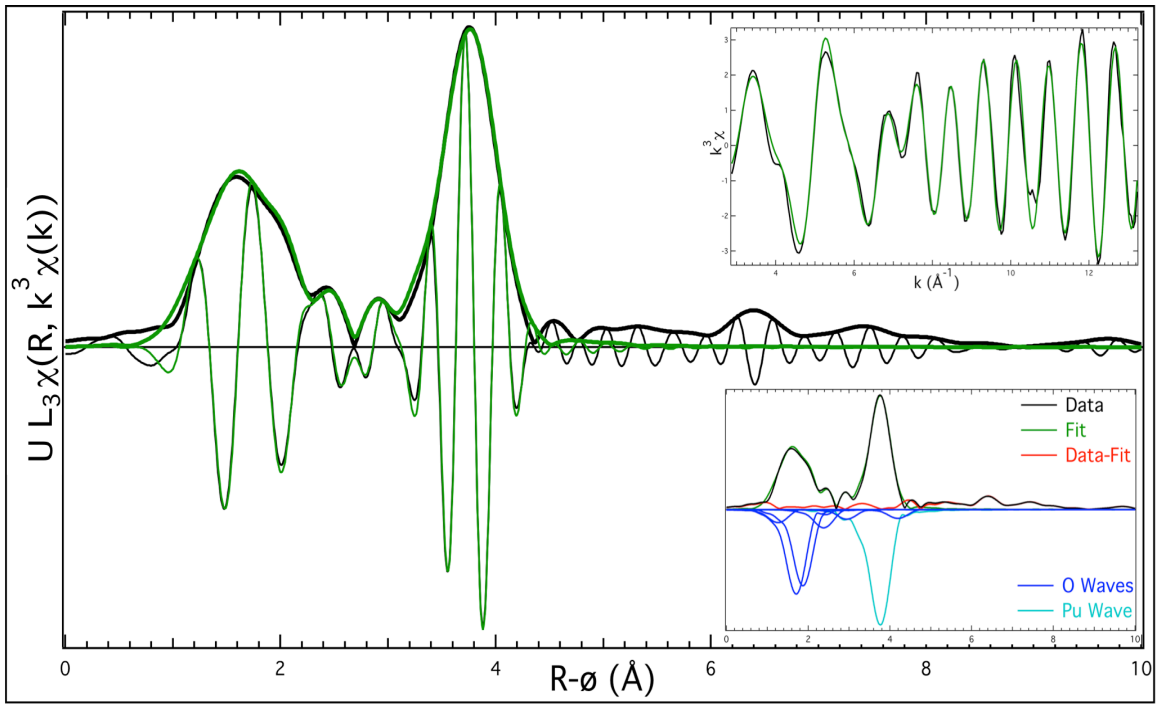

Figure 36. Uranium L_{III} EXAFS spectrum for UO_2 aged 5 months under HHHT conditions (2.80-13.25 k). Data is shown in black and the curve-fits in green. $k^3\chi$ plots are shown in the upper inset and individual shell contributions on the lower inset.

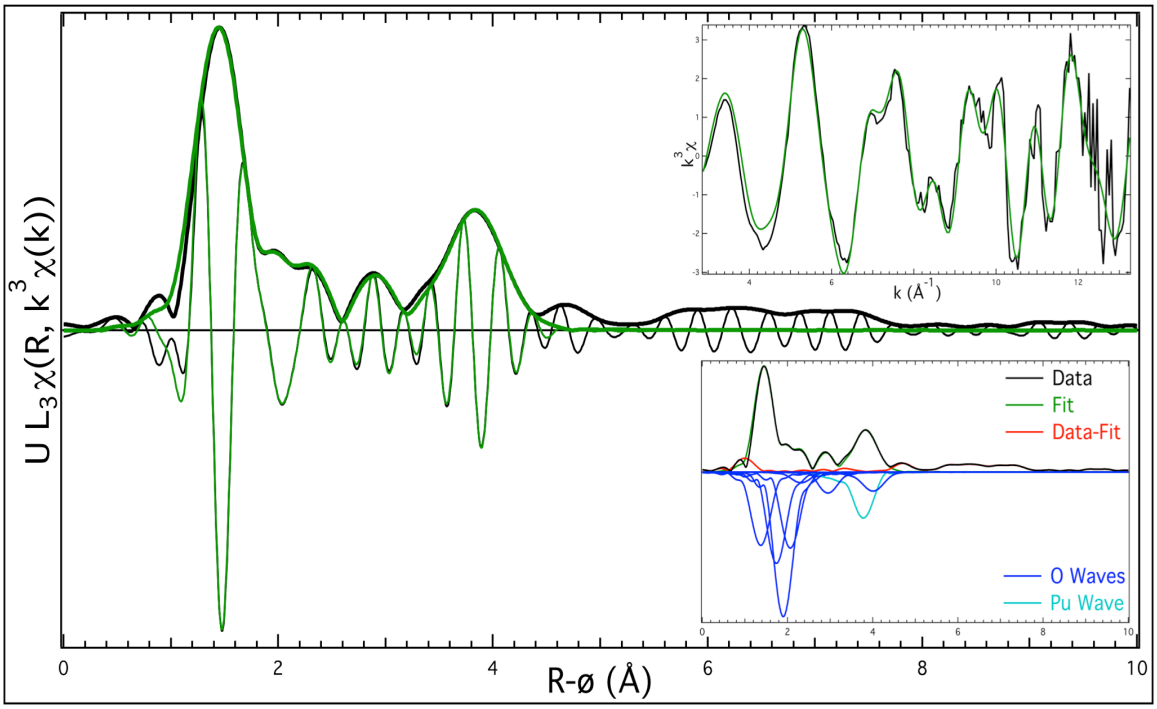

Figure 37. Uranium L_{III} EXAFS spectrum for UO_2 aged 15 months under HHHT conditions (2.80-13.25 k). Data is shown in black and the curve-fits in green. $k^3\chi$ plots are shown in the upper inset and individual shell contributions on the lower inset.

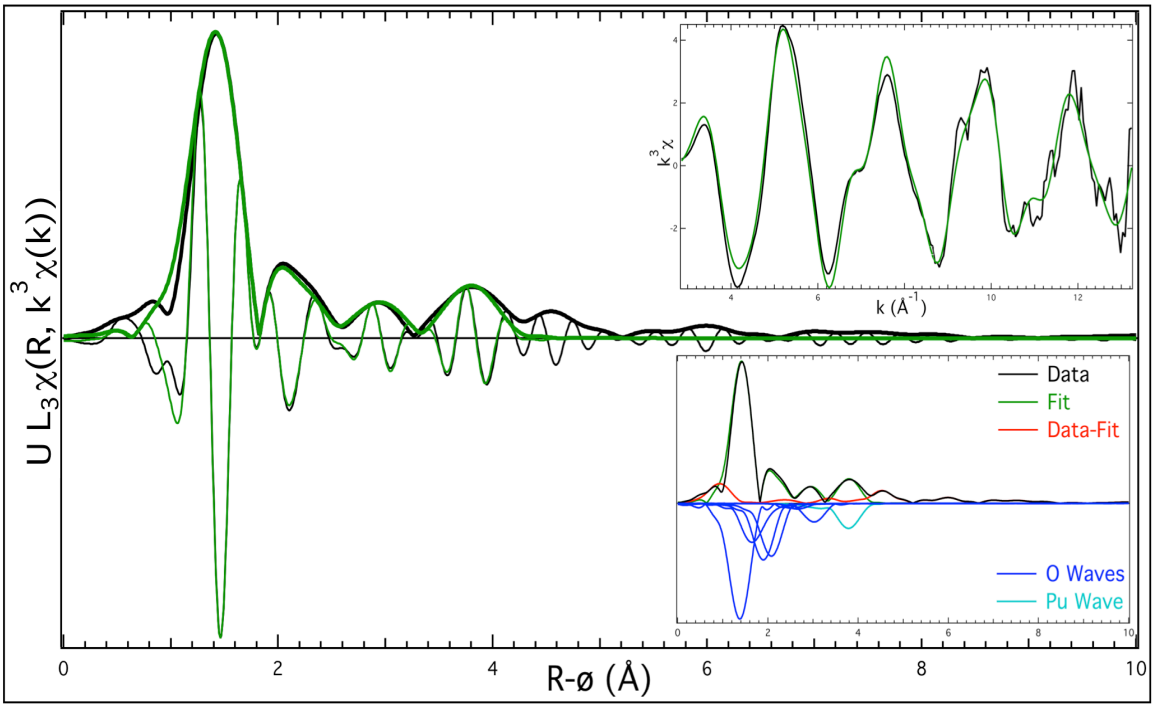

Figure 38. Uranium L_{III} EXAFS spectrum for UO_2 aged 27 months under HHHT conditions (2.80-13.25 k). Data is shown in black and the curve-fits in green. $k^3\chi$ plots are shown in the upper inset and individual shell contributions on the lower inset.

Table 11. Summarized fit results from the HHHT samples.

Sample	Shell	R (Å)	N	σ
Un-aged	O	2.023 (0.18)	0.537 (0.243)	0.012
	O	2.181 (0.023)	3.170 (1.876)	0.035
	O	2.371 (0.015)	6.725 (1.910)	0.038
	O	2.616 (0.016)	1.936 (0.845)	0.006
	U	3.861 (0.014)	12.246 (1.831)	0.046
	O	4.526 (0.022)	19.679 (4.356)	0.065
T = 5 Months	O	1.721 (0.021)	0.258 (0.080)	0.085
	O	2.178 (0.017)	3.011 (0.705)	0.085
	O	2.336 (0.016)	2.558 (0.616)	0.075
	O	2.853 (0.022)	1.116 (0.335)	0.085
	O	3.409 (0.018)	0.577 (0.180)	0.065
	U	3.869 (0.010)	3.702 (0.751)	0.049
	O	4.590 (0.048)	2.546 (0.803)	0.090
T = 15 Months	O	1.794 (0.015)	0.014 (0.243)	0.040
	O	2.168 (0.013)	1.562 (0.392)	0.020
	O	2.328 (0.011)	3.052 (0.689)	0.030
	O	2.493 (0.014)	1.721 (0.448)	0.020
	O	2.757 (0.020)	0.511 (0.161)	0.065
	O	3.372 (0.016)	0.870 (0.261)	0.020
	U	3.884 (0.016)	3.698 (1.066)	0.082
	O	4.508 (0.022)	7.795 (2.411)	0.090
T = 27 Months	O	1.800 (0.016)	2.392 (0.546)	0.070
	O	2.120 (0.015)	1.627 (0.460)	0.045
	O	2.316 (0.017)	1.812 (0.486)	0.060
	O	2.493 (0.019)	2.310 (0.627)	0.070
	O	3.051 (0.018)	0.267 (0.084)	0.050
	O	3.420 (0.022)	1.521 (0.456)	0.070
	U	3.894 (0.019)	3.183 (0.955)	0.096

3.4.5. Condition Comparison and Mechanism Proposal

The same basic trends have been seen in all aging conditions. Thus far, only general statements have been made regarding differences between conditions. Here, a more detailed comparison will be presented by overlaying EXAFS Fourier transforms for each time period samples were analyzed and referencing the diffraction data discussed thus far.

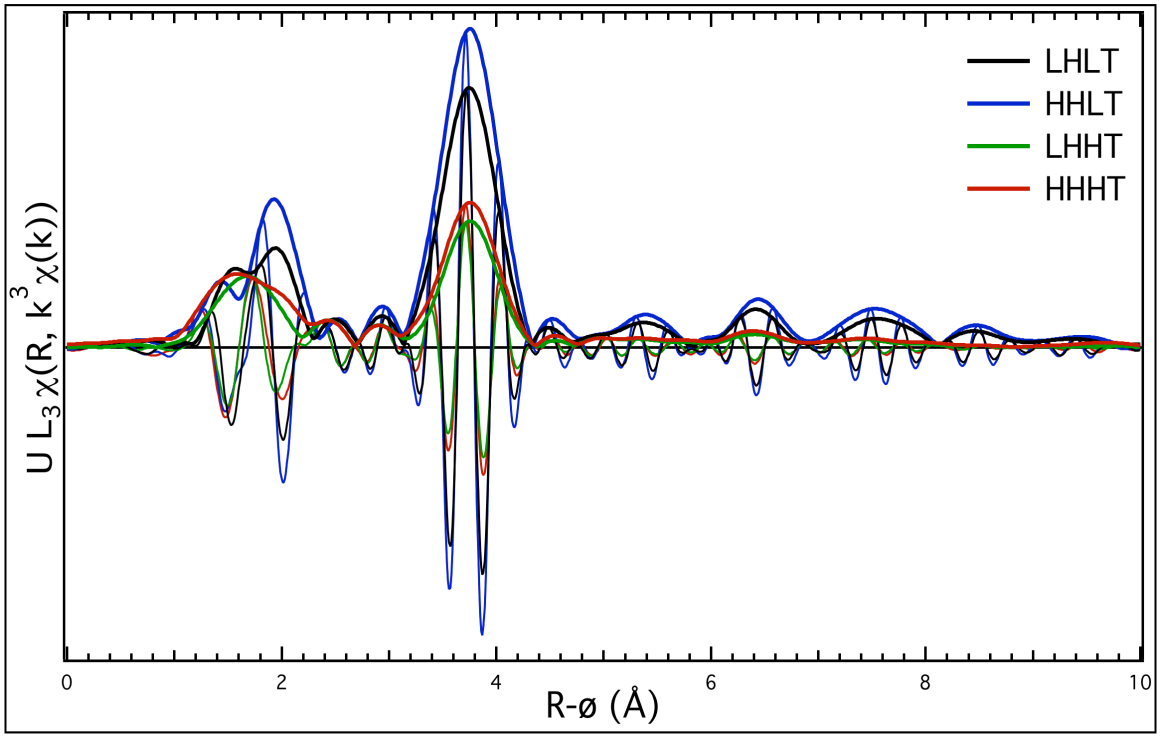

Figure 39. Fourier transform and real contribution overlay of all samples analyzed at 5 months.

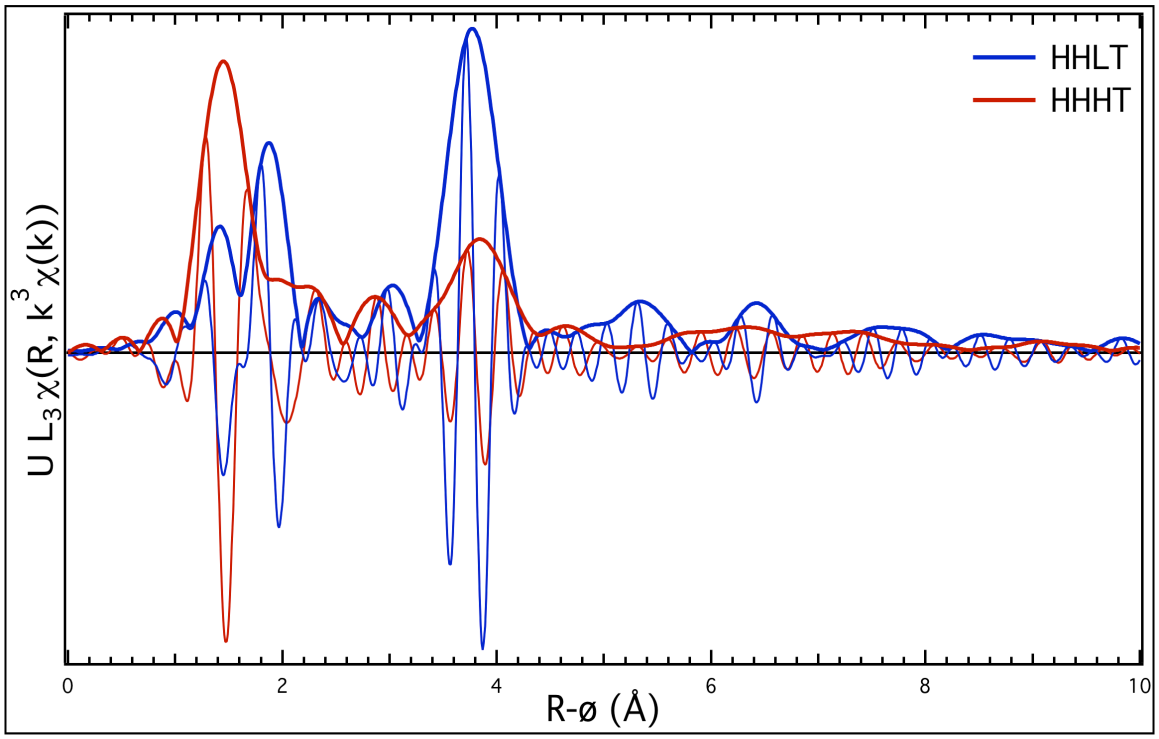

Figure 40. Fourier transform and real contribution overlay of the two samples analyzed at 15 months.

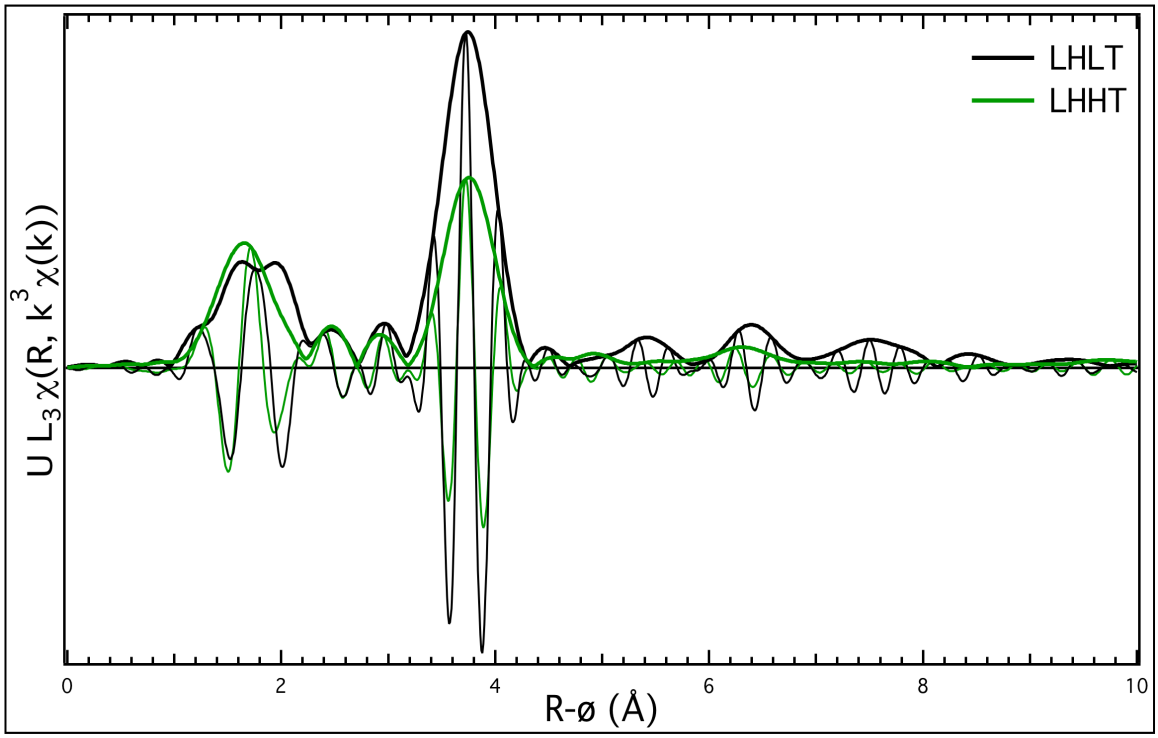

Figure 41. Fourier transform and real contribution overlay of the two samples analyzed at 19 months.

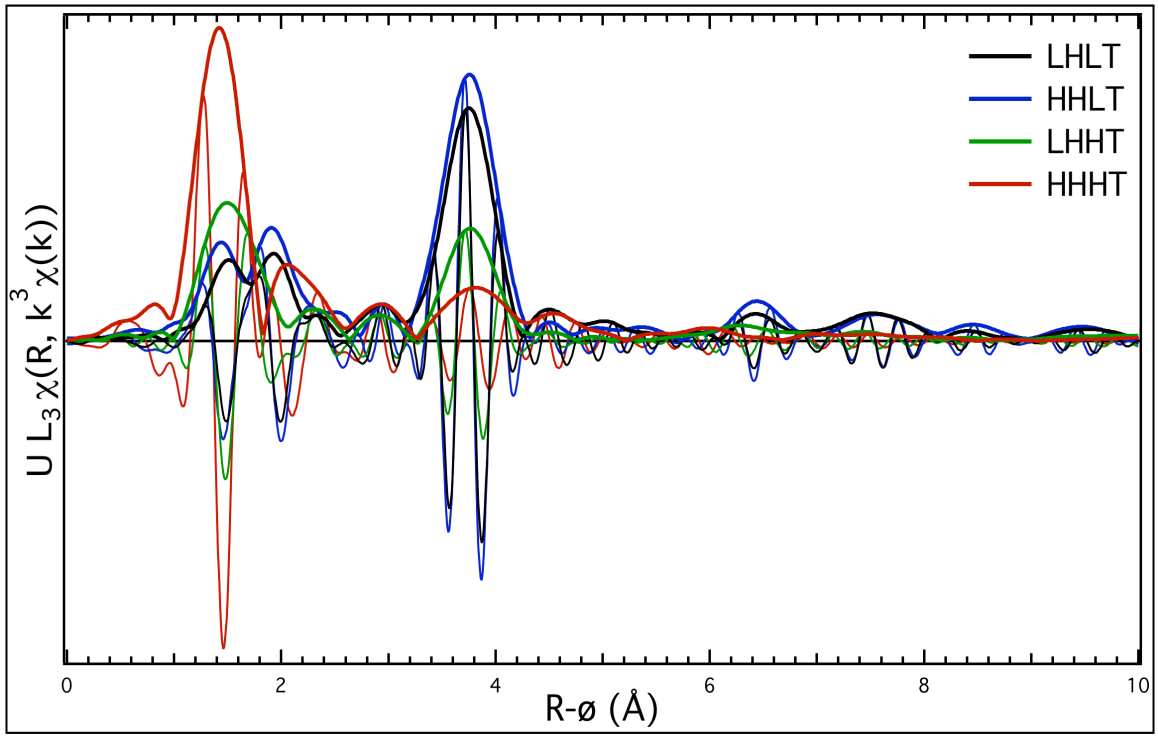

Figure 42. Fourier transform and real contribution overlay of all samples analyzed at 27 months.

Figure 39 shows the Fourier transform and real contribution for all samples analyzed with EXAFS spectroscopy at 3 months. No diffraction data was taken at this time interval. From the overlay of 3-month data, the disordering of the uranium-uranium bond is apparent from the decrease in amplitude of the crystallographic and non-crystallographic UO_2 shells. From least to most disorder, the rank is HHLT < LHLT < LHHT/HHHT. There is very little difference between the LHHT and HHHT samples throughout the spectra. The same trend is observed for the crystallographic nearest neighbor oxygen at ~2.37 Å (and the non-crystallographic shells). The region below ~2.3 Å is more difficult to compare; they are fairly close in structure in that area.

At 15 months, the LHLT diffraction data shows a broad, weak $UO_3 \cdot 2H_2O$ peak. The most predominant peaks of $UO_3 \cdot 2H_2O$ are also seen for LHHT and HHLT, but for those conditions the peak amplitudes are quite close and therefore more difficult to compare. In the HHHT exposure, any peaks indicative of UO_2 are nearly absent, and $UO_3 \cdot 2H_2O$ is the dominant species. Only the HHLT and HHHT samples were chosen for EXAFS analysis (Figure 40). The difference between the HHHT and HHLT exposures is more extreme. The HHHT sample is significantly more disordered with respect to both crystallographic and non-crystallographic shells, but has a much greater amplitude in the region below ~2.3 Å.

Diffraction analysis was not performed at 19 months, and only the LHLT and LHHT exposures were analyzed with EXAFS spectroscopy (Figure 41). The LHHT sample is more disordered than the LHLT sample in both the crystallographic and non-crystallographic regions of UO_2. The LHLT exposure has more definitive

structure below ~2.3 Å, but the LHHT exposure has more amplitude. This indicates a more disordered, oxidized species for the LHHT conditions.

At 27 months aging, both pXRD and EXAFS (Figure 42) analyses were performed on all samples. Diffraction data showed that the LHLT sample has a weak, broad peak indicative of $UO_3 \cdot 2H_2O$. The LHHT and HHLT exposures result in similar spectra once again, but there are a few small differences. For example, LHHT has more relative intensity for the peaks (about 4) of $UO_3 \cdot 2H_2O$, but those same peaks are slightly more defined in the HHLT exposure. In the HHHT data, any peaks indicative of UO_2 are completely absent, and $UO_3 \cdot 2H_2O$ is the dominant species. The EXAFS data is similar to the 3-month analysis in their order of decreasing crystallographic shell amplitudes, but differences are more significant. The LHLT and HHLT exposures are fairly similar throughout the spectra. The trend of increasing disorder of crystallographic and non-crystallographic shells of UO_2 combined with amplitude growth in the region below 2.3 Å continues, with the HHHT exposure being the most significant change.

Due to limits on data acquisition frequency, it is difficult to confidently suggest specific mechanisms for UO_2 aging under these conditions. However, some of the data allows for some suggestions. For example, HHHT had the most extreme affect on aging. It quickly aged to predominantly $UO_3 \cdot 2H_2O$. Based on diffraction, once the compound was present, it continues to become more ordered the longer it was aged. This ordering trend could be further manipulated to provide a chemical chronometer in cases where other information is known. Other comparisons imply different mechanisms across the aging conditions. The LHLT exposure produced

almost no $UO_3 \cdot 2H_2O$ in diffraction, but EXAFS data showed that it was more disordered than the HHLT exposure. The difference is small, but perhaps there is a stepwise process for the growth of $UO_3 \cdot 2H_2O$ that differs depending on conditions. It's possible that LHLT oxidizes on the surface, reducing the overall amount of ordered $UO_3 \cdot 2H_2O$ while below the surface the UO_2 lattice is still becoming disordered. The HHLT sample may just have a higher concentration of the uranyl species, possibly slowing further oxidation throughout the material. Finally, the HHLT and LHHT samples imply a difference in mechanism as well. As stated above, diffraction at 27 months showed that the predominant peaks of $UO_3 \cdot 2H_2O$ were more intense for the LHHT exposure, but more defined for the HHLT conditions. This may indicate a mechanism in which the slower growth of the $UO_3 \cdot 2H_2O$ species allows for a more ordered structure. If this were the case, the HHHT exposure would be less resolved, but it's likely that under such an extreme oxidizing environment, the quantity of $UO_3 \cdot 2H_2O$ present diminishes the ordering effects of growth rate.

3.5 Conclusion

The importance of uranium oxides in the nuclear fuel cycle and weapons production has resulted in an increased interest in answering questions about the basic chemistry of common uranium compounds. In recent decades uranium oxides have been the most common interdicted material[127]. An understanding of uranium oxide chemistry is therefore important to the nuclear forensics community. The uranium oxide system encompasses a range of stoichiometries; their complex chemical behavior allows for many phases, intermediates, and hydrolysis products.

Research on these compounds through the years has helped identify structured compounds of the system, but the mechanisms and intermediates between the ordered phases is still misunderstood. These mechanisms and compounds are especially important when considering exposure conditions important to environmental science and nuclear forensics. In this study, pXRD and EXAFS spectroscopy were used to evaluate the aging of UO_2 under well-controlled exposure conditions. This research sought to increase understanding of UO_2 behavior under various storage conditions, gain some basic chemical knowledge of the uranium oxygen binary system, and evaluate the combination of EXAFS and pXRD for gaining information related to nuclear forensics.

Uranium dioxide was prepared and aged with four sets of conditions outlined in Table 6 and denoted LHLT, LHHT, HHLT, and HHHT. In all pXRD data, the only species present were either UO_2 or $UO_3{\cdot}2H_2O$, so those literature lines and relative intensities were compared with throughout. Diffraction data suggested the LHLT environment has the smallest impact on UO_2 oxidation, followed by HHLT, LHHT, and HHHT respectively. This indicates that in a cold environment, humidity is less a factor in altering UO_2, but there was still a disordering of UO_2 peaks and growth of $UO_3{\cdot}2H_2O$, but not as significant as the other aging conditions. The LHHT conditions had only a slightly more significant effect on UO_2, and the HHHT conditions had the most impact by far. The HHHT conditions completely disordered UO_2 and formed seemingly ordered $UO_3{\cdot}2H_2O$ by 27 months. X-ray diffraction is a widely accessible technique; in experiments like this it should be used more often so that there is a better picture of the aging process. The LHLT, LHHT, and HHLT all had fairly small

differences in their growth of $UO_3 \cdot 2H_2O$. The LHLT has a very broad but relatively intense $UO_3 \cdot 2H_2O$ peak and the LHHT and HHLT had sharper peaks with similar relative intensities (less intense literature peaks were present as well). More pXRD data points coupled with EXAFS analysis could lead to more chemical signatures through a material's history related to nuclear forensics.

EXAFS results were consistent in the order of effect for the aging conditions. The fits produced varying results, making comparisons more difficult. Even so, the fits and transform overlays showed fairly clear trends as a function of aging. In all samples, as time went on, the uranium-uranium disorder increased, non-crystallographic shell order decreased (or disappeared), and the crystallographic bond at ~2.37 Å was overtaken by a multisite oxygen distribution with highest amplitude below ~2.3 Å. This growth is more extreme, but consistent with previous studies. Perhaps the most interesting result from the EXAFS analyses is that even after being heavily disordered as witnessed by diffraction, some remnants of a UO_2 uranium-uranium bond still remain. This shell remains even when no UO_2 is present in diffraction patterns. This highlights the importance of using a combination of these two chemical speciation techniques. Furthermore, the ordered peaks seen in the diffraction patters are not showing up in the local structure gained through EXAFS.

Aging experiments such as these expand the melee of current nuclear forensics protocols, but its important to note that analysis with pXRD and EXAFS spectroscopy alone have limited impact. Moreover, the use of simple and static aging conditions doesn't help in attributing exact exposure conditions or time under an

exposure condition. Above all though, these experiments help determine a model for uranium oxidation so that it is more applicable to more scenarios. Combination with isotopic information, intelligence, and other techniques within the realm of MFS is vital. Other common techniques that could aid these experiments include mass spectrometry and various types of imaging. Trace and isotopic analysis with mass spectrometry adds a number of areas of information to go along with chemical speciation. Optical imaging, electron imaging, and optical spectroscopies should also be used when appropriate. Furthermore, more experiments with the analyses discussed within this experiment should be performed to better understand their limitations and complementarity to the areas of analysis mentioned above. Although isotopic analysis and intelligence gathering obtain important information, they may overlook chemical information that can aid attribution. Two of the most common and advanced techniques for studying chemical speciation, pXRD and EXAFS, were used in this study to show the importance of their combination and the information they gather for purposes related to nuclear forensics and attribution. This work was successful in establishing a starting point for research with forensics application in mind, and there are some limitations, but above all this work has helped to establish a model for uranium oxide aging and oxidation under a range of exposure conditions.

CHAPTER 4

PARTICLE ANALYSIS OF A HETEROGENEOUS INDUSTRIAL SAMPLE

4.1 Abstract

In scenarios where chemical information is sought on actinides, such as nuclear forensics interdictions and environmental assessments, the differentiation and analysis of individual particles is required. Heterogeneous mixtures, environmental samples, or limited quantities are all sources for actinide particles. At Los Alamos National Laboratory (LANL), a number of samples were available that had been prepared under common industrial conditions. The samples varied greatly in their chemical composition, but one in particular was composed of two types of materials. This sample allowed for evaluation of individual particle differentiation and investigation of source material based on single particles. The particles were analyzed individually with scanning electron microscopy (SEM), inductively coupled plasma mass spectrometry (ICP-MS), powder X-ray diffraction (pXRD), μ-X-ray fluorescence (μ-XRF), and μ-extended X-ray absorption fine structure (μ-EXAFS) spectroscopy. Observations pointed to a possible scenario under which the sample was synthesized, so a replication was attempted. The replication produced a similar sample that showed results consistent with the original. This confirmed the proposed formation scenario and further demonstrated the utility in using chemical speciation and morphology for nuclear forensics analysis in a real world scenario.

4.2 Introduction

Over the years there has been an increased concern related to particle versus bulk analysis of actinides in environmental science and nuclear forensics. Bulk analysis yields an average of a large portion of material from a site, i.e. EXAFS on a highly contaminated soil containing many particles from a given site. Bulk information is important because it is more representative of a scenario and typically easier to perform. Using this representative bulk information is vital, but in many cases the combination of bulk and particle analyses is optimal for gaining the most information from a given scenario. In some instances a limited amount of material is available, with the majority of material coming from individual particles. In others, bulk analysis shows inconclusive or mixed results, representing a heterogeneous sample with a range of chemical compositions. In those cases analysis of individual particles can make sense of that information or provide better context for conclusions related to nuclear forensics analysis. These scenarios have highlighted the need to differentiate and analyze individual particles [10, 102, 143]. Because of these highlighted needs, particle analysis techniques have begun to be developed over the years, but this area of the field is still in its infancy. In order to demonstrate how chemical speciation can reveal chemical information pertinent to nuclear forensics on bulk samples, the author and colleagues conducted a series of analytical measurements on samples prepared under various synthesis routes common in industrial processes. A select few of the samples were to be aged along with the standards mentioned in Chapter 3, but the majority would simply be analyzed with techniques for comparison between samples and results from other

laboratories. Regardless of the chemical makeup of the samples, most appeared homogenous, but one in particular was clearly composed of two different types of particles: black and orange chunks in a ratio of approximately 9:1 (Figure 43).

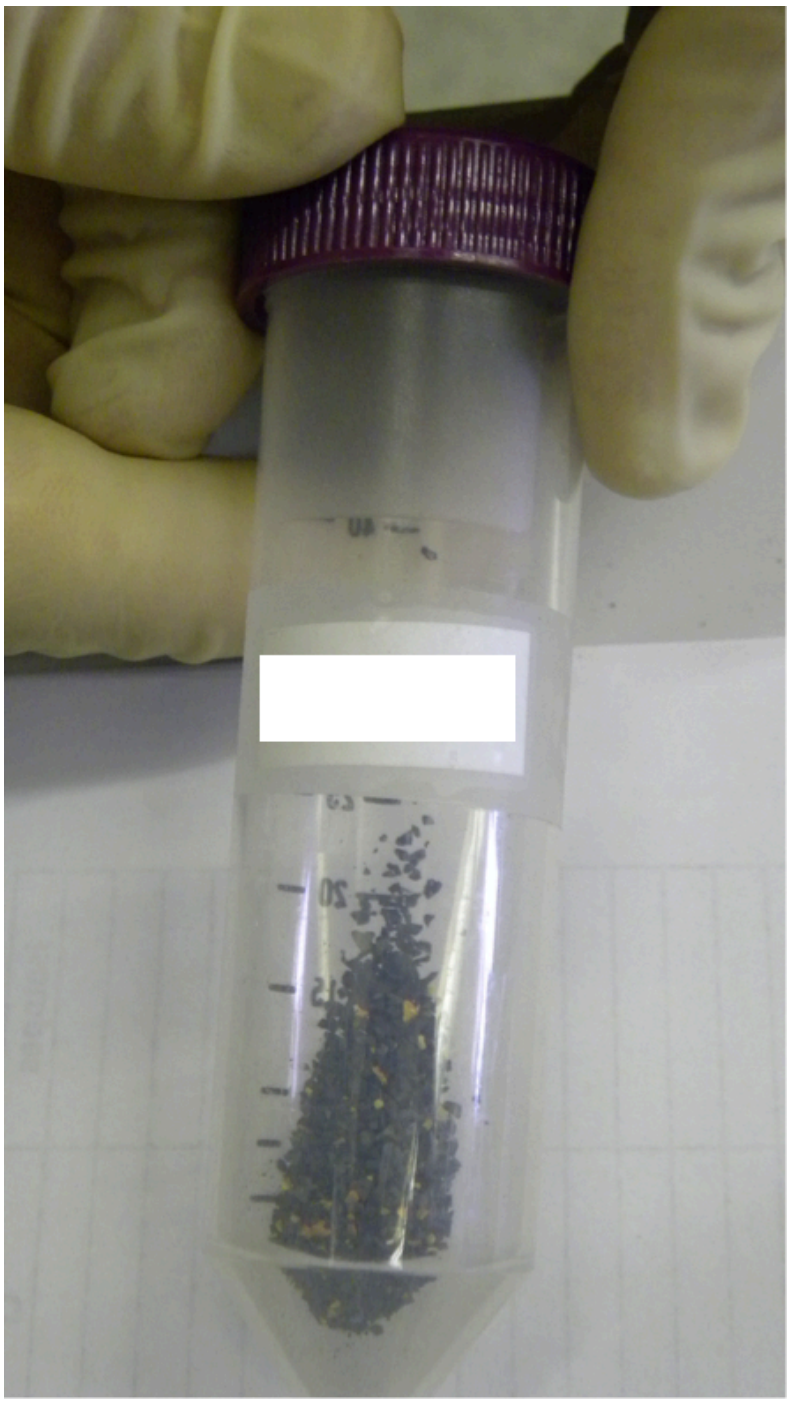

Figure 43. The industrial sample containing a mix of orange and black material.

The bulk sample had been analyzed with pXRD, bulk EXAFS spectroscopy, SEM, and ICP-MS. The results from these techniques were inconclusive or showed a mixed species. This sample provided an opportunity for individual particle characterization and differentiation of mixed sample. Because of this, the two types of particles were separated for individual analysis of each material. The separated materials were analyzed with the same bulk techniques as listed above, but individual particles of each type were also analyzed at the Stanford Synchrotron Radiation Lightsource Beamline 2-3 (SSRL BL 2-3), which has capabilities for microfocus analytical techniques, specifically μ-XRF and μ-EXAFS. Mass spectrometry was also repeated on the individual materials for both trace and isotopic information. This helped highlight the need for the combination of traditional nuclear forensics analyses along with the chemistry and morphology based ones discussed here.

The results showed that the black material was mostly U_3O_8 and the orange $UO_3 \cdot 2H_2O$. Because of the nature of the author's research focus, the origin of these two types of material and the reason they were in the same bulk sample were important questions. Within the sample, there were particles that incorporated both orange and black material, Figure 44.

Figure 44. “Transition particles” from the industrial sample.

These were designated as “transition particles”. The presence of these transition particles suggested the material came from the same synthesis and therefore source material. Some basic information on the sample preparations of the industrially prepared materials was available. However, analyses on those samples at LANL weren’t consistent with that information. For example, many of those syntheses

supposedly produced U_3O_8, but diffraction showed presence of starting materials, further oxidized species, and mixed compounds. Due to the uncertainty in that information, it has been excluded. However, it was noted that all those samples were prepared in a tube furnace with stainless steel tube. The presence of transition particles and the tube furnace setup, it was postulated that when the sample was prepared, it was left partially outside the heating zone. This resulted in two compounds, one being the starting material and one being the intended final product. The facilities at LANL have similar equipment, so a replication of a similar sample was performed. This work will outline the results from the mixed sample's individual particle analyses and attempted at replication. Furthermore particle analysis with the techniques used herein will be evaluated for relevancy to nuclear forensics.

4.3 Experimental

4.3.1 Industrial Sample Analysis

Particles were on the order of 0.5–1.0 mm in diameter, allowing for separation with tweezers. Out of the ~2 gram quantity of the bulk sample, about 300 mg was the orange material. Approximately 20 mg of each material was set aside for analysis with pXRD (see Section 2.5). For analysis with SEM, a small particle of each material type was placed on a stub coated with double-sided carbon tape. Due to the large size of the particles, they were crushed and smeared across the tape with a spatula. A particle of each type was set aside and prepared as outlined in Section 2.8.1 for μ-XRF/EXAFS analyses. Figure 45 shows the sample holder containing the

two particles chosen for analysis at BL 2-3. A limited quantity of material remained, so only one DR-IR sample was prepared, and the rest was used for ICP-MS as outlined in Section 2.7. There was only about 50 mg of the transition material in the sample. These were also set aside, but not analyzed due to difficulties in selecting specific areas for EXAFS spectroscopy based on elemental mapping; the XRF maps were near identical for both the black and orange particles. The analyses performed were completed as outlined in the respective sections of Chapter 2.

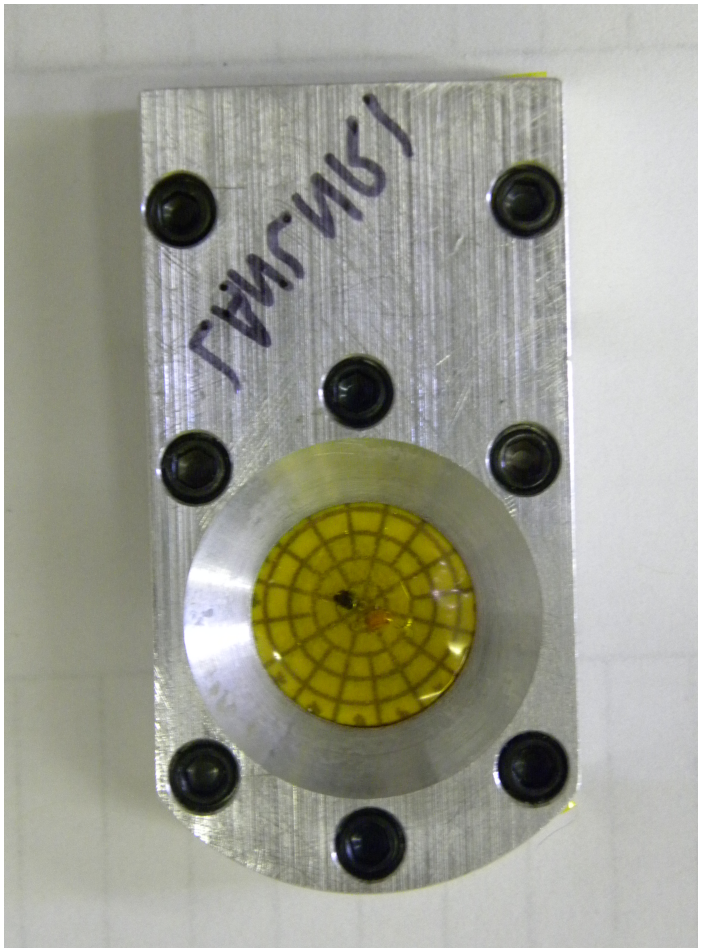

Figure 45. The μ-EXAFS spectroscopy sample holder containing the two types of particles from the industrial sample. A representative black particle is on the top left of the paper grid, and a representative orange particle on the bottom right.

4.3.2 Replication Procedure and Analysis

For the replication, powder-form uranium oxides were dissolved and precipitated as outlined in Section 2.2.4. The oxides were not column purified so that they might mimic any trends in contaminants as a function of heating. To replicate the sample, an oven boat was filled with UO_2O_2, dried, and fired to A-UO_3. Due to time constraints, mimicking exact $UO_3 \cdot 2H_2O$ was not performed, but A-UO_3 has a similar orange color to the received sample and provides for a similar EXAFS structure to the hydrated compound. Once A-UO_3 was synthesized (Figure 46), it was placed partially outside the heating zone of the tube furnace (see Section 2.2.5) so that a portion of the material in the boat would be converted to U_3O_8 (Figure 47). The oven was set to 975 °C for that synthesis. Although Section 2.2.5 notes that 800 °C is used throughout this work, the outside laboratory that performed this sample's synthesis used higher temperatures. In order to see the effect of further firing/reduction on morphology and trace content, a UO_2 sample was prepared from the remaining U_3O_8. The resulting compounds were characterized with pXRD, ICP-MS, and SEM.

Figure 46. Ceramic oven boat containing A-UO_3 in a platinum foil.

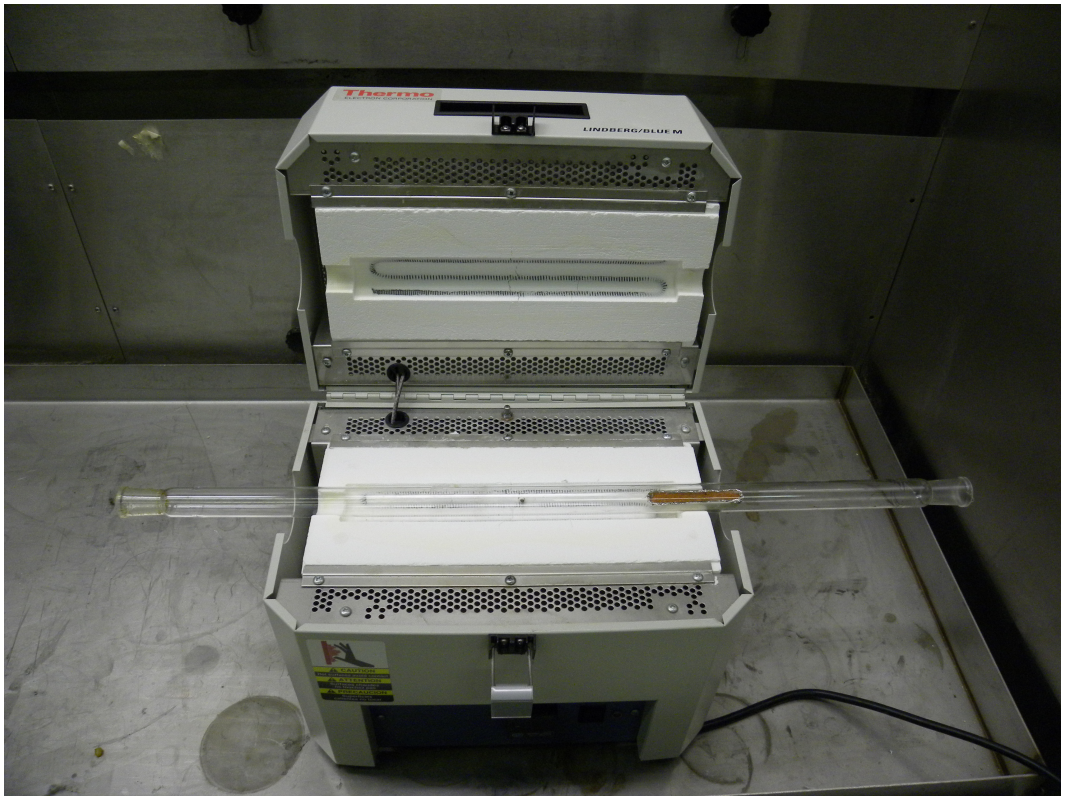

Figure 47. A-UO_3 in oven boat placed partially outside of the tube furnace.

4.4 Results: Industrially Prepared Sample

Results for SEM, ICP-MS, pXRD, micro-XRD, and micro-EXAFS for the industrially prepared sample are presented in the following sections. Summarized results are also shown (Table 13). The implications of the following results will be discussed in more detail in Section 4.6.

4.4.1 SEM

Figure 48 shows qualitative SEM images at varying magnifications representing the most common morphology of each particle. At high magnification, the difference in morphology between the orange and black materials is more obvious. However, there are some areas from the SEM images that show particles or areas with unusual morphology compared to the majority of the sample for each material. These areas (two for the black particle and four for the orange particle) and representative areas for the majority of each particle are shown with the resulting EDS spectra in Figure 49 and Figure 50. Although concentration of elements in these areas and in the entire samples are difficult to discern with EDS alone, it may indicate elemental correlations in the same way XRF does, but on a more precise scale. Also, EDS can identify trace elements that are not identified with other techniques.

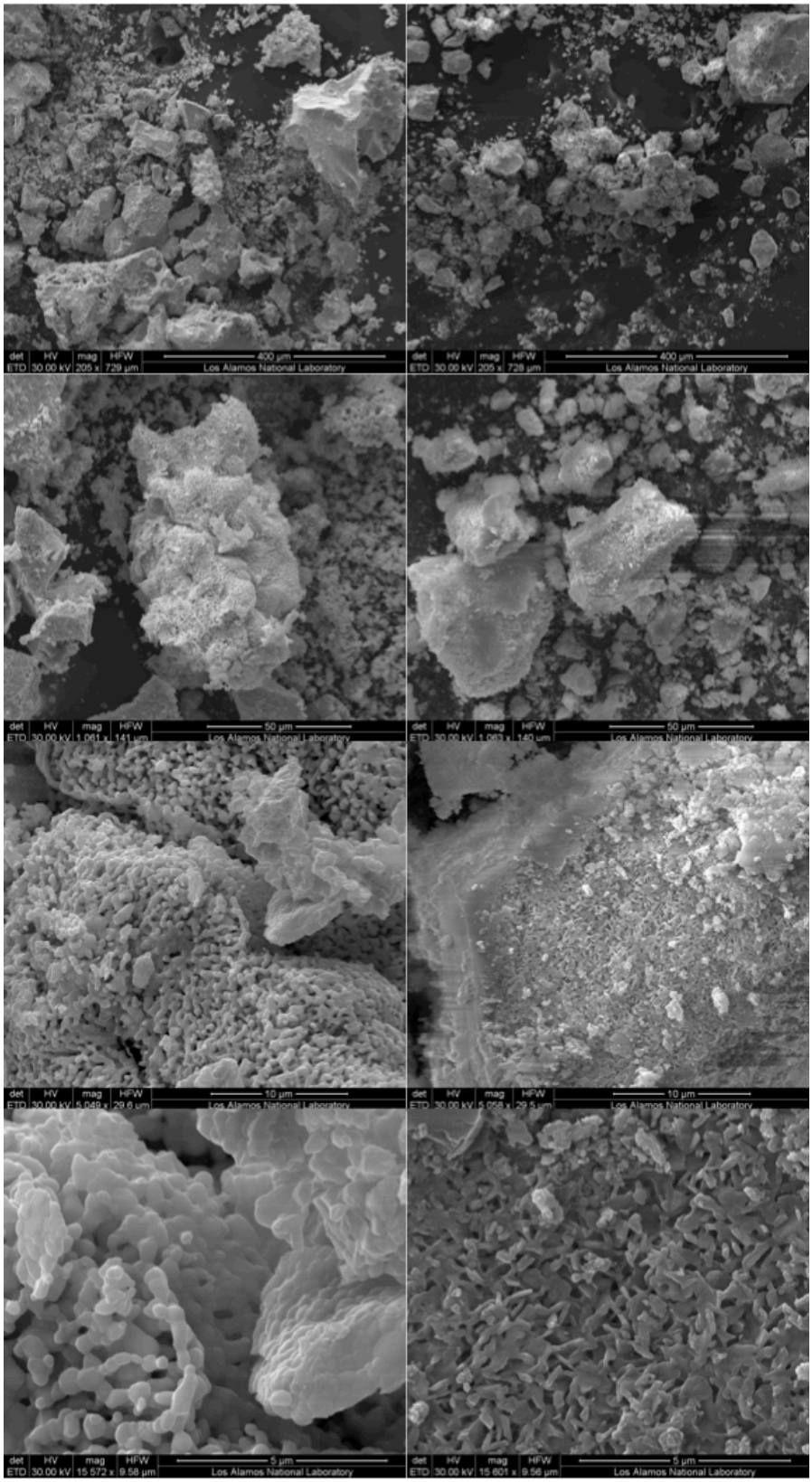

Figure 48. SEM images at varying magnifications (205x-15500x), showing the most common morphology of each sample. The orange particle is on the left column and the black particle is on the right.

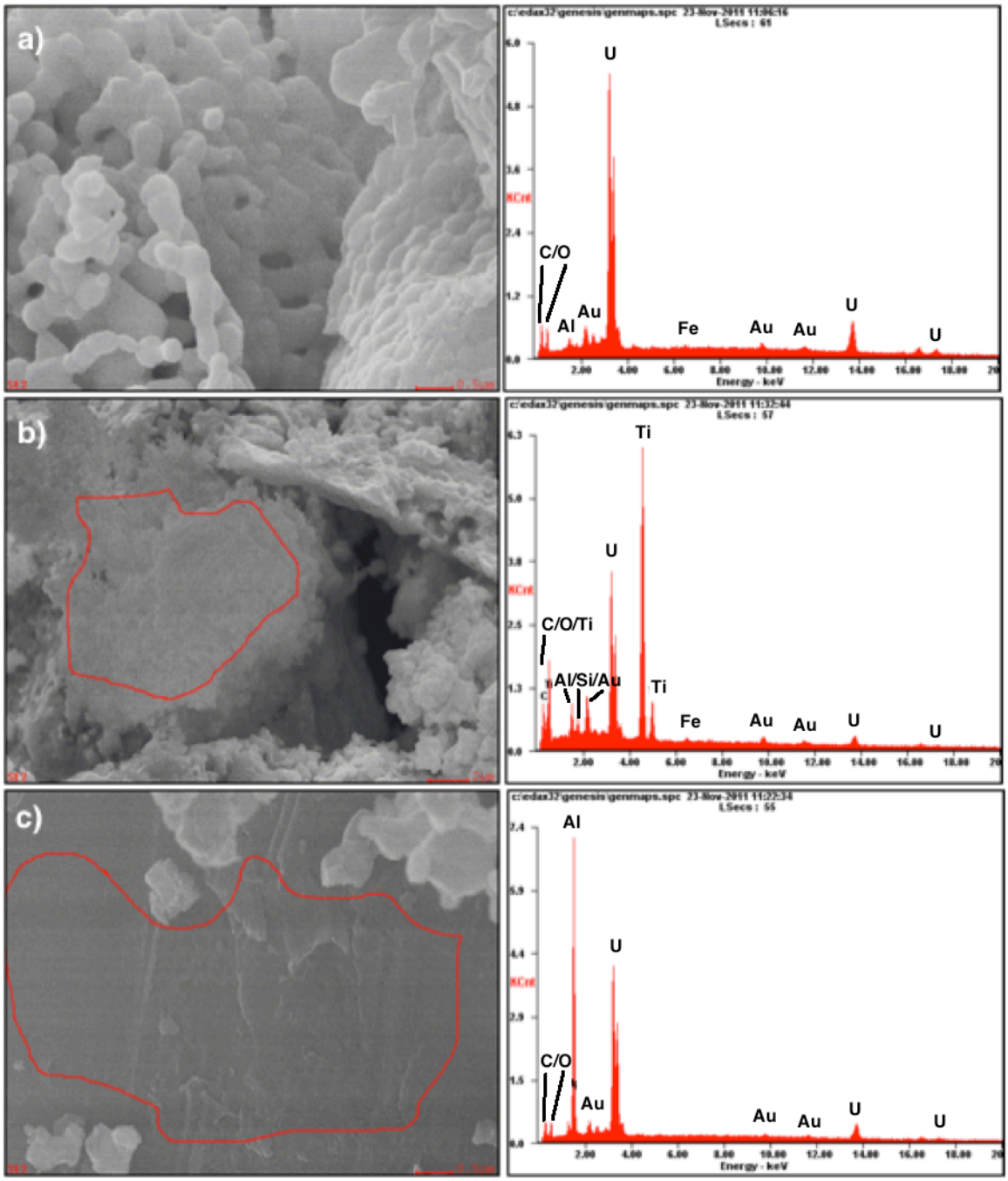

Figure 49. Areas from SEM of the black material. a) Representative morphology of the majority of the material and the resulting EDS spectrum, b) area with unusual morphology and the resulting EDS spectrum showing large titanium signal with uranium still present, c) area with unusual morphology and the resulting EDS spectrum showing large aluminum signal with uranium still present. All images were taken at ~15500x magnification.

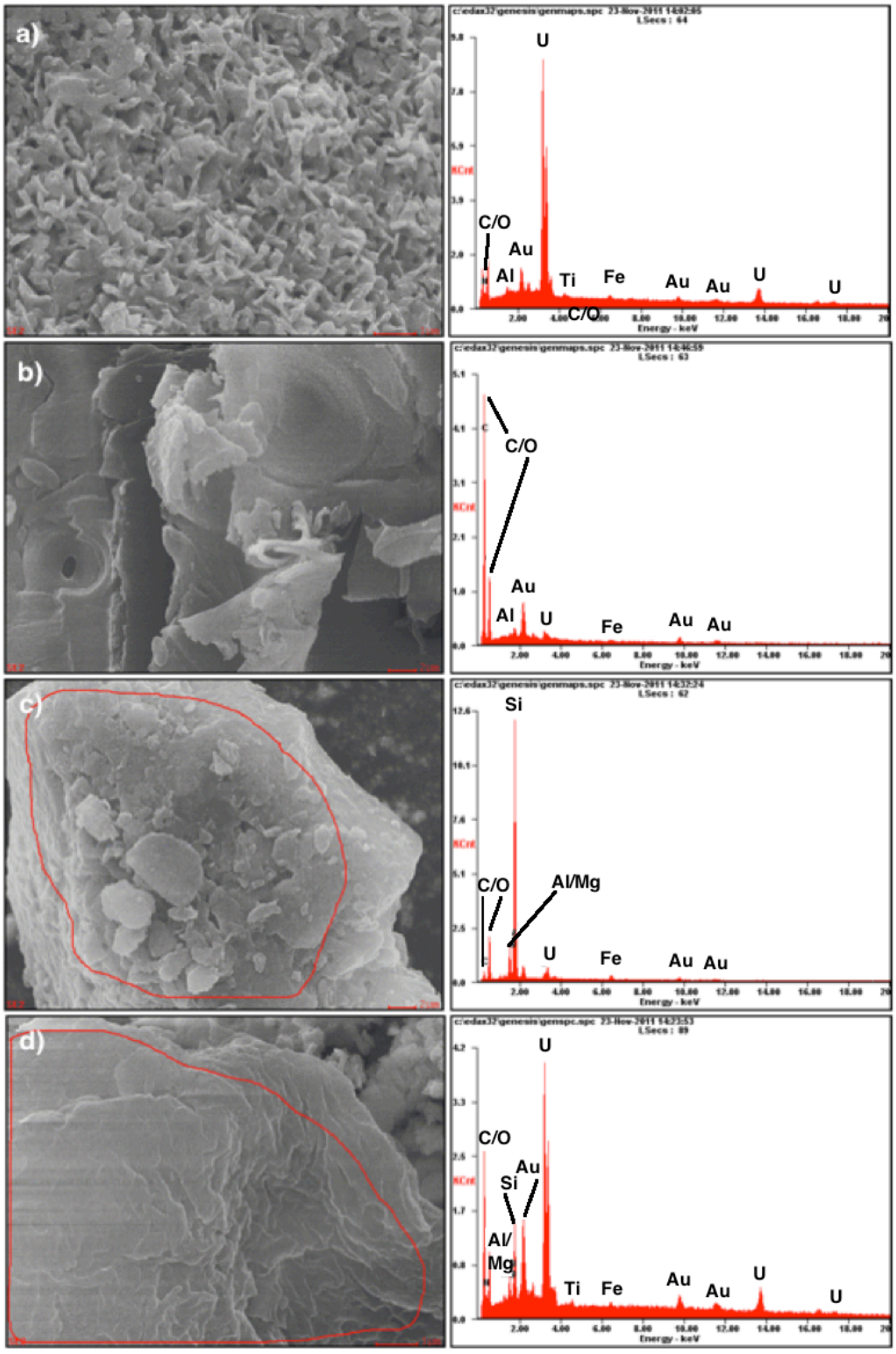

Figure 50. Areas from SEM of the orange material. a) Representative morphology of the majority of the sample and the resulting EDS spectrum showing mostly uranium, b) area with unusual morphology and the resulting EDS spectrum showing large carbon signal with almost no uranium present, c) area with unusual morphology and the resulting EDS spectrum showing large nickel signal with almost no uranium present, d) area with unusual morphology showing several element's signals (carbon, gold, silicon, uranium). All images were taken at ~15500x magnification.

4.4.2 ICP-MS

Table 12 shows results from ICP-MS of each material. Not all elements are shown; those that were below 0.05 μg/g uranium for each material were excluded. There are some elements where the black material had a higher (i.e. lanthanum, magnesium, titanium, iron, copper, silicon) or near identical (i.e. tin, yttrium, thorium) concentration of contamination, but overall the orange material had a much higher concentration for most elements. This increased concentration may result from compounds being volatilized in the furnace for the black material, but not outside of the furnace or these materials may originate from separate sources. Some discussion on these possibilities is included in the discussion section. Isotopic analysis showed very similar ratios for all uranium isotopics. The source material for each was depleted uranium with ^{236}U, suggesting that the material was recycled at some point in its history.

Table 12. Trace element content in μg/g uranium for selected elements for the black and orange particles.

Element	Black	+/-	Orange	+/-
B	1.26	0.61	10.30	2.00
Ge	0.16	0.33	0.76	0.28
As	67.36	2.77	89.28	4.21
Y	0.17	0.01	0.19	0.01
Zr	0.05	0.01	0.22	0.09
Nb	0.80	0.08	0.96	0.07
Mo	8.84	0.42	57.21	2.83
Cd	0.07	0.02	0.27	0.03
Sn	4.18	0.25	4.17	0.24
Sb	BDL	NA	1.62	0.09
Ba	BDL	NA	0.47	0.09
La	0.44	0.02	BDL	NA
W	0.25	0.02	0.37	0.04
Pb	0.20	0.01	0.16	0.01
Th	0.26	0.02	0.26	0.01
Mg	131.29	12.89	26.25	3.39
Ca	250.25	22.27	778.59	37.84
Ti	1.89	0.82	1.12	0.57
V	BDL	NA	0.05	0.05
Cr	4.70	0.32	7.74	0.71
Mn	0.77	0.12	1.17	0.08
Fe	117.77	15.69	71.34	5.94
Co	0.17	0.05	17.91	0.82
Ni	4.73	0.93	88.44	5.43
Cu	1.21	0.51	1.12	0.49
Zn	30.17	2.51	69.08	4.90
Sr	0.12	0.06	0.35	0.07
Na	16.65	5.28	26.54	4.07
Si	540.38	28.07	507.82	32.80
K	15.23	1.88	19.58	2.96
$^{234}U/^{238}U$	0.0000221	0.0000012	0.0000219	0.0000013
$^{235}U/^{238}U$	0.0028954	0.0000039	0.0028982	0.0000047
$^{236}U/^{238}U$	0.0001635	0.0000077	0.0001630	0.0000002

4.4.3 pXRD

Powder diffraction patterns are shown in Figure 51 and Figure 52. These figures also show the literature lines and relative intensities for U_3O_8 and $UO_3 \cdot 2H_2O$. The black material is mostly U_3O_8 with a small amount of $UO_3 \cdot 2H_2O$ with only a few unidentified lines. The orange material has a diffraction pattern that looks close to $UO_3 \cdot 2H_2O$, but peaks are slightly shifted and there are many unidentified lines. The orange material was also compared to other uranyl species, namely ammonium uranates, but none matched as well as $UO_3 \cdot 2H_2O$.

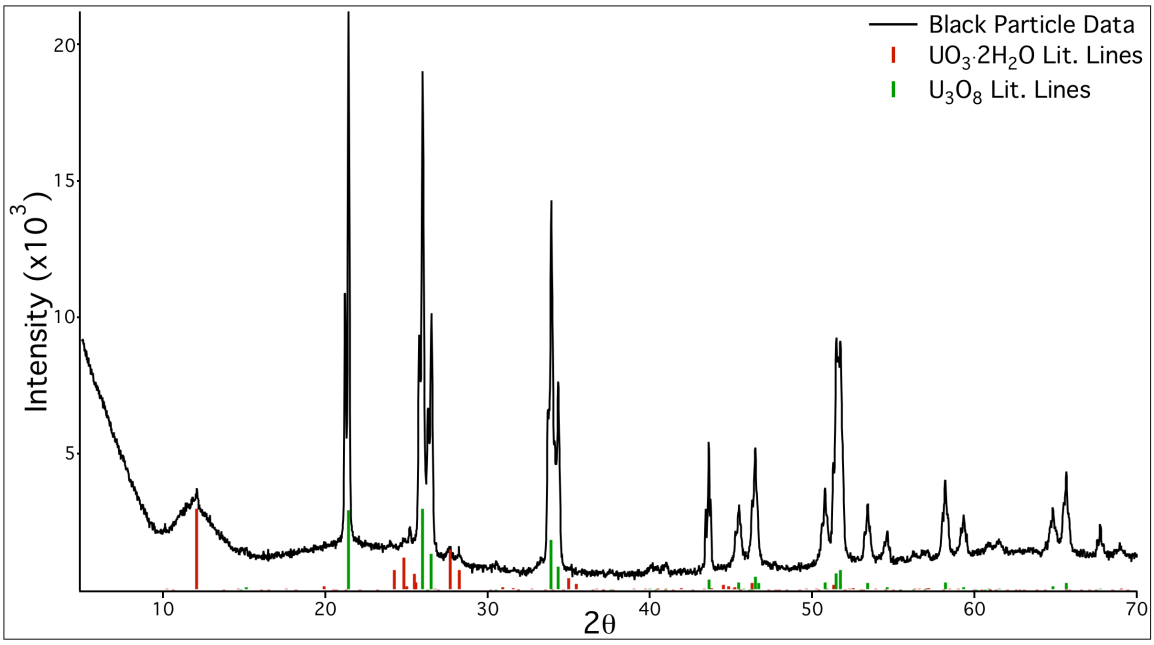

Figure 51. pXRD from the black particle showing the data and the literature lines/relative intensities for U_3O_8 and $UO_3 \cdot 2H_2O$.

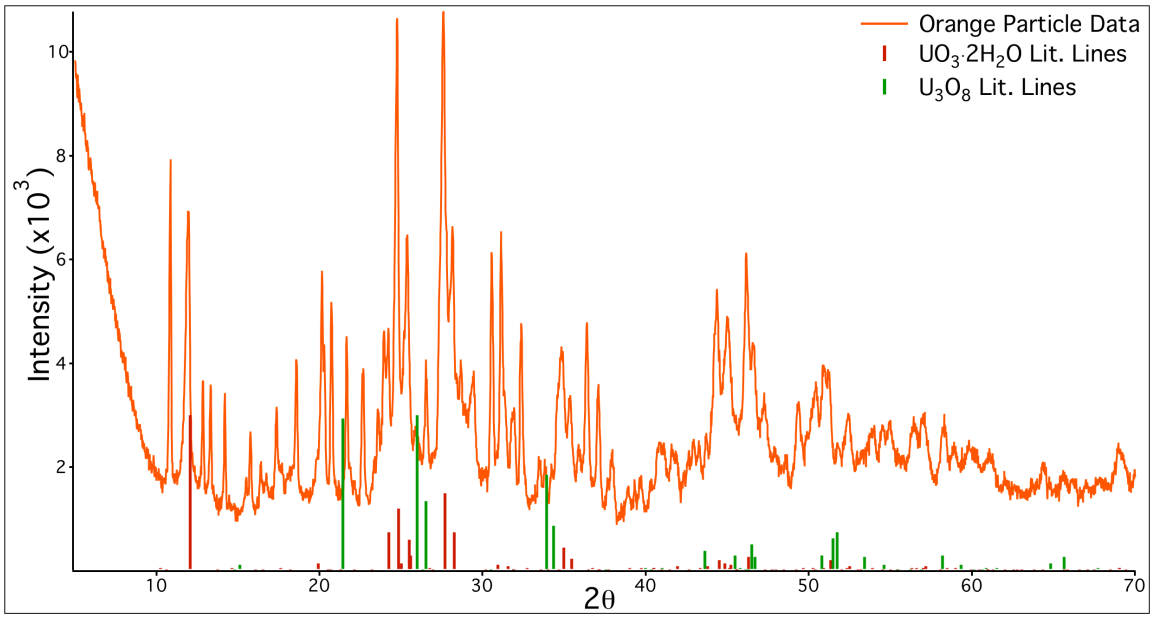

Figure 52. pXRD from the orange particle showing the data and the literature lines/relative intensities for U_3O_8 and $UO_3 \cdot 2H_2O$.

4.4.4 μ-XRF and μ-EXAFS

Figure 53 shows the elemental map from BL 2-3. No other fluorescence signals were seen in the detection range. Areas where initial EXAFS data were of good quality (denoted by the X's on the fluorescence map) were chosen for complete EXAFS analysis. Even though the data quality looked good initially, it was too noisy to obtain a fit with high confidence. Figure 54 and Figure 55 show the Fourier transforms for each particle, overlaid with samples of similar speciation. Due to noise in the data, crystal glitches, anomalies in the beam intensity, and other limits of particle analysis, there are shifts in the distances compared to the standard species distributions. Even so, particle pXRD data matches the compounds chosen for comparison quite closely. The black material is consistent with U_3O_8, but the orange material is somewhat harder to discern. There was no $UO_3 \cdot 2H_2O$ standard available for comparison, so an aged A-UO_3 was used (A-UO_3 was aged along with

UO_2 in the experiments discussed in Chapter 3). None of these compounds had high amplitude in the typical uranium-uranium bonding region, but their Fourier transforms are similar. Transforms for both particles exhibit shifts to lower distance in their distributions and in the imaginary and real (not shown) contributions to those transforms.

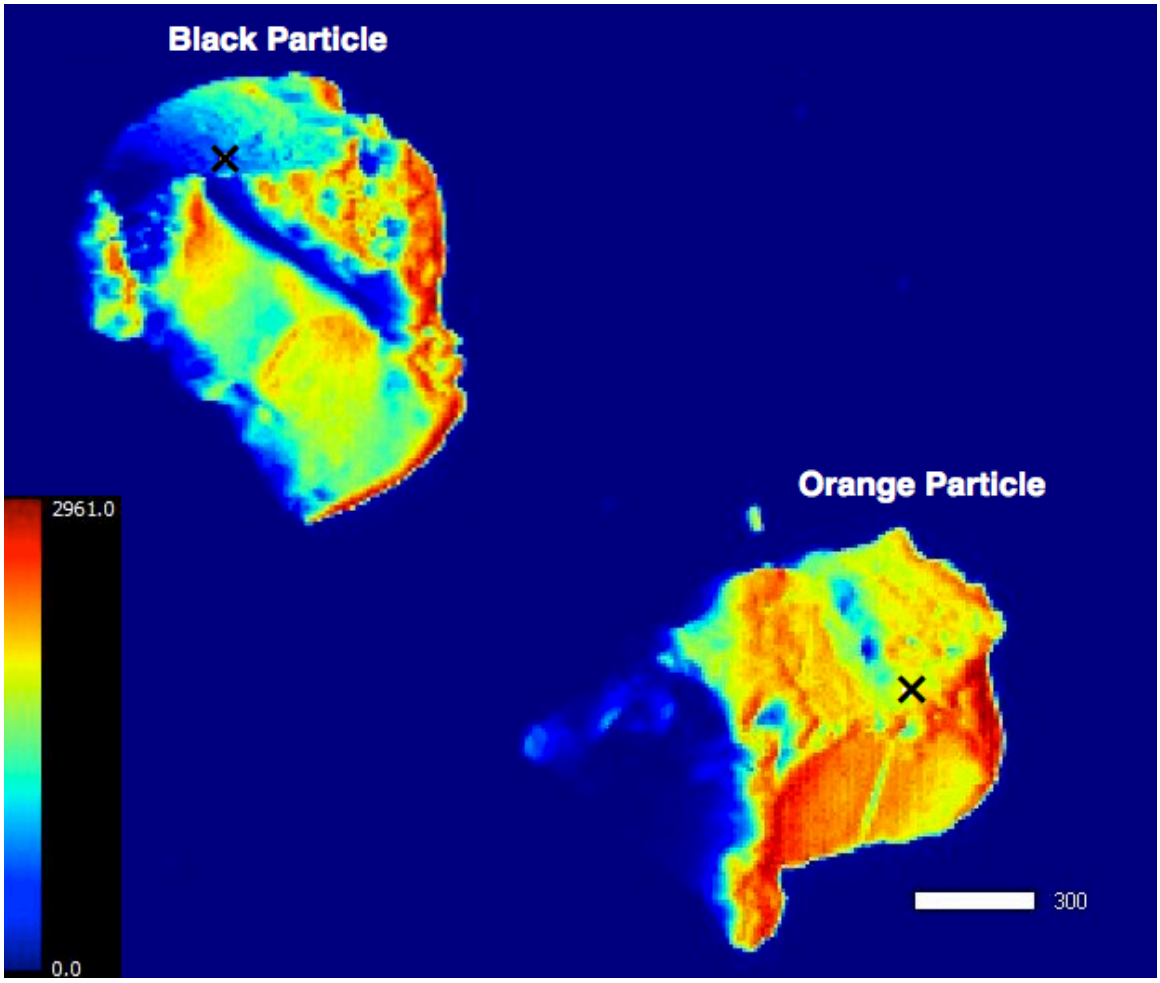

Figure 53. Uranium elemental map for the two particles. The "X" indicates the location for EXAFS analysis on each particle. Scale bar on bottom right is in microns.

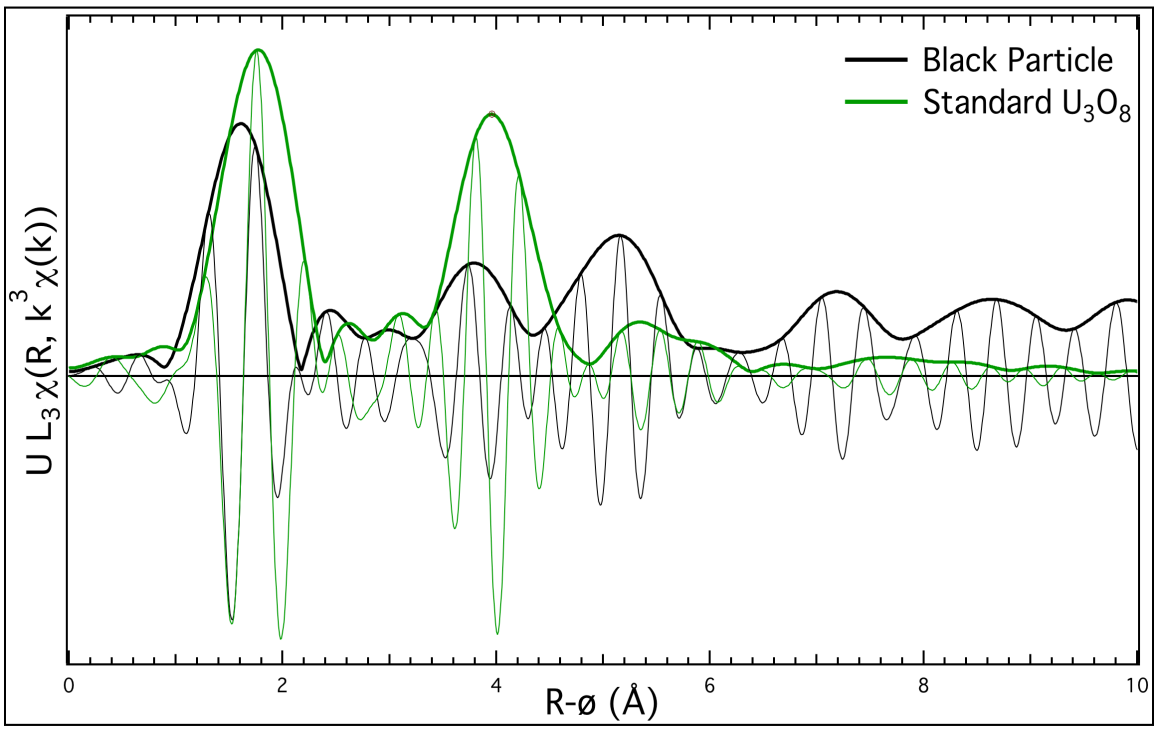

Figure 54. EXAFS results from the black particle overlaid with a standard U_3O_8. Distribution is shown with the imaginary contributions.

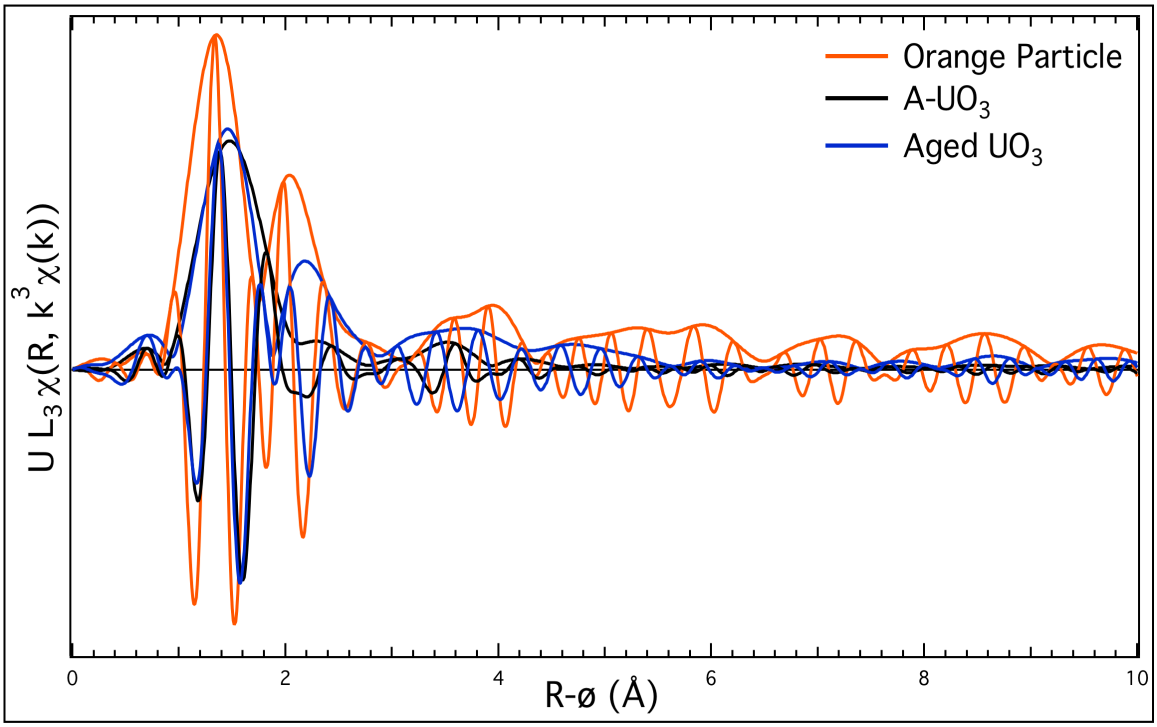

Figure 55. EXAFS results from the orange particle overlaid with a standard A-UO_3 and aged A-UO_3. Distribution is shown with the imaginary contributions.

Table 13. Summarized results for analyses on the Black and Orange materials in the industrially prepared sample.

Analysis	**Black vs. Orange**
ICP-MS Trace	Mostly Orange > Black, a few contaminants Black >
ICP-MS Isotopics	Depleted uranium, presence of ^{236}U indicates recycling
SEM Morphology	Differentiable morphologies for each
SEM Contaminants	Orange > Black, not statistically significant
pXRD	Black = U_3O_8 some $UO_3 \cdot 2H_2O$, Orange = Uranyl species
μ-XRF	Uranium only signal apparent
μ -EXAFS	Black = U_3O_8, Orange = Uranyl species

4.5 Results: Replication

4.5.1 Appearance

Figure 56 shows the material in the oven boat after being placed partially outside the heating zone at 975 °C. This resulted in black material on the left (the end in the oven), an orange material on the right, and a small "transition region" of brown material between the two. Material from each area was sampled and analyzed with SEM, ICP-MS, and XRD. The precipitation produced a much finer material than the received sample, so individual transition particles are difficult to discern.

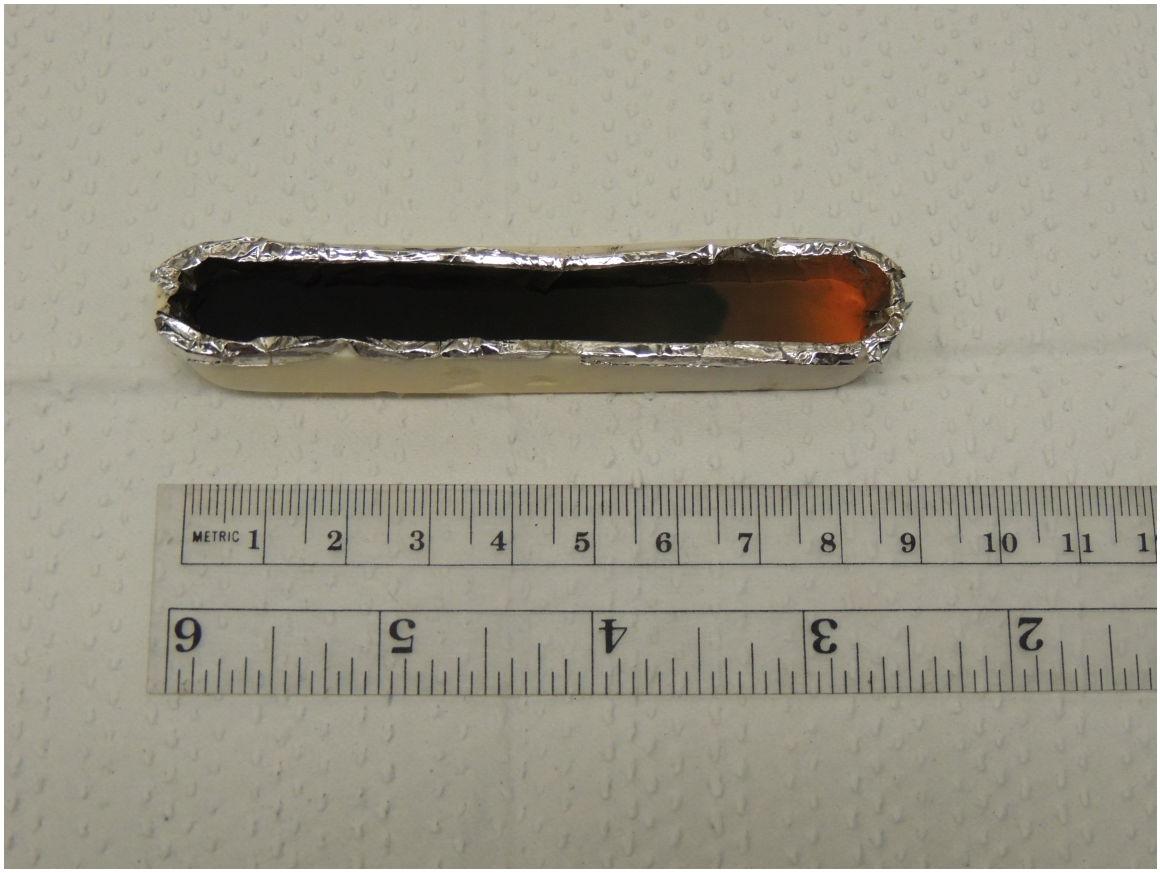

Figure 56. The oven boat after being placed partially outside the tube furnace at 950 °C.

4.5.2 ICP-MS

Trace analysis showed that A-UO_3 had the highest concentration of contaminants, followed by the brown material and U_3O_8 respectively (Table 14). These results support the hypothesis that the industrial sample's black material was exposed to a higher temperature than the orange.

Table 14. Trace element content in μg/g uranium for selected elements for the materials produced in the attempted replication.

Element	Black	+/-	Brown	+/-	Orange	+/-
Y	0.85	0.15	0.81	0.16	0.79	0.42
Zr	8.96	1.41	8.28	1.60	8.24	4.32
Nb	0.12	0.04	0.14	0.04	0.12	0.07
Mo	0.45	0.11	0.34	0.11	0.30	0.17
Sn	1.79	0.54	1.24	0.41	1.14	0.67
Sb	13.13	2.33	5.49	1.33	6.94	3.67
Ba	1.35	0.26	0.32	0.13	0.22	0.14
La	0.67	0.12	0.67	0.12	0.68	0.37
W	1.54	0.50	0.63	0.23	0.50	0.29
Th	0.77	0.13	0.79	0.13	0.77	0.40
Mg	6542.23	586.44	246.79	28.26	112.26	58.17
Ca	6567.86	1387.35	1325.85	292.68	486.68	264.35
Ti	12.76	3.11	13.10	2.55	11.93	6.55
V	3.09	0.75	2.58	0.61	3.03	1.68
Cr	0.28	0.12	NA	NA	NA	NA
Mn	3.53	0.60	NA	NA	NA	NA
Cu	4.20	0.79	0.39	0.42	0.82	0.50
Zn	20.96	3.63	17.21	3.46	17.87	9.67
Sr	3.90	0.80	0.95	0.65	0.55	0.34
K	65.50	12.64	39.53	13.37	39.45	22.10

4.5.3 pXRD

Diffraction on the replicated materials indicates that the black material is primarily U_3O_8 (Figure 57), the brown material less ordered U_3O_8 with some peaks consistent with oxidized or uranyl species (Figure 58), and the orange material a uranyl species (Figure 59). The material after being reduced with hydrogen is also shown (UO_2, Figure 60).

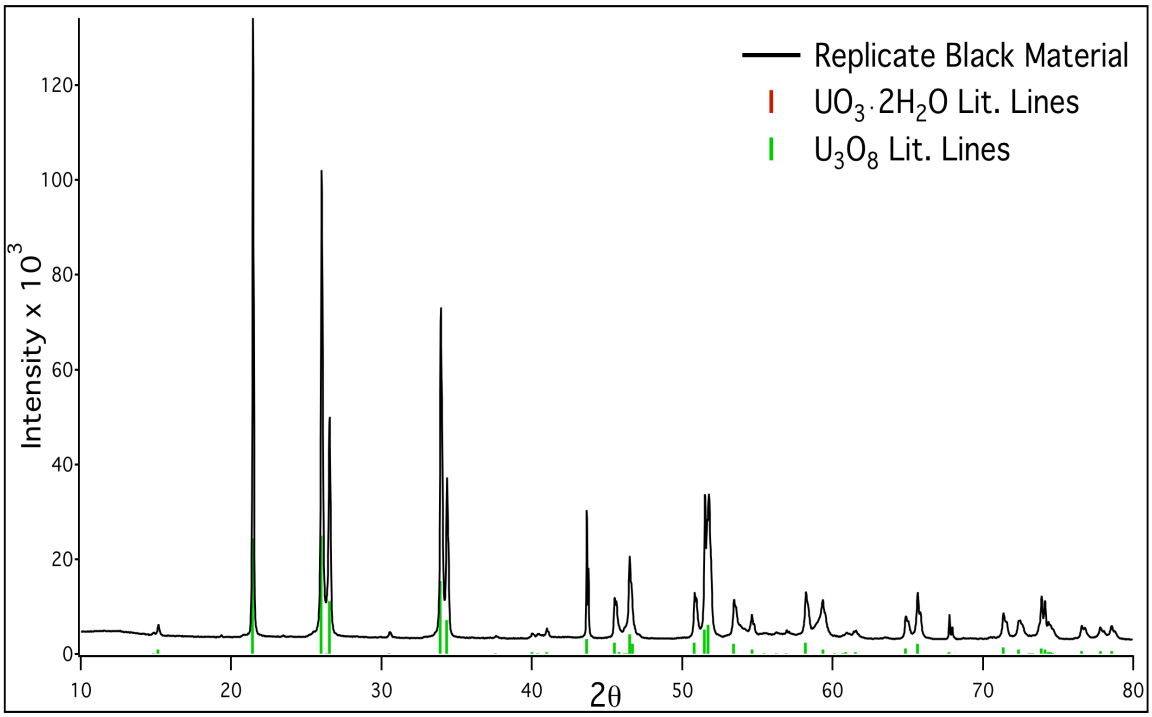

Figure 57. Powder diffraction data of the black material from the sample replication. Metaschoepite and U_3O_8 reference lines and intensities are included.

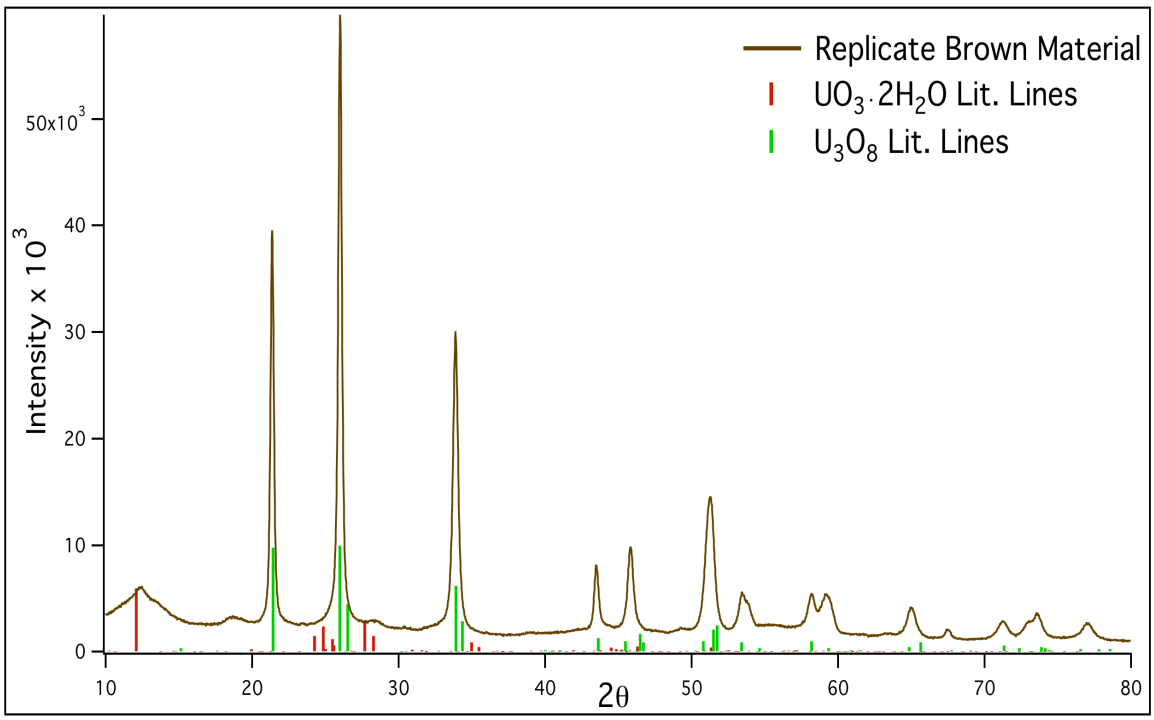

Figure 58. Powder diffraction data of the brown material from the sample replication. Metaschoepite and U_3O_8 reference lines and intensities are included

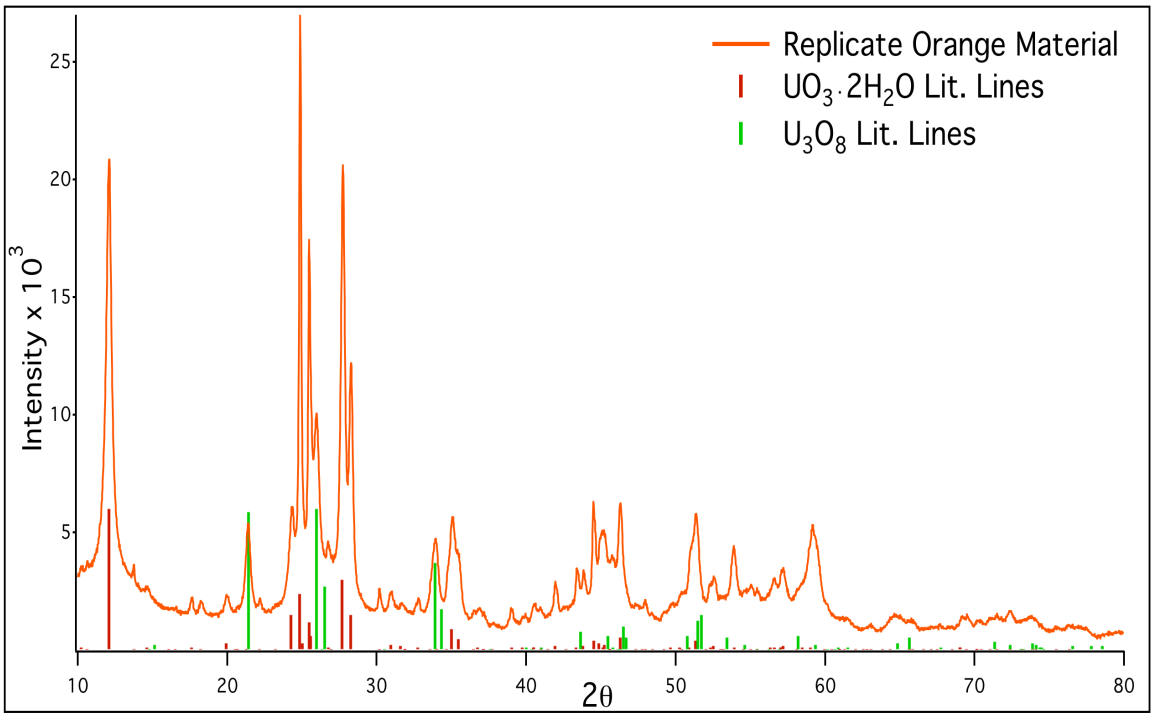

Figure 59. Powder diffraction data of the orange material from the sample replication. Metaschoepite and U_3O_8 reference lines and intensities are included

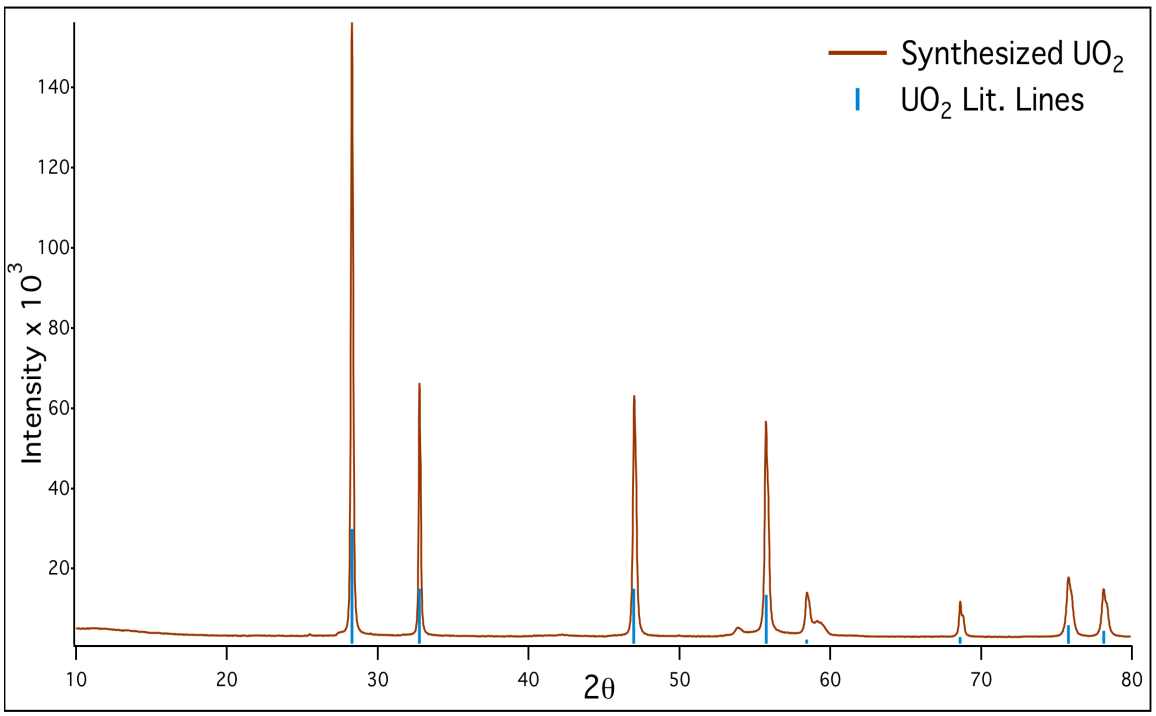

Figure 60. Powder diffraction data of the UO_2 synthesized from the remaining material from the sample replication. Uranium dioxide literature lines and intensities are included.

4.6 Discussion

The presence of transition particles in the industrially prepared sample implied that both materials originated from the same source material. This was slightly corroborated by the near identical isotopic ratios of the two materials. A number of the industrially prepared samples had similar isotopics so this was not conclusive evidence for the same starting material. Based on that assumption of same source material and the information available on the samples, it was postulated that a uranyl compound was placed partially outside a tube furnace in an attempt to produce U_3O_8, leaving a mixture of U_3O_8 and the original uranyl species.

The appearance of materials alone allowed for some conclusions related to the process conditions and opened possibilities for further experimentation to aid a forensics investigation. The replicated sample was composed of a much finer powder than the more agglomerated nature of the received sample. If the speciation of the materials is known and there is some evidence for a given precipitation, that precipitation it could be repeated at a range of conditions in order to replicate similar agglomerated products. Speciation analysis with XRD and EXAFS on the industrially prepared sample was consistent with the hypothesis that the intent was to make U_3O_8. However, the determination of the orange material was inconclusive. Both techniques point to a uranyl compound, but without further characterizations the exact speciation cannot be determined. This leaves little evidence for any single precipitation. The industrially prepared sample also had a much larger transition region (the brown material) than the very sharp gradient seen in the transition particles. If the synthesis scenario hypothesis is correct, this points to a furnace

setup with a much finer temperature gradient or some kind of zone divider [153]. It has been noted that the original sample had been synthesized in a tube furnace and used a stainless steel tube, which could corroborate this conclusion. However, if this had not been known already, it would be an excellent piece of evidence in a real life interdiction scenario for the material's history, namely the type of tube and/or furnace used for its synthesis. Finally, the fact that the material is heterogeneous at all points to a smaller scale process. Typically, manufacturers of large quantities of nuclear materials produce consistent, homogenous products (there are various steps including grinding, mixing, and consistent heating or other synthesis steps relating to homogenizing the material)[12, 32, 89].

The predominant morphologies in the black and orange material were consistent with the replicated samples in that the two types of material were different in each case. The replicated sample did not have the same types of unusual areas with trace element contamination though (not shown here). Based on experience with the uranyl peroxide precipitation, it is a method that produces a homogeneous precipitate and resulting uranium oxide compounds, explaining that result. The EDS spectra were therefore more consistent over the regions scanned.

Trace element analysis showed an overall higher concentration of contamination for the orange material in the received sample. Although not statistically relevant, the SEM results were consistent with this result; the orange material in the received sample had more areas with unusual morphology, specifically areas with carbon, silicon, nickel, and gold. There were some elements in the black material that had a higher concentration than in the orange material (lanthanum, magnesium, titanium,

iron, copper, and silicon). These anomalies most likely result from particles of contamination like those observed in the SEM imaging. For the black material, SEM showed areas with increased titanium and aluminum. The area with titanium is consistent with the ICP-MS results and aluminum was below detection limits. An interesting finding from the EDS data was the consistent presence of gold. It's origin is not clear, but it was below detection limits in the ICP-MS data, possibly indicating that it stems from a phenomenon of the SEM analysis.

The trend of decreased trace content through a heating process was also seen in the replicated sample. This implied that trace elements volatilized under fairly moderate temperatures (975 °C) even though the volatility of the elements and their oxides are typically much higher than 975 °C. This opens the possibility for process information based on the level of trace element composition, but only if more information is known. Some of the trace elements could be present due to contaminations from the tube of the furnace; they are consistent with stainless steel materials. It's possible the stainless steel tube was oxidized and would deposit contaminants during syntheses. Further analysis and future projects could include stainless steel contaminants, and analysis through a synthesis might lead to a significant chemical signature for forensics purposes.

4.7 Conclusion

Over the years particle differentiation and analysis has become a challenge in nuclear forensics analyses. Bulk information is valuable, but in cases with heterogeneous samples, individual particle analysis can yield additional information.

Furthermore, analysis of individual particles in a sample can help explain inconclusive results from bulk analysis both for nuclear forensics and environmental impact assessments. In this experiment, an industrially prepared uranium oxide sample had two types of materials, visible to the naked eye and manually separable. This provided individual particle analysis from a bulk sample for the purpose of nuclear forensics.

Based on the synthesis setup of the outside laboratory and the presence of transition particles, it was hypothesized that this sample was left partially outside of a tube furnace in an attempt to make U_3O_8. The analysis results of the sample and the attempted replication of this scenario were consistent with this hypothesis, but more work must be completed in order to determine the exact speciation of the starting material. This provided a evaluation of chemical characterizations for forensics purposes, and also demonstrated a few ways in which those observations could be used in those scenarios. One observation, a combination of particle size and appearance with chemical speciation, can be used to gain information on a sample's precipitation conditions. In this experiment, this cannot be performed until some information about the precipitation is gained. The materials' fine gradient could also lead to information on the type of furnace or heating setup used for its synthesis. Other conclusions based on analytical techniques were also useful. Specifically, analysis of trace content and/or EDS spectra can contribute knowledge to the material's history and possibly other contacted materials. Furthermore, when other information on a sample is known, analysis of trace content may indicate synthesis temperatures used. These facts illustrate how different analytical techniques are

complimentary in nuclear forensics scenarios. Overall, this experiment was an excellent proving ground for individual particle characterizations for forensics purposes.

CHAPTER 5

ANALYSIS OF ACTINIDE HOT PARTICLES FROM AN ACCIDENT SITE

5.1 Abstract

Extensive studies have been conducted on actinides in the environment; some have sought to analyze actinide particles, a common form in the environment. However, few have focused on chemical speciation and composition. Previous studies illustrated how information related to chemical speciation and surface composition is useful for source term characterization, a goal of molecular forensic science (MFS). X-ray diffraction (XRD), X-ray fluorescence (XRF), and X-ray absorption near edge structure (XANES) are often applied. The study discussed herein includes analysis of actinide particles of known history with microfocus XRD (μ-XRD) and XRF (μ-XRF), along with extended X-ray absorption fine structure (EXAFS) spectroscopy, a more sensitive probe of chemical speciation than XANES. Actinide particles originated from the BOMARC accident site, a location that has been studied for environmental and isotopic information in the past. Previous studies did not include analysis of chemical speciation and surface composition. Here, two BOMARC actinide particles were analyzed with the aforementioned techniques to study their chemical speciation and surface composition to evaluate source term information and to further establish MFS as a tool to do so. Results showed how uranium and plutonium behave under both extreme (the BOMARC fire) and environmental conditions (in soil ~47 years since the accident), and indicated interesting interactions when mixed. Furthermore, results were used to gain information related to source term and nuclear forensic science.

5.2 Introduction

The development of MFS has benefited from other scientific fields with similar focus and practice. The field of environmental science[21, 103] seeks to identify the fate and transport of nuclear materials in the environment by gathering chemical speciation information. This information provides insight into the mobility, possible weathering, and corrosion of actinide compounds[22]. Analysis of chemical speciation is aided by identifying the source term of the materials, a common goal with nuclear forensics. Isotopic analysis is the mainstay of nuclear forensics, as this gains information regarding nuclear material source term such as reactor type, time since a given separation, and enrichment levels[1, 4-8]. This information is exceedingly valuable, but often relies on assumptions (i.e. clean separations). Analysis of chemical speciation and composition can reveal complementary information such as processing conditions, chemical history, intent, and origin. Environmental science and nuclear forensics analyses have occasionally included chemical analysis of actinides and their particle forms. However, previous studies have been limited in use of techniques to probe for chemical speciation and have not looked for applications to nuclear forensics.

Chemical behavior of actinides is complicated and dynamic. In contact with air and H_2O, plutonium metal oxidizes rapidly, with the thermodynamically favored product nonstoichiometric PuO_{2+x}[92, 95, 96]. Uranium metal behaves similarly, but a range of possible intermediate oxide or oxy-hydroxide products exist, with uranyl oxy-hydroxide species being the endpoint[93]. Their chemistry is further complicated by the interaction of plutonium and uranium with one another[97-101],

other materials within their vicinity, and the range of exposure conditions present when many sites have been contaminated with actinides[10, 94, 154]. Further chemical interaction in the environment would be dependent on exposure, soil pH, redox conditions, and local microbial activity[23] as discussed in sections 1.2.3 and 1.2.4. In addition, size, shape, and oxidation gradients through a particle can lead to breakup and therefore increased weathering or ease in physical movement[10, 23].

Individual particle analysis is important because interdiction scenarios often involve materials with limited material quantity. In the environment, actinides are often present in particle form with a range of chemical speciation[10, 22, 43, 103-105]. There have been extensive studies on sites containing actinides in particle form around the globe. In those studies, XRF has identified source term information based on mixing of elements on material surfaces or by revealing inclusions of elements not seen with other techniques, whereas XRD has often been used to identify ordered components of interdicted materials or environmental samples when concentrations are adequate. A less often used probe of chemical speciation has been XANES, an absorption technique that focuses on the near edge of a specific element's absorption spectrum in order to compare oxidation states and coordination.

More specifically, after the Chernobyl accident, XANES, μ-XANES, XRD, and μ-XRF were used to identify two types of particles: a UO_2 core/oxidized surface (up to U_3O_8), and UO_2 core/reduced surface[98-101]. That individual particle analysis lead to conclusions on mixtures with other elements, as well as additional information on environmental impact and source term characterization. Another accident with a

weapon in Thule, Greenland used μ-XANES[22, 123]. Microfocus XANES showed that uranium was in the tetravalent state, while plutonium was either in the tetravalent state or in a 1:2 mixture of the tetravalent:hexavalent states. Depleted uranium particles from munitions leftover in Kuwait and Kosovo were also studied with μ-XANES and μ-XRD[124-126]. A summary of these studies, techniques used, and results is shown in Table 15. The overriding conclusion from those analyses was that actinide particle composition and speciation are highly dependent on the source term, which is vital for both forensics and environmental assessments.

Table 15. Some example studies on uranium/plutonium particles in the environment, the analysis techniques used, and summary of results.

Location	**Techniques**	**Results**
Chernobyl[98, 99]	XANES, XRF, XRD	UO_2 cores with oxidized or reduced surfaces
Thule[22]	XANES	uranium(IV) and plutonium(IV)/plutonium(IV/VI)
Kuwait/Kosovo[124, 125]	XANES, XRD	Range of uranium oxidation states/phases
BOMARC[10]	SEM, EDS, XRF	Range of mixtures, appearances, and elements present

Another source of samples of known history that contain characteristics relevant to nuclear forensics is the Boeing Michigan Aeronautical Research Center (BOMARC) accident site. BOMARC sites were located near the coasts and stored surface-to-air nuclear missiles as a defense against bomber fleets during the Cold War. At the McGuire Air Force Base BOMARC Missile Site near New Egypt, NJ a helium tank exploded on June 7, 1960. The explosion resulted in a fuel fire, which along with the following fire suppression dispersed nuclear material, namely plutonium, enriched

uranium, and depleted uranium in the immediate vicinity and areas around the site[155]. Remediation efforts removed most of the contamination, but surveying efforts showed areas including a restroom facility and firehouse still remained contaminated. In 2007 researchers from the Radiochemistry Department at the University of Nevada Las Vegas were part of a surveying and sampling effort in which soil cores were taken[10, 95]. Research included scanning electron microscopy (SEM), energy dispersive spectroscopy (EDS), synchrotron-based XRF, and both mass and radiometric isotopic analysis[10]. Those measurements provided insight into how the material had and would continue to behave in the environment and how source-term information can be obtained, but lacked information on chemical speciation. This study improves previous experiments by reporting a more detailed chemical analysis using μ-EXAFS, μ-XRD, and μ-XRF. This study seeks to expand this field of particle speciation analysis that has traditionally relied on more basic techniques like XANES, XRD, and XRF alone. Two hot particles from the BOMARC site were analyzed at Beamline 2-3 at the Stanford Synchrotron Radiation Lightsource (SSRL BL 2-3).

5.3 Experimental

5.3.1 Hot Particle Isolation and Sample Preparation

A handheld sodium iodide detector with lead collimators was used to localize hot particles within a soil core. Once the particle was localized, it was removed along with surrounding soil with a drinking straw. Soil was divided and the NaI detector used to further locate the particle. Particles were large enough to be manipulated

with tweezers. Particles were placed on a small paper containing a bromine-doped ink grid, facilitating the elemental mapping process as outlined in Section 2.8.1. Figure 13 shows how sample mounting on the filter paper is performed (refer to Chapter 4, Figure 45 for a photograph of a mounted particle sample for BL 2-3).

5.3.2 Elemental Mapping: μ-XRF

Microfocus XRF images were collected at the SSRL on BL 2-3 under dedicated operating conditions (3.0 GeV, 150 - 200 mA) using a silicon (220) double crystal monochromator. The microfocused beam (2 x 2 μm) was generated with a platinum-coated Kirkpatrick-Baez mirror pair (Xradia Inc.). For fluorescence imaging, the incident X-ray energy was set at three different energies: 18100 eV (above the plutonium L_{III} edge: 18059 eV), 18000 eV (below the plutonium L_{III} edge and above the uranium L_{III} edge: 17170 eV) and 17000 eV (below both the plutonium L_{III} and uranium L_{III} edges). These settings allow for elimination of interference from overlapping emission energies and enhance the separate identification of uranium and plutonium. The fluorescence emission lines, total count rates, and total fluorescence spectra were measured at room temperature using a Vortex silicon drift detector (SII NanoTechnology USA Inc.). The images were acquired by mounting the samples 45° to the incident x-ray beam and spatially rastering the samples in the microbeam using a Newport VP-25XA-XYZ stage (Figure 14). The ink grid discussed above in conjunction with BL 2-3's variable resolution settings allows particles on the micron scale to be located quickly.

5.3.3 μ-EXAFS and μ-XRD

After XRF maps were collected, specific points were chosen for μ-EXAFS and μ-XRD. Those points are identified on the fluorescence maps of each particle (Figure 61 and Figure 63). The EXAFS spectra were measured in fluorescence mode, using a nitrogen-filled ion chamber for the incident intensity and the fluorescence apparatus described above. Three scans were collected at each location of interest and subsequently averaged during the data analysis process. The data were analyzed using standard procedures including calibration (at 18059 eV and E_0 set at 18062 eV), normalization, EXAFS extraction, Fourier transformation, and curve-fits[92, 93]. The EXAFS data were extracted from the spectra by subtracting the absorption edge using a sum of an arctangent and a Gaussian fit to the absorption edge and peak; a polynomial spline function was fit to the rest of the spectrum. The resulting k^3-weighted EXAFS $\chi(k)$ spectra were fit using plutonium-oxygen and uranium-oxygen curve-fitting parameters calculated by FEFF7 (or when possible FEFF8). The Debye-Waller factor, σ, and the distance, R, from the absorber-scatterer pairs were varied for all fits, and the number of atoms, N, was varied where applicable.

X-ray diffraction patterns from locations of interest were measured with a CCD camera. Patterns were obtained with two measurements of 120 seconds exposure time (at 17500 eV) each. A sample of lanthanum hexaboride was used to calibrate the distance between the sample and the detector in an attempt to obtain accurate d-spacings. Diffraction patterns were analyzed and indexed with the software package available at BL 2-3.

5.4 Results and Discussion

5.4.1 Elemental Mapping: μ-XRF

A summary the following sets of results will be included at the end of this section (Table 21). Figure 61 and Figure 63 show high-resolution XRF maps of each particle with the larger one called “Particle 1” (Figure 61) and the smaller one “Particle 2” (Figure 63). The figures include the major fluorescing elements observed in each particle. Figure 62 and Figure 64 show spatial distribution correlations for uranium and plutonium for the entire area of the particles. Their corresponding Pearson coefficients, r, are also included. The Pearson function calculates a correlation value (r) between two variables. Doing so determines the degree to which variables are related[156, 157]. The function puts a specific value on correlations, allowing for comparison of elements or particles. If the r-value is higher, the variables are more strongly correlated. A number of correlations will be discussed in detail for Particle 1. Those correlations are summarized (Table 16).

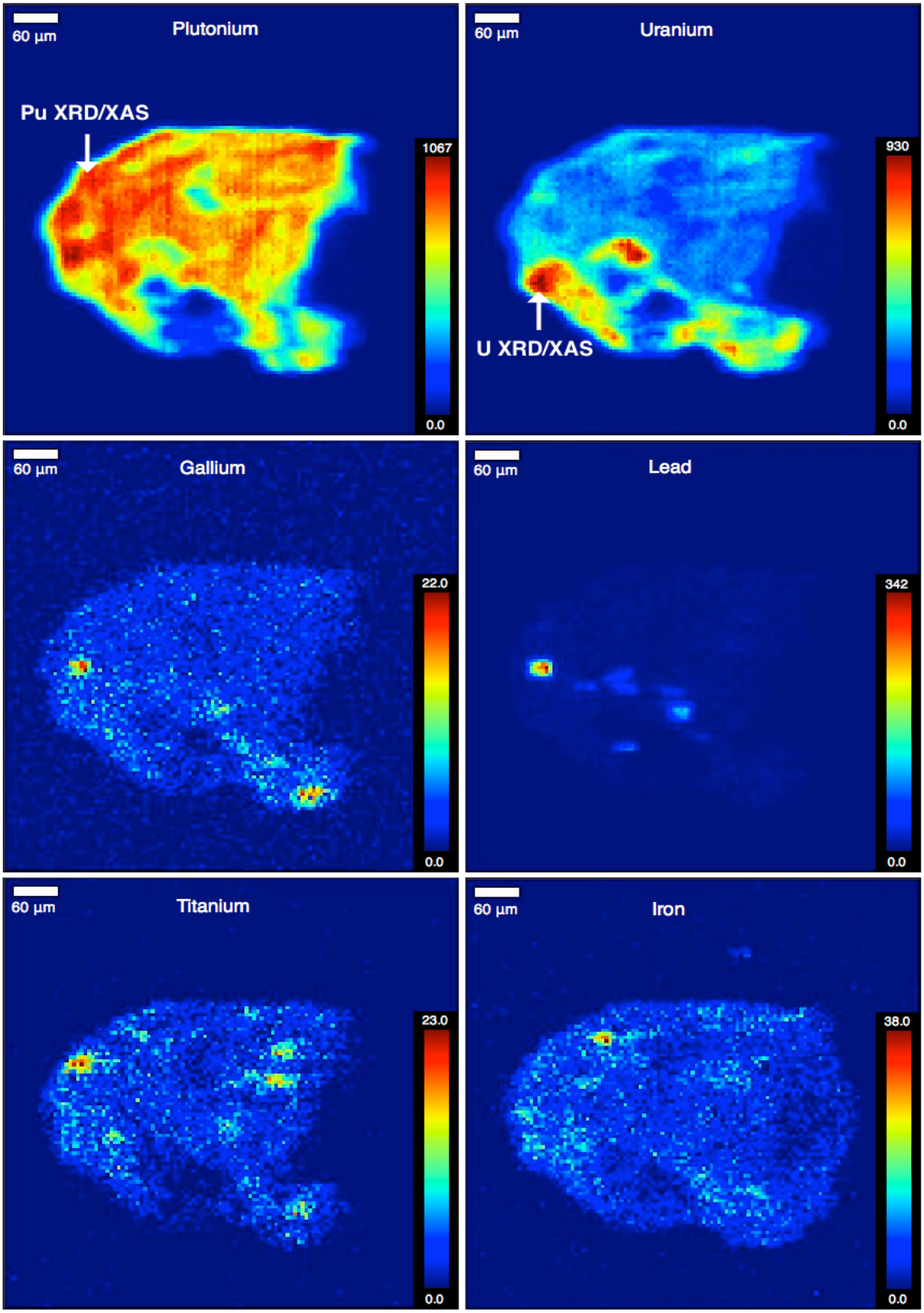

Figure 61. µ-XRF maps of Particle 1. Map acquisition was performed at 18100 eV with 2 µm^2 beam size and 100 ms dwell time. The scale bars show the element of interest count rate.

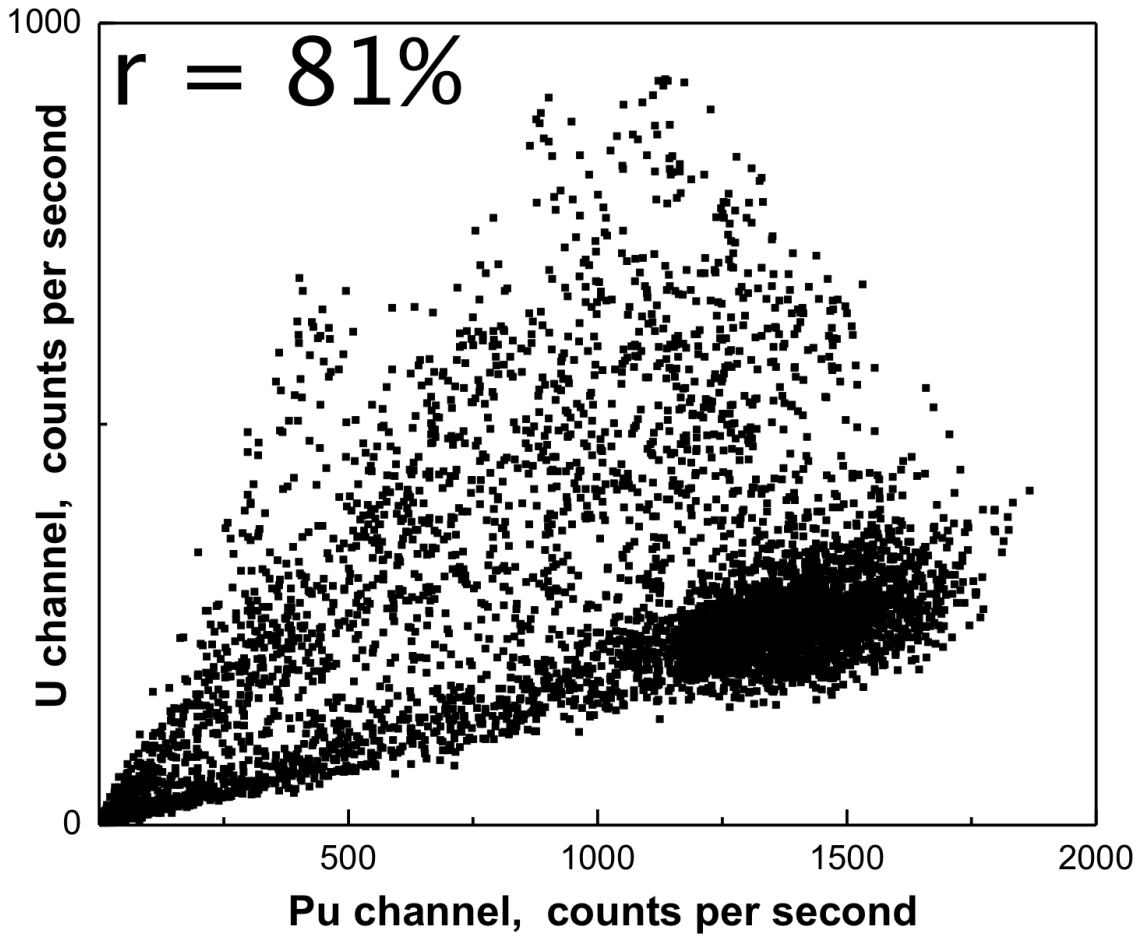

Figure 62. Spatial correlation plot for Particle 1 showing uranium and plutonium fluorescence intensities at each data point. Pearson function was applied to calculate r for this correlation.

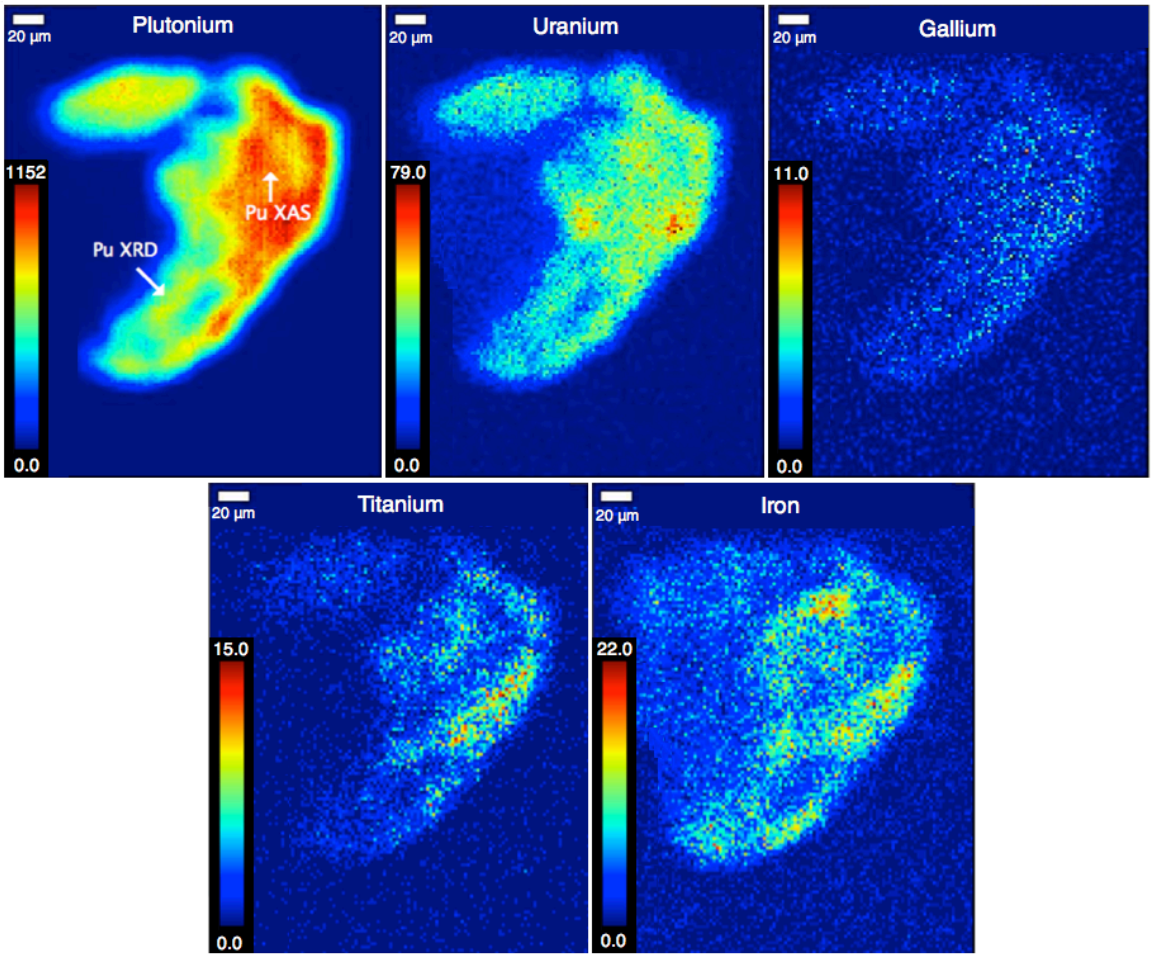

Figure 63. µ-XRF maps of Particle 2. Map acquisition was performed at 18100 eV with 2 µm^2 beam size and 100 ms dwell time. The scale bars show the element of interest count rate.

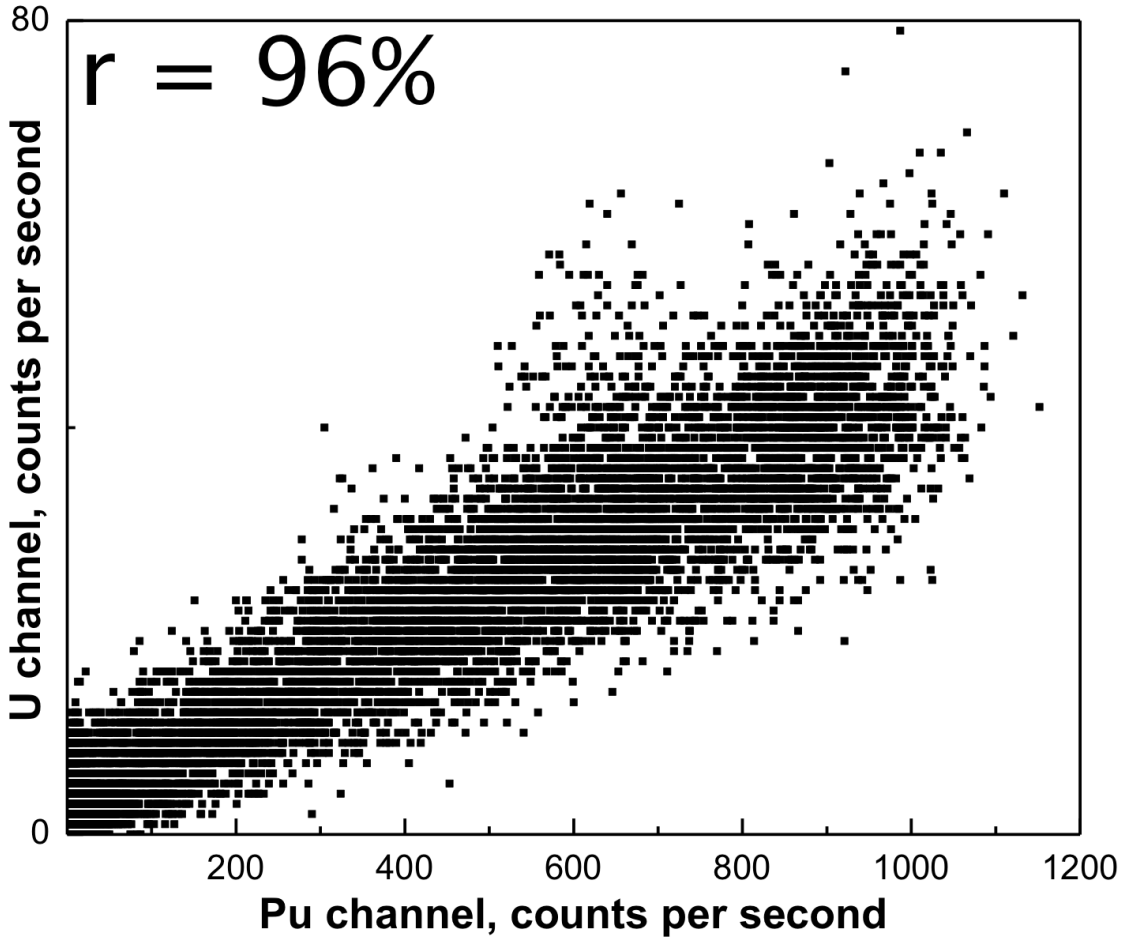

Figure 64. Spatial correlation plot for Particle 2 showing uranium and plutonium fluorescence intensities at each data point. Pearson function was applied to calculate r for this correlation.

Fluorescence data indicate the primary heavy element in each is plutonium, with varying amounts of other elements as discussed below. Particle 1 is about 300 x 300 *μm* with one sharp corner and a small spur on one side. There is a small region that contains neither plutonium nor uranium, indicating either a large pore or inclusion of fluorescence outside the detection range. Particle 2 is about 150 x 200 μm and has similar features to Particle 1 including a spur-like region and areas where no fluorescence in the detection range produced high counts.

For Particle 1, elements do not appear to be evenly distributed and occur as small separate domains with sufficiently high concentrations that the plutonium signal is reduced. This is evident in the correlation plot shown in Figure 62, where the highest numbers of plutonium counts are associated with low counts from the uranium. The uranium:plutonium ratios are widely dispersed with no regions that display any increased concentration of values. However, the linear region in the correlation plot indicates that there is a domain where the uranium and plutonium are evenly mixed in a ~1:4 ratio and other areas with more uranium extending even up to a 1:1 ratio where they are combined less homogeneously. The relatively large r-value over the entire particle is somewhat deceiving since the separate domains seem obvious. To depict this phenomenon further, the top and bottom halves of the particle were selected for correlation analysis. Bicolor plots (plutonium fluorescence is in red and uranium is in green), correlations, and calculated r-values for each half are shown in Figure 65 and Figure 66.

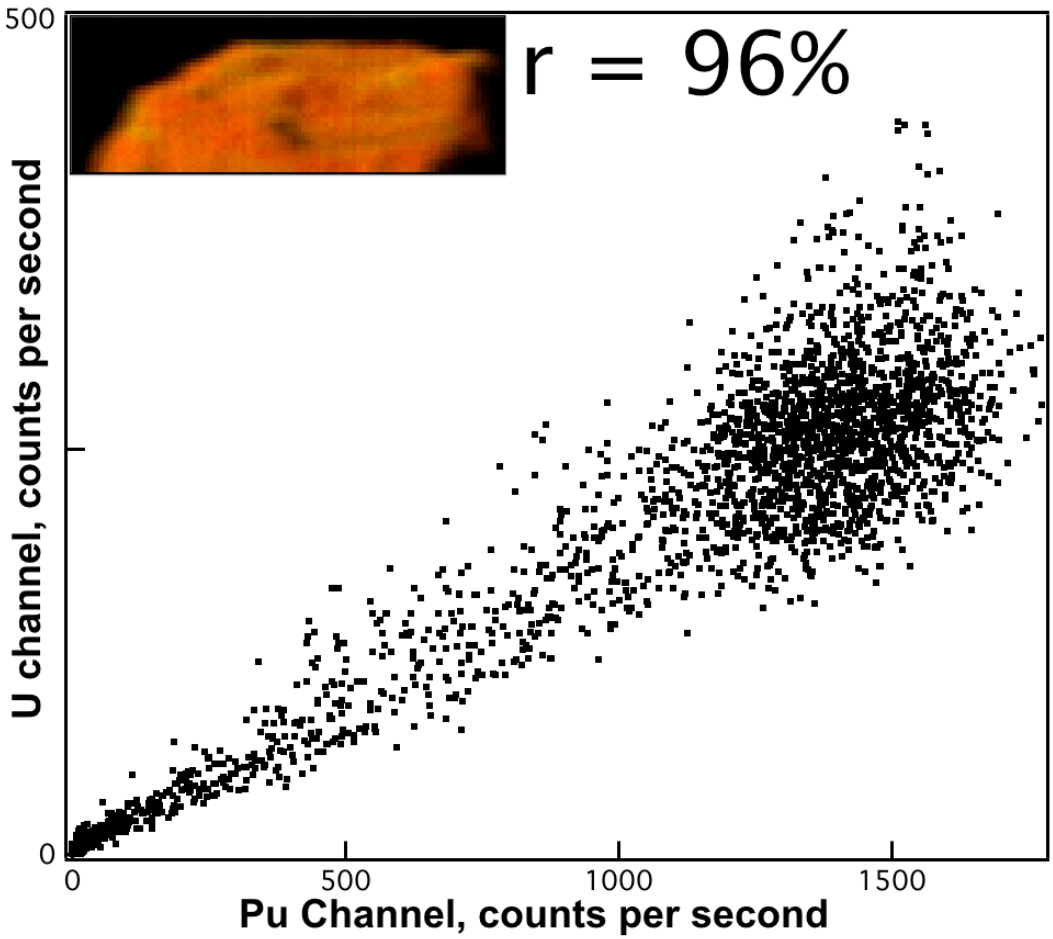

Figure 65. Correlation plot for the top half of Particle 1, including a bicolor fluorescence map (plutonium in red, uranium in green), and the Pearson r-value.

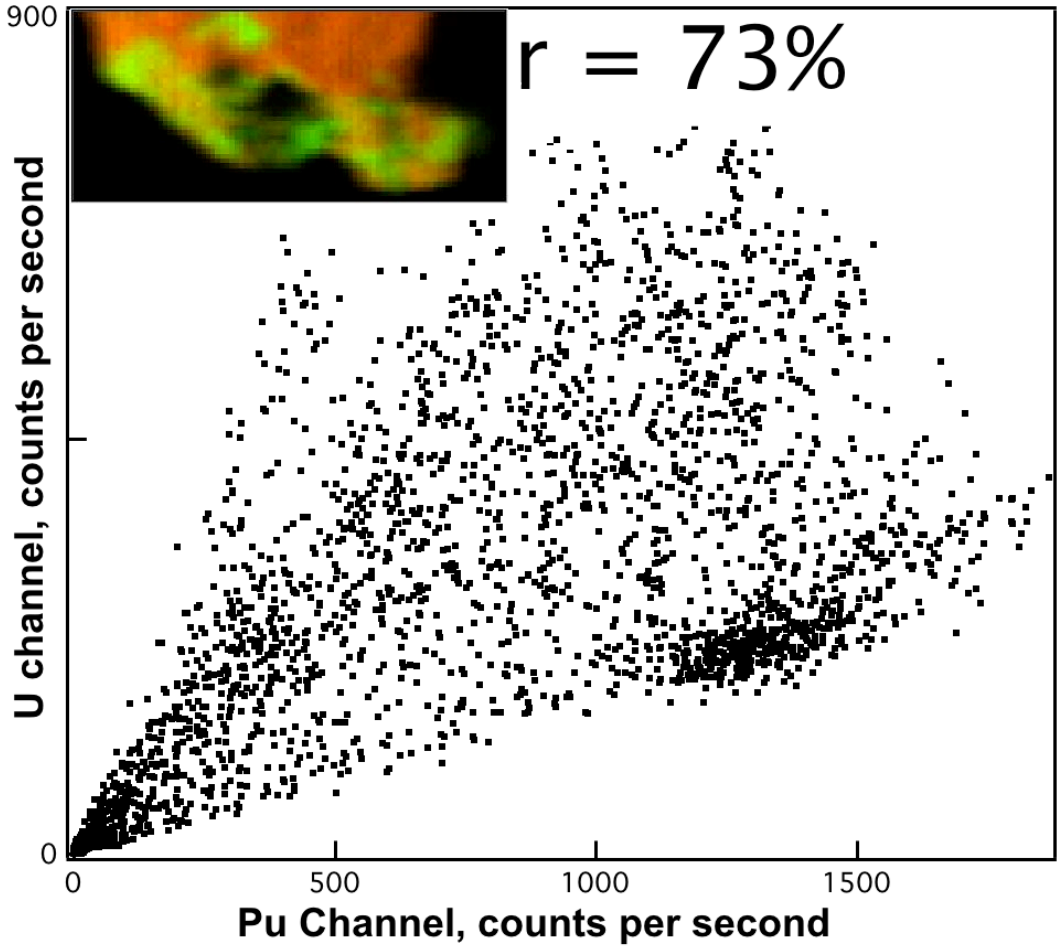

Figure 66. Correlation plot for the bottom half of Particle 1, including a bicolor fluorescence map (plutonium in red, uranium in green), and the Pearson r-value.

The top half is evenly mixed, indicated by the high r-value and the yellow color of the bicolor map. The bottom half has a much lower r-value and the bicolor map shows uranium and plutonium as separate domains. Clearly, there are two types of mixing within Particle 1. Analysis of data collected from the top half suggests complete vaporization followed by recombination or lengthier mixing, while data collected from the bottom half suggests elements were not vaporized and instead experienced a shorter mixing time of separate components. Even though the top half has a consistent mix of uranium and plutonium, other elements like gallium, lead,

and iron seem to have fused to the particle in a similarly to uranium and plutonium in the bottom half.

Particle 2 is also composed primarily of plutonium, but does not exhibit the same mixing in Particle 1. Uranium is correlated with the plutonium throughout the particle (Figure 64). This is a strong correlation and r-value, but the overall concentration of uranium is still quite low (1:15). Also, the other minor elements are evenly distributed throughout, suggesting that the entire particle and its constituents went through vaporization followed by recombination or lengthier mixing of components. Presence of other elements, specifically gallium, lead, iron, and titanium, point to other materials in the vicinity of the nuclear material. Previous work and in-house XRF performed at Los Alamos National Laboratory (LANL) have also suggested the presence of aluminum and silicon[10], but their low fluorescence energies are not detectable by the XRF system at BL 2-3. Particle 2 is homogeneously mixed for all elements including gallium (1% of total plutonium counts), iron (~2% counts), and titanium (~1% counts).

Particle 1 has two areas with gallium counts above background. From the maps alone, the spot on the bottom right of the particle appears to be correlated with plutonium. Figure 67 shows the correlation of gallium and plutonium over the entire particle, along with a bicolor map of the two elements and the r-value. Figure 68 shows the correlation, fluorescence maps, and r-value for just the spot on the bottom right of the particle. There, the r-value is 78% compared to only 69% for the entire particle. Figure 69 shows the same data for the gallium spot on the left, where the r-value is 0%, indicating no correlation with plutonium. Gallium and lead do

appear to be correlated at this location though. Figure 70 shows the correlation of gallium and lead for the entire particle along with a bi-color map for the two elements (gallium fluorescence is shown in green and lead fluorescence in red). This map indicates that the spot on the left side of the particle has a strong correlation of the two elements, but the Pearson value, r = 47% indicates a weak correlation over the entire particle. Figure 71 shows the correlation and fluorescence maps of just the area on the left. There, r = 74%, indicating a stronger correlation of gallium and lead, but still not a high degree of mixing. The other areas with lead and the other minor elements are not correlated with anything else and are present as separate domains.

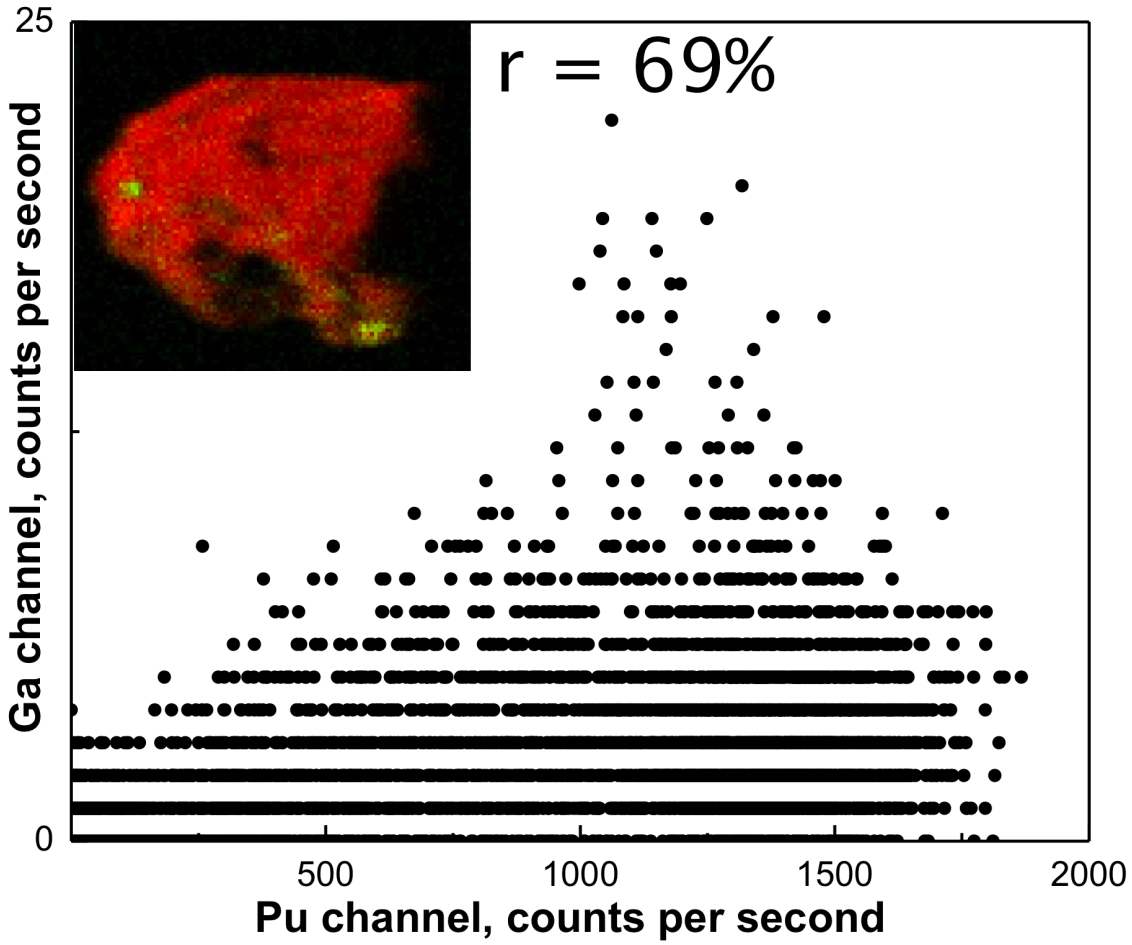

Figure 67. Spatial correlation plot for entire area of Particle 1 with gallium and plutonium intensities The left inset shows intensities of each element, with gallium in green and plutonium in red.

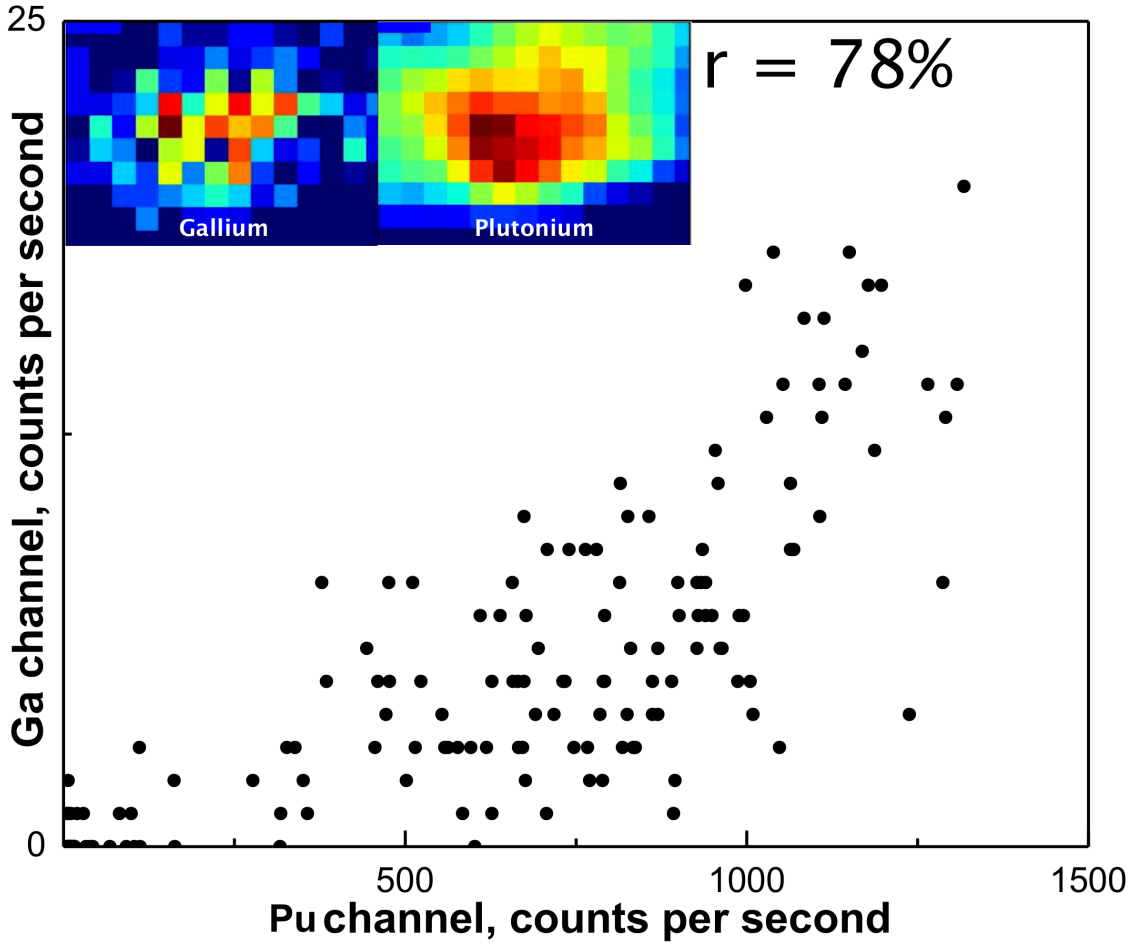

Figure 68. Spatial correlation plot for Particle 1 showing gallium and plutonium fluorescence intensities at the data points from the spot on the bottom right of the particle. The top left insets show zoomed in gallium and plutonium maps. Pearson function was applied to calculate r for this correlation.

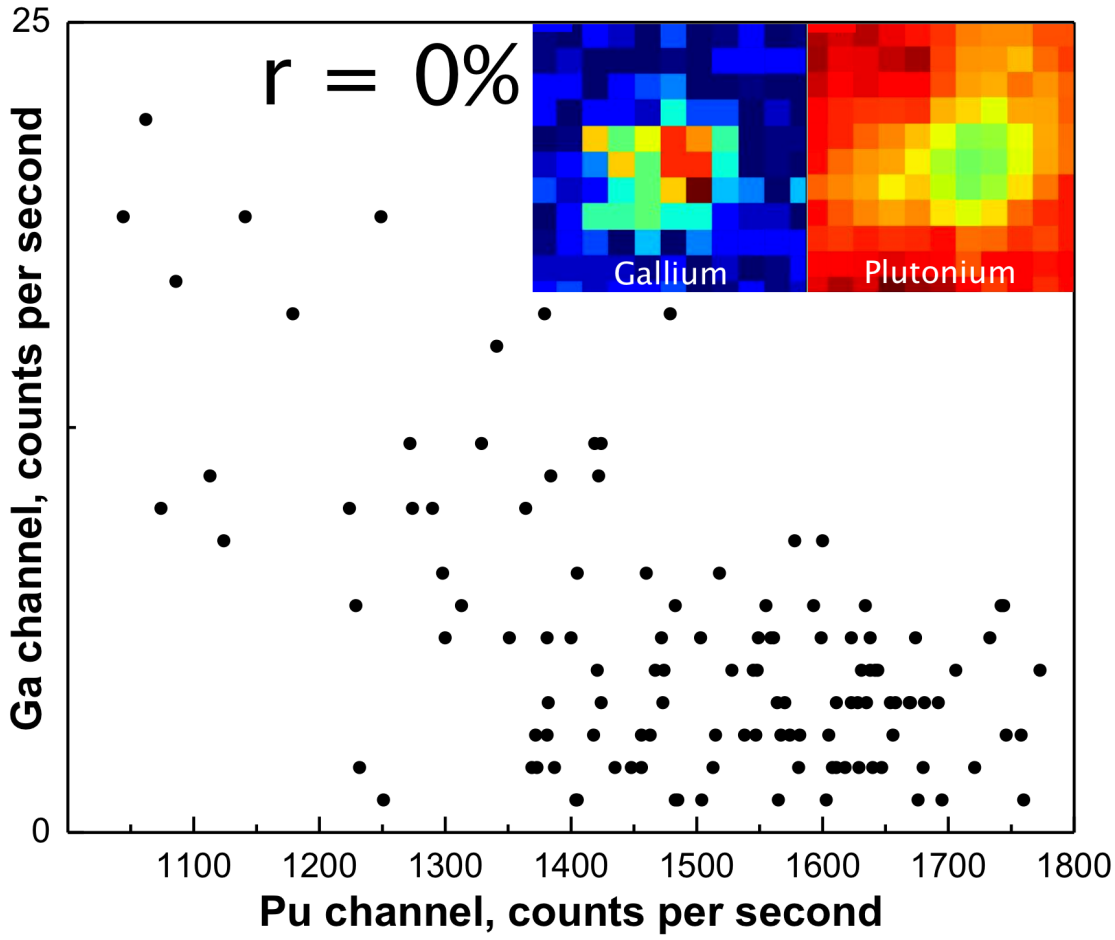

Figure 69. Spatial correlation plot for Particle 1 showing gallium and plutonium fluorescence intensities at the data points from the spot on the left side of the particle. The top right insets show zoomed in gallium and plutonium maps. Pearson function was applied to calculate r for this correlation.

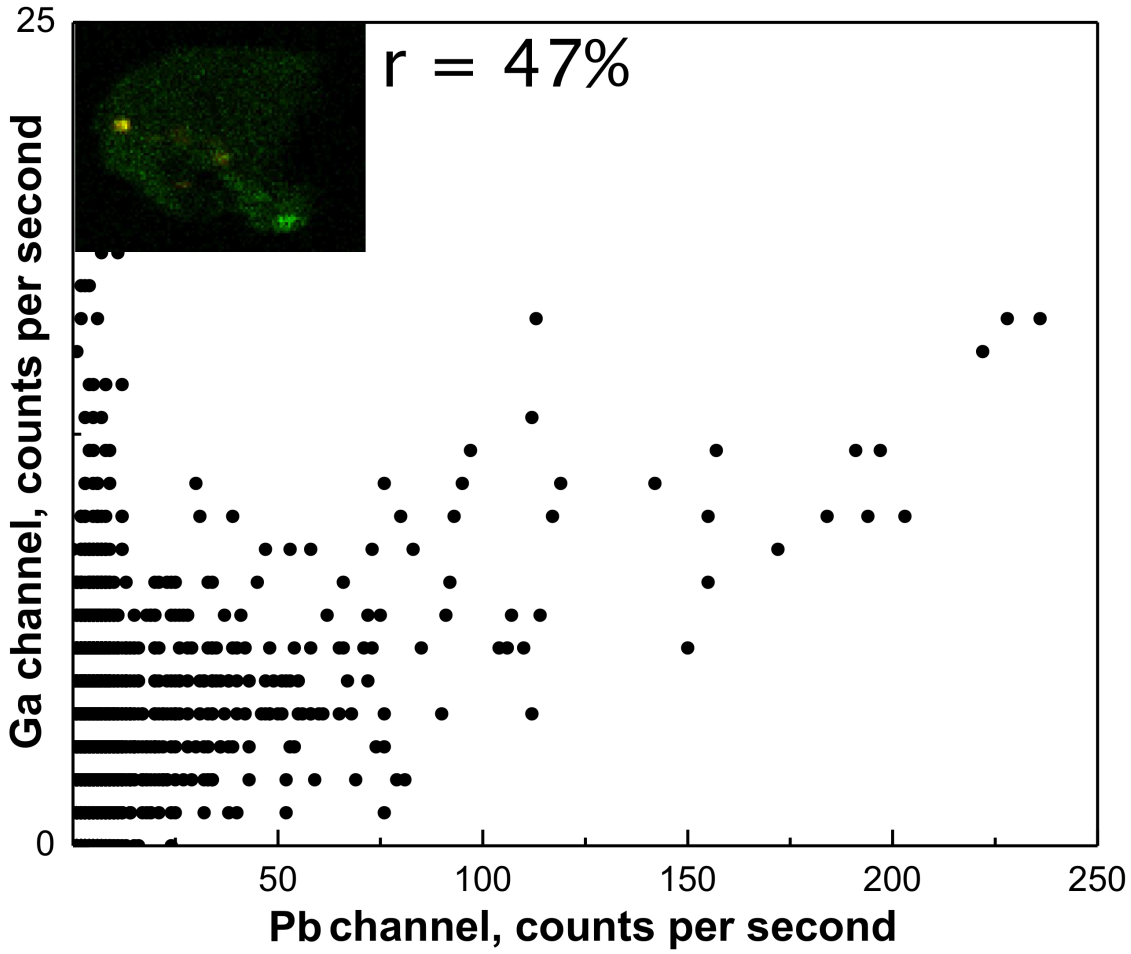

Figure 70. Spatial correlation plot for Particle 1 showing gallium and lead fluorescence intensities at all data points on the particle. The top left inset shows intensities of each element, with gallium in green and lead in red. Pearson function was applied to calculate r for this correlation.

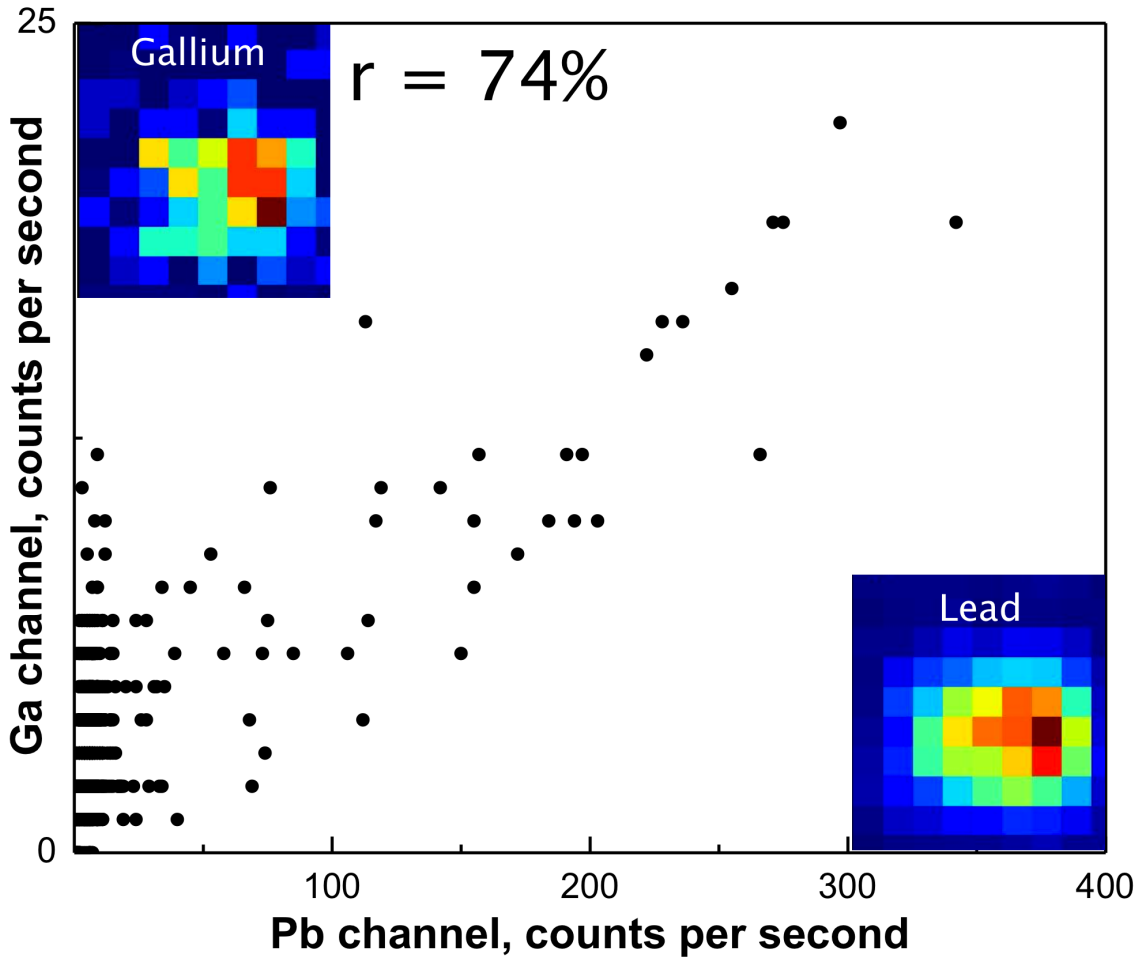

Figure 71. Spatial correlation plot for Particle 1 showing gallium and lead fluorescence intensities at the data points from the spot on the left side of the particle. The top left inset shows zoomed in gallium map, the bottom right shows the zoomed in lead map. Pearson function was applied to calculate r for this correlation.

Table 16. Summarized results from correlations discussed for Particle 1.

Element 1	Element 2	Area	r-value
Pu	U	Entire Particle	81%
Pu	U	Top Half	96%
Pu	U	Bottom Half	73%
Pu	Ga	Entire Particle	69%
Pu	Ga	Bottom Right Spot	78%
Pu	Ga	Left Spot	0%
Ga	Pb	Entire Particle	47%
Ga	Pb	Left Spot	74%

Overall, the quantification of elemental concentrations from XRF is difficult to evaluate due to variance in emission yield, presence of containment layers, and detector efficiency. Again, the variance in mixing present in these particles indicates distinctive interaction of elements in the formation of each particle. For Particle 1, it's likely that separation and reorganization occurred on the macroscopic level for most of the elements in the particle, with the top half undergoing more significant mixing of only uranium and plutonium (separate domains of minor elements likely mixed with the particle after this separation and reorganization). This area (initially) and Particle 2 likely formed on an atomic level after vaporization or after undergoing a longer time of interactions with the liquid forms of the elements involved. These types of scenarios along with speciation data may yield information on the source such as temperature exposure[10, 102, 121], and therefore the accelerant(s) in the fire. Because Particle 1 has areas that remained as separate domains in the ~47 years in the soil, and the two particles were sampled from the same location, it is unlikely either particle experienced any redistribution or reorganization when exposed to weathering. Therefore, these particles strongly represent the source material immediately post-fire.

5.4.2 μ-XRD Analysis

For Particle 1, two areas were chosen for diffraction: one in an area of high uranium concentration, and one in an area of high plutonium concentration. Although homogenously mixed, the concentration of uranium in Particle 2 was insufficient to produce a diffraction signal. Limitations and high uncertainty

resulting from broad diffraction peaks, indeterminate distance of sample and standard from the detector, and asymmetry in the diffraction pattern resulted in an error of approximately $\Delta d \pm 0.042$. These errors provide inaccurate lattice parameter determination, but trends in d-spacings are still apparent. Only those will be presented here, which are still useful for phase identification.

The diffraction patterns and index comparisons are shown in Figure 72 and Table 17, respectively. The patterns are strong, indicating a high degree of order. Particle 1 has a stronger signal than Particle 2. Furthermore, they cover a wide range of angles, suggesting the particles not highly crystalline. The spectra are similar in that they all show a cubic crystalline structure. Extracted d-spacings index well to the Fm3m space group of $PuO_2/UO_2/U_4O_9$ as seen in Table 17, with the key difference being the larger d-spacings for the area higher in uranium concentration. This trend is consistent with the literature d-spacing values for these species. This result suggests the ordered components in the particles are PuO_2-PuO_{2+x}, and UO_2-U_4O_9[92, 93, 96].

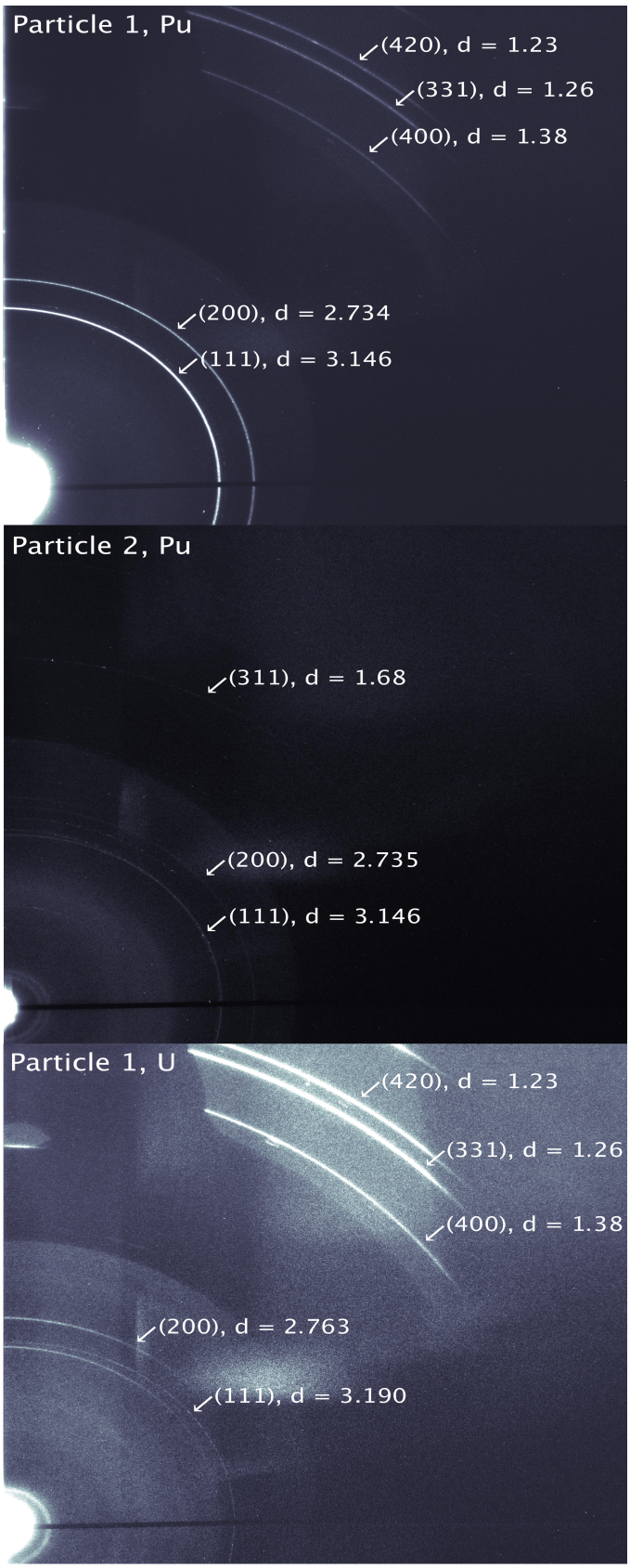

Figure 72. CCD diffraction patterns from each particle.

Table 17. Index patterns for the predominant d-spacings from experimental diffraction data along with the literature for PuO_2**[158]**, UO_2**[159]**, and some predominant lines from the U_4O_9 structure**[150]**.

Part. 1 Pu	**Part. 2 Pu**	**Lit. PuO_2**	**Part. 1, U**	**Lit. UO_2**	**Lit. U_4O_9**
3.146	3.146	3.1167	3.190	3.157	3.141
2.734	2.735	2.6991	2.763	2.734	2.720
NA	1.68	1.6276	NA	1.649	1.640
1.38	NA	1.3496	1.38	1.367	NA
1.26	NA	1.2384	1.26	1.254	NA
1.23	NA	1.2071	1.23	1.223	NA

5.4.3 μ-EXAFS Spectroscopy

Areas for EXAFS analysis were chosen for count rates (concentrated but with no detector saturation) for the element of interest in order to achieve the best statistics. The plutonium EXAFS, resulting curve-fits, and shell contributions for Particle 1 are shown in Figure 73. Similar plots for Particle 2 (Figure 74) and the $PuO_{2.00}$ (Figure 75) standard are reported.

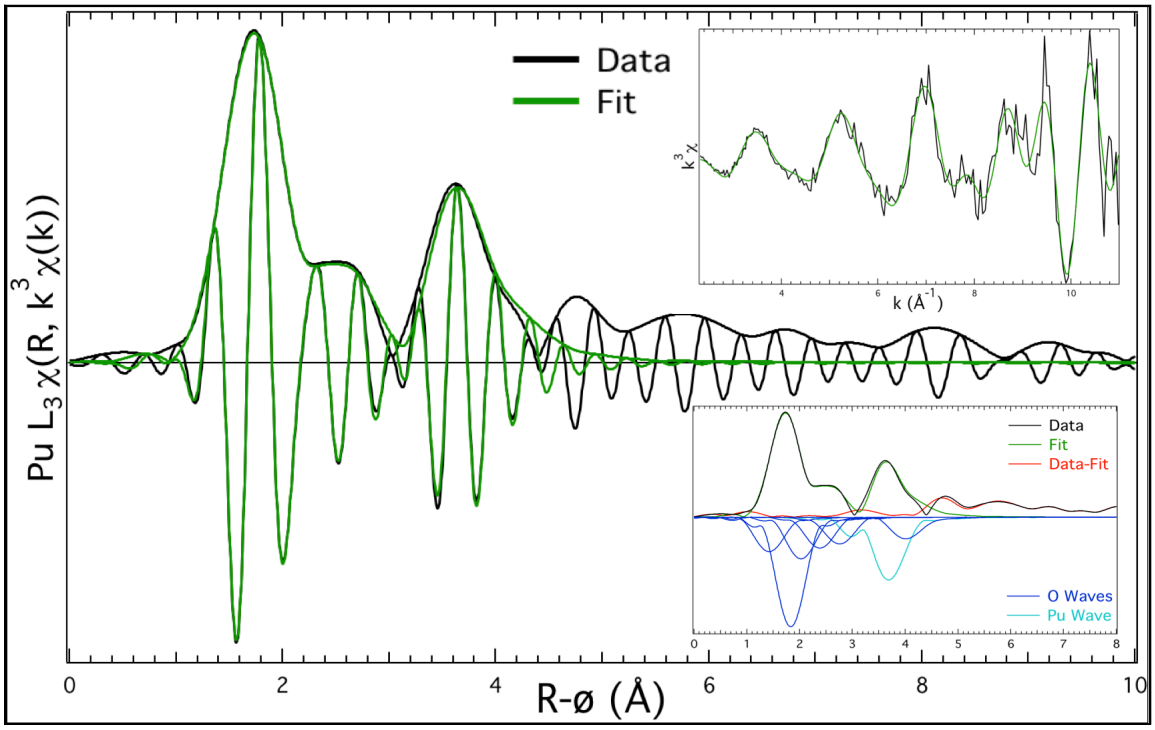

Figure 73. Plutonium L_{III} EXAFS spectrum from Particle 1 (2.3-11.0 k). Data is shown in black and the curve-fits in green. $k^3\chi$ plots are shown in the upper inset and individual shell contributions on the lower inset.

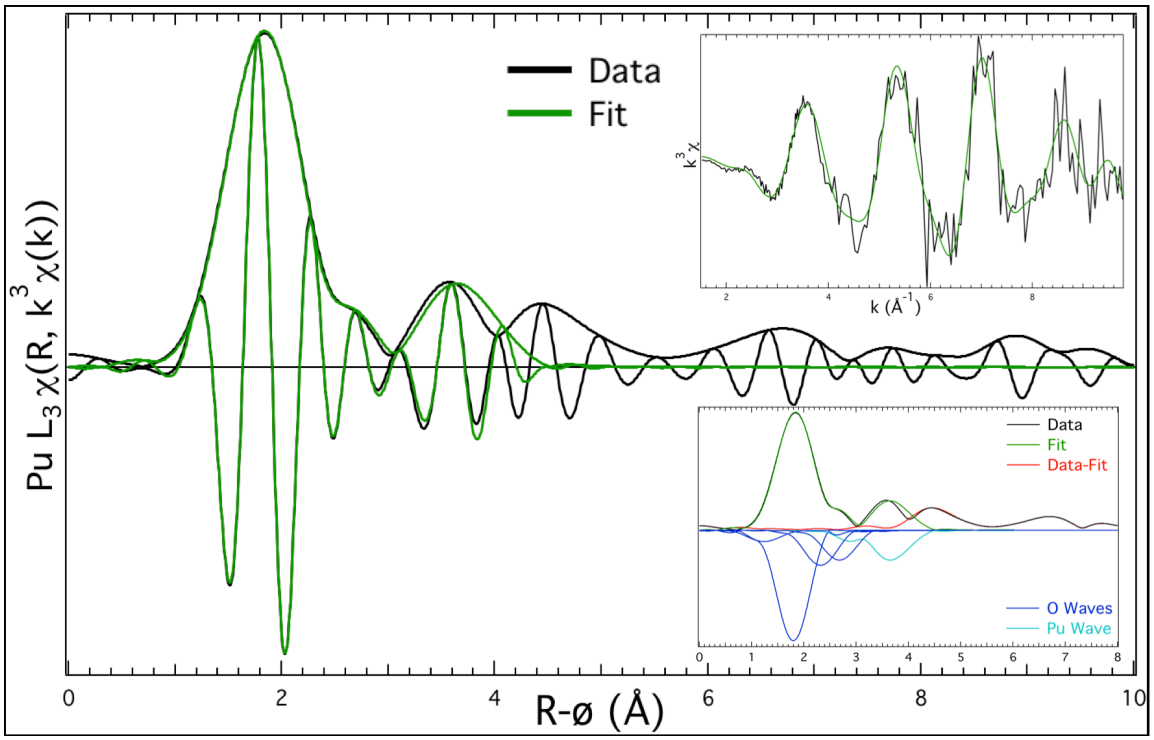

Figure 74. Plutonium L_{III} EXAFS spectrum from Particle 2 (1.5–9.8 k). Data is shown in black and the curve-fits in green. $k^3\chi$ plots are shown in the upper inset and individual shell contributions on the lower inset.

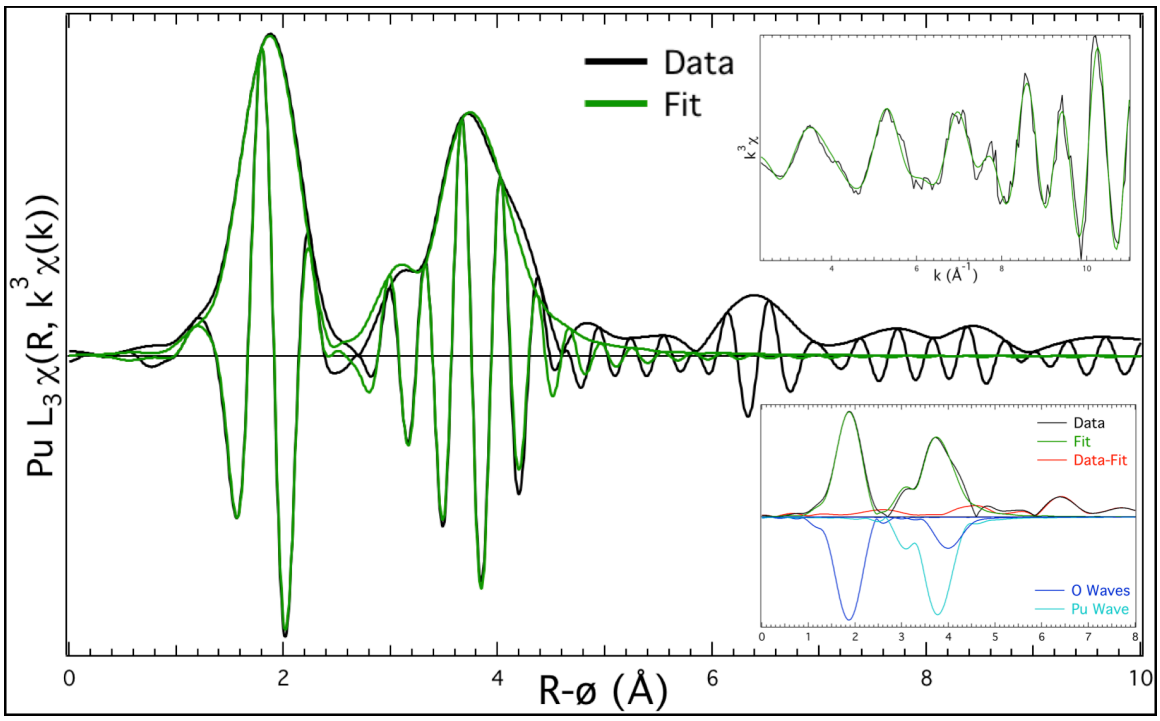

Figure 75. Plutonium L_{III} EXAFS spectrum from $PuO_{2.00}$ standard (2.3–11.0 k). Data is shown in black and the curve-fits in green. $k^3\chi$ plots are shown in the upper inset and individual shell contributions on the lower inset.

Plutonium EXAFS for each particle are similar in that they both show a PuO_{2+x} structure, consistent with related samples in previous studies[92, 96]. Their disorder is apparent by the need to fit a number of shells outside the crystallographic structure of PuO_2 in order to obtain a quality fit. This is further evidenced by the overlay of Fourier transforms with the reference $PuO_{2.00}$ (Figure 76). Both particles have lower amplitude than the reference, indicating less ordered systems, and Particle 2 is slightly less ordered than Particle 1. The reference oxide (from LANL) was measured at 80 K. Because the particles were measured at room temperature, their Fourier transform amplitudes are lower. However, the differences are significant enough that there is still a large amount of disorder present in the particles. The imaginary contribution of the data matches well for

each particle in the region containing the first three plutonium-oxygen shells (1.5-2.5 Å). They diverge significantly from 2.5-3.5 Å, and begin to converge in the region with the last two shells (plutonium at 3.75 Å and oxygen at 4.5 Å). This indicates that the first plutonium-oxygen region and the region containing more distant plutonium-oxygen contributions and the plutonium-plutonium shell match well for both particles and the reference. Fitted shell data including the shell, distance, number of atoms, and Debye-Waller factor (Debye-Waller factors were often fixed and so errors have been excluded) are shown for each sample in Tables 18-20.

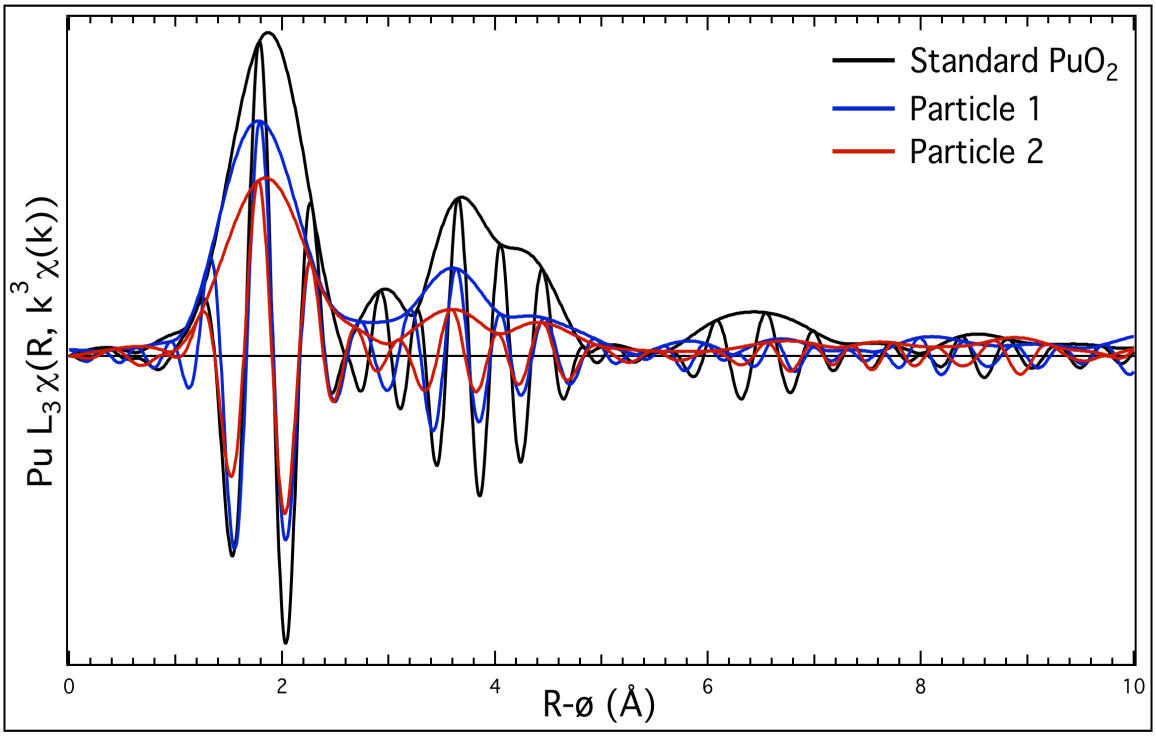

Figure 76. Overlay of the EXAFS spectra of the two particles and an ordered reference $PuO_{2.00}$ (2.3 – 9.8 k).

Table 18. Curve fits results for Particle 1 including shells fitted, number of atoms, and the Debye-Waller factor.

Shell	Distance (Å)	Atoms	σ
O	1.895 (0.019)	0.707 (0.212)	0.031
O	2.301 (0.017)	3.880 (1.034)	0.052
O	2.493 (0.021)	1.736 (0.521)	0.052
O	2.849 (0.022)	1.987 (0.633)	0.064
O	3.223 (0.024)	2.513 (0.825)	0.073
Pu	3.776 (0.016)	5.153 (1.449)	0.072
O	4.466 (0.017)	4.943 (1.538)	0.032

Table 19. Curve fits results for Particle 2 including shells fitted, number of atoms, and the Debye-Waller factor.

Shell	Distance (Å)	Atoms	σ
O	1.766 (0.026)	0.217 (0.076)	0.083
O	2.313 (0.022)	3.989 (1.044)	0.088
O	2.832 (0.026)	1.783 (0.601)	0.082
O	3.186 (0.026)	2.044 (0.613)	0.088
Pu	3.758 (0.023)	4.518 (1.355)	0.118

Table 20. Curve fits results for the PuO_2 standard used including shells fitted, number of atoms, and the Debye-Waller factor. This sample is in agreement with crystallographic diffraction data[158].

Shell	Distance (Å)	Atoms	σ
O	2.337 (0.0197)	7.987 (2.042)	0.081
Pu	3.829 (0.012)	9.036 (2.144)	0.055
O	4.474 (0.021)	14.323 (4.433)	0.061

Previous studies on related samples[92, 96] (i.e. plutonium from environmental sites and fired plutonium oxides) are more comparable to Particle 1 in that they require similar shells for quality fitting and a relatively long (1.85-1.9 Å) oxo contribution consistent with Pu(V). Particle 2 differs in that fewer shells were required to obtain a quality fit, and the oxo contribution is similar to Pu(VI) due to its comparable distance with the oxo present in uranyl species. This is an unusual result and may indicate a different valence mixture than Particle 1 and the

aforementioned previously studied samples. Ordered PuO_2 has a plutonium-oxygen shell at about 4.47 Å, but on initial data analysis there was a long flat feature in that region extending to 5 Å. When the reference fit was restricted to the k-range of the particles (9.8 k), it also showed this feature, but at slightly higher relative amplitude and shorter into R-space. Detailed analysis showed this feature was a result of a combination of limited k-range along with high frequency noise at the high end of the k range for the particle data. This explained the feature in all spectra, and the length to which it appears in the particle data. Another interesting feature is the non-crystallographic shells extending further into R-space. Even with the limited k-range data, the non-crystallographic shell at 6.5 Å is present for the standard. This feature isn't present in the particles, further indicating more disordered systems.

Uranium EXAFS analysis was performed on Particle 1. The data was quite poor (high noise and limited k-range) and is only compared to that of a highly ordered UO_2 reference collected at 80 K (Figure 77).

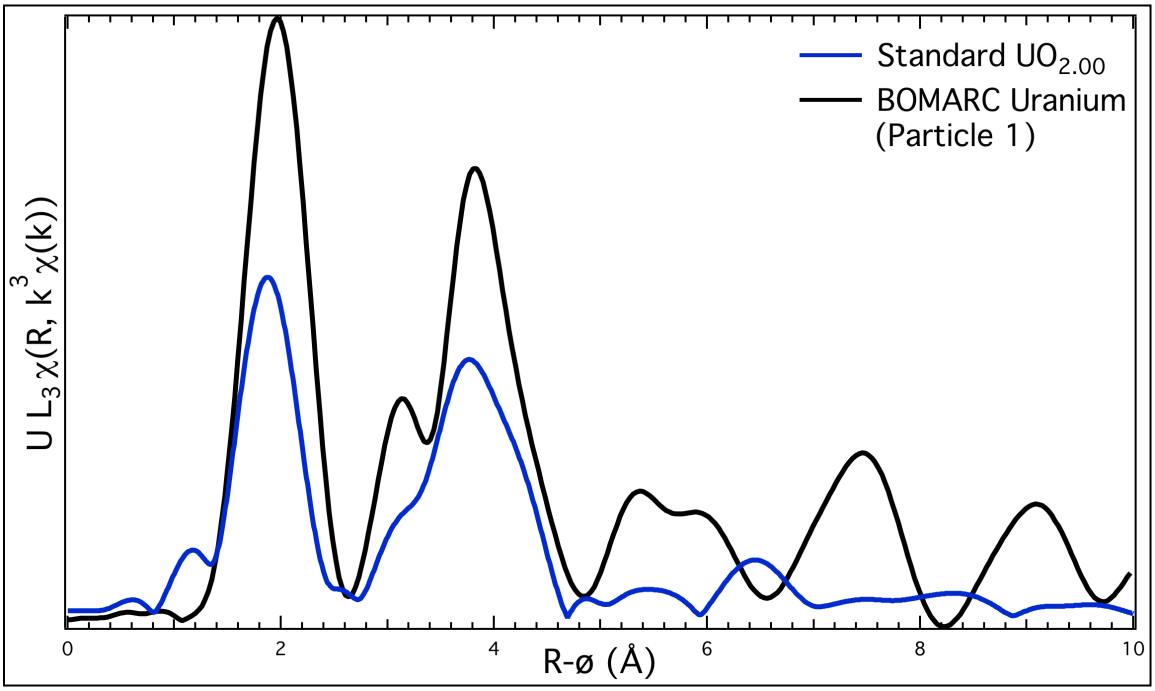

Figure 77. Particle 1 uranium EXAFS compared to an ordered UO_2 spectrum.

Due to limited k-range, a crystal glitch at BL 2-3, large background, and noise in the k-range, this data is somewhat misleading. The limited k-range for the standard eliminated the usual non-crystallographic shells beyond ~4.5 Å other than the one at ~6.5 Å. The other amplitudes beyond that region are most likely noise. Furthermore, the standard matches quite closely to single crystal data (not shown here) in amplitude and structure, but here it is much lower amplitude than the uranium EXAFS of Particle 1. Although high-fired oxides can produce highly ordered systems, the extreme amplitudes and unusual long R-range data reduce overall confidence in the data. The fact that there is no non-crystallographic shell at ~6.5 Å supports this low confidence. However, the distance of the uranium-uranium feature indicates UO_{2+x} species due to the close match with the same shell in the standard. As discussed previously, uranium is easily oxidized and considering the

moisture present both in the fire and in the environment, and the time that the material was exposed to weather, a more highly oxidized uranium species may be expected. The phase seen in the XRD and implied in the EXAFS indicates that the PuO_2 may inhibit the level of uranium oxidation when closely mixed, regardless of how evenly the two are distributed on a surface. This phenomenon has been seen before with both uranium-thorium and uranium-zirconium/carbon[97-101].

Table 21. Summary of results and conclusions from the aforementioned analyses.

Analysis	**Particle 1**	**Particle 2**
XRF	Heterogeneous, two mixing trends, multiple elements	Homogeneous, one mixing trend, multiple elements
XRD	Cubic, more ordered, shifted d-Spacings	Cubic, less ordered, shifted d-spacings
EXAFS	PuO_{2+x}/UO_{2+x}, long oxo, more ordered	PuO_{2+x}/UO_{2+x}, short oxo, less ordered

5.5 Conclusion

Particles are present in the environment in many forms and result from a number of scenarios related to the nuclear fuel cycle and existence of nuclear weapons. One incident involved the fire and dispersal of nuclear material at a BOMARC missile site in New Jersey. Although remediation efforts cleaned up the majority of the contamination, discrete particles remained at some locations around the site. Researchers collected and analyzed some of these particles, which were composed primarily of mixed uranium/plutonium species. Their analyses were extensive and mostly included evaluations related to traditional nuclear forensics. This work sought to analyze some of those particles in order to gain more information on the basic chemistry of uranium and plutonium in a high-

firing/weathering scenario. Furthermore, these analyses sought to gain information on the basis of MFS in order to lay groundwork and establish applications to current nuclear forensics protocols. Previous studies analyzed similar particles both from other sites and the BOMARC site with SEM and μ-XRF among other techniques, but were limited by their setup and scope. In this study, synchrotron-based microfocus techniques including μ-XRF, μ-EXAFS, and μ-XRD were used to investigate two such particles for their surface composition and chemical speciation.

X-ray fluorescence not only aided the μ-EXAFS and μ-XRD analysis process, but also proved its worth in determining source term information. The elemental maps showed two separate trends in elemental mixing. For Particle 1, it was clear that about half of the particle was formed under an extensive mixing of components or recombination after vaporization. The other half consisted of separate domains of both major (plutonium and uranium) and minor (gallium, lead, titanium, and iron) elements, indicating less extensive mixing process allowing for the agglomeration of separate domains. Particle 2 was completely homogeneous with respect to all elements, indicating an extensive mixing process of separate components or complete vaporization followed by recombination. The presence of minor elements and their correlations with each other also provides information on what may have been near the major elements during or after the fire, further yielding forensics information. These observations might allow for interpretations about the materials history including information on the fire, the temperature of the fire, proximity of elements both before and after the fire, and the interaction of elements while in the environment.

X-ray diffraction and EXAFS provided important chemical speciation information. Although the XRD data was fairly weak, it still provided for the determination of crystal structure and makes way for expansion and improvement of the microfocus technique for similar purposes. The EXAFS spectroscopy data yielded information on the chemical speciation of each particle and their differences to reference materials. These analyses concluded that both uranium and plutonium were in a UO_{2+x} or PuO_{2+x} form respectively. For plutonium, both particles were fairly disordered, with Particle 1 being more ordered than Particle 2. This might reflect the mixing possibilities or may lead to information related to how and when the particles were formed. The EXAFS results showed that Particle 1 was similar to previously studied plutonium oxides; it had an oxo bond indicative of Pu(V) contribution and a number of oxygen shells outside of the reference crystallographic region for PuO_2. Particle 2 was somewhat unusual in that it had a shorter oxo bond and fewer oxygen shells required to obtain a quality fit. Although not seen before in PuO_{2+x} species, this might represent a plutonyl contribution to the structure. If the oxo is simply shifted it might result from a weakness in the data. In any case, more work should be conducted on these and similar particles to expand this work for both basic understanding and for nuclear forensics purposes. Uranium EXAFS data was somewhat inconclusive, but was consistent with the UO_{2+x} form. Perhaps the most interesting conclusion from the chemical speciation data is that uranium was in a lower oxidation state, somewhere between UO_2-U_4O_9, even after being exposed to weathering for ~47 years. This is consistent with previous studies, and overall

these results indicate that when uranium is combined with elements with stable lower oxidized chemical, it stabilize uranium in a lower oxidation state.

Overall, this work was successful in demonstrating the utility and limitations of MFS for use in obtaining information related to nuclear forensics applications and basic chemical behavior. Specifically, it showed how it was useful in a scenario where only a small number of hot particles are available. This experiment and others like it at LANL have provided groundwork for how chemical speciation and composition can add to the current nuclear forensics melee in attributing information about nuclear materials history and fate.

CHAPTER 6

Chapter 6: The Effects of Ball-Milling on Uranium Dioxide

6.1 Abstract

The combination of chemical speciation and morphological analysis is ideal for obtaining information related to nuclear forensics because of the signatures they can expose along chemical processing routes. Sample preparation methods have a significant impact on the resulting data from many of these analysis techniques. In this experiment, different treatment methods were applied to uranium dioxide to determine the physicochemical effects on morphology, particle size distribution, the resulting powder X-ray diffraction (pXRD) analysis and extended X-ray absorption fine structure (EXAFS) spectroscopy data quality, and changes in chemical speciation with those techniques. Uranium dioxide was either untreated, ground in a mortar and pestle, or milled in a Wig-L-Bug milling device for different time periods. Samples were then prepared for scanning electron microscopy (SEM), laser scattering particle size distribution analysis, XRD, and EXAFS. Results from laser scattering and SEM analyses highlighted the importance of combining these techniques fur nuclear forensics. Treatments reduced particle size and resulted in lower amplitudes for both pXRD and EXAFS. EXAFS fits were unusual, so more work should be conducted. Based on these results a protocol for the preparation of samples for these techniques is presented.

6.2 Introduction

In order to obtain optimal quality EXAFS spectroscopy data, great care must be taken when preparing samples. For bulk measurements, sample preparation is usually an area in which experimenters have some control. Sample quantity[160, 161], particle size, and distribution homogeneity are key in reducing effects from beam spot/energy heterogeneities and self-absorption effects[162]. A common method is grinding a sample followed by dilution with boron nitride, and finally pressing the sample into a given holder cell[30, 160, 161]. For diffraction, samples are often ground in a mortar and pestle and then spread on a sample holder and affixed in some manner. Morphological analysis with SEM can be prepared similarly. Traditional preparation methods consistently yield high quality data, but if other preparations or protocols yield higher quality results, they should be evaluated. EXAFS, pXRD, and SEM are excellent techniques for analysis of chemical speciation and morphology for nuclear forensics information. Because of their commonality, a protocol should be established to determine an optimal sample preparation for these analysis techniques. In an attempt to do so, UO_2 was prepared and either untreated, ground in a mortar and pestle, or milled in a Wig-L-Bug device for a range of time periods. These samples were then evaluated with the aforementioned techniques to study effects on particle size distribution, quality of data, and changes in chemical speciation due to heating caused by the Wig-L-Bug device or exposure to air during the preparation.

6.3 Experimental

6.3.1 Synthesis and Wig-L-Bug Procedure

Uranyl peroxide was precipitated from UO_2Cl_2 in solution at a pH of 3.0 (maximum) as outlined in Section 2.2.4. The solution was allowed to equilibrate for about half an hour before filtration. The resulting uranyl peroxide, UO_2O_2, was dried under vacuum and then heated at 100 °C for two hours. The dried material was synthesized to amorphous uranium trioxide (A-UO3) and then to UO_2 as outlined in Section 2.2.5. After slowly cooling under hydrogen gas and allowed to equilibrate with atmosphere, the sample was divided into five 350 mg quantities. The first quantity was not treated at all. One quantity was ground for 5 minutes in a mortar and pestle. The remaining three quantities were each placed in a stainless steel Wig-L-Bug cell with a 3/8" polystyrene bead and milled in the instrument for 5, 30, and 60 minutes. Material from each quantity was set aside for analysis: 250 mg for laser scattering particle size distribution analysis, 10 mg for pXRD, 10 mg for EXAFS, and a very small amount for SEM.

6.3.2 Laser Scattering Particle Size Distribution

Material (250 mg) from each quantity was placed in an ethylene glycol bath connected to the Horiba LA-950 instrument. This instrument cycles the ethylene glycol-sample mix through the laser scattering and ultrasound stages which breaks up particle aggregates after each pass until an asymptote in size is reached and the particles have the same size distribution after each pass. The size as a function of time under sonication, the final distribution, and final size are reported.

6.3.3 SEM

A small amount of material from each quantity was poured onto a carbon tape-backed SEM stub. Backscatter and secondary electron images were obtained with a FEI Quanta 200F field emission scanning electron microscope. Images were taken at magnifications ranging from ~200x to 25000x.

6.3.4 pXRD

Approximately 10 mg of each quantity was poured over a grease-coated pXRD holder. Excess material was removed and this was repeated until an even layer remained on the grease. Spray adhesive was applied to affix the samples in place. Data was collected on a Bruker D8 Advance using unconditioned copper radiation, and a 1-D silicon strip detector (Lynxeye). Qualitative analysis, including measurement of crystallite sizes was performed using Jade software[137], and the International Center for Diffraction Data (ICDD) powder data files[138].

6.3.5 EXAFS

Approximately 10 mg of each quantity was placed in a Wig-L-Bug cell with about 60 mg boron trinitride and milled for 5 minutes. The material was then pressed into EXAFS spectroscopy sample holders for analysis at Beamline 11-2 at the Stanford Synchrotron Radiation Lightsource. Data collection and analysis were performed as outlined in Section 2.4.2.

6.4 Results

6.4.1 Particle Size Distribution

The initial particle size from large to small, before any sonication, was 60 minutes milling, 30 minutes milling, no treatment, 5 minutes milling, and 5 minutes grinding. It took 5 to 25 minutes of sonication to reach a final particle size for each sample (Figure 78). From large to small the final particle size was ordered no treatment, grinding, 5 minutes milling, and 30/60 minutes milling. This final size and distribution are provided (Figure 79). Starting material (UO_2O_2) characteristics can range depending on the conditions under which it is precipitated. The technician familiar with the laser scattering analysis noted that this UO_2 did not require a long sonication time compared to other uranium oxides. This might indicate that the starting material was a finer precipitate than other preparations. Distribution size is difficult to discern from this data (and logarithmic plot), but the samples with smaller mean size have narrower distributions (with the exception being untreated UO_2). The results are summarized in Table 22. It should be noted that the software accompanying the Horiba instrument does not provide error for many of the measurements it takes.

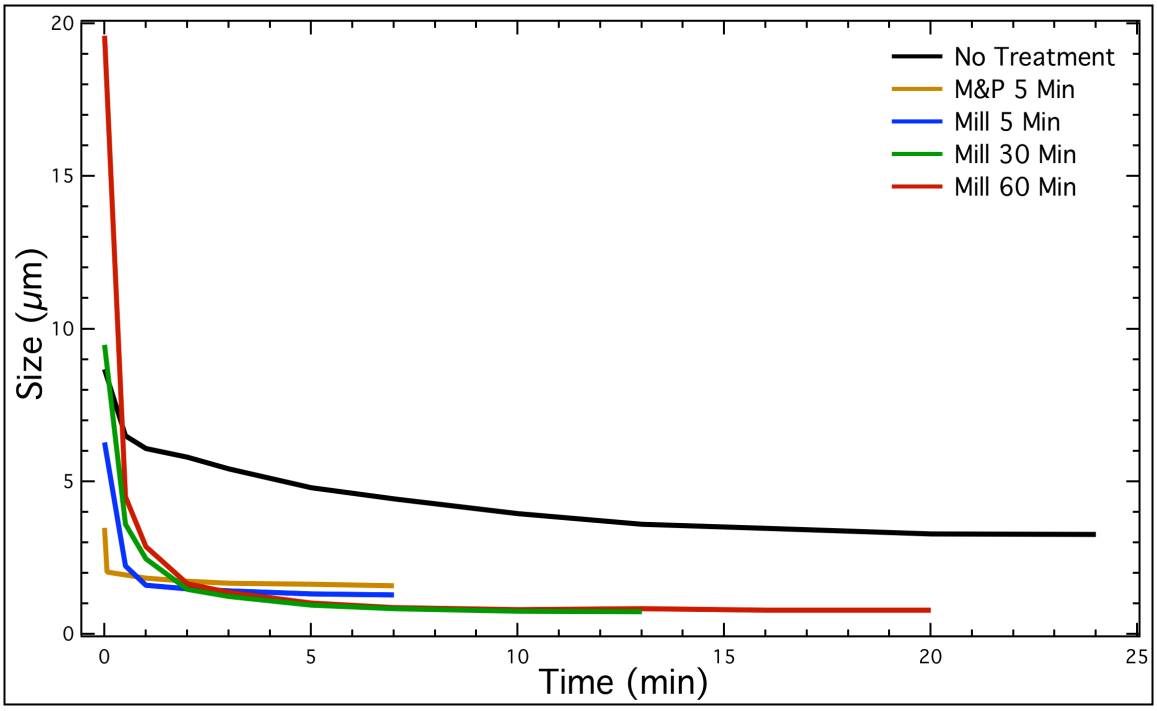

Figure 78. Particle size as a function of time under sonication for each quantity. The quantity treated with the mortar and pestle is denoted "M&P" and the ones treated with the Wig-L-Bug are denoted "Mill".

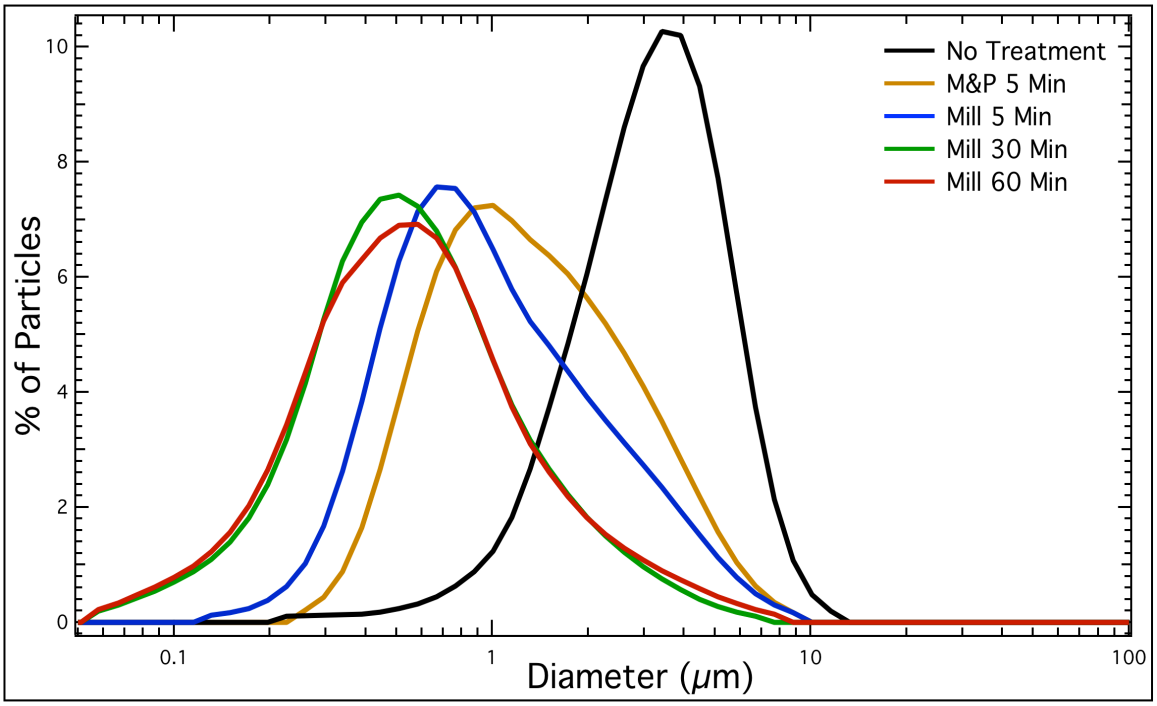

Figure 79. Final particle size distributions for each sample.

Table 22. Final size and time to reach that size for each sample errors were not obtained from the analysis.

Treatment	Final Mean Size (μm)	Time (Min)
None	3.272	24
Grind 5 Min	1.583	7
Mill 5 Min	1.277	7
Mill 30 Min	0.733	13
Mill 60 Min	0.780	20

6.4.2 Morphology

Scanning electron microscopy images were taken at x200, x1000, x15000, and x25000 magnification for all samples. Images at x5000 were taken for the ground sample and all milled samples. There doesn't appear to by any change in morphology over the different treatments and times. However, these images do support the laser scattering results in that the smallest units are forming into larger aggregates the longer they are milled. From these results, it is not clear why.

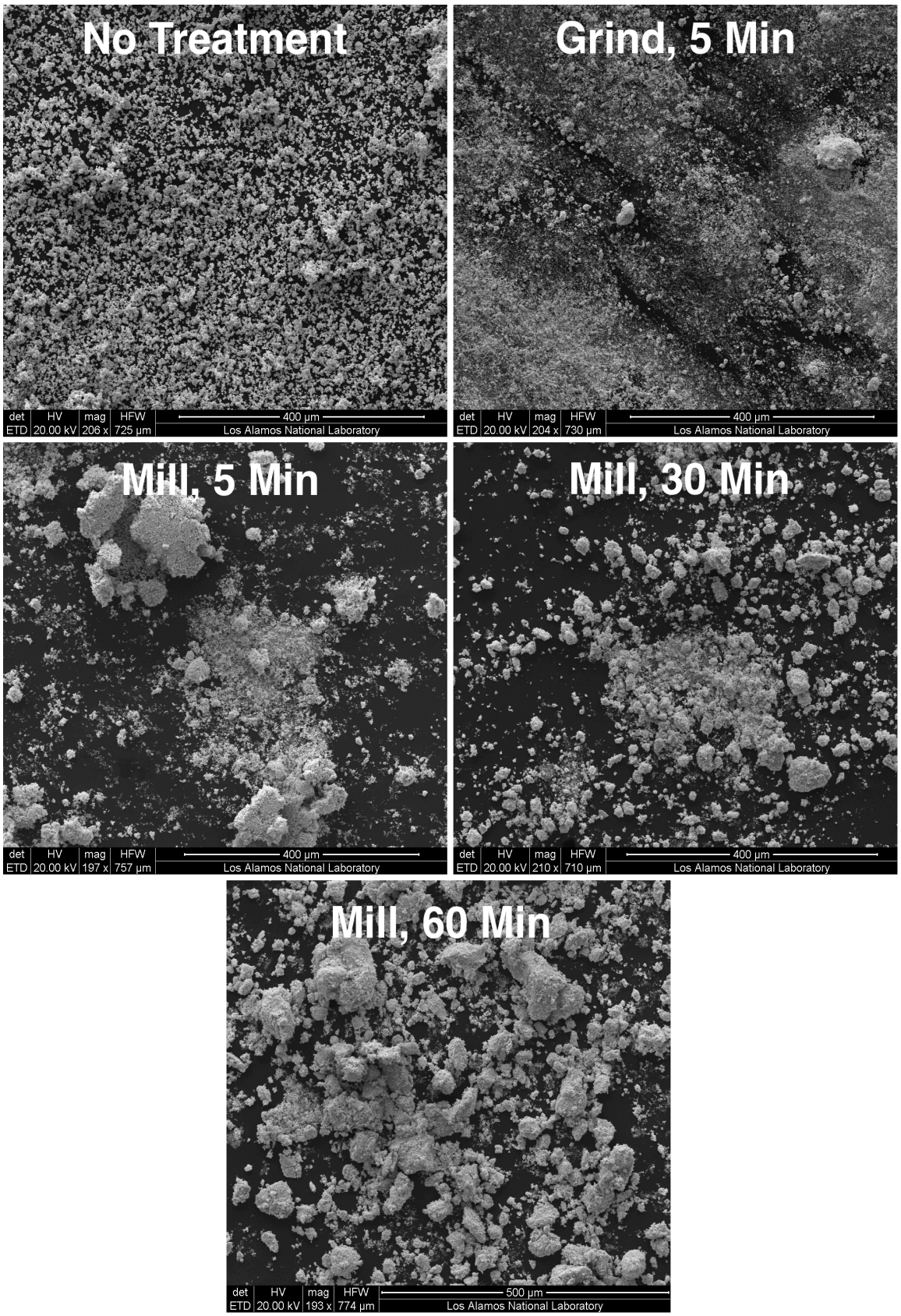

Figure 80. SEM images of all samples taken at x200 magnification.

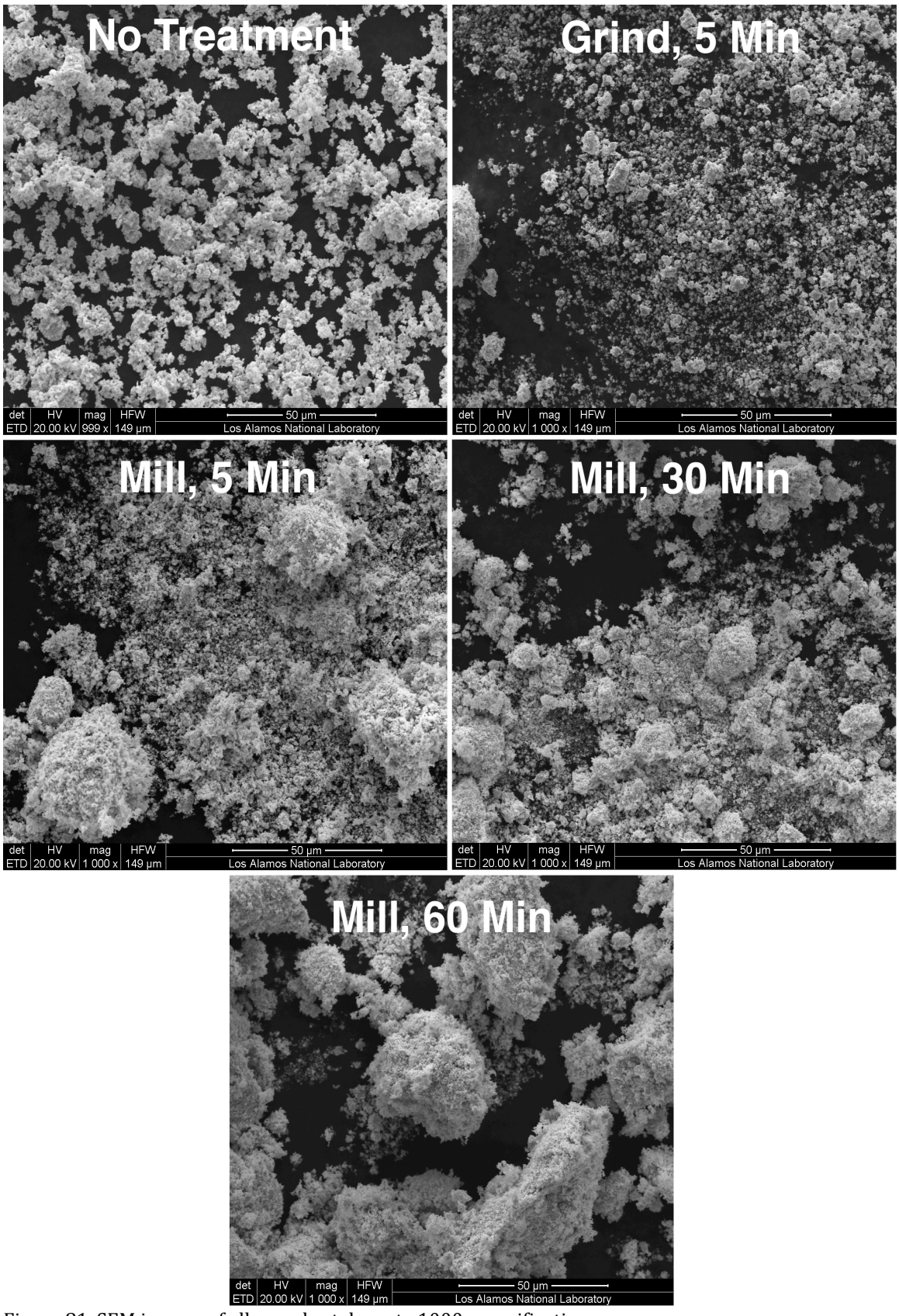

Figure 81. SEM images of all samples taken at x1000 magnification.

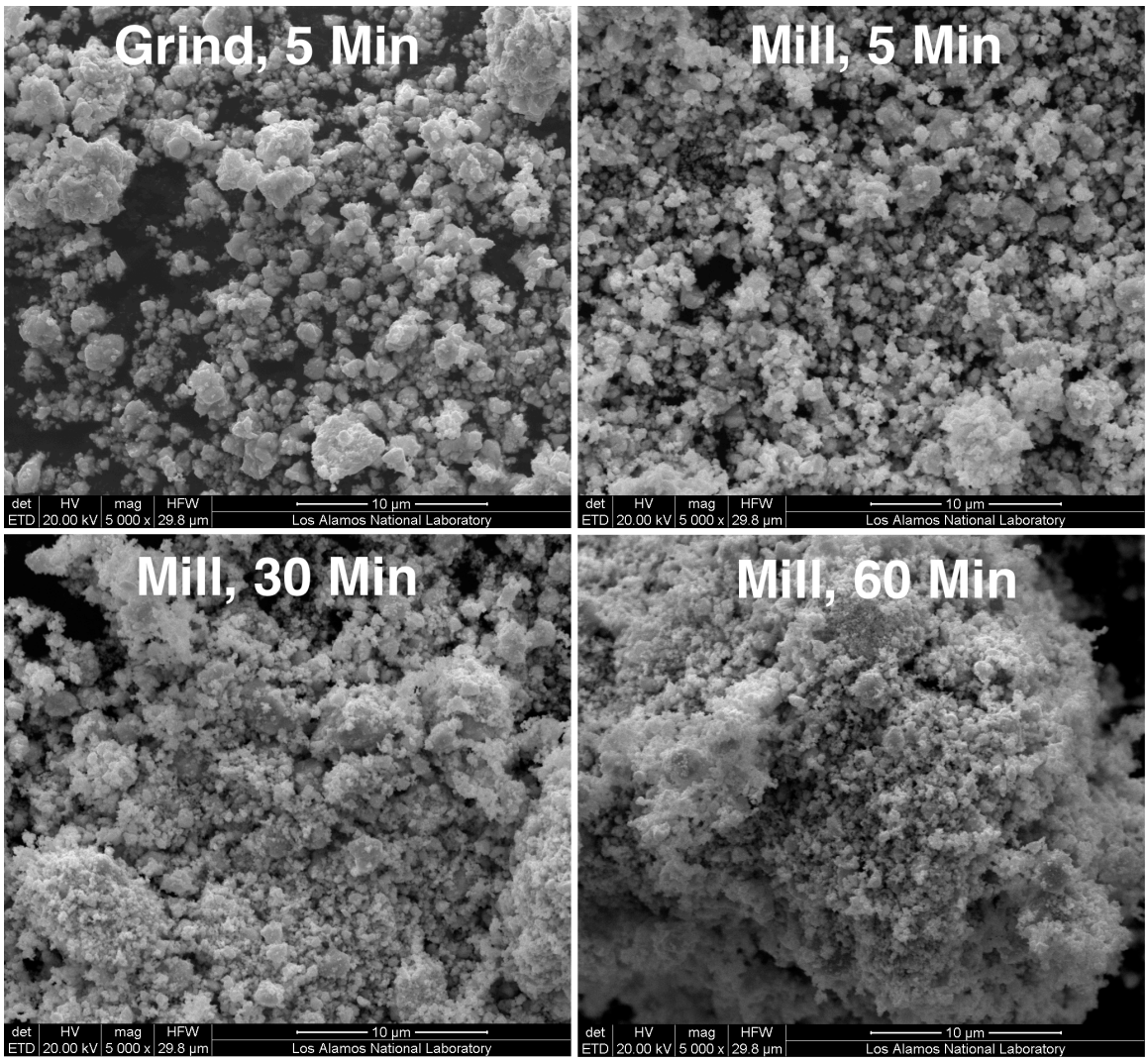

Figure 82. SEM images of all treated samples taken at x5000 magnification.

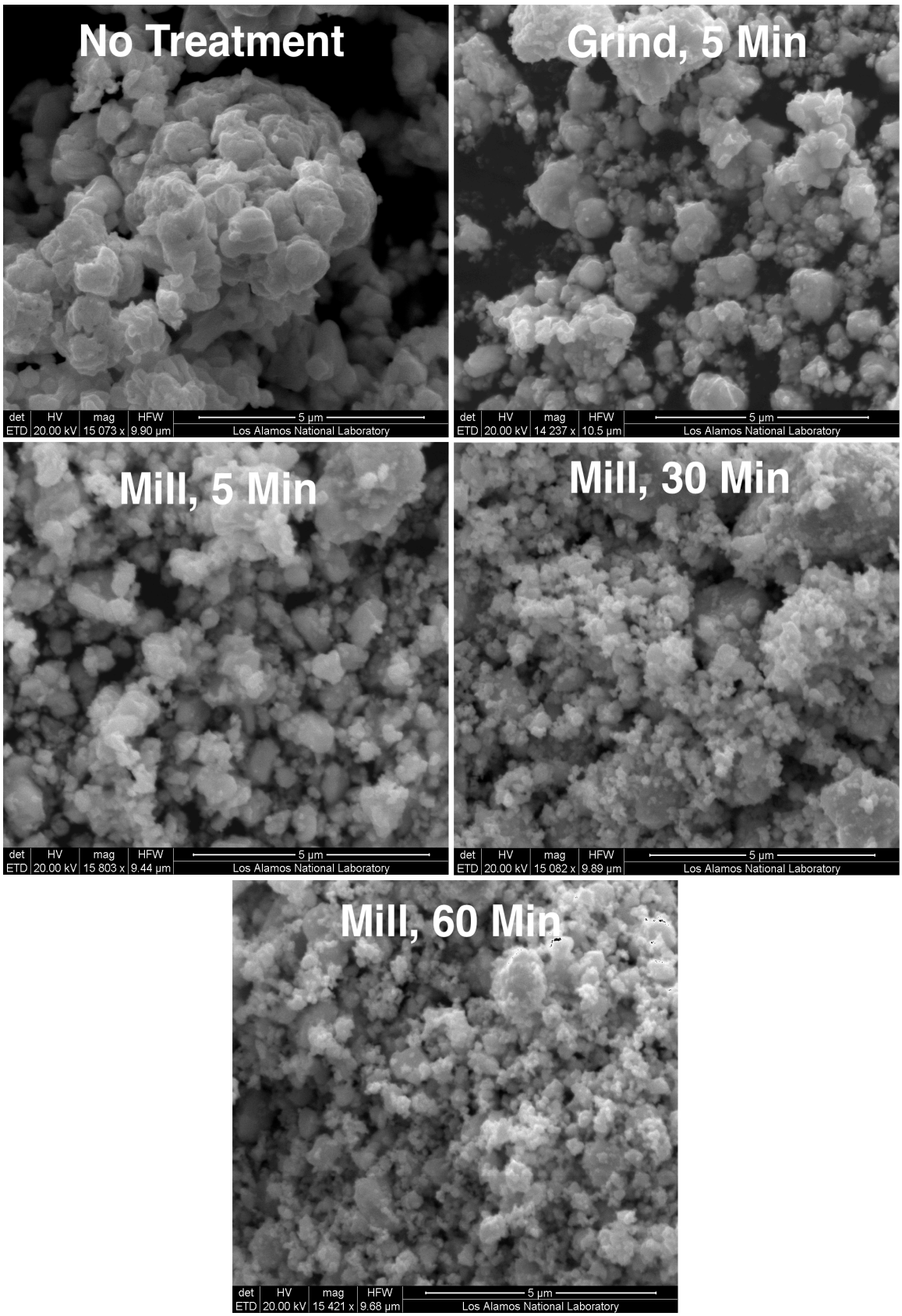

Figure 83. SEM images of all samples taken at x15000 magnification.

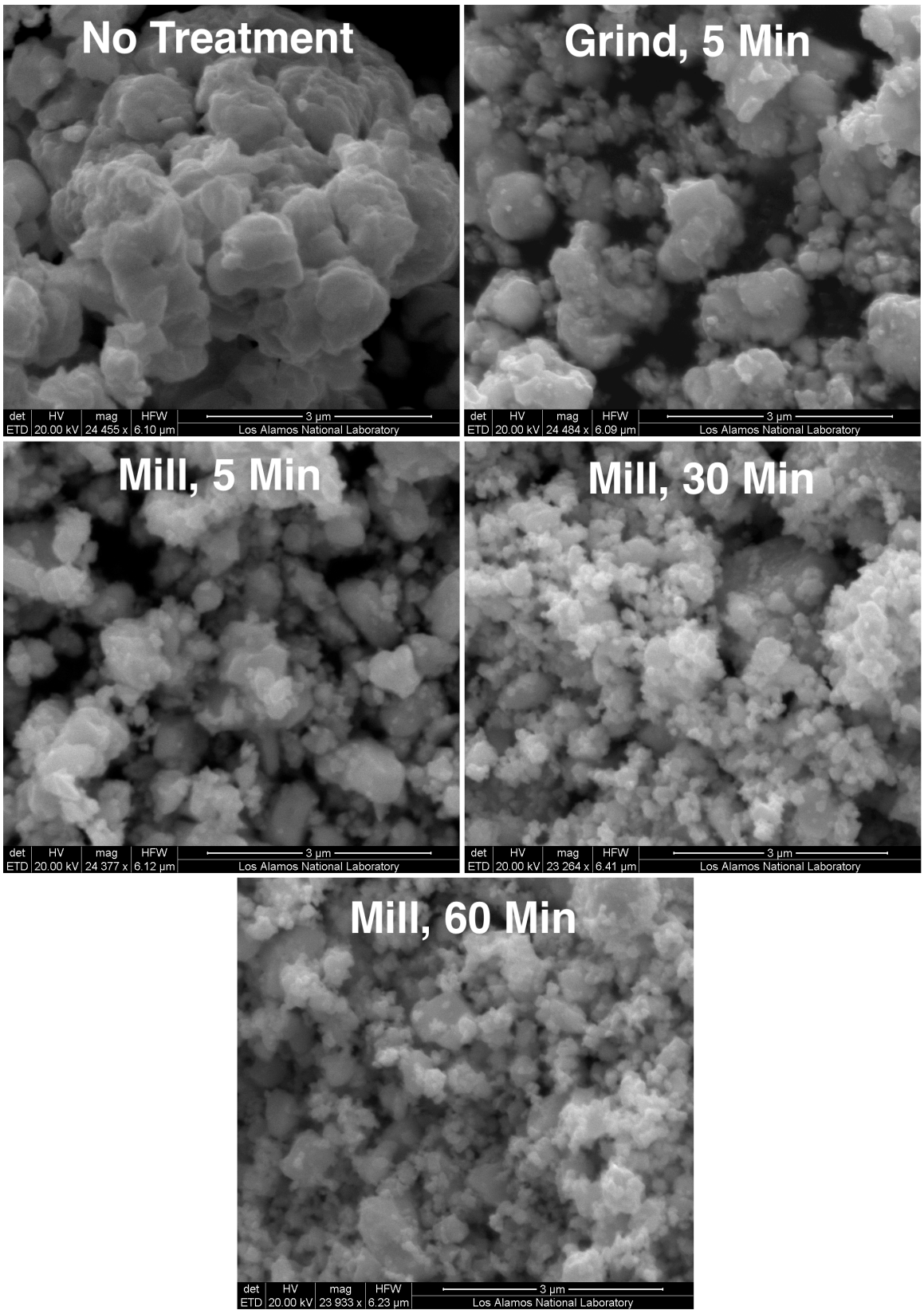

Figure 84. SEM images of all samples taken at x25000 magnification.

6.4.3 pXRD Analysis

The pXRD patterns and reference lines for UO_2 are shown in Figure 85. It's difficult to discern differences between quantities at the scaling shown, so individual peaks are also shown (Figure 86). Peaks are shifted higher in angle (~1°) than the reference peaks, but the sample milled for 60 minutes is closest. The holders used did not have a sample divot (the instrument normally uses a holder with a divot which lowers the sample relative to the X-ray source and detector), explaining the peak shifts. There is trend of decreasing intensity as a function of treatment. In a given sample, a number of factors affect the intensity of peaks, specifically the amount of material used, crystallite size, level of order, and oxidation. Finally, the crystallite sizes[163] for two planes (Figure 87) decrease as a function of treatment. There are two unidentified peaks in all samples at 54° and 59°. The trends and source of contamination will be addressed further in Section 6.5.

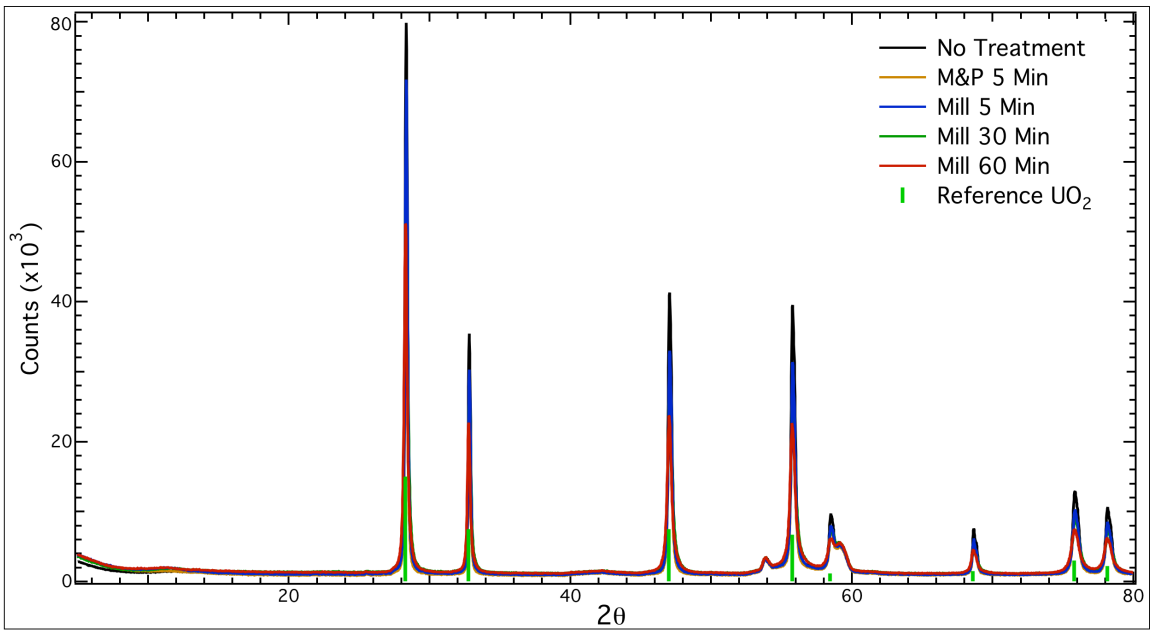

Figure 85. pXRD patterns for all samples and literature lines and intensities for crystallographic UO_2.

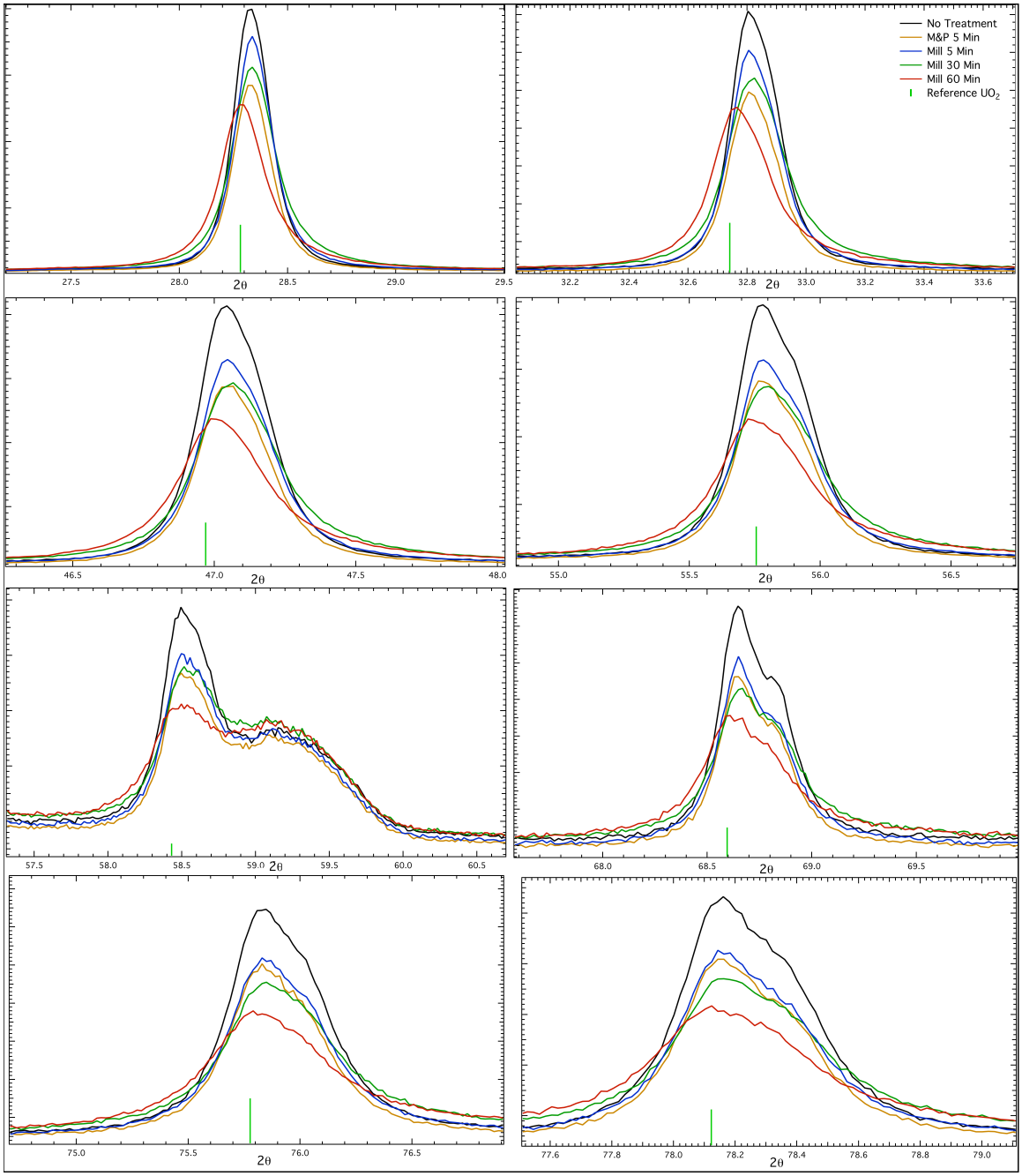

Figure 86. The major peaks of the UO_2 spectra expanded for comparison. The y-axis units are number of counts for each peak.

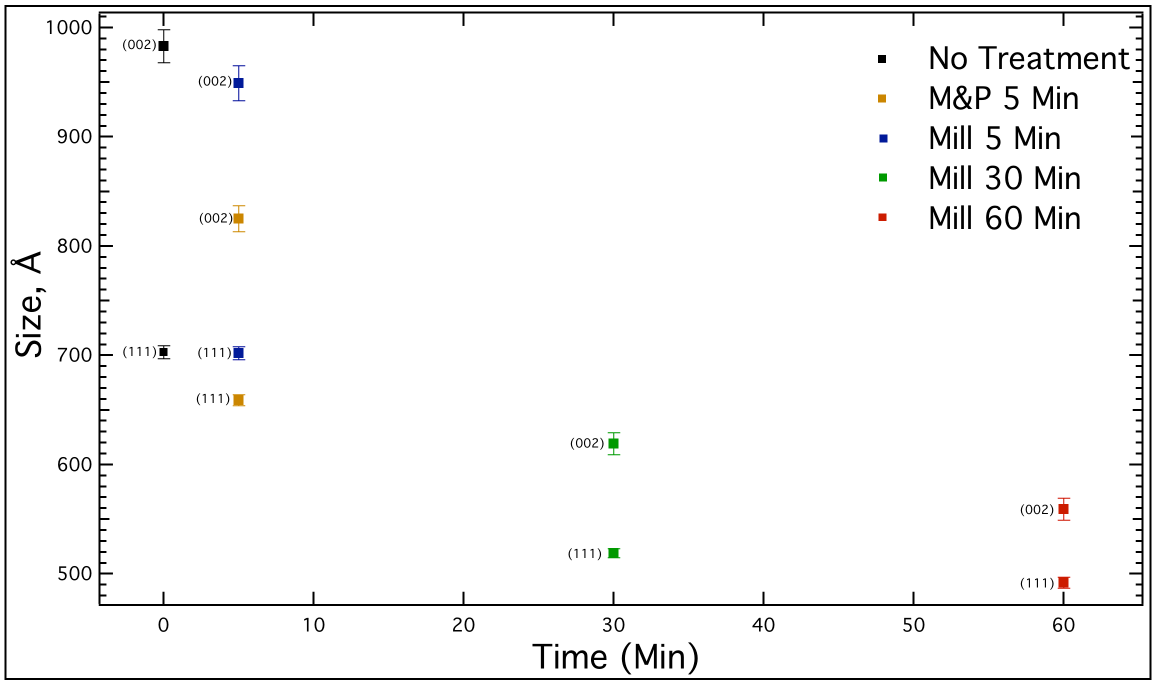

Figure 87. Crystallite sizes for the (111) and (002) planes.

6.4.4 EXAFS Spectroscopy

Uranium EXAFS were taken for each sample in the range 3.0-14.2 k. The EXAFS, curve fitting results, and shell contributions for each sample are reported (Figure 88 through Figure 92). To simplify comparisons, only the region from 1.7-4.7 Å was fitted. A Fourier transform overlay for all samples, including the imaginary contributions is also provided (Figure 93). These overlays were quite close except for in the nearest-neighbor oxygen region (Figure 94). All data except the sample milled for 5 minutes were obtained from fluorescence. The fluorescence for the sample milled for 5 minutes had abnormalities from a crystal glitch and noise at higher k. The transmission data for all samples produced unusual fitting results.

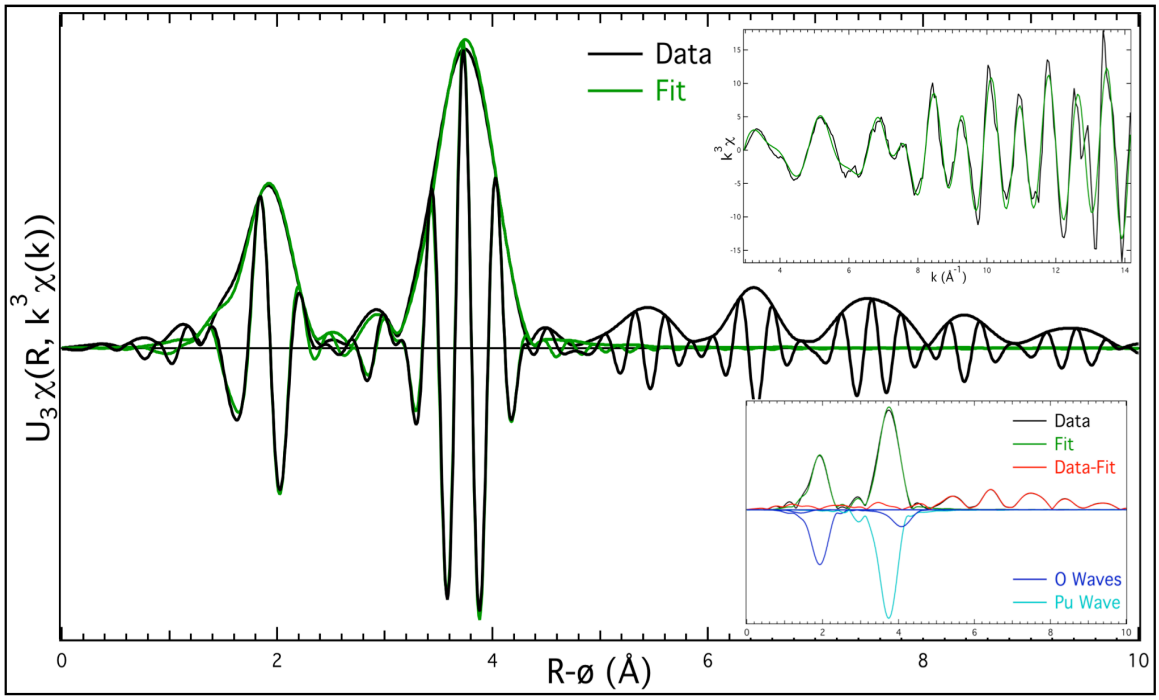

Figure 88. Uranium L_{III} EXAFS spectrum from for untreated UO_2 standard (3.0-14.2 k). Data is shown in black and the curve-fits in green. $k^3\chi$ plots are shown in the upper inset and individual shell contributions on the lower inset.

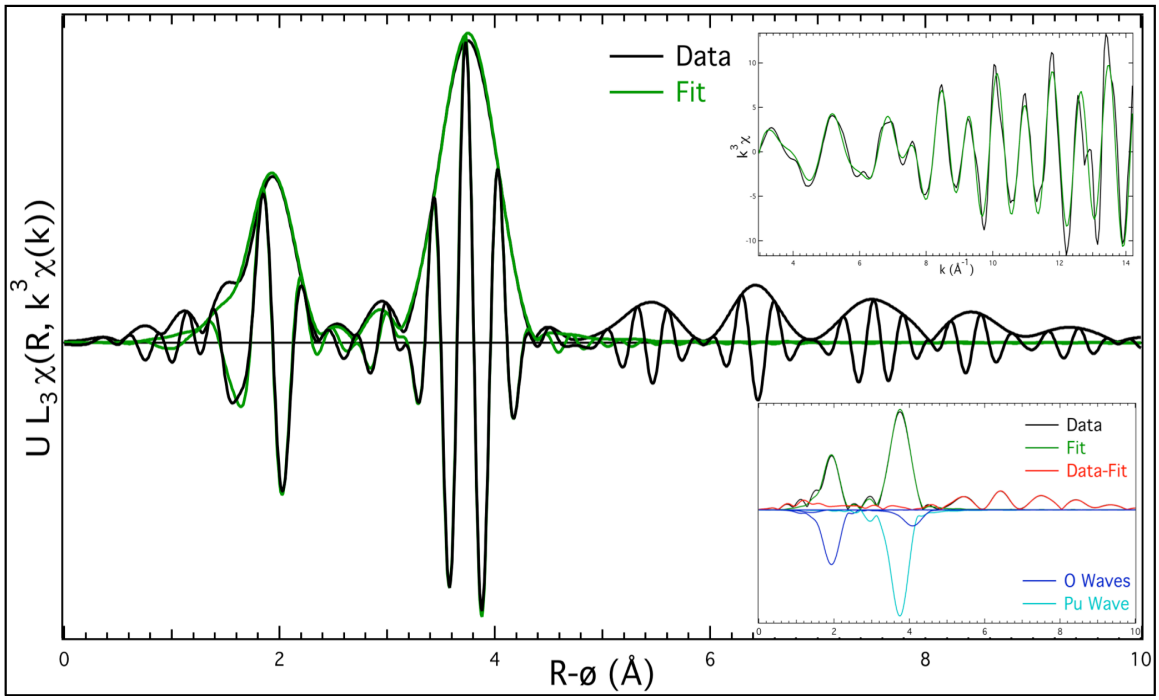

Figure 89. Uranium L_{III} EXAFS spectrum from for ground UO_2 sample (3.0-14.2 k). Data is shown in black and the curve-fits in green. $k^3\chi$ plots are shown in the upper inset and individual shell contributions on the lower inset.

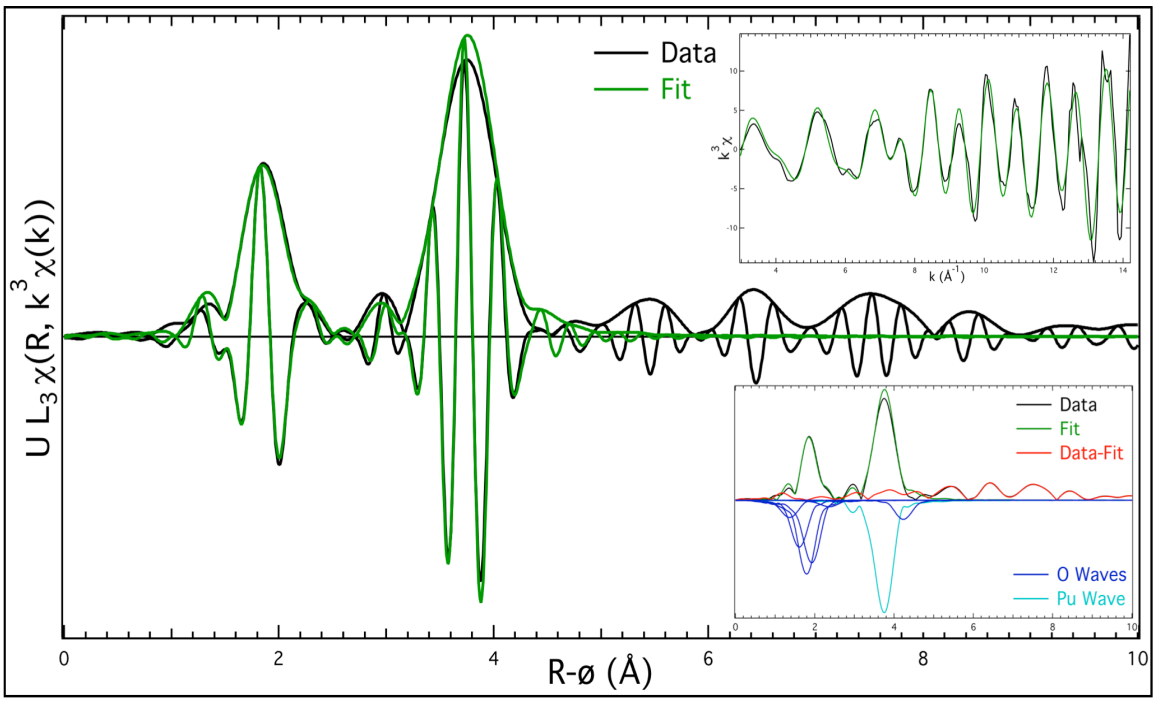

Figure 90. Uranium L_{III} EXAFS spectrum from for UO_2 sample milled for 5 minutes (3.0-14.2 k). Data is shown in black and the curve-fits in green. $k^3\chi$ plots are shown in the upper inset and individual shell contributions on the lower inset.

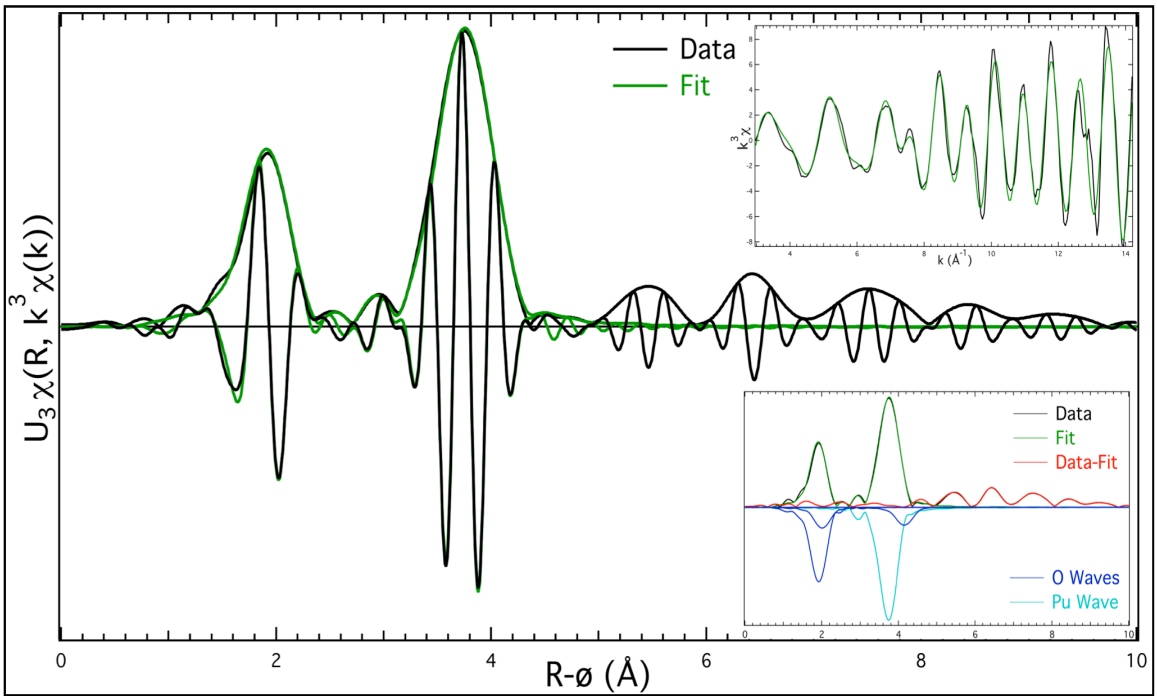

Figure 91. Uranium L_{III} EXAFS spectrum from for UO_2 sample milled for 30 minutes (3.0-14.2 k). Data is shown in black and the curve-fits in green. $k^3\chi$ plots are shown in the upper inset and individual shell contributions on the lower inset.

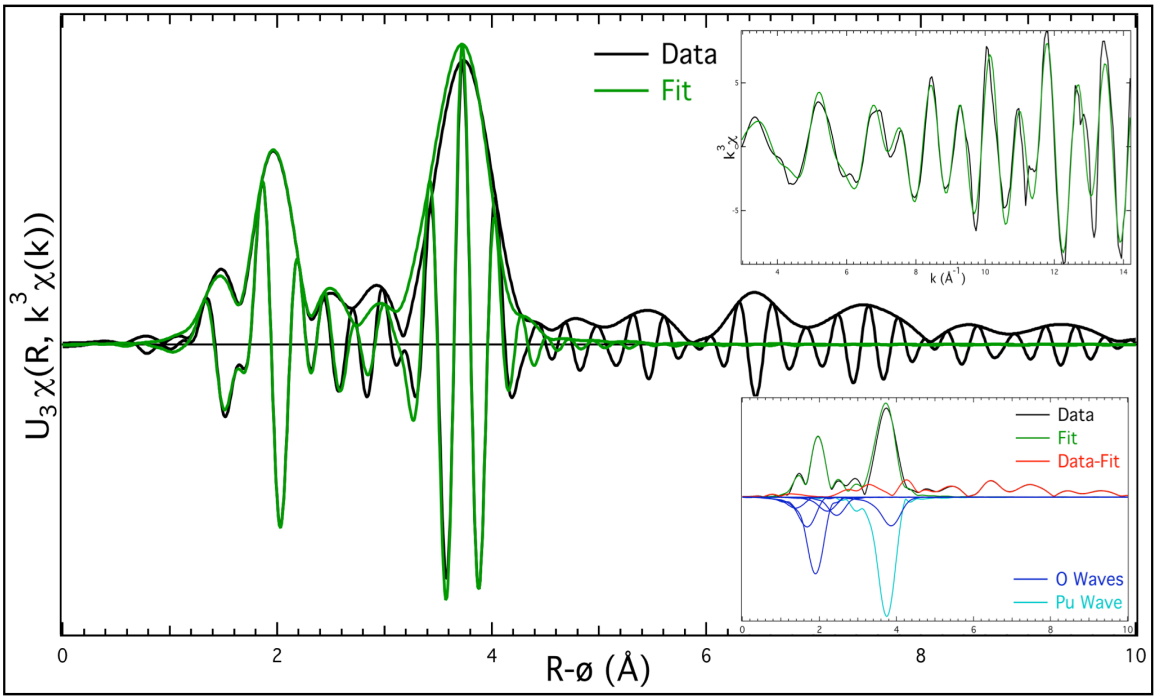

Figure 92. Uranium L_{III} EXAFS spectrum from for UO_2 sample milled for sixty minutes (3.0-14.2 k). Data is shown in black and the curve-fits in green. $k^3\chi$ plots are shown in the upper inset and individual shell contributions on the lower inset.

Table 23. Curve fits results for all samples including shells fitted, number of atoms, and the Debye-Waller factor, σ.

Sample	Shell	Distance (Å)	Atoms	σ
$UO_{2.00}$	O	1.853 (0.017)	0.148 (0.048)	0.042 (0.011)
	O	2.354 (0.021)	5.981 (1.736)	0.062 (0.024)
	U	3.869 (0.011)	10.689 (2.691)	.052 (0.009)
	O	4.539 (0.026)	22.970 (7.216)	0.092 (0.013)
Grind, 5 Min	O	1.840 (0.015)	0.190 (0.063)	0.082 (0.002)
	U	2.356 (0.021)	4.898 (1.402)	0.062 (0.023)
	O	3.871 (0.010)	8.545 (2.107)	0.052 (0.009)
	O	4.540 (0.025)	18.068 (5.641)	0.092 (0.014)
Mill, 5 Min	O	1.811 (0.020)	0.847 (0.268)	0.060 (0.026)
	O	2.040 (0.017)	2.303 (0.691)	0.040 (0.053)
	O	2.234 (0.016)	4.541 (1.265)	0.040 (0.022)
	O	2.369 (0.019)	5.768 (1.640)	0.060 (0.017)
	O	2.822 (0.028)	1.321 (0.419)	0.080 (0.039)
	U	3.871 (0.010)	8.684 (2.151)	0.050 (0.010)
	O	4.621 (0.017)	9.300 (2.907)	0.050 (0.144)
Mill, 30 Min	O	2.342 (0.018)	3.902 (1.051)	0.056 (0.018)
	O	2.448 (0.018)	1.070 (0.334)	0.040 (0.023)
	U	3.870 (0.010)	5.341 (1.260)	0.046 (0.009)
	O	4.575 (0.021)	8.419 (2.629)	0.071 (0.019)
Mill, 60 Min	O	1.842 (0.023)	0.675 (0.213)	0.080 (0.173)
	O	2.142 (0.023)	2.489 (0.747)	0.076 (0.020)
	O	2.345 (0.018)	5.815 (1.547)	0.060 (0.017)
	O	2.654 (0.023)	1.766 (0.555)	0.075 (0.015)
	O	2.886 (0.018)	1.894 (0.589)	0.050 (0.014)
	U	3.869 (0.011)	12.122 (2.917)	0.070 (0.007)
	O	4.386 (0.023)	26.945 (8.084)	0.090 (0.019)

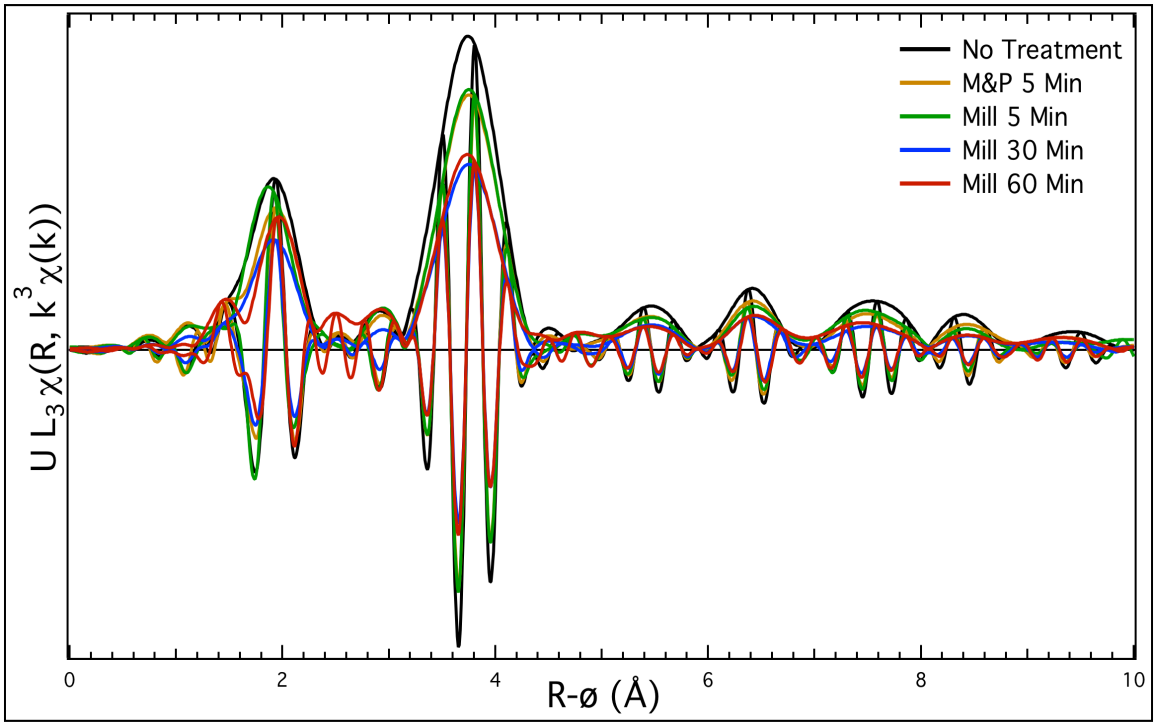

Figure 93. Overlay of the EXAFS spectra of for all samples (3.0-14.2 k).

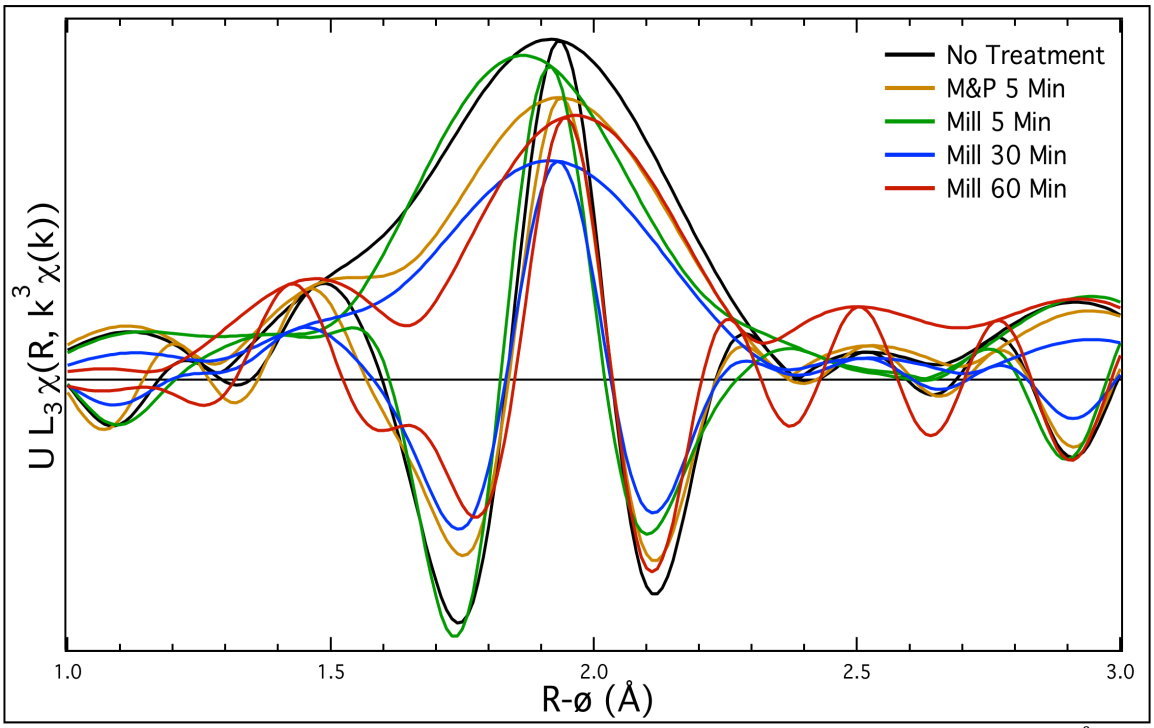

Figure 94. Overlay of the EXAFS spectra of for all samples for only the oxygen region of 1.0-3.0 Å (3.0-14.2 k).

6.5 Discussion

The results from laser scattering analysis and SEM support several outcomes from milling in the Wig-L-Bug. First, the final particle size decreases as a function of treatment time, reaching an ending point around half an hour. Trials with more data points should be conducted in order to gauge how long this might take for a given setup. Second, smaller particles tend to form larger aggregates as the milling time increases. The starting particle size before sonication and the large aggregates seen in the longer milling times from the SEM support this. Finally, longer milling time creates a larger particle size distribution. Again, this reached an endpoint around half an hour. The sample from the mortar and pestle treatment had the smallest starting particle size before sonication and was comparable to the 5 minute milled sample in final particle size and time to reach final particle size. However, at higher magnification the SEM images seem to indicate that there is more variability in particle size for the mortar and pestle sample, but morphology is only qualitative for this experiment and one imaging area is not representative of the entire sample. Furthermore, this is not supported by the laser scattering results. Even though aggregate formation was noticeable over time from the SEM analysis, aggregates in an unknown sample might be harder to differentiate from base particle size. Because of this, care must be taken in analyzing samples when only SEM is performed to study particle size. Optimally, these two techniques should be combined in order to obtain the most information on particle size, aggregate size, and distribution.

X-ray diffraction analysis indicates highly ordered UO_2 with a contaminant present in all samples (the peaks at 54° and 59°). The origin of the unidentified peaks is unknown. The uranium source material was not purified with column chromatography, but based on other experiments using the same material, was not unusually contaminated. It is possible that the sample holders were the source of contamination due to inadequate cleaning. In any case there is not enough information to determine the source of those peaks. The very slight peak shifts result from the use of flat sample holders. It's difficult to determine if sample preparation or a difference in chemical speciation was the cause of the difference for the sample milled for 60 minutes. The crystallite sizes are consistent with the decreasing particle sizes, but this might also indicate disordering of the material or oxidation. Due to these possibilities, it's difficult to draw conclusions based on crystallite sizes in this type of an experiment.

The EXAFS results were unusual. Crystallographic UO_2 should only have three shells (uranium-oxygen shells at ~2.37 Å and ~4.53 Å and a ~3.87 Å). All samples in this case had at least four, with the most common fourth being a relatively longer uranium-oxo bond distance at ~1.8 Å. This may indicate slight oxidation, but this shell is often present in samples of pure stoichiometric $UO_{2.00}$ (i.e. single crystal) that have been exposed to atmosphere for only a short time. Comparison to aqueous tetravalent actinide species may help determine if this is truly a result of sample oxidation or some phenomenon resulting from EXAFS spectroscopy. In order to obtain a quality fit on the quantity milled for 30 minutes, the oxo shell was removed; when it was introduced the fit of other shells were drastically changed. Even so, its

presence in the transform is still apparent. Overall the fits diverged significantly. Some quantities only required four total shells to obtain a quality fit, while others required up to seven shells. Due to these inconsistent and unusual fitting results, comparing them is difficult. However, the Fourier transform overlay in Figure 93 does provide for a few trend observations. The peak amplitude for both the ~2.37 Å and ~3.87 Å shells decreases as a function of milling, with the quantities treated for 5 minutes (both the one ground in the mortar and pestle and the one milled) being very similar. Furthermore, the overlays of the Fourier transforms show the quantities are quite similar in the uranium-uranium region, the non-crystallographic region, and only slightly different in the nearest-neighbor oxygen region. The only sample that was significantly different from the standard was the quantity milled for 60 minutes. This is apparent in the zoomed in overlay in Figure 94 and the fitting results in Table 23. The quantity milled for 5 minutes also required seven shells to reach a quality fit, but as noted in the results section, this was taken from transmission data as opposed to fluorescence for the other samples. The oxygen region is slightly shifted. This shift and the unusual fitting results may result from abnormalities in the beam, poor sample preparation (inconsistent mass used, contaminants, or errors in sample pressing), imposed spline subtractions similar to the other samples, or because spline subtractions differed slightly.

6.6 Conclusion

In this experiment two treatments on UO_2 were used to determine questions related to particle size distribution, morphology, particle damage, and resulting

pXRD and EXAFS spectroscopy data quality. One sample was ground for five minutes in a mortar and pestle, and other samples were milled in a Wig-L-Bug for 5, 30, and 60 minutes. Milling the samples resulted in a consistent trend in particle size (decreasing as a function of treatment time) and distribution, seen both by the SEM and laser scattering results. It is difficult to gauge particle damage, but it was not apparent any of the treatments caused this. X-ray diffraction of the samples indicated decreased crystallite size, increased disorder, oxidation, or some combination. Results from EXAFS spectroscopy were difficult to compare, but treatments decreased shell amplitudes. This could be due to oxidation or some other disordering mechanism. This setup should be modified to keep the samples cool and under an inert gas to ensure as little oxidation during sample preparations as possible.

More work should be performed in order to determine optimal sample preparation for these methods and across the different types of materials encountered in environmental and interdiction scenarios. For basic studies on particle size, aggregate size, and distribution, laser scattering particle size analysis and SEM should be combined for a complete picture on these parameters. For ordered samples (i.e. prepared under laboratory conditions under a well established method), pXRD preparation is less important. For EXAFS spectroscopy, a more consistent preparation should be performed to study the effects these treatments have on data quality. Furthermore, more analysis of fitting results not perfectly consistent with stoichiometric crystallographic UO_2 should be performed in order to determine if these results are related to sample oxidation or result from EXAFS

spectroscopy analysis. Overall it should be kept in mind that when encountering real world samples, the less materials are treated for sample preparations, the more they will represent the true nature of the materials. This experiment will be repeated with a purified UO_2 starting material. More milling times, smaller polystyrene beads, and different numbers of beads will be used in the next experiment. Finally, the next experiment will include an analysis with boron trinitride in order to determine mixing consistency and the effects milling with this material has on EXAFS spectroscopy results.

CHAPTER 7

CONCLUSIONS AND FUTURE WORK

7.1 Summaries and Conclusion

Common analytical techniques have been integrated to evaluate the utility in their use for nuclear forensics analyses and lay groundwork for their application to nuclear forensics protocols. This area, called molecular forensic science (MFS), seeks to aid nuclear forensics investigations by determining chemical speciation, morphology, trace content, and related information in order to gain knowledge on the origin, processing history, intent, and storage conditions of nuclear materials. The efficacy of the application of these techniques relies upon their ability to answer questions related to nuclear forensics, i.e. who made it, where was it made, where was it stored, how old is it? Although the main focus of this work was basic research and development into the application of techniques to gain nuclear forensics information, a secondary goal was to advance knowledge in areas related to the basic chemical behavior of actinides, specifically uranium and plutonium. To perform these evaluations, a number of experiments were performed including an analysis of bulk uranium dioxide aging, particle analysis of a heterogeneous sample, particle analysis of mixed uranium/plutonium particles from an accident site, and analysis of a preparation method for some of the characterizations common in MFS. This work has shown how MFS can aid in answering questions pertinent to nuclear forensics and has expanded the basic understanding of uranium and plutonium chemistry. Perhaps more importantly, these experiments opened up many new possibilities for future efforts in MFS.

The chemistry of actinide oxides is quite complex. Uranium dioxide is fairly open to oxidation and favors a uranyl oxy-hydroxide endpoint, while PuO_{2+x} is the favored endpoint under most conditions for plutonium. How these oxides reach their endpoint, how fast, and what mechanisms they follow are still not understood with high certainty. To evaluate MFS for the aging of an important set of nuclear materials, uranium oxides, UO_2 was aged under four conditions mimicking a range of common climates (specific temperature and humidity for both). Samples were analyzed at various time periods with pXRD and EXAFS spectroscopy to study changes in chemical speciation, structure, and growth of oxidized species. Analysis with EXAFS spectroscopy showed that all aged samples had similar trends in oxidation including the growth of a multisite oxygen distribution most dominant below ~2.3 Å and a consistent disordering of the uranium-uranium bond. Although pXRD showed that $UO_3 \cdot 2H_2O$ was the only species growing over time, EXAFS data did not show any growth of that species, other than the aforementioned multisite oxygen distribution. This is an important result because it highlights the complementarity of pXRD and EXAFS spectroscopy in these studies. Furthermore, the fact that a uranium-uranium bond indicative of UO_2 remains in the EXAFS even after significant disordering is a critical piece of forensics information. For example, if a sample is interdicted and analysis with XRD shows an oxidized species, investigators might end the chemical analysis there. However, if EXAFS spectroscopy is also performed, it might indicate the starting material based on the local structure. Analysis of the EXAFS data alone did not indicate separate mechanisms for each aging condition, but the combination of pXRD did imply

different mechanisms. For example, although the HHLT and LHLT samples have nearly identical order in the uranium-uranium bond over time, the HHLT sample grew in significantly more ordered $UO_3 \cdot 2H_2O$ based on pXRD results. In addition, it was clear that the lower the temperature, the less effect humidity has on uranium dioxide. This was an important experiment in laying down groundwork and establishing protocols for MFS analyses. Uranium dioxide is an obvious place to start due to its fairly rapid oxidation and commonality in the nuclear fuel cycle and weapons production. Although the experiment expanded knowledge of uranium aging and underscored areas in which forensics information can be obtained from these analyses, determining aging conditions or aging time might be overly optimistic for nuclear forensics investigations. Even so, the simple trends observed from this study leave that possibility open for future investigations.

In the realm of nuclear forensics, questions over bulk versus particle analysis have been identified as an area of importance. Although bulk measurements give a representative average of information, analysis of particles gives a more complete picture of a given scenario. Depending on the number of particles analyzed, their results may not be representative. On the other hand, if particles from a site or sample exhibit a range of characteristics, each one might allow for more information related to nuclear forensics needs. At LANL, a number of uranium oxide samples prepared under typical industrial processes were available for analysis. Bulk analysis did well in characterizing most of these compounds, but some were inconclusive or unclear due to their heterogeneity. One sample in particular was composed of two types of material, black particles and orange particles. In order to

evaluate MFS for particle analysis and answer related questions concerning particle versus bulk, these materials were separated and each type analyzed with various techniques. Analyses pertinent to this work included pXRD, μ-XRF, and μ-EXAFS. Based on the presence of transition particles and the limited information on the samples' original syntheses, it was postulated that the sample had been heated partially outside a stainless steel tube furnace. This scenario was replicated on a smaller scale and was successful in doing so. The replicated material was similar in appearance and chemistry to the industrially prepared sample. This evaluation was successful in determining information about the source of the original sample, verifying that the two types of particles likely originated from the same starting material, showing how MFS particle analysis can aid nuclear forensics investigations, and opening possibilities for new experiments and signatures related to MFS.

Other particle investigations often involve analysis of environmental samples. Actinides are mostly present in the environment from activities associated with the nuclear fuel cycle and weapons accidents. One accident involved a fire at the McGuire Air Force Based BOMARC Site. Uranium and plutonium were spread by the fire and post-fire activities. Sampling was performed and particles had been previously studied with a number of techniques. Those studies were mostly focused on evaluations related to traditional nuclear forensics (i.e. localization, sample preparation, forensics conclusions). Studies on actinide particles from similar sites have lacked complete analysis on the basis of chemical speciation. In one experiment, the author analyzed two BOMARC uranium/plutonium particles with μ-XRF, μ-XRD, and μ-EXAFS spectroscopy. Analysis with μ-XRF implied two types of

mixing in the fire. Particle 1 seemed to have been mixed with a combination of extensive mixing in some areas (the top half of the particle showed that uranium and plutonium were quite homogeneous) and less extensive mixing of separate domains (plutonium and uranium on the bottom half of the particle and minor elements throughout the particle were heterogeneously mixed), while Particle 2 was extensively mixed with respect to all observed elements. These results allow for conclusions about proximity of elements before and during the fire, temperatures, and components. X-ray diffraction was useful in phase identification, indicating a cubic crystalline for both plutonium and uranium. This was further evidenced in EXAFS spectroscopy, which showed plutonium was in a PuO_{2+x} form and uranium in a UO_2-U_4O_9 form. Considering the fire, suppression, and weathering exposure of the particles, a reduced uranium species was initially somewhat surprising. However, previous studies on mixtures of uranium and stable tetravalent species showed that this is fairly common. This is an interesting aspect of uranium chemistry that has not been studied extensively in the literature.

The milling analysis was a very basic analysis of the effects of milling UO_2 on particle size distribution, morphology, and quality of pXRD and EXAFS spectroscopy results, whether from oxidation, particle damage, or particle size. This study showed that laser scattering particle size distribution and SEM should be conducted in tandem when analyzing for particle agglomeration and particle size distribution. Sample preparation is less important for those techniques, but less manipulation should be conducted on real world samples so that they better represent the source term. X-ray diffraction analyses showed that less manipulation is ideal for the most

resolved peaks. Crystallite size calculation was consistent with trends in particle size, but that could be due to disordering or oxidation of materials through the treatments applied. Unfortunately the EXAFS data did not imply an optimal sample preparation procedure, so traditional preparations will be used until these experiments are repeated.

These studies were successful in demonstrating the utility in applying MFS to nuclear forensics. These studies have outlined possibilities for fingerprinting pre-detonation nuclear materials. With more work, analyses that fall under MFS can suggest processing conditions or routes, geologic origins of ores, and maybe even pinpoint storage conditions when more information is available. These types of analyses can also aid in determining if two samples originated from the same source. Furthermore, MFS techniques can be used to investigate particles, a vital ability in nuclear forensics. Particle analysis can suggest origins by revealing correlated elements or determining chemical speciation. This type of information is valuable alone, but above all, MFS results must be combined with more conventional analyses of nuclear materials for nuclear forensics information. This combination ensures that the most information possible is presented to decision makers when necessary. The application of MFS depends highly on the specific scenario in question. The techniques used in this work didn't deviate much; chemical speciation, morphology, and, and trace analysis were the most common. However, one of the most beneficial outcomes of this work is the presentation of a number of different experiments relating to nuclear forensics. The few scenarios presented illustrate

how MFS can be applied a number of ways depending on what is required and sought after.

7.2 Recommendations for Future Work

The work presented herein has expanded knowledge of basic chemical behavior of some actinides under a number of scenarios, established a basis for application of MFS to nuclear forensics analyses, and highlighted the importance of combining a melee of techniques to do so. There still remains a large amount of work made possible by some of this research. Although the experiments discussed provided insight into the aforementioned areas, they also revealed areas in which more effort can be concentrated to expand this field.

For the aging of materials, this study used four sets of conditions based on a range of common atmospheric conditions. These were a good starting point, but if nuclear forensics information is the ultimate goal, conditions more applicable to current proliferation concerns should be used instead. For example, there are specific countries or regions where proliferation is a concern; mimicking those specific climates may be useful for the forensics community. Here it was shown that using a lower temperature slowed down aging, even when a higher relative humidity was used. If only information related to basic chemical is desired, lower temperatures should be used so that the changes are seen more slowly. Finally, these experiments implied different mechanisms for different aging conditions. These experiments should be repeated with more data points taken with techniques that are more accessible (pXRD and SEM for example).

Particle analysis has become more common in environmental and nuclear forensics scenarios. This work was successful in showing the analysis of particles from two different scenarios. For the heterogeneous sample, several possibilities for future experiments were mentioned. One centers on analysis of contaminants through a process. Whether that process is a heating in a tube furnace, synthesis at different temperatures, a given precipitation, or separation, all of these techniques likely affect trace content. Some may affect it more than others, or to a greater degree for a given element(s). Evaluating these trends is an obvious next step for answer nuclear forensics questions related to process conditions. In addition, analysis of particle size based on process conditions should also be evaluated. Environmental particles exhibit a wide array of chemical speciation, and are highly dependent on the source term. If EXAFS spectroscopy experimental time allocation allows for it, the particles from the BOMARC study should be further analyzed. Particles should be measured at lower temperature for higher quality data and at more locations on the particles to determine if other areas provide better data. More particles from the site (and other sites) should be evaluated to expand the pool of knowledge in these areas. Moreover, more detailed analyses in a closed forum should be performed to properly evaluate the tasks outlined for the experiment. Finally, more experiments should be conducted on uranium oxides and how to prepare them for multiple MFS analysis techniques. Sonication, grinding, and milling should be further evaluated using more treatment times, bead sizes, and analysis methods. For EXAFS spectroscopy, a more consistent preparation will be used for better comparison.

This research was funded in part by the University of Nevada, Las Vegas Radiochemistry program and LANL under a Laboratory Directed Research and Development project. The work was performed under the Nuclear Forensics Graduate Fellowship Program, which is sponsored by the U.S. Department of Homeland Security, Domestic Nuclear Detection Office and the U.S. Department of Defense, Defense Threat Reduction Agency. In addition, LANL research funding also contributed to this work.

BIBLIOGRAPHY

1. May, M., Nuclear Forensics: Role, State of the Art, Program Needs. AAAS, 2008.
2. Security, D.o.H. National Technical Nuclear Forensics Center 2012; Available from: http://www.dhs.gov/xabout/structure/gc_1298646190060.shtm.
3. Betti, M., G. Tamborini, and L. Koch, Use of secondary ion mass spectrometry in nuclear forensic analysis for the characterization of plutonium and highly enriched uranium particles. Analytical Chemistry, 1999. 71(14): p. 2616-2622.
4. Koch, L., Traces of Evidence: Nuclear Forensics and Illicit Trafficking, in IAEA Bulletin2003, IAEA.
5. Mayer, K., M. Wallenius, and T. Fanghanel, Nuclear forensic science - From cradle to maturity. Journal of Alloys and Compounds, 2007. 444: p. 50-56.
6. Mayer, K., M. Wallenius, and I. Ray, Nuclear forensics - a methodology providing clues on the origin of illicitly trafficked nuclear materials. Analyst, 2005. 130(4): p. 433-441.
7. Orlov, A.V., Illicit Nuclear Trafficking & the New Agenda, in IAEA Bulletin2004, IAEA.
8. Wallenius, M., K. Mayer, and I. Ray, Nuclear forensic investigations: Two case studies. Forensic Science International, 2006. 156(1): p. 55-62.
9. WNA. Uranium Enrichment. 2011 December 2011; Available from: http://www.world-nuclear.org/info/inf28.html.

10. Gostic, R., Characterization of Plutonium Particles Originating from the BOMARC Accident - 1960, in Chemistry2010, University of Nevada Las Vegas: Las Vegas, NV.
11. WNA. The Nuclear Fuel Cycle. 2011 December 2011; Available from: http://www.world-nuclear.org/info/inf03.html.
12. Wilson, P.D., The Nuclear Fuel Cycle: From Ore to Waste1996: Oxford Science Publications.
13. Burns, P.C., The Crystal Chemistry of Uranium. Reviews in Mineralogy 1999. 38: p. 23-90.
14. Finch, R. and T. Murakami, Systematics and Paragenesis of Uranium Minerals. Reviews in Mineralogy <D>, 1999. 38: p. 91-179.
15. Christensen, D.H., Naturally Occurring Radioactive Materials from Uranium Mining (Environmental Science, Engineering, and Technology)2011: Nova Science Publishers, Inc. 298.
16. Jones, M.J., Geology, Mining, and Extractive Processing of Uranium: Symposium Proceedings1976: Institution of Mining and Metallurgy. 171.
17. Larsen, R.P., Dissolution of Uranium Metal and its Alloys. Analytical Chemistry, 1959. 31(4): p. 545-549.
18. Morss, L.R., N.M. Edelstein, and J. Fuger, The Chemistry of the Actinide and Transactinide Elements. 4 ed2011: Springer Netherlands.
19. Maerli, B.M., Components of Naval Nuclear Fuel Transparency, in NATO-EAPC Fellowship Report2001, Norweigian Institute of International Affairs.

20. Hesketh, R., Uranium Enrichment and Nuclear Weapon Proliferation. New Scientist, 1983. 98(1362): p. 795-795.

21. Clark, D.L., D.R. Janecky, and L.J. Lane, Science-Based Cleanup of Rocky Flats, in Physics Today2006.

22. Eriksson, M., et al., Source term identification of environmental radioactive Pu/U particles by their characterization with non-destructive spectrochemical analytical techniques. Spectrochimica Acta Part B-Atomic Spectroscopy, 2005. 60(4): p. 455-469.

23. Salbu, B., O.C. Lind, and L. Skipperud, Radionuclide speciation and its relevance in environmental impact assessments. Journal of Environmental Radioactivity, 2004. 74(1-3): p. 233-242.

24. Nuclear Forensics and Attribution Act, in H.R. 7302010.

25. Nonproliferation, B.o.I.S.a. Nuclear Forensics. 2012 March 28, 2012]; Available from: http://www.state.gov/t/isn/rls/fs/187035.htm.

26. Document, J.S. Statement of Activity and Cooperation to Counter Nuclear Smuggling. in 2012 Nuclear Security Summit. 2012. Seoul, South Korea.

27. Waseda, Y., E. Matsubara, and K. Shinoda, X-Ray Diffraction Crystallography: Introduction, Examples, and Solved Problems. 1st ed2011: Springer.

28. Bressler, C., R. Abela, and M. Chergui, Exploiting EXAFS and XANES for time-resolved molecular structures in liquids. Zeitschrift Fur Kristallographie, 2008. 223(4-5): p. 307-321.

29. Conradson, S.D., et al., X-ray Absorption Fine Structure Spectroscopy Determines Local Structure and Bonding in Actinide-Oxide Structural

Variants, in Actinide Research Quarterly2004, Nuclear Materials Technology/Los Alamos National Laboratory

30. Newville, M., Fundamentals of XAFS, 2004, Consortium for Advanced Radiation Sources: Chicago, IL.

31. Teo, B.K., EXAFS: Basic Principles and Data Analysis. Inorganic Chemistry Concepts. Vol. 9. 1986: Springer-Verlag.

32. Hausen, D.M., Characterizing and classifying uranium yellow cakes: A background. Jom-Journal of the Minerals Metals & Materials Society, 1998. 50(12): p. 45-47.

33. Tsuboi, M., M. Terada, and T. Shimanouchi, Optically Active Lattice Vibrations of Alpha Uranium Trioxide. Journal of Chemical Physics, 1962. 36(5): p. 1301-&.

34. Siegel, S. and H.R. Hoekstra, Examination of Symmetry of Alpha Uranium Trioxide. Inorganic & Nuclear Chemistry Letters, 1971. 7(6): p. 497-&.

35. Choppin, G.R., Actinide speciation in the environment. Radiochimica Acta, 2003. 91(11): p. 645-649.

36. Choppin, G.R. and A. Morgenstern, Distribution and movement of environmental plutonium. Plutonium in the Environment, ed. A. Kudo. Vol. 1. 2001. 91-105.

37. Rommel, H. and J.I. Kim, Colloid Generation and Solid-Liquid Distribution of Transuranic Elements in Natural Aquifter Systems. Application of Distribution Coefficients to Radiological Assessment Models1986: Elsevier.

38. Choppin, G.R., Aspects of Plutonium Solution Chemistry Acs Symposium Series, 1983. 216: p. 213-230.

39. Vallet, V., Actinide quantum chemistry: A modeling tool to study coordination chemistry and thermodynamics. Abstracts of Papers of the American Chemical Society, 2004. 227: p. U82-U82.

40. Kudo, A., Plutonium in the Environment. Radioactivity in the Environment, ed. M.S. Baxter. Vol. Volume 1. 2000, Oxford, UK: Elsevier.

41. Choppin, G.R. and P.J. Wong, The chemistry of actinide behavior in marine systems. Aquatic Geochemistry, 1998. 4(1): p. 77-101.

42. Dahlman, R.C., E.A. Bondietti, and L.D. Eyman, Biological Pathways and Chemical Behavior of Plutonium and Other Actinides in the Environment. Acs Symposium Series, 1976(35): p. 47-80.

43. Molero, J., et al., Particulate Distribution of Plutonium and Americium in Surface Waters from the Spanish Mediterranean Coast. Journal of Environmental Radioactivity, 1995. 28(3): p. 271-283.

44. Choppin, G.R., Redox Speciation of Plutonium in Natural Waters Journal of Radioanalytical and Nuclear Chemistry-Articles, 1991. 147(1): p. 109-116.

45. Morse, J.W. and G.R. Choppin, The Chemistry of Transuranic Elements in Natural Waters. Reviews in Aquatic Sciences, 1991. 4(1): p. 1-22.

46. Orlandini, K.A., W.R. Penrose, and D.M. Nelson, Pu(V) as the Stable Form of Oxidized Plutonium in Natural Waters. Marine Chemistry, 1986. 18(1): p. 49-57.

47. Watters, R.L., The Environmental Behavior of Plutonium. Health Physics, 1980. 39(6): p. 1040-1040.

48. Baes, C.F. and R.E. Mesmer, The Thermodynamics of Cation Hydrolysis. American Journal of Science, 1981. 281(7): p. 935-962.

49. Grenthe, I., et al., Redox Potentials and Redox Reactions in Deep Groundwater Systems. Chemical Geology, 1992. 98(1-2): p. 131-150.

50. Guillaumont, R., Special issue - Speciation: Databases and analytical methods - Preface. Radiochimica Acta, 2003. 91(11).

51. Choppin, G.R., Solution Chemistry of the Actinides. Radiochimica Acta, 1983. 32(43).

52. Kim, J.I., Chemical Behaviour of Transuranic Elements in Natural Aquatic Systems, in Handbook on the Physics and Chemistry of the Actinides, A.J. Freeman and C. Keller, Editors. 1986, Elsevier.

53. Kim, J.I., Actinide Colloid Generation in Groundwater. Radiochimica Acta, 1991. 52-3: p. 71-81.

54. Kim, J.I., et al., Hydrolysis Reactions of Am(III) and Pu(VI) Ions in Near Neutral Solutions. Acs Symposium Series, 1984. 246(7).

55. Kim, J.I., G. Buckau, and R. Klenze, Natural Colloids and Generation of Actinide Pseudocolloids in Groundwater. Natural Analogues in Radioactive Waste Disposal, 1987.

56. Kim, J.I., G. Buckau, and W. Zhuang, Humic colloid generation of transuranic elements in groundwater and their migration behaviour. Scientific Basis for Nuclear Waste Management X, 1987: p. 747-56.

57. Lierse, C., W. Treiber, and J.I. Kim, Hydrolysis Reactions of Np(V). Radiochimica Acta, 1985. 38(1): p. 27-28.

58. Lloyd, M.H. and R.G. Haire, The Chemistry of Plutonium in Sol-Gel Processes. Radiochimica Acta, 1978. 25(3-4): p. 139-148.

59. Olofsson, K., et al., Formation and Properties of Actinide Colloids, 1983, SKBF/KBS.

60. Rai, D., R.J. Serne, and J.L. Swanson, Solution Species of Plutonium in the Environment. Journal of Environmental Quality, 1980. 9(3): p. 417-420.

61. Righetto, L., et al., Surface Interactions of Actninides with Alumina Colloids. Radiochimica Acta, 1988. 44-5: p. 73-75.

62. Yariv, S. and H. Cross, Geochemistry of Colloid Systems1979: Springer.

63. Cleveland, J.M., Critical Review of Plutonium Equilibria of Environmental Concern Jenne, Everett A.1979. 321-338.

64. Pentreath, R.J., The Analysis of Pu in Environmental Samples - A Brief Historical Perspective. Applied Radiation and Isotopes, 1995. 46(11): p. 1279-1285.

65. Vongunten, H.R. and P. Benes, Speciation of Radionuclides in the Environment. Radiochimica Acta, 1995. 69(1): p. 1-29.

66. Silva, R.J. and H. Nitsche, Actinide environmental chemistry. Radiochimica Acta, 1995. 70-1: p. 377-396.

67. Wimmer, H., J.I. Kim, and R. Klenze, A Direct Speciation of Cm(III) in Natural Aquatic Systems by TRLFS. Radiochimica Acta, 1992. 58-9: p. 165-171.

68. Lis, S. and G.R. Choppin, Luminescence Lifetimes of Aqueous Europium Perchlorate, Chloride, and Nitrate Solutions. Materials Chemistry and Physics, 1992. 31(1-2): p. 159-161.

69. Choppin, G.R. and Z.M. Wang, Correlation between ligand coordination number and the shift of the F-7(0)-5D(0) transition frequency in Europium(III) complexes. Inorganic Chemistry, 1997. 36(2): p. 249-252.

70. Degueldre, C., et al., Colloids in Water from a Subsurface Fracture in Granitic Rock, Grimsel Test Site, Switzerland. Geochimica Et Cosmochimica Acta, 1989. 53(3): p. 603-610.

71. Webb, P.A., A Primer on Particle Sizing by Static Laser Light Scattering. Micromeritics Technical Workshop Series, 2000.

72. Buchinger, F., et al., Nuclear ground state properties of strontium isotopes by laser spectroscopy. AIP Conference Proceedings, 1988(164): p. 197-200.

73. Knopp, R., F.J. Scherbaum, and J.I. Kim, Laser induced breakdown spectroscopy (LIBS) as an analytical tool for the detection of metal ions in aqueous solutions. Fresenius Journal of Analytical Chemistry, 1996. 355(1): p. 16-20.

74. Scherbaum, F.J., R. Knopp, and J.I. Kim, Counting of particles in aqueous solutions by laser-induced photoacoustic breakdown detection. Applied Physics B-Lasers and Optics, 1996. 63(3): p. 299-306.

75. Morss, L.R., et al., The Chemistry of the Actinides and Transactinides, 4th Ed. 4th ed. Vol. 1. 2011: Springer. 3682.

76. Aronson, S., R.B. Roof, and J. Belle, Kinetic Study of the Oxidation of Uranium Dioxide. Journal of Chemical Physics, 1957. 27(1): p. 137-144.

77. Geng, H.Y., et al., Stability mechanism of cuboctahedral clusters in UO(2+x): First-principles calculations. Physical Review B, 2008. 77(18).

78. Hongliang, S., et al., Electronic structures and mechanical properties of uranium monocarbide from first-principles LDA + U and GGA + U calculations. Physics Letters A, 2009. 373(39).

79. McEachern, R.J., A review of kinetic data on the rate of U3O7 formation on UO2. Journal of Nuclear Materials, 1997. 245(2-3): p. 238-247.

80. Andersson, D.A., et al., Cooperativity among defect sites in AO(2+x) and A(4)O(9) (A=U,Np,Pu): Density functional calculations. Physical Review B, 2009. 79(2).

81. Andersson, D.A., et al., Role of di-interstitial clusters in oxygen transport in UO2+x from first principles. Physical Review B, 2009. 80(6).

82. Andersson, D.A., et al., Stability and migration of large oxygen clusters in UO2+x: Density functional theory calculations. J. Chem. Phys., 2012. 136(23): p. 10.

83. Desgranges, L., et al., Neutron Diffraction Study of the in Situ Oxidation of UO2. Inorganic Chemistry, 2009. 48(16): p. 7585-7592.

84. McEachern, R.J. and P. Taylor, A review of the oxidation of uranium dioxide at temperatures below 400 degrees C. Journal of Nuclear Materials, 1998. 254(2-3): p. 87-121.

85. Rousseau, G., et al., Contribution of the synchrotron diffraction study of the oxidation of uranium dioxide at 250 degrees C. Journal De Physique Iv, 2004. 118: p. 127-134.

86. Taylor, P., et al., The influence of specimen roughness on the rate of formation of U3O8 on UO2 in air at 250 degrees C. Journal of Nuclear Materials, 1998. 256(2-3): p. 213-217.

87. Ferriss, E.D.A., et al., UO2 corrosion in an iron waste package. Journal of Nuclear Materials, 2009. 384(2): p. 130-139.

88. Finch, R.J., et al., Oxidative corrosion of spent UO2 fuel in vapor and dripping groundwater at 90 degrees C, in Scientific Basis for Nuclear Waste Management Xxii, D.J.L.J.H. Wronkiewicz, Editor 1999. p. 431-438.

89. Hodgson, G., Uranium Dioxide Production, 1991, British Nuclear Fuels plc: United Kingdom.

90. Shoesmith, D.W., Fuel corrosion processes under waste disposal conditions. Journal of Nuclear Materials, 2000. 282(1): p. 1-31.

91. Leenaers, A., et al., Oxidation of spent UO2 fuel stored in moist environment. Journal of Nuclear Materials, 2003. 317(2-3): p. 226-233.

92. Conradson, S.D., et al., Charge distribution and local structure and speciation in the UO2+x and PuO2+x binary oxides for x <= 0.25. Journal of Solid State Chemistry, 2005. 178(2): p. 521-535.

93. Conradson, S.D., et al., Local structure and charge distribution in the UO2-U4O9 system. Inorganic Chemistry, 2004. 43(22): p. 6922-6935.

94. Totemeier, T.C., A review of the corrosion and pyrophoricity behavior of uranium and plutonium, 1995, U.S. DOE ANL.

95. Haschke, J.M., T.H. Allen, and L.A. Morales, Reaction of plutonium dioxide with water: Formation and properties of PuO2+x. Science, 2000. 287(5451): p. 285-287.

96. Conradson, S.D., et al., Speciation and unusual reactivity in PuO2+x. Inorganic Chemistry, 2003. 42(12): p. 3715-3717.

97. Sunder, S. and N.H. Miller, XPS and XRD studies of (Th,U)O-2 fuel corrosion in water. Journal of Nuclear Materials, 2000. 279(1): p. 118-126.

98. Lind, O.C., Characterisation of radioactive particles in the environment using advanced techniques, 2006: Norway.

99. Salbu, B., Source-related characteristics of radioactive particles: A review. Radiation Protection Dosimetry, 2000. 92(1-3): p. 49-54.

100. Salbu, B., Actinides Associated with Particles, in Plutonium in the Environment, A. Kudo, Editor 2001. p. 121-138.

101. Salbu, B., et al., High energy X-ray microscopy for characterisation of fuel particles. Nuclear Instruments & Methods in Physics Research Section a-Accelerators Spectrometers Detectors and Associated Equipment, 2001. 467: p. 1249-1252.

102. IAEA, Radioactive Particles in the Environment: Sources, Particle Characterization, and Analytical Techniques, 2011, IAEA: Vienna, Austria.

103. Conradson, S.D., et al., X-Ray Absorption Spectroscopy of Plutonium Particles at the Rocky Flats US Nuclear Weapons Production Site, in Actinide

Nanoparticle Research, S.N. Kalmykov and M.A. Denecke, Editors. 2011, Springer.

104. Crocker, G.R., J.D. O'Connor, and E.C. Freiling, Physical and Radiochemical Properties of Fallout Particles. Health Physics, 1966. 12.

105. Pellow, P.G.D., et al., Measurements on the In Vitro Dissolution of Hot Particles from Muroroa Atoll, 1998.

106. (UNSCEAR), U.N.S.C.o.t.E.o.A.R., Report 2000: Sources and Effects of Ionizing Radiation, 2000, UNSCEAR: New York.

107. DOE, U.S., Linking Legacies - Connecting the Cold War Nuclear Weapons Production Processes to their Environmental Consequences, 1997, U.S. DOE Office of Environmental Management. p. 36-37.

108. Burns, P.A., et al., Plutonium Contaminated Fragments at the Taranaki Site at Maralinga, 1986, Australian Radiation Laboratory.

109. Burns, P.A., et al., Characteristics of Plutonium and Americium Contamination at the Former UK Atomic Weapons Test Ranges at Maralinga and EMU. Applied Radiation and Isotopes, 1995. 46(11): p. 1099-1107.

110. Cooper, M.B., et al., Characterization of Pu Contamination at the Former Nuclear Weapons Testing Range at Maralinga in South Australis. Journal of Radioanalytical and Nuclear Chemistry, 1994. 177(1): p. 161-184.

111. Lokan, H., Residual Radioactive Contamination at Maralinga and Emu, 1985, Australian Radiation Laboratory.

112. Hamilton, T.F., et al., Frequency distribution, isotopic composition and physical characterization of plutonium-bearing particles from the Fig-Quince

zone on Runit Island, Enewetak Atoll. Journal of Radioanalytical and Nuclear Chemistry, 2009. 282(3): p. 1019-1026.

113. Jernstrom, J., et al., Characterization and source term assessments of radioactive particles from Marshall Islands using non-destructive analytical techniques. Spectrochimica Acta Part B-Atomic Spectroscopy, 2006. 61(8): p. 971-979.

114. Simon, S.L., et al., A Comparison of Macroscopic and Microscopic Measurements of Plutonium in Contaminated Soil from the Republic of the Marshall Islands. Journal of Radioanalytical and Nuclear Chemistry-Articles, 1995. 194(1): p. 197-205.

115. IAEA, Preliminary Investigation of the Morphology and Composition of Some Hot Particles Collected at the Colette Motu of Mururoa Atoll by Optical Microscopy and X Ray Microfluorescence, 2000, IAEA.

116. Kvasnikova, E., Radiochemical and Physical Characterization of Radioactive Particles in the Environment, 2003, IAEA: Moscow.

117. Yamamoto, M., T. Tsukatani, and Y. Katayama, Residual radioactivity in the soil of the semipalatinsk nuclear test site in the former USSR. Health Physics, 1996. 71(2): p. 142-148.

118. Smith, J.N., et al., (PU)-P-239,240 transport into the Arctic Ocean from underwater nuclear tests in Chernaya Bay, Novaya Zemlya. Continental Shelf Research, 2000. 20(3): p. 255-279.

119. Toivonen, H., et al., A Nuclear Incident at a Power Plant in Sosnovyy-Bor, Russia. Health Physics, 1992. 63(5): p. 571-573.

120. Wakeford, R., The Windscale reactor accident-50 years on. Journal of Radiological Protection, 2007. 27(3): p. 211-215.

121. Devell, L., Nuclide Composition of Chernobyl Hot Particles. Bergbau und Industriemuseum, 1988. 16: p. 23-34.

122. Kashkarov, L.L., et al., Hot Particles in Soil from Chernobyl AES Region. Radiation Measurements, 1995. 25(1-4): p. 413-414.

123. Bielewski, M., et al., Nondestructive spectrometric study on a radioactive particle embedded in a marine sediment. Microscopy and Microanalysis, 2008. 14(4): p. 321-327.

124. Danesi, P.R., et al., Depleted uranium particles in selected Kosovo samples. Journal of Environmental Radioactivity, 2003. 64(2-3): p. 143-154.

125. Lind, O.C., et al., Solid state speciation and potential bioavailability of depleted uranium particles from Kosovo and Kuwait. Journal of Environmental Radioactivity, 2009. 100(4): p. 301-307.

126. Salbu, B., et al., Oxidation states of uranium in depleted uranium particles from Kuwait. Journal of Environmental Radioactivity, 2005. 78(2): p. 125-135.

127. IAEA Illicit Trafficking Database, 2004, IAEA.

128. Gostic, J., Evaluation of Extraction Chromatography Resins for Rapid Actinide Analysis, in Chemistry2009, University of Nevada Las Vegas: Las Vegas, NV.

129. Obermoller, H.R., D.A. White, and S. Lagos, Resin Adsorption of Anionic Chloride Complexes for Uranium Isotope Chemical Exchange Reactions. Hydrometallurgy, 1991. 27(1): p. 63-74.

130. CRC Handbook of Chemistry and Physics. 89 ed, ed. D.R. Lide2008-2009: CRC Press. 2736.

131. Anovitz, L.M., et al., The effect of changes in relative humidity on the hydration rate of Pachuca obsidian. Journal of Non-Crystalline Solids, 2006. 352(52-54): p. 5652-5662.

132. Conradson, S.D., XAFS: A Technique to Probe Local Structure. Los Alamos Science, 2000(26).

133. Wiedemann, H., Synchrotron Radiation2002: Springer.

134. Rehr, J.J., A.L. Ankudinov, and B. Ravel, Feff Project, 2002-Present, University of Washington Phyisics Department.

135. Ankudinov, A.L. and J.J. Rehr, Relativistic calculations of spin-dependent x-ray-absorption spectra. Physical Review B, 1997. 56(4): p. R1712-R1715.

136. Stern, E.A., Number of Relevant Independent Points in X-Ray Absorption Fine Structure Spectra. Physical Review B, 1993. 48(13): p. 9825-9827.

137. Jade 9.3, 2010, Materials Data Incorporated: Livermore, CA.

138. PD-4+, 2010, International Center for Diffraction Data: Newton Square, PA.

139. Burger, S., L.R. Riciputi, and D.A. Bostick, Determination of impurities in uranium matrices by time-of-flight ICP-MS using matrix-matched method. Journal of Radioanalytical and Nuclear Chemistry, 2007. 274(3): p. 491-505.

140. Zimmer, M., W.S. Kinman, and S. Baldwin, A Novel Method for the Measurement of Trace Elements in Uranium Rich Materials. Journal of radioanalytical and Nuclear Chemistry, under review, 2012.

141. Lide, D.R. and H.P.R. Frederiske, The CRC Handbook of Chemistry and Physics 78th Ed1997: CRC-Press. 2512.

142. McGraw-Hill, McGraw-Hill Concise Encyclopedia of Science and Technology, Sixth Edition. Vol. 1. 2009: McGraw-Hill Professional. 2688.

143. Felmy, A.R., K.J. Cantrell, and S.D. Conradson, Plutonium contamination issues in Hanford soils and sediments: Discharges from the Z-Plant (PFP) complex. Physics and Chemistry of the Earth, 2010. 35(6-8): p. 292-297.

144. Henke, K.R., J.C. Bryan, and M.P. Elless, Structure and powder diffraction pattern of 2,4,6-trimercapto-s-triazine, trisodium salt (Na3S3C3N3 center dot 9H2O). Powder Diffraction, 1997. 12(1): p. 7-12.

145. Calvert, C., Design, Synthesis, and Characterization of Materials for Controlled Line Deposition, Environmental Remediation, and Doping of Porous Manganese Oxide Material2009, Ann Arbor, MI: ProQuest.

146. Ericson, A., et al., Structural Characterization by EXAFS Spectroscopy of the Binuclear Iron Center in Protein-A of Methane Monoxygenase from Methylococcus-Capsalutus (Bath). Journal of the American Chemical Society, 1988. 110(7): p. 2330-2332.

147. Stumpf, S., et al., TRLFS and EXAFS investigations of lanthanide and actinide complexation by triflate and perchlorate in an ionic liquid. Radiochimica Acta, 2008. 96(1): p. 1-10.

148. Weller, M.T., M.E. Light, and T. Gelbrich, Structure of uranium(VI) oxide dihydrate, UO3 center dot 2H(2)O; synthetic meta-schoepite

(UO2)(4)O(OH)(6)center dot 5H(2)O. Acta Crystallographica Section B-Structural Science, 2000. 56: p. 577-583.

149. Clark, D.L., et al., Chemical speciation of the uranyl ion under highly alkaline conditions. Synthesis, structures, and oxo ligand exchange dynamics. Inorganic Chemistry, 1999. 38(7): p. 1456-1466.

150. Masaki, N. and K. Doi, Analysis of the Superstructure of U4O9 by Neutron Diffraction. Acta Crystallographica Section B-Structural Crystallography and Crystal Chemistry, 1972. B 28(MAR15): p. 785-&.

151. Loopstra, B.O., CRYSTAL-STRUCTURE OF ALPHA-U3O8. Journal of Inorganic & Nuclear Chemistry, 1977. 39(9): p. 1713-1714.

152. Greaves, C. and B.E.F. Fender, Structure of Alpha-UO3 by Neutron and Electron Diffraction. Acta Crystallographica Section B-Structural Science, 1972. 28(DEC15): p. 3609-3614.

153. Applied Test Systems, I., Furnaces Laboratory and Industrial, I.P.B. Applied Test Systems, Editor 2003, Applied Test Systems, Inc: Butler, PA.

154. McCulla, W.H., et al., Boeing Michigan Aeronautical Research Center (BOMARC) Missile Accident Site Mitigation Review, 1996, Los Alamos National Laboratory: Los Alamos, NM.

155. Rademacher, S.E., J.L. Hubbell, and G.R. Cicotte, Boing Michigan Aeronautical Research Center (BOMARC) Missile Shelters and Bunkers Scoping Suvery Workplan, U. AFIOH, Editor 2007, USAF AFIOH: Brooks City, TX.

156. Speed, T., A Correlation for the 21st Century. Science, 2011. 334: p. 2.

157. Sedgwick, P., Pearson's correlation coefficient. British Medical Journal, 2012. 344.

158. Belin, R.C., et al., New hermetic sample holder for radioactive materials fitting to Siemens D5000 and Bruker D8 X-ray diffractometers: application to the Rietveld analysis of plutonium dioxide. Journal of Applied Crystallography, 2004. 37: p. 1034-1037.

159. Barrett, S.A., et al., The Preparation and Structure of Barium Uranium Oxide BAUO3+X. Acta Crystallographica Section B-Structural Science, 1982. 38(NOV): p. 2775-2781.

160. Ravel, B., Introduction to EXAFS Experiments and Theory, 2000, University of Washington.

161. Bunker, G., Introduction to XAFS: A Practical Guide to X-Ray Absorption Fine Structure2010: Cambridge University Press.

162. Booth, C.H. and F. Bridges, Improved self-absorption correction for fluorescence measurements of extended X-ray absorption fine-structure. Physica Scripta, 2005. T115: p. 202-204.

163. Patterson, A.L., The Scherrer formula for x-ray particle size determination. Physical Review, 1939. 56(10): p. 978-982.

VITA

Graduate College
University of Nevada, Las Vegas
Dallas David Reilly

Degrees:
Bachelor of Arts, Chemistry, 2004
Carthage College

Dissertation Title: Molecular Forensic Science Analysis of Nuclear Materials

Special Honors and Awards:
Nuclear Forensics Graduate Fellow
Glenn T. Seaborg Research Institute Summer Research Fellow, Los Alamos National Laboratory

Dissertation Examination Committee:
Chairperson, Kenneth R. Czerwinski, Ph.D.
Committee Member, Marianne P. Wilkerson, Ph. D.
Committee Member, Steven D. Conradson, Ph. D.
Committee Member, Julie M. Gostic, Ph. D.
Committee Member, Kenton J. Moody, Ph. D.
Graduate Faculty Representative, Ralf Sudowe, Ph. D.